

# A Search for New Physics in the Dilepton Channel with the ATLAS Detector at the LHC

A Dissertation

Presented to

The Faculty of the Graduate School of Arts and Sciences

Brandeis University

Physics

Gabriella Sciolla, Department of Physics, Advisor

In Partial Fulfillment

of the Requirements for the Degree

Doctor of Philosophy

by

Eric Andrew Vitus Fitzgerald

February, 2014



The signed version of this form is on file in the Graduate School of Arts and Sciences.

This dissertation, directed and approved by Eric Andrew Vitus Fitzgerald's committee, has been accepted and approved by the Graduate Faculty of Brandeis University in partial fulfillment of the requirements for the degree of:

**DOCTOR OF PHILOSOPHY**

Malcolm Watson, Dean

Graduate School of Arts and Sciences

Dissertation Committee:

Gabriella Sciolla, Department of Physics, Chair

Craig Blocker, Department of Physics

Frank Taylor, Department of Physics, Massachusetts Institute of Technology

©Copyright by

Eric Andrew Vitus Fitzgerald

2014

For Stephanie.

# Acknowledgments

I would like to give my humble gratitude to my advisor Prof. Gabriella Sciolla for giving me a second chance to finish my Ph.D. Her motivation and support over the last two and half years to finish this research and thesis has been absolutely instrumental for me. She always knew the right questions to ask, and I am a better physicist because of her guidance.

There are so many people at Brandeis to thank! Of course, our particle physics group has been wonderful to work with. Dr. Rozmin Daya, who was the guiding hand for all my  $Z'$  work. Stefano Zambito and Alessio Venturini, those uncountable lunches and coffees at the CERN canteen talking physics and anything else were useful beyond measure. Prof. Craig Blocker, who sat on the committee, read this whole thesis, and gave excellent feedback. Prof. Jim Bensinger and Dr. Christoph Amelung, who answered every question I ever had about ATLAS muons. And all the current and former students, Dr. Scott Aefsky, Dr. Dan Pomeroy, Dr. Serdar Gozpinar, Lou Bianchini, Laurel Coffey, Keith Zengel, Glenn Amundsen. You made the graduate school experience much more bearable.

Thanks as well to all the physicists that taught me throughout the years. I began my studies at the University of Oregon, under Prof. David Strom, who introduced me to the world of experimental particle physics. From MIT, I want to specially thank Frank Taylor, who saw me begin my career at ATLAS many years ago and now was able see the completion sitting on the thesis committee. And Prof. Robert Jaffe, who helped in innumerable ways

at MIT.

Last, but never least, I must thank my family, especially my loving and patient wife, Stephanie. Her support throughout my graduate school career has been nothing short of amazing. Our son, Julian, who has been a true joy to watch grow. My parents, Tom & Marianne, who have given me everything I could ask for. My brother, Tim, with whom it's always fun to talk politics and games. And my in-laws, David & MarSi Vitus, who gave me a room of my own.

# Abstract

## A Search for New Physics in the Dilepton Channel with the ATLAS Detector at the LHC

A dissertation presented to the Faculty of  
the Graduate School of Arts and Sciences of  
Brandeis University, Waltham, Massachusetts

by Eric Andrew Vitus Fitzgerald

This thesis presents a search for a new, neutral heavy gauge boson decaying to lepton pairs using data from the ATLAS detector at the LHC. This search is performed in two channels, using both electron-pair and muon-pair final states. The results use the full 2012 ATLAS data set from  $pp$  collisions at a center-of-mass energy of  $\sqrt{s} = 8$  TeV with an integrated luminosity of  $21 \text{ fb}^{-1}$ . No statistically significant signal is found, and limits are placed on a variety of  $Z'$  models. A Sequential Standard Model  $Z'$ , with identical couplings to fermions as the Standard Model  $Z^0$  boson, is excluded at the 95% confidence level for masses lower than 2.79 TeV in the electron channel, 2.53 TeV in the muon channels, and 2.90 TeV with the channels combined. Limits are placed on additional  $Z'$  models based on the grand unification group  $E_6$ , with lower masses ranging from 2.43 to 2.58 TeV.

# Preface

This thesis is the culmination of 10 years of graduate school and study. I may not have enjoyed every minute of that time, but I always strived to learn a little more about how the universe works. It will be a little long in places, but I hope my love of our understanding of particle physics shows through.



# Contents

<b>Abstract</b>	<b>vii</b>
<b>Preface</b>	<b>viii</b>
<b>1 Introduction</b>	<b>1</b>
<b>2 The Standard Model</b>	<b>4</b>
2.1 History - From Dirac to Now . . . . .	4
2.2 Quantum Field Theory . . . . .	8
2.3 The Standard Model . . . . .	50
2.4 New Physics Beyond the Standard Model . . . . .	63
2.5 New Particle Phenomenology . . . . .	71
<b>3 The LHC &amp; ATLAS</b>	<b>79</b>
3.1 History - From Rutherford to Now . . . . .	80
3.2 The Large Hadron Collider . . . . .	84
3.3 The ATLAS Detector . . . . .	94
3.4 Acceptance & Reconstruction at ATLAS . . . . .	123
<b>4 Analysis Event Selection</b>	<b>137</b>
4.1 Data & Monte Carlo Samples . . . . .	138
4.2 $Z'$ Search Requirements . . . . .	143
4.3 Electron Channel . . . . .	155
4.4 Muon Channel . . . . .	165
4.5 Systematic Uncertainties . . . . .	182
<b>5 <math>Z'</math> Search &amp; Limit Setting</b>	<b>186</b>
5.1 History - Prior $Z'$ Searches to Now . . . . .	186
5.2 Bayesian Search & Limit Setting . . . . .	190
5.3 ATLAS Search for a $Z'$ . . . . .	197
5.4 ATLAS Limits on a $Z'$ . . . . .	202

CONTENTS

<b>6</b>	<b>Conclusion</b>	<b>204</b>
<b>A</b>	<b>Drell-Yan Cross Section Corrections</b>	<b>206</b>
A.1	QCD NNLO Corrections . . . . .	207
A.2	EW NLO Corrections . . . . .	210
A.3	Total Corrections . . . . .	213
<b>B</b>	<b>Drell-Yan Systematics</b>	<b>215</b>
B.1	PDF Uncertainty . . . . .	215
B.2	PDF Choice, Scale, and $\alpha_S$ Uncertainty . . . . .	218
B.3	Beam Energy Uncertainty . . . . .	221
<b>C</b>	<b>Electron Scale Factors</b>	<b>222</b>
C.1	Trigger Scale Factors . . . . .	223
C.2	Isolation Scale Factors . . . . .	228
<b>D</b>	<b>Electron Fake Factors</b>	<b>232</b>
D.1	Matrix Method . . . . .	232
D.2	Real Electron Rates . . . . .	236
D.3	Fake Electron Rates . . . . .	237
D.4	Total Fake Background . . . . .	241
<b>E</b>	<b>Muon Resolution</b>	<b>245</b>
E.1	Momentum Resolution . . . . .	245
E.2	Momentum Corrections . . . . .	247
E.3	Two Station Muon Resolution . . . . .	251
E.4	Muon Resolution Systematic Uncertainty . . . . .	254

# List of Tables

3.1	Pseudo-rapidity coverage, granularity, and longitudinal segmentation of the ECAL and Presampler. From [160], Table 1-3. . . . .	112
3.2	Pseudo-rapidity coverage, granularity, and longitudinal segmentation of the Hadronic calorimeters. From [160], Table 1-3. . . . .	115
3.3	The most common unprescaled trigger menu chains for 2012 data taking. From [178], Slide 19. . . . .	126
4.1	Uncertainty on $Z'$ cross sections due to PDF and $\alpha_S$ variations at the 90% C.L. From Appendix F, Table 37 in [217]. . . . .	149
4.2	$K$ -factors obtained for POWHEG DY samples from FEWZ. From [217], Table 2.	151
4.3	Dielectron event yield tables with statistical (top), systematic (middle) and total (bottom) uncertainties. The first column is used to normalize the MC total to the observed data total. . . . .	163
4.4	Dimuon event yield tables for the <b>tight channel</b> with statistical (top), systematic (middle) and total (bottom) uncertainties. The first column is used to normalize the MC total to the observed data total. . . . .	174
4.5	Dimuon event yield tables for the <b>loose channel</b> with statistical (top), systematic (middle) and total (bottom) uncertainties. The first column is used to normalize the MC total to the observed data total. . . . .	177
4.6	Dimuon event yield tables for the <b>tight + loose channel</b> with statistical (top), systematic (middle) and total (bottom) uncertainties. The first column is used to normalize the MC total to the observed data total. . . . .	180
4.7	A summary of the systematic uncertainties in the electron and muon channels at three mass points. A “-” indicates the uncertainty is negligible (below 3%), while an “N/A” indicates the uncertainty does not apply to that channel. For the muon channel the listed terms are for the tight channel and the terms in parentheses are for the loose analysis, if it differs. . . . .	185

LIST OF TABLES

5.1 The observed 95% C.L. mass limits for a variety of  $Z'$  models from various experiments. The LEP II results combine the output from the four experiments, each with an integrated luminosity of  $\sim 700 \text{ pb}^{-1}$ . The full combination and result is from Table 3.15 in [3]. The  $D\bar{O}$  results in the  $ee$  channel are from Table III in [4] and  $\mu\mu$  channel from [5]. The CDF results in the  $ee$  channel are from Table II in [6] and  $\mu\mu$  channel from Table I in [7]. The ATLAS results combined the  $ee$  and  $\mu\mu$  channels and are from Tables 5 & 6 in [8]. The CMS results combined data from  $\sqrt{s} = 7$  and 8 TeV and the  $ee$  and  $\mu\mu$  channels, the results are from Table 2 in [9]. . . . . 189

5.2 Largest positive and negative local significance deviations in all analysis channels. The total muon channel is dominated by the tight muon channel. . . . 200

5.3 Upper Table: The 95% C.L. mass limits for the SSM  $Z'$  in the three analysis channels. The  $\mu\mu$  limit is the combination of the tight and loose muon channels. Lower Table: The 95% C.L. mass limits for the  $E_6$ -derived  $Z'$  in the combined channel. . . . . 202

A.1 NLO NC Drell-Yan production differential cross sections using the CT10 PDF set calculated with FEWZ ( $G_\mu$  scheme) and the POWHEG generated cross section for the given invariant mass bins. The masses are in GeV, and the cross sections are in pb/GeV. The statistical error  $\Delta_{\text{stat}}$  is fully dominated by POWHEG. The deviation between external and MC cross sections is evaluated per mass bin with  $\Delta_{\text{match}} = 100 \times (1 - \sigma_{\text{FEWZ}}/\sigma_{\text{Powheg}})$ , and the statistical MC error is propagated to  $\Delta_{\text{stat,match}}$ . From [217], Appendix E, Table 36. . . . . 208

C.1 Trigger SFs for leading and subleading electrons vs  $E_T$  and  $\eta$  with statistical and systematic errors. From [217], Appendix L, Tables 45,46. . . . . 227

C.2 Isolation SFs for leading and subleading electrons vs  $E_T$  and  $\eta$  with statistical and systematic errors. From [217], Appendix L, Tables 47,48. . . . . 231

E.1 The  $b$  resolution parameters measured in data and simulation. From Appendix B, Table 36 in [217]. . . . . 253

E.2  $Z'$  signal yields from different muon resolution systematic variations. The signals were normalized to an integrated luminosity of  $21 \text{ fb}^{-1}$ . From [217], Appendix C, Table 37. . . . . 255

# List of Figures

2.1	An example PDF, the MSTW2008NLO from [85], and the bands are the the 68% C.L. error bars. The left plot is at an energy scale of 3.16 GeV, while the right plot is at an energy scale of 100 GeV or approximately the $Z^0$ boson mass. The right plot shows the $u$ quark contribution enhanced at higher $Q^2$ in the ranges below $x = 0.1-0.2$ . . . . .	61
2.2	The Feynman diagram for the Drell-Yan process of lepton pair production at a hadron collider. The other outgoing particles are labeled $X$ and can be anything. . . . .	76
3.1	An aerial view of CERN, with the LHC ring superimposed on the surface. The major experiments and other accelerating rings are also shown. “CERN / Aerial view of the CERN”, © Maximilien Brice and Ars Electronica, used under a Creative Commons license. . . . .	85
3.2	Left: Total luminosity delivered to the ATLAS experiment by the LHC during the three data-taking years of Run I. Right: Average number of interactions during a bunch crossing during the 2011 and 2012 data-taking years. From [154]. . . . .	88
3.3	A high-pileup event showing $Z^0 \rightarrow \mu\mu$ . There are 25 reconstructed vertices, where each vertex has at least 3 tracks, and each track has at least 3 Pixel and 6 SCT hits. The track colors correspond to the associated vertex, and the bright yellow tracks are the high- $p_T$ muon pair that form the $Z^0$ candidate. From [156]. . . . .	89
3.4	The accelerator complex at CERN. From [157]. . . . .	91
3.5	A cross section of a dipole magnet for the LHC. From [158]. . . . .	92
3.6	An annotated diagram of the full ATLAS detector. From [162]. . . . .	95
3.7	A cross section of the ATLAS detector, showing where the different types of particles interact with the various detectors. Each sub-detector performs a function to measure the energy or charge and momentum of a specific class of particles. From [162]. . . . .	99
3.8	An electron shower inside the ATLAS “accordion” electromagnetic calorimeter. From [162]. . . . .	101

LIST OF FIGURES

3.9	The iconic view of the ATLAS detector. This shows the 8-fold azimuthal symmetry of the toroid magnet system, where the 8 coils have orange tape. This also shows the size of the ATLAS detector. ©CERN, from [162]. . . .	104
3.10	The layout of the ATLAS inner detector. From [169]. . . . .	106
3.11	Top: layout of the ATLAS Liquid Argon calorimeter. Bottom: the sampling tower structure of the barrel ECAL. The strip towers show the granularity of the three layers in the ECAL. From [173]. . . . .	111
3.12	The ATLAS calorimeters including the hadronic tile calorimeter barrel and extended barrel sections, and the endcap and forward LAr calorimeters. From [162], ©CERN. . . . .	113
3.13	The ATLAS muon spectrometer. Top: Azimuthal view showing the 8-fold symmetry and Large/Small sector differences. Bottom: “Quarters” view in the $r$ - $z$ plane for both the Large and Small sectors. From [175]. . . . .	118
3.14	The total bending power of the ATLAS muon spectrometer toroidal field in the different $\eta$ regions. In the barrel ( $ \eta  < 1.05$ ), the red curve corresponds to the Large sectors and the black curve to the Small sectors. In the endcaps ( $ \eta  > 1.05$ ), the red curve corresponds to the Small sectors and the black curve to the Large sectors. From [175]. . . . .	120
3.15	A layout of a typical MDT chamber for the muon system showing the layers of tubes, support structure, and alignment sensors. From [176]. . . . .	121
3.16	ATLAS muon trigger chambers, showing the typical trajectories of low- and high- $p_T$ muons. From [177]. . . . .	123
3.17	Left: How the trigger determines the Regions of Interest in an event, by singling out the region(s) that meet the LVL1 trigger threshold in the calorimeters or muon spectrometer. Right: Data acquisition at ATLAS, showing the data flow through the three trigger stages and event readout. Level 3 is the event filter stage described in the text. From [178]. . . . .	125
3.18	ATLAS Trigger stream rates for 2012 data taking, showing the total event-writing rate due to the various triggers. From [180]. . . . .	127
3.19	Two E/gamma events in the ECAL. Left: A single, isolated photon. Right: A $\pi^0$ event showing the double peak from the decay to two photons. Electron identification needs to discriminate between these types of events in the ECAL, using clustering (to remove $\pi^0$ or non-prompt conversions), track matching (to remove prompt photons), and hadronic leakage (to remove $\pi^\pm$ and jets). From [182]. . . . .	130

LIST OF FIGURES

3.20	Left: Electron reconstruction efficiency vs. the measured $\eta$ of the electron, comparing the early 2012 data results to the 2011 data. The efficiency is best in the barrel, and decreases in the endcaps. Right: Electron reconstruction efficiency vs. the measured $E_T$ of the electron, using two different 2012 datasets to compare low- and high- $E_T$ . Electron reconstruction efficiency improves with $E_T$ . From [182]. . . . .	132
3.21	Left: Muon trigger efficiency in the barrel ( $ \eta  < 1.05$ ) for the mu24i_tight trigger. Right: Muon trigger efficiency in the endcap ( $ \eta  > 1.05$ ) for the mu24i_tight trigger. This is seeded by the L1_MU15 trigger. Both use a tag-and-probe method for $Z^0 \rightarrow \mu\mu$ decays to calculate the efficiencies. The efficiencies also include the geometric acceptance of the trigger chambers in their respective regions. From [188]. . . . .	134
3.22	Left: Muon reconstruction efficiency vs. $\eta$ . Right: Muon reconstruction efficiency vs. $p_T$ . These are for combined muons only, and show the high reconstruction efficiency for muons in the dataset. From [188]. . . . .	135
4.1	Left: Dielectron invariant mass overlaid with dedicated 2000 GeV SSM sample and reweighted signal template. Right: Dimuon invariant mass with the same histograms. This shows the reweighting procedure reproduces the expected signal in the same way as the dedicated samples. In both cases the interference with the SM DY background is included, and both sets of samples follow the SM background in the 1000-1500 GeV range. For the dedicated samples (the dark blue histogram), the production is cut-off at half the pole mass value, 1000 GeV, leaving low mass tails below this value. From [217], Appendix I, Figure 99. . . . .	148
4.2	Left: The nominal fit for the Top background in the muon channel. The black histogram is the Top background and statistical errors, the blue lines show the fit range, and the pink dashed line is the stitching point. Right: The resulting final distribution is shown, with the “statistical” errors in green and the combined errors in red. . . . .	154
4.3	$Z'$ signal templates at representative mass points for the dielectron selection (left), and the detector acceptance times efficiency for the expected signal (right). . . . .	159
4.4	The dielectron invariant mass spectrum after event selection. The binning is constant in $\log(m_{ee})$ . The Top and Dijet & $W$ +jets backgrounds have been fit and extrapolated to cover the full mass range. Two representative $Z'$ signals have been overlaid. The ratio in the lower plot shows the agreement between the observed and expected distributions. The error bars on the data points are statistical and the band in the ratio plot is the combined systematic error. . . . .	162

LIST OF FIGURES

4.5	Leading (left) and subleading (right) electron kinematic distributions after event selection. The top row are the $p_T$ distributions, the middle row are the $\eta$ distributions, and the bottom row are the $\phi$ distributions. . . . .	164
4.6	Left: $Z'$ signal templates at representative mass points. Right: The detector acceptance times efficiency for the expected signal. Top: Tight channel. Bottom: Loose channel. . . . .	170
4.7	The dimuon invariant mass spectrum in the <b>tight channel</b> after event selection. The binning is constant in $\log(m_{\mu\mu})$ . The Top background has been fit and extrapolated to cover the full mass range. Two representative $Z'$ signals have been overlaid. The ratio in the lower plot shows the agreement between the observed and expected distributions. The error bars on the data points are statistical and the band in the ratio plot is the combined systematic error. . . . .	173
4.8	Leading (left) and subleading (right) distributions in the muon <b>tight channel</b> after event selection. The top row are the $p_T$ distributions, the middle row are the $\eta$ distributions, and the bottom row are the $\phi$ distributions. . . . .	175
4.9	The dimuon invariant mass spectrum in the <b>loose channel</b> after event selection. The binning is constant in $\log(m_{\mu\mu})$ . The Top background has been fit and extrapolated to cover the full mass range. Two representative $Z'$ signals have been overlaid. The ratio in the lower plot shows the agreement between the observed and expected distributions. The error bars on the data points are statistical and the band in the ratio plot is the combined systematic error. . . . .	176
4.10	Leading (left) and subleading (right) distributions in the muon <b>loose channel</b> after event selection. The top row are the $p_T$ distributions, the middle row are the $\eta$ distributions, and the bottom row are the $\phi$ distributions. . . . .	178
4.11	The dimuon invariant mass spectrum in the <b>tight + loose channel</b> after event selection. The binning is constant in $\log(m_{\mu\mu})$ . The Top background has been fit and extrapolated to cover the full mass range. Two representative $Z'$ signals have been overlaid. The ratio in the lower plot shows the agreement between the observed and expected distributions. The error bars on the data points are statistical and the band in the ratio plot is the combined systematic error. . . . .	179
4.12	Leading (left) and subleading (right) distributions in the muon <b>tight + loose channel</b> after event selection. The top row are the $p_T$ distributions, the middle row are the $\eta$ distributions, and the bottom row are the $\phi$ distributions. . . . .	181



*LIST OF FIGURES*

4.13	PDF Choice systematic uncertainty as a function of invariant mass in the tight dimuon channel. This shows the difference between the systematic error evaluated as a function of the true and reconstructed invariant mass. The black histogram is the % systematic error evaluated at the true invariant mass. The red histogram is the % systematic error evaluated at the reconstructed invariant mass, using the procedure outlined in the text. The red histogram is “smeared” due to the worsening resolution of the high- $p_T$ muons from the larger invariant mass events. Before the start of the search region at 130 GeV the reconstructed systematic error is not needed (red histogram) and is set to zero. The reconstructed systematic error histograms are computed for each systematic error in each channel. . . . .	184
5.1	The LLR search for a $Z'$ signal in the various dilepton invariant mass histograms. Upper Left: Dielectron channel. Upper Right: Dimuon channel, combining the tight and loose selections. Bottom: Combined dilepton channel. The circles represent the “most-signal-like” points and the $p$ -value is the global probability to observe such a deviation in the data assuming background-only.	199
5.2	Local significance of deviations including statistical and systematic uncertainties between data and the expected SM background for each bin in the search region from 128 to 4500 GeV. These are for the separate channels, with dielectron (top left), dimuon tight + loose (top right), dimuon tight (lower left), and dimuon loose (lower right) selections. . . . .	201
5.3	Expected and observed 95% C.L. limits on $(\sigma B)_{Z'}$ as a function of $m_{Z'}$ in the various analysis channels. Upper Left: Dielectron channel. Upper Right: Dimuon channel, combining the Tight and Loose selections. Bottom: Combined dilepton channel. The green and yellow bands show the $\pm 1\sigma$ and $\pm 2\sigma$ posterior errors on the expected $(\sigma B)_{Z'}$ limit. The thickness of the SSM $Z'$ band indicates the theoretical uncertainty on the model parameters, and applies to the other theory curves as well. . . . .	203
A.1	Higher-order QCD corrections for the two MC DY samples, using NNLO PDF sets. The upper plot shows the ratio of six NNLO QCD prediction to CT10 NLO used in POWHEG, the lower plot uses the same PDF sets compared to MSTW LO used in PYTHIA. From [217], Appendix E, Figure 85. . . . .	209
A.2	Upper plot: Higher-order EW corrections across LO and NNLO QCD orders, comparing the factored and additive results. This shows the additive results, obtained from factoring at a lower order, is consistent across QCD orders. Lower plot: Systematic uncertainty due to the additional EW corrections as a function of $m_{\ell\ell}$ . From [217], Appendix E, Figure 87. . . . .	211

LIST OF FIGURES

A.3	Uncertainty due to the photon-induced cross section as a function of $m_{\ell\ell}$ . The nominal value is calculated in FEWZ using POWHEG with MSTWNNLO and includes the higher-order EW corrections. The correction and upper and lower uncertainty bands come from the LO corrections added to the nominal value, based on the different quark mass schemes. From [217], Appendix E, Figure 89. . . . .	212
A.4	The total $K$ -factor for the POWHEG samples to reweight them to the “best” theory. This includes NNLO QCD and higher-order EW effects. The upper and lower limits at the 90% error envelope are shown shaded, the lower $K$ -factor value at higher $m_{\ell\ell}$ is due to the difference in PDF value using the ABM11 PDF set compared to the nominal MSTWNNLO PDF set. From [217], Appendix E, Figure 90. . . . .	214
A.5	The resulting cross sections after reweighting both PYTHIA LO DY samples and POWHEG NLO DY samples are compared across the full mass range. The error bars are the statistical uncertainty only. This shows excellent agreement between the two, and validates this as a consistent reweighting scheme. From [217], Appendix E, Figure 92. . . . .	214
B.1	The total asymmetric uncertainty on the Drell-Yan cross section as a function of invariant mass $m_{\ell\ell}$ . The four eigenvector groups are shown in color, and the black is the total symmetric uncertainty following the MSTW2008 prescription. The left plot shows the lower mass range below $m_{\ell\ell} < 1500$ GeV, and the right plot shows the full mass range. From [217], Appendix G, Figure 98. . . . .	218
B.2	The total asymmetric uncertainty on the Drell-Yan cross section as a function of invariant mass $m_{\ell\ell}$ . The colors correspond to each source as calculated in this Appendix. The black curve is the total symmetric uncertainty following the MSTW2008 prescription, for comparison with the PDF eigenvector uncertainties in Figure B.1. The left plot shows the lower mass range below $m_{\ell\ell} < 1500$ GeV, and the right plot shows the full mass range. From [217], Appendix G, Figure 100. . . . .	220
B.3	The relative uncertainty on the Drell-Yan and $W^\pm$ production cross section due to the input beam energy, as calculated in VRAP. From [263]. . . . .	221
C.1	Upper Left: Leading electron ( $\sim EF\_g35\_loose$ ) SFs as a function of $E_T$ . Upper Right: Sub-leading electron ( $\sim EF\_g25\_loose$ ) SFs as a function of $E_T$ . Lower plots are the same, as a function of $\eta$ . From [217], Appendix L, Figures 119,120. . . . .	226
C.2	Upper Left: Leading electron isolation SFs as a function of $E_T$ . Upper Right: Sub-leading electron isolation SFs as a function of $E_T$ . Lower plots are the same, but as a function of $\eta$ . From [217], Appendix M, Figures 122,123. . .	230

LIST OF FIGURES

D.1	The real electron rates estimated from the Drell-Yan Monte Carlo. Left: Leading electron. Right: Sub-leading electron. These are binned in $p_T$ and split into three $\eta$ regions, excluding the crack region. From [217], Figure 2. . . . .	236
D.2	Comparison of the fake rates $f_i$ calculated with the three different methods described. Left: leading electron. Right: sub-leading electron. These are binned with respect to $p_T$ , and the rows correspond to different $\eta$ regions of the ECAL (barrel and three endcap ranges). The error bars are statistical only. From [217], Figure 9. . . . .	240
D.3	Top: Total fake electron background estimate over all the methods. The circles apply the real electron rates ( $r_i \neq 1$ ), while the other two use the approximation $r_i = 1$ . The peak at 91 GeV is due to real electron dilution in the samples, and is lower in the loose fail <i>medium++</i> track matching sample due to the better rejection of real electrons. Bottom: Ratio of the various background estimates to the nominal value. The nominal selection is the single object selection with the real electron rates used. The ratio shown is from 116-1500 GeV. From [217], Figures 14,15. . . . .	242
E.1	Top Row: smearing parameters for the ID (left) and MS (right) with the MUID chain. Bottom Row: scale corrections for the ID (left) and MS (right) with the MUID chain. From [266], Figures 7,8,13. . . . .	250
E.2	The dimuon invariant mass at the $Z^0$ peak with MUID CB muons. Left: No corrections applied to the MC. Right: Smearing and scale corrections applied to the MC. From [266], Figure 14. . . . .	250
E.3	$\Delta\theta_{seg}/B_{int}$ plotted with respect to $q/p$ for two station muons in the Large sectors. The straight line slope is the constant $C$ . From Appendix B, Figure 70 in [217]. . . . .	252
E.4	Resolution distributions in $p\Delta\theta_{seg}/qB_{int}$ for the Large sectors. These are fit with a single Gaussian. Left: Low momentum $p=39-41$ GeV. Right: High momentum $p=130-150$ GeV. From [217], Appendix B, Figure 71. . . . .	253
E.5	The two station muon resolution $\sigma$ as a function of momentum $p$ . This is fit with expected resolution function in Equation (E.1). The extracted $b$ parameter is called $p_2$ here. The curves separate the Large and Small sectors due to their different performance. Left: Resolution in MC. Right: Resolution in data. From [217], Appendix B, Figure 73. . . . .	254
E.6	The systematic uncertainty on the total background due to the muon resolution as a function of invariant mass. Left: Tight muon channel. Right: Loose muon channel. From [217], Appendix C, Figure 74. . . . .	255

# Chapter 1

## Introduction

The Standard Model describes the matter content and interactions of all the established particles. It is composed of fermions that are in representations of the gauge group  $SU(3)_C \otimes SU(2)_L \otimes U(1)_Y$ , and the postulate of gauge invariance determines their interactions and the intermediate gauge boson spectrum. There are 25 input parameters to the Standard Model, and many particle interactions have been studied extensively in physics for more than 40 years to measure these parameters and test the predictions of the Standard Model. Thus far, no significant deviation has been observed between the Standard Model's predictions and experimental results.

With the discovery of the Higgs boson in July 2012 [1, 2], the final piece of the Standard Model has been measured. However, several questions remain about our observed universe that do not appear in the Standard Model. For example, ‘Why is our universe made of matter?’ or ‘Why do the parameters in the Standard Model have their observed values?’. Many possible extensions of the Standard Model have been proposed to resolve some of these questions, and these models often predict new particles and interactions which is generically called “New Physics”. This thesis describes a search for one such new particle, a neutral

## CHAPTER 1. INTRODUCTION

gauge boson  $Z'$  that decays to leptons.

The Large Hadron Collider (LHC) at the European Organization for Nuclear Research (CERN) is the world's leading high-energy physics facility. It collides two beams of protons with a center-of-mass energy  $\sqrt{s} = 8$  TeV and an instantaneous luminosity of  $7 \times 10^{33} \text{ cm}^{-2}\text{s}^{-1}$ . CERN hosts numerous experiments, and at the LHC there are two general-purpose detectors: A Toroidal LHC ApparatuS (ATLAS) and the Compact Muon Solenoid (CMS). This thesis uses the data recorded at ATLAS during the 2012 operations to search for a narrow resonant peak in the dilepton mass spectrum.

The search for new particles in the dilepton channel has a long history in physics and is a traditional benchmark for limiting extensions of the Standard Model. Previous limits on the mass of possible  $Z'$  bosons from the Large Electron-Positron collider and the Tevatron collider range from 700 to 1800 GeV [3, 4, 5, 6, 7]. Limits from the Large Hadron Collider experiments CMS and ATLAS place a 95% C.L. lower mass limit of 2590 GeV [8, 9]. This thesis searches across two channels using electron-pair and muon-pair final states. No statistically significant deviation from the Standard Model is observed, and 95% C.L. lower mass limits are placed. The lower mass limit for the benchmark model is:

$$M_{Z'_{SSM}} > 2.90 \text{ TeV}.$$

Mass limits are also placed on additional  $Z'$  bosons, ranging from 2.38-2.54 TeV. These are currently the most stringent limits on possible  $Z'$  particles.

This thesis is organized as follows. The second chapter describes quantum field theory and the Standard Model in some detail. There is also a discussion of some of the motivations and mathematics behind a few extensions of the Standard Model that include  $Z'$  bosons. The third chapter describes the experimental apparatus. The LHC and ATLAS are incredibly

## CHAPTER 1. INTRODUCTION

complex machines, and this only gives the briefest treatments of their technical marvel. The last part of the third chapter describes how data taken from ATLAS is transformed into computer files that encode the underlying physics events. The fourth chapter describes how the event selection finds the lepton pairs in the data, in both the electron and muon channels. The fifth chapter describes how, with the observed and simulated data, the search and limits are placed on new  $Z'$  particles. A conclusion contains the results of the search and an outlook for the remainder of the LHC program. In addition, five appendices are included covering in more detail some of the technical aspects of data taking and analysis techniques. These address the weighting and rescaling of the simulated data to the Standard Model and associated systematic uncertainties, and the corrections applied to the electron and muon channels. Throughout this thesis, I try and give a sense of the history to these physics endeavors, for

*“If I have seen farther it is by standing on the shoulders of giants.”*

— Isaac Newton

# Chapter 2

## The Standard Model

The Standard Model of Particle Physics is a quantum field theory incorporating a wide variety of phenomena observed in nature. It is the current best understanding of how the universe works, and describes all fundamental interactions with the exception of gravity. The Standard Model predicts the rates of all types of events in the LHC environment, and these events are the largest background in the search for new physics at the LHC. This chapter describes the theoretical underpinnings of the Standard Model and then discusses possible extensions of this theory that can potentially resolve some of the outstanding issues in particle physics.

### 2.1 History - From Dirac to Now

The revolution in modern physics came from the discovery of the Theory of Relativity (1905, 1915) by Albert Einstein [10, 11] and Quantum Theory (1920s) by Max Planck [12], Niels Bohr [13, 14], Louis de Broglie [15], Erwin Schrödinger [16], Werner Heisenberg [17], Max Born [18], and others. There was a need to unify the two theories by incorporating the

## CHAPTER 2. THE STANDARD MODEL

relativistic concepts of space-time and causality with the probabilistic nature of waves & particles and unitary time evolution in quantum mechanics. In 1928, Paul Dirac laid out the first attempt at incorporating relativity with the quantum mechanics of electrons, which led to the prediction of anti-particles [19, 20]. He followed this with the first attempt to understand the quantum nature of the electromagnetic field by quantizing the photon as an infinite set of quantum harmonic oscillators using creation and annihilation operators [21]. However, it was quickly realized that these theories had problems where the first-order perturbative corrections gave infinity as the answer [22, 23]. Throughout the 1930s, 40s, and 50s, much theoretical work was done to understand these quantum field theories.

The infinities arise due to the quantum nature of the corrections - during the intermediate process the particles can essentially travel anywhere or take on any amount of energy, which produces a divergence in the calculation. In 1947, Willis Lamb presented a result at the Shelter Island Conference [24] showing a deviation in the fine structure in hydrogen that was not predicted by standard quantum theory [25]. Hans Bethe, on the train ride home from the conference, gave a first derivation of this shift using quantum field theory perturbations and a simple cut-off to “regulate” the theory [26]. Since the final result is independent of the cut-off, this is said to be “regularized” and is a valid physical result. Julian Schwinger adopted a somewhat different approach by separating the divergences and showing they cancel to calculate the anomalous magnetic moment of the electron [27], which was another puzzling experimental result in shifts that did not correspond to the prediction of standard quantum theory [28, 29, 30, 31]. In 1949, Wolfgang Pauli and Felix Villars formalized this procedure, known as regularization, to show how seemingly divergent calculations in perturbations can give sensible, finite results [32]. Richard Feynman [33, 34, 35], Julian Schwinger [36, 37, 38, 39, 40, 41], and Sin-Itiro Tomonaga [42, 43, 44, 45] independently in the 1950s all developed a fully covariant (that is, compatible with Special Relativity)



## CHAPTER 2. THE STANDARD MODEL

and gauge invariant (a different problem arising from additional degrees of freedom in the dynamics of the theory) formulation of how properly quantized electrons interact with the quantum electromagnetic field. Freeman Dyson also made substantial contributions and showed how the Feynman approach using the path-integral and “diagrams” is equivalent to the more algebraic operator approach of Tomonaga and Schwinger [46, 47]. This theory, known as Quantum Electro-Dynamics (QED), is considered the “crown jewel” of theoretical particle physics [48].

The success of QED led to the further development of quantum field theories as a viable set of theories to describe nature. In 1954, C. N. Yang and R. L. Mills extended the idea of using the generators of the gauge symmetry (the charge in the case of QED) to cases where they don’t commute [49]. These types of quantum field theories are known as Yang-Mills or non-Abelian gauge theories. In 1960, Sheldon Glashow [50] applied the  $SU(2)$  symmetry group to the weak interactions and showed the vector boson particle spectrum can reproduce the known experimental results after partially breaking the symmetries, if one includes an additional  $U(1)$  symmetry group. There was a problem, however, because the gauge bosons of the partially broken symmetry were massless. This is a general property of gauge bosons after the breaking or partial breaking of a symmetry, a result discovered by Yochiro Nambu [51] and Jeffery Goldstone [52]. The resulting massless particles are called Nambu-Goldstone bosons. To match the known experimental results, massive gauge bosons were needed but these do not obey the symmetries of the theory. To solve this problem, Philip Anderson [53], Francois Englert & Robert Brout [54], Peter Higgs [55], and Gerald Guralnik, Carl Hagan & Tom Kibble [56], all independently developed what is known as the Higgs mechanism that allowed for massive gauge bosons that preserved the underlying symmetry of the theory after breaking local gauge invariance. In 1967, Steven Weinberg [57] and Abdus Salam [58] applied the Higgs mechanism to the  $SU(2) \otimes U(1)$  theory proposed by Glashow. The

## CHAPTER 2. THE STANDARD MODEL

resulting theory describes the known interactions of leptons (electrons, muons, tau particles, their anti-particles, as well as electron-, muon-, tau-neutrinos and anti-neutrinos) and forms the basis of the Standard Model.

In addition to leptons, there is another class of particles called hadrons, with two subclasses: baryons (such as the proton and neutron) and mesons (such as the pion and kaon). These particles interact in a much different fashion than the leptons, and there are many more types of hadrons than the 12 species of leptons. The large number of species of hadrons has led to it being called “The Particle Zoo” only somewhat in jest. In order to classify all these hadrons, Kazuhiko Nishijima in 1955 [59] and Murray Gell-Mann in 1956 [60], proposed to assign a new quantum number “strangeness” in addition to the “isospin” quantum number to each particle and organize the resulting spectrum into group multiplets. Not every multiplet was filled, which led to the prediction of the  $\Omega^-$  particle, discovered in 1964 [61]. The constituents of the hadrons carrying the quantum numbers were called “quarks”. While the Quark Model served to classify the known hadrons, it did not explain their interactions. In 1969, James Bjorken and E. Paschos [62] and Richard Feynman [63] proposed hadrons were composed of point-like objects called “partons” that interacted (at high enough energies) in a similar way to leptons. It was quickly realized quarks and partons were the same objects, just described in different ways. The Parton Model showed how these constituents interacted with leptons at high energy (uniting them with the Electro-Weak Theory of Glashow, Salam, and Weinberg), while the Quark Model was an empirical study of how they interacted amongst themselves at low energy. Uniting these two pictures, in 1973 David Gross and Frank Wilczek [64] and David Politzer [65] showed the gauge theory with the  $SU(3)$  symmetry group exhibited precisely this behavior, called “asymptotic freedom.” The strength of the coupling at low energies is very large, allowing the quarks to bind together to form hadrons, while at high energies the coupling strength falls off and quarks behave as

## CHAPTER 2. THE STANDARD MODEL

freely interacting partons. These two gauge theories, the  $SU(3)$  theory of the quarks and  $SU(2) \otimes U(1)$  theory of both the quarks and leptons, is the Standard Model.

Numerous other developments in the understanding of quantum field theories occurred in the 1970s. Kenneth Wilson showed how the regularization of quantum field theories can be used to study their behaviors at different energy scales in a process called “renormalization” [66, 67], a key step to understanding the asymptotic freedom of the  $SU(3)$  gauge theory of quark interactions. Martinus Veltman and Gerardus ’t Hooft showed that all gauge theories can be properly regularized and renormalized [68]. Makoto Kobayashi and Toshihide Maskawa, building upon earlier work by Nicola Cabibbo of “mixing” between quarks [69] and the discovery of CP violation in the kaon meson system [70], predicted two new particles, the bottom and top quarks [71]. Similar work extending the leptonic particle spectrum was done by Bruno Pontecorvo [72] and Ziro Maki, Masami Nakagawa, and Shoichi Sakata [73]. The theoretical understanding of the three “generations” of matter (quarks: up/down, strange/charm, top/bottom. leptons: electron, muon, tau with neutrinos) and their gauge theory interactions  $SU(3)$  and  $SU(2) \otimes U(1)$ , was mostly completed by 1980. In total there are about 25 total free parameters, depending on how one counts neutrino masses and mixing. These parameters and the interactions based on the symmetries of the theory have been extensively measured and tested with no significant observed deviation in experimental particle physics to date. It is an amazing testament to human ingenuity.

## 2.2 Quantum Field Theory

Quantum field theory is the tool used to understand particles and their interactions. It joins the two modern physics successes of quantum mechanics and special relativity and can be applied to a variety of problems using a variety of techniques under the heading of quantum

## CHAPTER 2. THE STANDARD MODEL

field theory. This section will develop some of the basic structures of this important and powerful tool. For a more complete treatment of quantum field theory, see the excellent books by Michael Peskin and Daniel Schroeder [74], Steven Weinberg [75], Lowell Brown [76], Lewis Ryder [77], or many, many others.

### 2.2.1 Lagrangian Dynamics

In Lagrangian mechanics, the quantity governing how a system behaves is the action. The action  $S$  is the integral of the Lagrangian over time, or if the system includes spatial coordinates as inputs, the integral of the Lagrangian density over both space and time. Throughout this thesis, I will only be using fields, which have a value at every point in space and all times and will denote the Lagrangian density  $L$ , and refer to it simply as the Lagrangian.

$$S = \int L d^3\mathbf{x}dt. \quad (2.1)$$

The principle of least action states that classical solutions of a Lagrangian are at the field configurations that extremize the action. The Lagrangian is a function of some set of fields  $\phi(x, t)$  and their derivatives  $\partial_\mu\phi(x, t)$ . I will drop the explicit dependence on  $(x, t)$  for the fields, but it is always implicitly there, and the volume element will be shortened to  $d^3\mathbf{x}dt = d^4x$ .

$$\begin{aligned} 0 &= \delta S = \int \delta L(\phi, \partial_\mu\phi) d^4x \\ 0 &= \int \left( \frac{\partial L}{\partial \phi} \delta\phi + \frac{\partial L}{\partial(\partial_\mu\phi)} \delta(\partial_\mu\phi) \right) d^4x \\ 0 &= \int \left( \frac{\partial L}{\partial \phi} \delta\phi + \partial_\mu \left( \frac{\partial L}{\partial(\partial_\mu\phi)} \delta\phi \right) - \partial_\mu \left( \frac{\partial L}{\partial(\partial_\mu\phi)} \right) \delta\phi \right) d^4x \end{aligned}$$

## CHAPTER 2. THE STANDARD MODEL

The middle term is a total derivative and if we assume the field configuration is stable at the boundaries, must vanish. The first and last terms each multiply  $\delta\phi$ , however the change in action must vanish for any small but arbitrary change in field configuration. This can be factored out, and the two terms must cancel each other to satisfy the principle of least action. These are the Lagrangian equations of motion:

$$0 = \frac{\partial L}{\partial \phi} - \partial_\mu \left( \frac{\partial L}{\partial (\partial_\mu \phi)} \right). \quad (2.2)$$

It should be noted that, while the Lagrangian formulation is the most popular for quantum field theory, it is also possible to formulate quantum field theory using the Hamiltonian as the fundamental quantity and the equations of motion that result from the fields and their conjugate momenta.

### Noether's Theorem

One of the most remarkable results of Lagrangian theory shows how the symmetries of a system are related to the conserved quantities in that system. This is called Noether's Theorem, for Emmy Noether [78]. It states that for a change in the field configuration of a system, if it leaves the equations of motion intact, then there is a corresponding conservation law. A symmetry is defined to be when the fields can be changed but leave this equations of motion unchanged. The equations of motion are from the condition that the action is at an extremum, so the Lagrangian can change at most by a total derivative. The field and Lagrangian transform as:

$$\phi \rightarrow \phi + \alpha \delta\phi, \quad (2.3)$$

$$L \rightarrow L + \alpha \partial_\mu J^\mu, \quad (2.4)$$

CHAPTER 2. THE STANDARD MODEL

where  $\alpha$  is the deformation parameter and  $J^\mu$  is a quantity that vanishes at the boundaries.

Varying the Lagrangian through the change in fields results in:

$$\begin{aligned} & \frac{\partial L}{\partial \phi} \alpha \delta \phi + \frac{\partial L}{\partial (\partial_\mu \phi)} \alpha \delta (\partial_\mu \phi) \\ & \alpha \frac{\partial L}{\partial \phi} \delta \phi + \alpha \partial_\mu \left( \frac{\partial L}{\partial (\partial_\mu \phi)} \delta \phi \right) - \alpha \partial_\mu \left( \frac{\partial L}{\partial (\partial_\mu \phi)} \right) \delta \phi \\ & \alpha \left( \frac{\partial L}{\partial \phi} - \partial_\mu \left( \frac{\partial L}{\partial (\partial_\mu \phi)} \right) \right) \delta \phi + \alpha \partial_\mu \left( \frac{\partial L}{\partial (\partial_\mu \phi)} \delta \phi \right). \end{aligned}$$

This change in field configuration is assumed to be a symmetry and therefore preserves the equations of motion, so the first two terms cancel. The total derivative term must equal the change in the Lagrangian  $J^\mu$ , up to some piece whose derivative must vanish. This extra piece I'll call  $j^\mu$ :

$$\begin{aligned} J^\mu &= \left( \frac{\partial L}{\partial (\partial_\mu \phi)} \right) \delta \phi - j^\mu \\ \Rightarrow \partial_\mu j^\mu &= 0 \quad \& \quad j^\mu = \left( \frac{\partial L}{\partial (\partial_\mu \phi)} \right) \delta \phi - J^\mu. \end{aligned} \tag{2.5}$$

So if a symmetry of the fields can be found, there must exist a conserved current  $j^\mu$ . An alternative way to think about this is to integrate the conserved current over all space and time:

$$\begin{aligned} 0 &= \int \partial_\mu j^\mu d^4x = \int \partial_0 j^0 d\mathbf{x} dt - \int \nabla \cdot \vec{j} d\mathbf{x} dt \\ \Rightarrow Q &= \int j^0 d\mathbf{x}. \end{aligned} \tag{2.6}$$

$Q$  is a constant which depends on the field configuration at the boundary and is constant in time.

One of the best examples of this relation between symmetries and conservation laws

## CHAPTER 2. THE STANDARD MODEL

is Lorentz symmetry, the local translation invariance in space and time coordinates. For simplicity, I'll illustrate using the Lagrangian for a single, massive scalar field:

$$L = \frac{1}{2} \partial_\mu \phi \partial^\mu \phi - \frac{1}{2} m^2 \phi^2.$$

After a change in the coordinates, the field configuration transforms by a single derivative for small enough changes (the first-order term in a Taylor expansion):

$$\begin{aligned} x^\mu &\rightarrow x^\mu + \epsilon^\mu \\ \phi &\rightarrow \phi + \epsilon^\mu \partial_\mu \phi. \end{aligned}$$

The Lagrangian must also only change by a single derivative:

$$L \rightarrow L + \epsilon^\mu \partial_\mu L = L + \epsilon^\nu \partial_\mu (\delta_\nu^\mu L).$$

The conserved Noether current in equation (2.5) uses the changes in the field configuration  $\delta\phi = \partial_\mu \phi$  and the Lagrangian  $J = \delta_\nu^\mu L$ , and in this example is:

$$\begin{aligned} T_\nu^\mu &= (\partial_\nu \phi)(\partial^\mu \phi) - \delta_\nu^\mu \left( \frac{1}{2} \partial_\mu \phi \partial^\mu \phi - \frac{1}{2} m^2 \phi^2 \right) \\ 0 &= \partial_\mu T_\nu^\mu \end{aligned}$$

This is the stress-energy tensor for the single, massive scalar field theory. The transformation used four different deformations, with the field changing in four directions (three spatial, one time), which resulted in four conserved currents and four conserved charges. The four

## CHAPTER 2. THE STANDARD MODEL

conserved charges can be calculated when  $\mu = 0$ , using equation (2.6):

$$Q_0 = \int \left( \frac{1}{2} \partial_0 \phi \partial^0 \phi + \frac{1}{2} \partial_i \phi \partial^i \phi + \frac{1}{2} m^2 \phi^2 \right) d\mathbf{x}, \quad (2.7)$$

$$Q_i = \int (\partial_i \phi \partial^0 \phi) d\mathbf{x}. \quad (2.8)$$

The terms being integrated in equation (2.7) correspond to the Hamiltonian density, therefore the first conserved quantity is the total energy of the system. The second equation (2.8) is the total momentum of the system. In words, Lorentz symmetry or local translation invariance, through Noether's Theorem, gave rise to the conservation of energy and momentum. A similar calculation, where the system is invariant under rotations  $x^i \rightarrow \omega_j^i x^j$ , leads to the conservation of angular momentum. Special relativity is based on Lorentz symmetry which includes invariance under coordinate boosts and rotations. Therefore, any theory that obeys Lorentz symmetry will automatically conserve energy, momentum, and angular momentum. All theories considered in this thesis will fall into this category.

### The Interaction Picture and Path Integral

For a given initial state configuration, to evolve the configuration to a different state, the time-evolution is a unitary operator and is determined by the Hamiltonian of the system. The Hamiltonian can depend on the position and the momentum of the state.

$$\langle \phi_F | U(x, p, t) | \phi_I \rangle = \langle \phi_F | e^{-iHT} | \phi_I \rangle \quad (2.9)$$

This is the propagation amplitude between the states. Without loss of generality, assume the state is an eigenstate of the position operator. A complete set of quantum mechanical



## CHAPTER 2. THE STANDARD MODEL

states can be inserted at any intermediate point:

$$\langle \phi_F | e^{-iHT''} \left[ \left( \prod_j \int dx_j \right) |x_j\rangle \langle x_j| \right] e^{-iHT'} | \phi_I \rangle.$$

This can be done iteratively, using smaller and smaller time slices:

$$\langle \phi_F | e^{-iH\epsilon} \left[ \left( \prod_j \int dx_j \right) |x_j\rangle \langle x_j| \right] e^{-iH\epsilon} \dots e^{-iH\epsilon} \left[ \left( \prod_k \int dx_k \right) |x_k\rangle \langle x_k| \right] e^{-iH\epsilon} | \phi_I \rangle.$$

Each factor of  $e^{-iH\epsilon}$  is a transition between two states. This can be done  $N$  times, with a time step  $\epsilon = T/N$  between each intermediate insertion. The amplitude between states that must be calculated is:

$$\langle \phi_{k+1} | e^{-iH\epsilon} | \phi_k \rangle.$$

In general, the Hamiltonian can contain terms which depend on the position, the momentum, or both. If a term only depends on the position, the matrix element is simple to calculate since the states are eigenstates of position:

$$\prod_i \langle \phi_{k+1} | f(x^i) | \phi_k \rangle = f(x_k) \prod_i \delta(x_k^i - x_{k+1}^i).$$

The left-hand side is in terms of states and operators, while the right-hand side is simply a function which can be evaluated. The delta-functions can be re-written as exponentials using a Fourier transform between position and momentum space:

$$\delta(x_k - x_{k+1}) = \int \frac{dp_k}{2\pi} e^{ip_k \cdot (x_k - x_{k+1})}.$$

CHAPTER 2. THE STANDARD MODEL

For terms that depend only on the momentum, the position eigenstates can be transformed into momentum eigenstates again using a Fourier transform:

$$\prod_i \langle \phi_{k+1} | g(p^i) | \phi_k \rangle = \prod_i \int \frac{dp_k^i}{2\pi} g(p_k^i) e^{i \sum p_k^i \cdot (x_k^i - x_{k+1}^i)}.$$

For terms that contain mixtures of position and momentum operators, using the commutation relations the operators can be ordered with the position operators on the left and momentum operators on the right or vice-versa, called normal or anti-normal ordering. To make the similarity between the  $k$  and  $k + 1$  states more clear, there is also Weyl ordering where the position operators between the two states are symmetrically placed on the left and right hand sides. It is always possible to order the operators in this way.

Once properly ordered, the Hamiltonian between intermediate states can be evaluated.

$$\langle \phi_{k+1} | e^{-i\epsilon H(x,p)} | \phi_k \rangle = \left( \prod_i \int \frac{dp_k^i}{2\pi} \right) \exp \left[ -i\epsilon H \left( \frac{q_k + q_{k+1}}{2}, p_k \right) \right] \times e^{i \sum p_k^i \cdot (x_k^i - x_{k+1}^i)} \quad (2.10)$$

For the  $N$  insertions, the full transition amplitude is:

$$\begin{aligned} \langle \phi_F | e^{-iHT} | \phi_I \rangle &= \left( \prod_{k=1}^N \prod_i \int dx_k^i \int \frac{dp_k^i}{2\pi} \right) \\ &\times \exp \left[ i \sum_{k=1}^N \left( \sum_i p_k^i \cdot (x_k^i - x_{k+1}^i) - \epsilon H \left( \frac{q_k + q_{k+1}}{2}, p_k \right) \right) \right]. \end{aligned}$$

The  $\epsilon$  can be factored out, with the first term including  $\frac{x_k^i - x_{k+1}^i}{\epsilon}$ . Taking the limit  $N \rightarrow \infty$  or  $\epsilon \rightarrow 0$ , the exponential term changes to the continuous limit with  $\dot{x}^i$  and  $\int dt$ . Each differential path  $dx_k$  and  $dq_k$  must be taken into account, which is denoted  $\mathcal{D}x\mathcal{D}p$ . The  $2\pi$

CHAPTER 2. THE STANDARD MODEL

is absorbed into this notation.

$$\langle \phi_F | e^{-iHT} | \phi_I \rangle = \left( \prod_i \int \mathcal{D}x \mathcal{D}p \right) \times \exp \left[ i \int_0^T dt \left( \sum_i p_k^i \dot{x}^i - H(x, p) \right) \right]. \quad (2.11)$$

The terms in the exponential is exactly the definition of the classical Lagrangian; once integrated this is the classical action. The full “path integration” is over all positions and momenta at each time in the integration, essentially the total phase space, weighted by the classical action  $e^{iS}$ . This was initially proposed by Dirac [21], Feynman applied this to non-relativistic quantum mechanics [79] and then used it in his development of quantum field theory [33].

For fields, the integration over phase space becomes an integration over all possible field configurations:

$$\langle \phi_F | e^{-iHT} | \phi_I \rangle = \int \mathcal{D}\phi \exp \left[ i \int_0^T dt \mathcal{L}(\phi, \partial_\mu \phi) \right]. \quad (2.12)$$

This is the expression for the transition amplitude for a field between an an initial state  $\phi_I$  and final state  $\phi_F$  over time  $T$ , and is called the propagator. A similar quantity is called the two-point correlation function,  $\langle 0 | T \{ \phi(x_1) \phi(x_2) \} | 0 \rangle$ . This is the amplitude between two vacuum states, with the time-ordered product of two field configurations as the operator being evaluated. The time-ordering ensures that if  $x_1^0 > x_2^0$ , then the order of the fields in the exponential behave correctly. In terms of the path-integral, this can be related to the quantity:

$$\int \mathcal{D}\phi \phi(x_1) \phi(x_2) \exp \left[ i \int_{-T}^T d^4x \mathcal{L}(\phi, \partial_\mu \phi) \right].$$

Returning to the original expression (2.12) using the Hamiltonian time-evolution in terms

CHAPTER 2. THE STANDARD MODEL

of the path-integral, the transition amplitude can be split up into three factors. Each factor is fixed at the start and end configurations determined by  $\phi_I$ ,  $\phi_F$ , and the two intermediate configurations  $\phi_1(x_1)$  and  $\phi_2(x_2)$ :

$$\iint \mathcal{D}\phi_1 \mathcal{D}\phi_2 \phi_1(\vec{x}_1) \phi_2(\vec{x}_2) \langle \phi_F | e^{-iH(T-x_2^0)} | \phi_2 \rangle \langle \phi_2 | e^{-iH(x_2^0-x_1^0)} | \phi_1 \rangle \langle \phi_1 | e^{-iH(T-x_1^0)} | \phi_I \rangle.$$

The completeness relation for  $\phi_1$  and  $\phi_2$  holds, except there is an additional factor of  $\phi_1(x_1)$  and  $\phi_2(x_2)$ . However by factoring out the time-dependence of the field operators into  $e^{iHx^0} \phi(\vec{x}) e^{-iHx^0}$ , they are not dynamic Heisenberg operators but static Schrödinger operators for the creation/annihilation of the fields. Then the completion relation  $1 = \int \mathcal{D}\phi |\phi\rangle \langle\phi|$  can be used to eliminate the intermediate dynamic states:

$$\langle \phi_F | e^{-iH(T-x_2^0)} \phi_{Sch}(\vec{x}_2) e^{-iH(x_2^0-x_1^0)} \phi_{Sch}(\vec{x}_1) e^{-iH(T-x_1^0)} | \phi_I \rangle.$$

If the time-ordering had been different, the signs and order for  $x_1$  and  $x_2$  would have flipped, but otherwise this expression would be true, exactly as need for time-ordering. Re-introducing the time-dependence for the intermediate operators returns to the standard Heisenberg-picture of the correlation function:

$$\langle \phi_F | e^{-iHT} T \{ \phi(x_1) \phi(x_2) \} e^{-iHT} | \phi_I \rangle.$$

To find the exact expression for the vacuum two-point correlation function, the initial and final states should be projected solely onto the vacuum state. This can be done by introducing a small imaginary component to the time,  $T \rightarrow T(1 - i\epsilon)$ , then taking the limit  $T \rightarrow \infty$ .

## CHAPTER 2. THE STANDARD MODEL

The state  $|\phi_I\rangle$  can be decomposed into eigenstates of  $H$ .

$$e^{-iHT} |\phi_I\rangle = \sum_j e^{-iE_j T} |j\rangle \langle j | \phi_I\rangle \longrightarrow e^{-iE_0 \infty(1-i\epsilon)} \langle 0 | \phi_I\rangle |0\rangle$$

This leaves a couple of factors that need to be removed to complete the relation between the two-point vacuum correlation function and the path-integral formulation using field operators. These factors, the phase introduced by the small imaginary term and the normalization factor from the overlap between the vacuum and initial states, also appear in the “bare” state evolution after performing the same limit.

$$\langle \phi_F | e^{-iHT} \cdot e^{-iHT} | \phi_I\rangle \longrightarrow \langle 0 | \phi_I\rangle \langle \phi_F | 0\rangle \langle 0 | e^{-iE_0 \infty(1-i\epsilon)} \cdot e^{-iE_0 \infty(1-i\epsilon)} | 0\rangle$$

Dividing the two results gives the correct two-point correlation function:

$$\langle 0 | T\{\phi(x_1)\phi(x_2)\} | 0\rangle = \lim_{T \rightarrow \infty(1-i\epsilon)} \frac{\int \mathcal{D}\phi \phi(x_1)\phi(x_2) \exp \left[ i \int_{-T}^T d^4x \mathcal{L}(\phi, \partial_\mu \phi) \right]}{\int \mathcal{D}\phi \exp \left[ i \int_{-T}^T d^4x \mathcal{L}(\phi, \partial_\mu \phi) \right]}. \quad (2.13)$$

Higher-order correlation functions can be obtained by simply inserting more factors of  $\phi$  into the time-ordering or the numerator path-integral.

### Feynman Rules and Diagrams

To apply this to calculations, there needs to be a set of rules to follow for how to compute these correlation functions. Instead of using the energy eigenfunction decomposition of the fields, the fields are expanded in momentum space:

$$\phi(x) \rightarrow \int \frac{d^4p}{(2\pi)^4} e^{-ip \cdot x} \phi(p).$$

CHAPTER 2. THE STANDARD MODEL

The simplest Lagrangian, having only a kinetic and mass term, transforms into:

$$\int d^4x L_0 = \int d^4x \left[ \frac{1}{2}(\partial_\mu)^2 - \frac{1}{2}m^2\phi^2 \right] \longrightarrow -\frac{1}{2} \int \frac{d^4p}{(2\pi)^4} (m^2 - p^2) |\phi(p)|^2.$$

The denominator for the correlation functions in (2.13) in terms of the path-integral changes the  $\mathcal{D}\phi$  into integration over every possible value of  $p$  taken on by  $\phi(p)$ :

$$\begin{aligned} \int \mathcal{D}\phi \exp \left[ i \int d^4x \mathcal{L}(\phi, \partial_\mu\phi) \right] &\longrightarrow \left( \prod_p \int d\phi_p \right) \exp \left[ -i \frac{1}{2} \int \frac{d^4p}{(2\pi)^4} (m^2 - p^2) |\phi_p|^2 \right] \\ &= \prod_p \left\{ \int d\phi_p \exp \left[ -i \frac{1}{2} \frac{1}{(2\pi)^4} (m^2 - p^2) |\phi_p|^2 \right] \right\} \\ &= \prod_p \left\{ \sqrt{\pi \frac{-i2(2\pi)^4}{m^2 - p^2}} \right\}. \end{aligned}$$

Between the first and second lines, the integral over all  $p$  can be re-expressed as a sum, which when combined with the product over all  $p$ , turns the path-integral into a product over each separate momentum. Between the second and third lines, the standard Gaussian integration is performed. However the integrand is purely imaginary, and in order to close the contour integral a small rotation is performed in the complex plane in momentum space. To close this contour, the rotation needed must close  $-i(m^2 - p^2)$ , so in terms of  $p^2 \rightarrow p^2 + i\epsilon$ . This must match with what was done in the time-ordering projection,  $p^0 \rightarrow p^0(1 + i\epsilon)$ . The final result for the denominator is:

$$\int \mathcal{D}\phi \exp \left[ i \int d^4x \mathcal{L}(\phi, \partial_\mu\phi) \right] \longrightarrow \prod_p \sqrt{\pi \frac{-i2(2\pi)^4}{m^2 - p^2 - i\epsilon}}. \quad (2.14)$$

CHAPTER 2. THE STANDARD MODEL

In the numerator, there are two additional factors of  $\phi$  in the integration:

$$\int \mathcal{D}\phi \phi(x_1)\phi(x_2) \exp \left[ i \int d^4x \mathcal{L}(\phi, \partial_\mu \phi) \right] \longrightarrow$$

$$\left( \prod_p \int d\phi_p \right) \int \frac{d^4p_1 d^4p_2}{(2\pi)^8} e^{-ip_1 \cdot x_1} \phi_p(p_1) e^{-ip_2 \cdot x_2} \phi_p(p_2) \exp \left[ -i \frac{1}{2} \int \frac{d^4p}{(2\pi)^4} (m^2 - p^2) |\phi_p|^2 \right].$$

For most values of  $p_1$  and  $p_2$ , this integrand is zero by Fourier's Theorem; only when  $p_1 = \pm p_2$  will this not automatically vanish. When  $p_1 = +p_2$ , the two  $\phi_p$  factors have the same sign, so the real and imaginary terms cancel each other. When  $p_1 = -p_2$ , the two  $\phi_p$  terms are conjugates because  $\phi(-p) = \phi^*(p)$ . With the integrand positive definite, the same integration tricks done for the “bare” denominator can be employed. The only change is when  $p = p_1$ . The product includes an additional factor of  $|\phi_p|^2$  in the integration.

$$= \int \frac{d^4p_1}{(2\pi)^8} e^{-ip_1 \cdot (x_1 - x_2)} \left( \prod_p \int d\phi_p \right) |\phi_{p_1}(p_1)|^2 \exp \left[ -i \frac{1}{2} \int \frac{d^4p}{(2\pi)^4} (m^2 - p^2) |\phi_p|^2 \right]$$

$$= \int \frac{d^4p_1}{(2\pi)^8} e^{-ip_1 \cdot (x_1 - x_2)} \prod_p \left\{ \int d\phi_p |\phi_{p_1}(p_1)|^2 \exp \left[ -i \frac{1}{2} \frac{1}{(2\pi)^4} (m^2 - p^2) |\phi_p|^2 \right] \right\}$$

$$= \int \frac{d^4p_1}{(2\pi)^8} e^{-ip_1 \cdot (x_1 - x_2)} \left\{ \prod_p \sqrt{\pi \frac{-i2(2\pi)^4}{m^2 - p^2 - i\epsilon}} \right\} \times \frac{-i \frac{1}{2} \cdot 2(2\pi)^4}{m^2 - p^2 - i\epsilon}$$

The middle factor is precisely the product found for the denominator. Again, the analytic continuation into the imaginary plane for  $p^0$  was employed to have the integral converge. The two-point correlation function is, in analytic form:

$$\langle 0 | T \{ \phi(x_1) \phi(x_2) \} | 0 \rangle = \int \frac{d^4p}{(2\pi)^4} \frac{i e^{-ip \cdot (x_1 - x_2)}}{p^2 - m^2 + i\epsilon} \equiv D(x_1 - x_2). \quad (2.15)$$

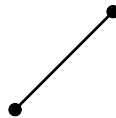
This is the probability for a particle to propagate from a point  $x_1$  to  $x_2$ . The phase  $+i\epsilon$  ensures the proper time-ordering between  $x_1$  and  $x_2$ . Higher-order correlation functions work

CHAPTER 2. THE STANDARD MODEL

very similarly. Each additional field in the correlation function acts as creation/annihilation operator. Each set of fields must be paired off correctly in order to return to the vacuum state. These are called “contractions”, and higher-order correlation functions are the sum over all possible two-point contractions. Wick’s Theorem states that any order of correlation functions can be reduced in such a manner. For example, the four-point correlation function is:

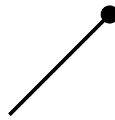
$$\begin{aligned} \langle 0|T\{\phi(x_1)\phi(x_2)\phi(x_3)\phi(x_4)\}|0\rangle &= D(x_1-x_2)D(x_3-x_4) \\ &\quad +D(x_1-x_3)D(x_2-x_4) \\ &\quad +D(x_1-x_4)D(x_2-x_3) \end{aligned}$$

A clever and useful way to organize these calculations was developed by Richard Feynman, and are called Feynman diagrams. For example, the two-point correlation function can be drawn:



$$= \frac{i}{p^2-m^2+i\epsilon}.$$

The evolution from the vacuum state to the field configuration is called an external line:



$$= e^{-ip \cdot x}.$$

The calculation above assumed a free theory, there were no interactions to change how the particle behaved. An additional interaction term can be added to the Lagrangian:

$$L \rightarrow L_0 - \frac{\lambda}{4!}\phi^4.$$

The potential term,  $V = \frac{\lambda}{4!}\phi^4$ , is positive-definite and bounds the theory at infinity. Assum-



## CHAPTER 2. THE STANDARD MODEL

ing the interaction is small  $\lambda \ll 1$ , the action can be Taylor-expanded:

$$\exp \left[ i \int d^4x L \right] \simeq \exp \left[ i \int d^4x L_0 \right] \left( 1 - i \int d^4x \frac{\lambda}{4!} \phi^4 + \dots \right).$$

The expansion results in terms exactly like the four-point correlation function, however all four fields are at the same point  $x$ . Moving to momentum space, the integrals over  $d^4p$  become  $\delta$ -functions enforcing conservation of momentum. Evaluating this term leaves:

$$\text{Perturbation} = -i\lambda(2\pi)^4 \delta(p_1 + p_2 + p_3 + p_4).$$

The initial factor of  $1/4!$  in the interaction term ensured when we included all possible combinations of  $\phi^4$  in the Wick contractions the remaining perturbation did not have  $4!$ .

The perturbation can be incorporated into Feynman diagrams:

$$\begin{array}{c} \diagup \\ \bullet \\ \diagdown \end{array} = -i\lambda .$$

### Spinors

Particles with non-integer spin obey anti-commutation relations rather than commutation relations. This comes from a very deep relation between how particles with spin transform under Lorentz transformations; for a full discussion of the link between spin, statistics, and their (anti-)commutation relations, see Streater & Wightman's *PCT, Spin and Statistics, and All That* [80]. In order to find a representation of the Lorentz group that satisfies the anti-commutation relations needed for fermionic statistics in 3+1 dimensions the minimum

## CHAPTER 2. THE STANDARD MODEL

size of the representation is 4x4. These are the Dirac gamma matrices,  $\gamma^\mu$ .

$$\{\gamma^\mu, \gamma^\nu\} = 2\eta^{\mu\nu}$$

$$\gamma^0 = \begin{pmatrix} 0 & 1 \\ 1 & 0 \end{pmatrix}, \quad \gamma^i = \begin{pmatrix} 0 & \sigma_i \\ -\sigma_i & 0 \end{pmatrix}$$

The generators of the Lorentz algebra are built up from the Dirac matrices:

$$S^{\mu\nu} = \frac{i}{4} [\gamma^\mu, \gamma^\nu],$$

$$\text{Boosts: } S^{0i} = \frac{i}{4} [\gamma^0, \gamma^i] = -\frac{i}{2} \begin{pmatrix} \sigma_i & 0 \\ 0 & -\sigma_i \end{pmatrix},$$

$$\text{Rotations: } S^{ij} = \frac{i}{4} [\gamma^i, \gamma^j] = \frac{1}{2} \epsilon^{ijk} \begin{pmatrix} \sigma_k & 0 \\ 0 & \sigma_k \end{pmatrix}.$$

Fields that transform under this representation of the Lorentz group are called spinors, and all fermions such as electrons are these types of particles. The equation of motion for such particles without any interactions is:

$$(i\gamma^\mu \partial_\mu - m)\psi = (i\rlap{\not{D}} - m)\psi = 0.$$

The field  $\psi$  is a 4-component spinor. The term with  $\gamma^\mu \partial_\mu$  acts on both the Lorentz and spinor indices of  $\psi$  such that the whole term transforms as a spinor. This also introduces the Feynman slash notation, where any Lorentz vector contracted with a Dirac gamma matrix is “slashed”, such as  $\gamma^\mu \partial_\mu \equiv \rlap{\not{D}}$ . The Lagrangian for such a particle should be a Lorentz scalar. In order to construct a proper Lorentz scalar, the conjugate spinor is needed. However, due to the extra factor of  $i$  in the Boosts matrices, this is not a unitary representation of the Lorentz group. Therefore, the natural guess of  $\psi^\dagger \psi$  will not be invariant under boosts. Introducing

## CHAPTER 2. THE STANDARD MODEL

an extra factor of  $\gamma^0$  ensures that boosts and rotations are preserved as a symmetry:

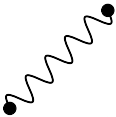

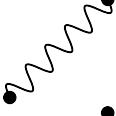

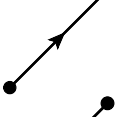

$$\psi^\dagger\psi \rightarrow \psi^\dagger\gamma^0\psi \equiv \bar{\psi}\psi.$$

This preserves the full Lorentz symmetry. Another common set of notation is introduced here, the “bar” notation for spinors, such as  $\psi^\dagger\gamma^0 \equiv \bar{\psi}$ . The full Lorentz-invariant, spin- $\frac{1}{2}$  Lagrangian is:

$$L_{\text{Dirac}} = \bar{\psi}(i\gamma^\mu\partial_\mu - m)\psi. \quad (2.16)$$

The Feynman rules for calculating propagation and interaction of particles were shown for a simple scalar theory, called the Klein-Gordon theory. Particles with integer spin have a very similar set of rules for how they propagate and interact. However, for particles with non-integer spin such as electrons that obey anti-commutation relations, several of the results we derived will not apply. Instead the integration uses Grassman variables which obey the proper anti-commutation relations. Many of the same tools can still be applied, but modified to take into account the behavior of the fermionic variables. The various rules for writing Feynman diagrams are:

CHAPTER 2. THE STANDARD MODEL

Massless Vector Propagator		= $\frac{-i\eta_{\mu\nu}}{p^2+i\epsilon}$ ,
Massless Vector External Line		= $\epsilon_\mu(p)$ ,
Massive Vector Propagator		= $\frac{-i}{p^2-m^2+i\epsilon} \left( \eta_{\mu\nu} - \frac{p_\mu p_\nu}{m^2} \right)$ ,
Massive Vector External Line		= $\epsilon_\mu(p)$ ,
Fermion Propagator		= $\frac{i(\not{p}+m)}{p^2-m^2+i\epsilon}$ ,
Fermion External Line		= $u^s(p)$ .

The external components for vector bosons are  $\epsilon_\mu$ , which denote their polarization. The external component for fermions are spinors. Interaction rules will depend on the structure of the perturbation potential in the Lagrangian.

### 2.2.2 Lie Algebras and Interactions

One of the most important discoveries in theoretical physics is the power of gauge symmetry to describe how particles interact. This comes from assuming particles are states in a Hilbert space that transform under the operation of a group, and that the physics results are independent of the choice of transformation. Before fully describing the consequences of this postulate, this section will describe a little group theory needed to understand this theory. A wonderful textbook that covers this subject in full detail is Howard Georgi's *Lie Algebras in Particle Physics* [81].

## CHAPTER 2. THE STANDARD MODEL

### A Little Group Theory

A group is a set of elements with an operation that obeys the following four axioms:

1. *Closure.* For any two elements in the group, the result of their operation is in the group.

$$\forall a, b \in G, \quad a \cdot b \in G.$$

2. *Associativity.* The calculation is independent of the order of operations.

$$\forall a, b, c \in G, \quad (a \cdot b) \cdot c = a \cdot (b \cdot c)$$

NOTE: this is not the same as the calculation is independent of the order of the elements! (In general  $a \cdot b \neq b \cdot a$ .)

3. *Identity.* There exists an element in the group that leaves every element of the group the same under the operation on both sides.

$$\forall a \in G, \quad \exists e \in G \text{ such that } e \cdot a = a \cdot e = a.$$

4. *Inverse.* For every element in the group, there is an element when operated together gives the identity.

$$\forall a \in G, \quad \exists a^{-1} \in G \text{ such that } a \cdot a^{-1} = a^{-1} \cdot a = e.$$

A representation is a mapping  $D$  of the group into a set of linear operators that obeys the natural composition of the group, i.e.  $D(ab) = D(a)D(b)$ , and preserves the identity  $D(e) = 1$ . A subgroup is a group  $G$  whose elements are all in a group  $H$ . Trivial subgroups

## CHAPTER 2. THE STANDARD MODEL

are the identity element and the whole group. Not all groups have them, but there are non-trivial subgroups as well. One important fact about finite groups is there exists a unitary representation for every finite group, one where  $D^\dagger(g) = D(g^{-1})$ .

Suppose a group depends on a continuous parameter or set of parameters  $\alpha_a$ , i.e. the elements of the group can be written  $g(\alpha_a)$ . Then for infinitesimal  $\alpha_a$ , a representation of the group can be written:

$$D(\alpha) = 1 + i\alpha_a T_a + \mathcal{O}(\alpha^2).$$

The factor  $i$  is convention. The objects  $T_a$  are the “generators” of the group. Moving to finite  $\alpha_a$ , this can be re-written:

$$D(\alpha) = \lim_{N \rightarrow \infty} \left( 1 + i \frac{\alpha_a T_a}{N} \right)^N = e^{i\alpha_a T_a}.$$

This is the exponential parameterization of a group. In general, the generators  $T_a$  will not commute with each other. These form a Lie algebra defined by their commutation relations:

$$[T^a, T^b] = i f^{abc} T^c. \tag{2.17}$$

The constants  $f_{abc}$  are the structure constants of the Lie algebra, and they uniquely define the Lie algebra. The structure constants are completely anti-symmetric. If the structure constants vanish so the generator(s) commute, this is called an Abelian algebra. Conversely, all non-commuting algebras are called non-Abelian. The generators obey the Jacobi identity:

$$[T^a, [T^b, T^c]] + [T^c, [T^a, T^b]] + [T^b, [T^c, T^a]] = 0. \tag{2.18}$$

## CHAPTER 2. THE STANDARD MODEL

The representation of a group can act on states in a Hilbert space:

$$|s\rangle \rightarrow |s'\rangle = D(g) |s\rangle = e^{i\alpha^a T^a} |s\rangle.$$

A linear operator in the Hilbert space acts on a state and must return back a state because of the group axioms. Therefore the operators in the Hilbert space must transform as:

$$\begin{aligned} \mathcal{O} |s\rangle &\rightarrow e^{i\alpha^a T^a} \mathcal{O} |s\rangle \\ &= e^{i\alpha^a T^a} \mathcal{O} e^{-i\alpha^a T^a} e^{i\alpha^a T^a} |s\rangle \\ &= \mathcal{O}' |s'\rangle \\ \Rightarrow \mathcal{O}' &= e^{i\alpha^a T^a} \mathcal{O} e^{-i\alpha^a T^a}. \end{aligned}$$

These algebras and their structure have profound consequences for particle physics.

### 2.2.3 Gauge Theory

Noether's Theorem shows how a symmetry of a system leads to conserved currents and charges. One such symmetry is "gauge symmetry", where the fields themselves are symmetric under certain transformations. Symmetric means in this case that the physics observables remain the same under these gauge transformations. In classical electromagnetism with no sources, all of the dynamics can be written in terms of a potential field,  $A_\mu$ . The Lagrangian is:

$$L_{\text{EM}} = -\frac{1}{4} F_{\mu\nu} F^{\mu\nu}, \quad F_{\mu\nu} = \partial_\mu A_\nu - \partial_\nu A_\mu.$$

The Lagrangian, when put in terms of the fields  $E^i = F^{0i}$  and  $B^i = \epsilon^{ijk} F_{jk}$ , is  $\frac{1}{2}(E^2 - B^2)$ . This is the kinetic energy of the EM field, not the total energy which is proportional to

## CHAPTER 2. THE STANDARD MODEL

$E^2 + B^2$ . The equations of motion are:

$$\partial_\mu F^{\mu\nu} = 0,$$

which are precisely Maxwell's equations [82] with no currents or charges. The Lagrangian is invariant under Lorentz transformations, so this theory obeys Special Relativity. In addition, the field tensor  $F_{\mu\nu}$  is invariant under a certain class of changes in the potential field, which leaves the Lagrangian invariant as well:

$$A_\mu \rightarrow A_\mu + \partial_\mu \lambda(x) \implies F_{\mu\nu} \rightarrow F_{\mu\nu} \quad \text{and} \quad L_{\text{EM}} \rightarrow L_{\text{EM}}.$$

This is an example of a “gauge transformation”. Because the Lagrangian is invariant, all observable physical results are independent of the choice of gauge function  $\lambda(x)$  and there will be an associated conserved current with this symmetry. This section will explore how this class of symmetries forms the basis for modern particle physics.

### Abelian Gauge Theory

The fields for particles are postulated to be states in a Hilbert space that transform under a representation of a Lie algebra. This transformation is assumed to be a gauge transformation so the physics must remain invariant. The simplest example for a quantum field theory with gauge symmetry is a complex scalar field:

$$L = \frac{1}{2} |\partial_\mu \phi(x)|^2 - \frac{1}{2} m^2 |\phi(x)|^2.$$

The Lagrangian for this theory is invariant under a change in phase of the field  $\phi$ , i.e. the field is multiplied by a complex number whose modulus is 1. This is an Abelian gauge theory,



## CHAPTER 2. THE STANDARD MODEL

the generator is simply 1.

$$\phi(x) \rightarrow e^{i\alpha} \phi(x) \Rightarrow L \rightarrow L$$

This is a “global” gauge transformation, every point of the field  $\phi(x)$  is changed by the same phase. If the gauge transformation parameter  $\alpha$  instead depended on the position  $x$ , then this would no longer be a symmetry of the theory. In this case, the gauge transformation is said to be a “local” symmetry, and this is a much larger symmetry than the global transformation case. What is needed to ensure that this theory is invariant under local gauge transformations? Under this transformation, the Lagrangian adds the following terms:

$$\begin{aligned} \phi(x) &\rightarrow e^{i\alpha(x)} \phi(x), \\ \Rightarrow L &\rightarrow L + \frac{1}{2} \left( (\partial_\mu \alpha)^2 |\phi|^2 + i(\partial_\mu \alpha)(\phi(\partial^\mu \phi^*) - (\partial^\mu \phi)\phi^*) \right). \end{aligned}$$

In order to preserve local gauge symmetry, something else is needed to cancel these additional terms. To do this, a new field is introduced  $A_\mu$  that is also changes under the local gauge transformation:

$$\phi(x) \rightarrow e^{i\alpha(x)} \phi(x) \quad \text{and} \quad A_\mu \rightarrow A_\mu + \partial_\mu \alpha(x).$$

Because a new field is introduced, a kinetic term is needed in the Lagrangian. This term is  $-\frac{1}{4}F_{\mu\nu}F^{\mu\nu}$ , and the transformation of the field  $A_\mu$  leaves this invariant, so no further additional terms are added. In addition to the kinetic term for the new gauge field, there must be interaction terms between  $\phi$  and  $A_\mu$  that cancel the terms added by the gauge transformation of  $\phi$ :

$$L \rightarrow L - \frac{1}{4}F_{\mu\nu}F^{\mu\nu} + \frac{1}{2}(A_\mu)^2|\phi|^2 + \frac{i}{2}A_\mu(\phi(\partial^\mu \phi^*) - (\partial^\mu \phi)\phi^*).$$

## CHAPTER 2. THE STANDARD MODEL

The new interaction terms cancel the terms created when the derivative acted on the local gauge transformation. This fact can be exploited to make the derivative term for  $\phi$  manifestly gauge invariant:

$$\partial_\mu \phi(x) \rightarrow (\partial_\mu - iA_\mu(x))\phi(x).$$

The new derivative interaction including the field  $A_\mu$  is called the gauge covariant derivative. In the same way that constructing terms using the covariant derivative  $\partial_\mu$  preserves Lorentz symmetry, using the gauge covariant derivative preserves local gauge symmetry as well as Lorentz symmetry. The strength of the interaction between the gauge field and the matter field is denoted with a coupling constant, usually  $g$  or  $e$ .

$$D_\mu \equiv \partial_\mu - igA_\mu(x) \tag{2.19}$$

$$\phi(x) \rightarrow e^{ig\alpha(x)}\phi(x) \quad \text{and} \quad A_\mu \rightarrow A_\mu + \partial_\mu\alpha(x) \tag{2.20}$$

The Lagrangian is now:

$$L = \frac{1}{2}|D_\mu\phi(x)|^2 - \frac{1}{2}m^2|\phi(x)|^2 - \frac{1}{4}F_{\mu\nu}F^{\mu\nu}. \tag{2.21}$$

No additional interaction or kinetic terms are allowed as they would violate the postulated gauge symmetry. In particular the field  $A_\mu$  must remain massless in order to preserve gauge invariance.

Now that the Lagrangian is invariant under local gauge symmetry, what are the associated

## CHAPTER 2. THE STANDARD MODEL

conserved currents? First, the equations of motion for the two fields are:

$$\begin{aligned}
 \partial_\mu F^{\mu\nu} &= ig[\phi(\partial^\nu \phi^*) - (\partial^\nu \phi)\phi^*] + 2g^2 A^\nu |\phi|^2 \\
 \rightsquigarrow \partial_\mu F^{\mu\nu} &= ig[\phi(D^\nu \phi)^* - (D^\nu \phi)\phi^*], \\
 \partial_\mu [D^\mu \phi] &= -m^2 \phi - igA_\mu D^\mu \phi \\
 \rightsquigarrow 0 &= (D_\mu D^\mu + m^2)\phi \text{ and c.c.}
 \end{aligned}$$

The first term is Maxwell's equations again, now with a source current built up from the fields. If the coupling constant  $g$  is interpreted as a unit of charge carried by the field  $\phi$ , this is the total EM current carried by the field. The third line is exactly the same equations of motion for a free scalar field, with the replacement  $\partial_\mu \rightarrow D_\mu$ . The conserved Noether current is:

$$\begin{aligned}
 j^\mu &= (D^\mu \phi)(-ig\phi^*) + (D^\mu \phi)^*(ig\phi) \\
 &= ig[\phi(D^\nu \phi)^* - (D^\nu \phi)\phi^*].
 \end{aligned}$$

The conserved current is the vector previously interpreted to be the EM current in Maxwell's equations. The  $\mu = 0$  term, integrated over all space, will correspond to the total charge and the  $j^i$  terms are the flow of charge into or out of the system. Therefore the postulate of local gauge symmetry for a complex scalar field has led to electromagnetism and conservation of charge.

The promotion of the global gauge transformation to a local symmetry required the introduction of a new gauge field. This then reproduced Maxwell's equations in the equations of motion and the associated conserved quantity from Noether's Theorem was the EM current. This promotion can be accomplished with the minimal coupling prescription:

1. Promote gauge transformation to a local symmetry,  $\phi(x) \rightarrow e^{ig\alpha(x)}\phi(x)$ .

## CHAPTER 2. THE STANDARD MODEL

2. Introduce gauge field  $A_\mu \rightarrow A_\mu + \partial_\mu \alpha(x)$  with kinetic term  $-\frac{1}{4}F_{\mu\nu}F^{\mu\nu}$ .
3. Change all covariant derivatives of  $\phi$  to gauge covariant derivatives,  

$$\partial_\mu \rightarrow D_\mu = \partial_\mu - igA_\mu(x).$$
4. Equations of motion and conserved currents are preserved, modified with the gauge covariant derivative acting on the field  $\phi$ .

This example was for a scalar field, but the same steps can be applied to a single spin- $\frac{1}{2}$  particle such as the electron. The free Lagrangian, equations of motion, and conserved current under a global gauge transformation are:

$$\begin{aligned} L &= \bar{\psi}(i\not{D} - m)\psi, \\ 0 &= (i\not{D} - m)\psi \text{ and conjugate,} \\ j^\mu &= g\bar{\psi}\gamma^\mu\psi. \end{aligned}$$

Promoting the global gauge symmetry to a local symmetry following the minimal coupling prescription results in the QED Lagrangian. In this special case, the coupling constant is traditionally denoted  $e$ , the electric charge of the electron:

$$\begin{aligned} L &= \bar{\psi}(i\not{D} - m)\psi - \frac{1}{4}F_{\mu\nu}F^{\mu\nu}, \\ \partial_\mu F^{\mu\nu} &= e\bar{\psi}\gamma^\mu\psi, \\ 0 &= (i\not{D} - m)\psi \text{ and conjugate,} \\ j^\mu &= e\bar{\psi}\gamma^\mu\psi. \end{aligned}$$

As before, the conserved current is the charge of the electron field density and enters into Maxwell's equations. The equations of motion for  $\psi$  is the Dirac equation for the electron, including the interaction with the EM field.

### Non-Abelian Gauge Theory

The previous examples assumed that the gauge transformation  $\alpha$  commuted with everything; this is an example of Abelian gauge transformation. What if instead, the transformation was generated by a non-Abelian Lie algebra. The non-commutative part can be represented as in equation (2.17):

$$[T^a, T^b] = if^{abc}T^c.$$

The field is being gauge transformed by a phase, but now that phase depends on this algebra, with a possible gauge rotation for each generator of the algebra:

$$\psi \rightarrow \exp[ig \cdot \alpha^a T^a] \psi.$$

The covariant derivative in equation (2.19) must include the factors from the algebra:

$$\partial_\mu \rightarrow D_\mu = \partial_\mu - igA_\mu^a T^a.$$

Instead of a single new gauge field, there are as many gauge fields as the dimension of the algebra, indicated by the index  $a$ . To see how  $A_\mu^a$  transforms under these non-Abelian gauge transformation, insert this into the derivative term:

$$D_\mu \psi \rightarrow (\partial_\mu - igA_\mu^a T^a + \text{gauge field transformation}) \exp[ig \cdot \alpha^a T^a] \psi.$$

## CHAPTER 2. THE STANDARD MODEL

The gauge field transformation must depend on  $T^a$ . To simplify the calculations, assume that  $\alpha \ll 1$  and expand the exponential:

$$\begin{aligned} D_\mu \psi &\rightarrow (\partial_\mu - igA_\mu^a T^a - ig(\delta A_\mu^a) T^a) [1 + ig \cdot \alpha^a T^a] \psi \\ &= (\partial_\mu - igA_\mu^a T^a - ig(\delta A_\mu^a) T^a + ig(\partial_\mu \alpha^a) T^a \\ &\quad + ig\alpha^a T^a \partial_\mu + g^2 A_\mu^a \alpha^b T^a T^b + g^2 (\delta A_\mu^a) \alpha^b T^a T^b) \psi \end{aligned}$$

The last term contains  $(\delta A_\mu^a) \alpha^b$ , which must be at least quadratic in  $\alpha$  and can be safely dropped. The covariant derivative is a linear operator on the field  $\psi$ , and so must transform as the field would normally to be gauge covariant. Therefore, the above expression must be equal to:

$$\begin{aligned} \exp[ig \cdot \alpha^a T^a] D_\mu \psi &= [1 + ig \cdot \alpha^a T^a] D_\mu \psi \\ &= (\partial_\mu - igA_\mu^a T^a + ig\alpha^a T^a \partial_\mu + g^2 A_\mu^a \alpha^b T^a T^b) \psi. \end{aligned}$$

Equating and canceling terms, the transformation for  $A_\mu^a$  is:

$$\begin{aligned} g^2 A_\mu^a \alpha^b T^b T^a &= -ig(\delta A_\mu^a) T^a + ig(\partial_\mu \alpha^a) T^a + g^2 A_\mu^a \alpha^b T^a T^b \\ 0 &= -i(\delta A_\mu^a) T^a + i(\partial_\mu \alpha^a) T^a + gA_\mu^a \alpha^b [T^a, T^b] \\ \Rightarrow \delta A_\mu^a &= +\partial_\mu \alpha^a - gf^{abc} \alpha^b A_\mu^c. \end{aligned}$$

This transformation of  $A_\mu^a$  will not leave the field strength tensor  $F_{\mu\nu}$  invariant unlike the Abelian case. Instead, the gauge field kinetic term  $F_{\mu\nu} F^{\mu\nu}$  must remain invariant. The field strength tensor  $F_{\mu\nu}^a$  is modified to accommodate local gauge symmetry in such a way to ensure the kinetic term  $F_{\mu\nu}^a F^{\mu\nu a}$  is remains invariant:

$$F_{\mu\nu}^a = \partial_\mu A_\nu^a - \partial_\nu A_\mu^a + gf^{abc} A_\mu^b A_\nu^c$$

## CHAPTER 2. THE STANDARD MODEL

The extra terms in the field tensor produce new interactions between the gauge fields themselves. These self-interaction terms can have vertices with 3 or 4 gauge fields interacting at one point. This is a self-interacting field theory first described by Yang and Mills for the case when the  $T^a$  are the Pauli matrices, the generators for  $SU(2)$ .

### Symmetry Breaking, Goldstone's Theorem, & the Higgs Mechanism

An interesting class of phenomena happen when a symmetry of a system is broken. Breaking a symmetry means re-arranging terms such that the original symmetry of the theory is no longer manifest but the physical dynamics are made clear. A simple example is a set of  $N$  scalar fields  $\phi^i$  that can rotate into each other:

$$\phi^i \rightarrow R^{ij} \phi^j.$$

When  $N = 2$ , this is equivalent to a single complex scalar field and  $R^{ij}$  is a phase rotation. This is a real-valued generalization of that example, called the linear sigma model. For  $N$  fields, the symmetry is  $O(N)$ , the group of orthogonal rotations. The Lagrangian including a  $\phi^4$  interaction term is:

$$L = \frac{1}{2}(\partial_\mu \phi^i)^2 - \frac{1}{2}m^2(\phi^i)^2 - \frac{\lambda}{4}((\phi^i)^2)^2.$$

This is manifestly invariant under the rotations  $R^{ij}$ . If, instead of the standard mass term the sign is flipped to be positive, then the potential will no longer be minimized at  $\phi^i = 0$ .

CHAPTER 2. THE STANDARD MODEL

In this case the potential is minimized at some non-zero field value:

$$\begin{aligned} L &= \frac{1}{2}(\partial_\mu \phi^i)^2 + \frac{1}{2}\mu^2(\phi^i)^2 - \frac{\lambda}{4}((\phi^i)^2)^2, \\ V &= +m^2(\phi^i)^2 - \frac{\lambda}{4}((\phi^i)^2)^2, \\ (\phi^i)_{\min}^2 &= \frac{\mu^2}{\lambda}. \end{aligned}$$

The last line is a condition on the total value of all the fields combined. However because of the rotational freedom, this can always be set so that only one field has a non-zero value. Without loss of generality this can be chosen to be the  $N^{\text{th}}$  field:

$$\phi_{\min}^i = \begin{pmatrix} 0 \\ \vdots \\ 0 \\ \frac{\mu}{\sqrt{\lambda}} \end{pmatrix}.$$

This minimum value  $\frac{\mu}{\sqrt{\lambda}}$  is often denoted  $v$ , which stands for “vacuum expectation value” (VEV). The remaining  $N - 1$  fields  $\phi^i$  are unchanged, while the  $N^{\text{th}}$  field can be written  $v + \sigma(x)$  with  $\sigma(x)$  the dynamical part of the field. Returning to the original Lagrangian and using the new designation for the  $N^{\text{th}}$  field:

$$\begin{aligned} L &= \frac{1}{2}(\partial_\mu \phi^i)^2 + \frac{1}{2}(\partial_\mu \sigma)^2 + \frac{1}{2}\mu^2(\phi^i)^2 + \frac{1}{2}\mu^2(v + \sigma)^2 - \frac{\lambda}{4}((\phi^i)^2 + (v + \sigma)^2)^2 \\ &= \frac{1}{2}(\partial_\mu \phi^i)^2 + \frac{1}{2}(\partial_\mu \sigma)^2 - \frac{1}{2}(2\mu^2)\sigma^2 - \sqrt{\lambda}\mu\sigma^3 - \sqrt{\lambda}\mu\sigma(\phi^i)^2 - \frac{\lambda}{4}((\phi^i)^2 + \sigma^2)^2. \end{aligned}$$

The field that acquired a VEV now has a positive mass  $\sqrt{2}\mu$ , while the remaining  $N - 1$  fields are massless. The remaining fields have a manifest rotational invariance  $O(N - 1)$ , which is said to be unbroken and the original symmetry  $O(N)$  is said to be hidden or spontaneously broken. This began as a theory where the physical dynamics were unclear due to the “wrong



## CHAPTER 2. THE STANDARD MODEL

sign” on the mass term, but after spontaneous symmetry breaking, the dynamics are clear and the original symmetry is hidden.

The  $N - 1$  massless scalars appearing after the spontaneous symmetry breaking was not an accident and is a general result in any field theory, called Goldstone’s Theorem. It states that for every spontaneously broken continuous symmetry, there must be a corresponding massless particle called a Goldstone boson. In this example with the group of orthogonal rotations  $O(N)$ , there are  $\frac{N(N-1)}{2}$  possible rotations between the  $N$  original fields. After breaking the symmetry, the manifest rotational group is  $O(N - 1)$  with  $\frac{(N-1)(N-2)}{2}$  possible rotations between the  $N - 1$  fields. The difference is  $\frac{N(N-1)}{2} - \frac{(N-1)(N-2)}{2} = N - 1$ , exactly the number of remaining massless particles. This is an exact result in quantum field theory, and the particles can not acquire a mass term at any order in perturbation theory.

The Higgs mechanism is a clever trick that evades Goldstone’s theorem by instead giving mass to the gauge fields in a theory. This can be demonstrated using the example of a complex scalar field and an Abelian gauge field in equation (2.21), with a modified potential. Again, the mass term will be sign will be “wrong” in the potential:

$$V = -\frac{1}{2}\mu^2|\phi|^2 + \frac{\lambda}{4}(|\phi|^2)^2.$$

In precisely the same way as the previous case, the field  $\phi$  will acquire a VEV and spontaneously break the  $U(1)$  local gauge symmetry. The minimum is at the field value  $|\phi|^2 = \frac{\mu^2}{\lambda}$ . Using the  $U(1)$  symmetry, the minimum can be chosen to be purely real and positive at  $v = +\sqrt{\frac{\mu^2}{\lambda}}$ . The remaining dynamic parts of the field, corresponding to the real and imaginary parts, will be denoted by  $\sigma$  and  $\pi$ :

$$\phi(x) = v + (\sigma(x) + i\pi(x)).$$

## CHAPTER 2. THE STANDARD MODEL

According to the previous analysis, the  $\sigma$  field acquires a mass and the  $\pi$  field is the massless Goldstone boson. The potential term is now:

$$V = -\frac{1}{4}\mu^2 v^2 + \mu^2 \sigma^2 + \sqrt{\lambda}\mu\sigma^3 + \sqrt{\lambda}\mu\sigma\pi^2 + \frac{\lambda}{4}(\sigma^2 + \pi^2)^2.$$

The  $\sigma$  field has mass  $m_\sigma = \sqrt{2}\mu$  and the  $\pi$  field is massless. The kinetic term including the gauge field is now:

$$\begin{aligned} \frac{1}{2}|D_\mu\phi|^2 &= \frac{1}{2}|(\partial_\mu - igA_\mu)(v + \sigma(x) + i\pi(x))|^2 \\ &= \frac{1}{2}|\partial_\mu\sigma + i\partial_\mu\pi - igvA_\mu - igA_\mu\sigma - igA_\mu\pi|^2 \\ &= \frac{1}{2}\left[(\partial_\mu\sigma)^2 + (\partial_\mu\pi)^2 + g^2v^2A_\mu A^\mu + g^2\sigma^2A_\mu A^\mu + g^2\pi^2A_\mu A^\mu \right. \\ &\quad \left. - 2gvA_\mu(\partial^\mu\pi) - 2g\sigma A_\mu(\partial^\mu\pi) - 2gA_\mu(\partial^\mu\pi)\pi \right. \\ &\quad \left. + g^2v\sigma A_\mu A^\mu + g^2v\pi A_\mu A^\mu + g^2\sigma\pi A_\mu A^\mu\right]. \end{aligned}$$

This explicitly shows the interactions between the scalar fields and the gauge field. In addition to the interactions, there is now a term that only depends on  $A^2$ :

$$\frac{1}{2}g^2v^2A_\mu A^\mu = \frac{1}{2}m_A^2A^2.$$

This is a mass term, so the gauge field has acquired a mass after breaking gauge symmetry. The mass depends on the VEV acquired by the scalar field and the coupling constant. The  $\pi$  field as the Goldstone boson has a variety of interactions with both  $\sigma$  and  $A_\mu$ , but this is not a physical field. The simplest way to understand this is to note that there is still the underlying  $U(1)$  gauge symmetry between the  $\sigma$  and  $\pi$  fields. This can always be chosen to ensure the field  $\phi$  is purely real and removes the field  $\pi$  from the theory. By choosing an

## CHAPTER 2. THE STANDARD MODEL

explicit gauge where  $\pi = 0$  and a real VEV, the Lagrangian is now:

$$\begin{aligned} L = & -\frac{1}{4}F_{\mu\nu}F^{\mu\nu} + \frac{1}{2}(\partial_\mu\sigma)^2 + \frac{1}{2}m_A^2 A_\mu A^\mu + \frac{1}{2}m_\sigma^2\sigma^2 \\ & + \frac{1}{2}g^2\sigma^2 A_\mu A^\mu + \frac{1}{2}g^2v\sigma A_\mu A^\mu - \sqrt{\lambda}\mu\sigma^3 + \frac{\lambda}{4}\sigma^4 + \frac{1}{4}\mu^2v^2. \end{aligned}$$

The first line contains the kinetic and mass terms for both the remaining massive scalar field and the gauge field. The second line contains the various cubic and quartic interactions between the  $\sigma$  field and the gauge field as well as self-interactions. By acquiring a VEV and spontaneously breaking the manifest gauge symmetry, the scalar field obtains a mass and gives a mass to the gauge field while the expected massless Goldstone boson can be gauged away. This is the Higgs mechanism. Colloquially, the gauge field  $A_\mu$  is said to “eat” the Goldstone boson and gain a mass. This example was for the Abelian case, and the same process also works for the non-Abelian case where each of the gauge fields  $A_\mu^a$  gains a mass through the Higgs mechanism.

### 2.2.4 Regularization & Renormalization

Historically, the largest impediment to using relativistic quantum field theory to calculate how particles interact was the problem of infinities. At leading order the amplitudes calculated using Feynman diagrams or algebraic methods worked perfectly, but when quantum corrections for these processes were calculated the result was divergent. To deal with these divergences, a systematic program of “regularization” is needed. Pauli & Villars showed the first such procedure in [32], where a large “cutoff” parameter  $\Lambda$  is introduced into the calculations. Once all contributions at a given order in the perturbation series have been calculated and added together, the final physical result should be independent of  $\Lambda \rightarrow \infty$ . A different procedure was introduced by 't Hooft & Veltman in [68] called “dimensional reg-

## CHAPTER 2. THE STANDARD MODEL

ularization”, where the divergent integrals are analytically continued away from the normal four dimensions where they give infinity, evaluated, then returned back to four dimensions. Both methods of regularization keep track of exactly how the calculations diverge. The next step to deal with the infinities is to separate what is a physically measurable quantity from the “bare” quantities of the theory. This is the process where the infinities are systematically gathered together and canceled in all physical processes, called “renormalization”. A common method for dealing with this separation is to split the “bare” parameters of a given theory into the physical quantities and a set of “counterterms”. By defining a consistent set of renormalization conditions on the parameters, this can be done in a systematic way that gives sensible results for all calculations in a theory.

A simple example of this is the basic scalar field theory with a  $\phi^4$  interaction term. This follows the treatment in Peskin & Schroeder’s textbook [74]. The Lagrangian is:

$$L = \frac{1}{2}(\partial_\mu\phi)^2 - \frac{1}{2}m^2\phi^2 - \frac{\lambda}{4!}\phi^4.$$

The quantities in the Lagrangian do not, *a priori*, have anything to do with the physical quantities observed in the laboratory. Instead these should be labeled as bare quantities  $m \rightarrow m_0$  and  $\lambda \rightarrow \lambda_0$ . The field itself can also be shifted by the quantum corrections, requiring field strength renormalization:

$$\phi = Z^{1/2}\phi_R. \tag{2.22}$$

This rescales the Lagrangian to:

$$L = \frac{1}{2}Z(\partial_\mu\phi_R)^2 - \frac{1}{2}m_0^2Z\phi_R^2 - \frac{\lambda_0}{4!}Z^2\phi_R^4.$$

CHAPTER 2. THE STANDARD MODEL


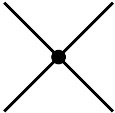

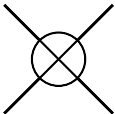
Now the physical parameters measured in the laboratory can be put in terms of the bare parameters and  $Z$ , along with the appropriate counterterms to absorb any divergences that arise. The physical quantities and counterterms are:

$$Z = 1 + \delta_Z, \quad m_0^2 Z = m^2 + \delta_m, \quad \lambda_0 Z^2 = \lambda + \delta_\lambda. \quad (2.23)$$

These are the parameters used in the Lagrangian:

$$L = \frac{1}{2}(\partial_\mu \phi_R)^2 - \frac{1}{2}m^2 \phi_R^2 - \frac{\lambda}{4!} \phi_R^4 + \frac{1}{2} \delta_Z (\partial_\mu \phi_R)^2 - \frac{1}{2} \delta_m \phi_R^2 - \frac{\delta_\lambda}{4!} \phi_R^4.$$

The first three terms are exactly the standard  $\phi^4$ -theory, now with the renormalized field and physical mass and coupling constant. The second set of three terms look very similar to the first three, but have the counterterms in place of the physical quantities. These must be included in the calculations to absorb the infinities. The resulting Feynman rules are:

Propagator		= $\frac{i}{p^2 - m^2 + i\epsilon}$ ,
Vertex		= $-i\lambda$ ,
Propagator Counterterm		= $i(p^2 \delta_Z - \delta_m)$ ,
Vertex Counterterm		= $-i\delta_\lambda$ .

For the counterterms to systematically absorb all infinities, a set of physical conditions are imposed that must be true at all orders in the perturbation theory:

$$\begin{aligned} \text{Full Propagator} &= \frac{i}{p^2 - m^2} + \text{terms with no poles} \Big|_{p^2=m^2}, \\ \text{Full Vertex} &= -i\lambda \Big|_{(p_1+p_2)^2=(p_3+p_4)^2=4m^2}. \end{aligned} \quad (2.24)$$

The full propagator condition actually specifies two conditions. The first is that the location

CHAPTER 2. THE STANDARD MODEL

of the pole in the propagator must correspond to the physical mass. The other part of this condition is that the residue must be 1, where a residue away from 1 would correspond to a change in  $Z$ . The full vertex specifies that the measured coupling at threshold scattering corresponds to the physical coupling constant. By consistently applying these conditions order-by-order in perturbation theory, the superficial divergences can be regulated.

Applying these rules and conditions to the two-particle to two-particle scattering amplitude will give the first-order renormalized corrections to the coupling constant. The sum of leading- and first-order diagrams are: The second diagram from the left (the first one-loop

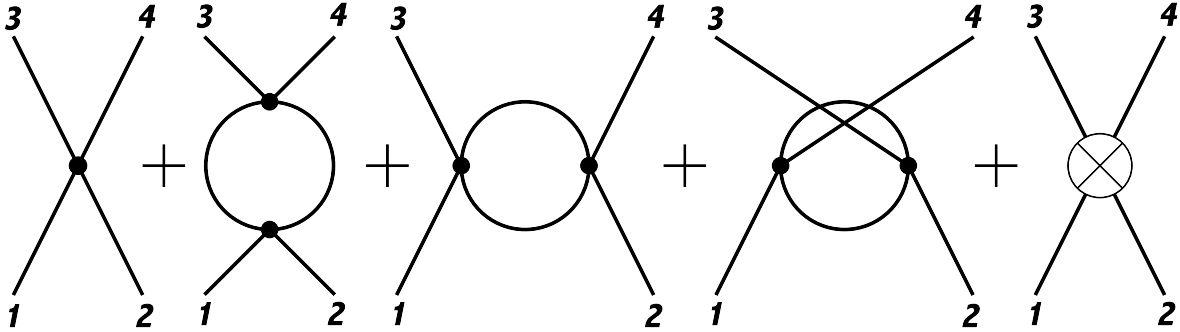


diagram) is:

$$\begin{aligned}
 \text{1-loop diagram} &= \frac{1}{2} \times (-i\lambda) \int \frac{d^4k}{(2\pi)^2} \frac{i}{(k+p_1+p_2)^2 - m^2 + i\epsilon} (-i\lambda) \frac{i}{k^2 - m^2 + i\epsilon} \\
 &= \frac{\lambda^2}{2} \int \frac{d^4k}{(2\pi)^2} \frac{1}{((k+p_1+p_2)^2 - m^2)(k^2 - m^2)} \\
 &= (-i\lambda^2)^2 \times iF(p_1+p_2).
 \end{aligned}$$

The other two diagrams have the same set of integrals, with  $p_2 \rightarrow -p_3$  and  $p_2 \rightarrow -p_4$ . This changes the dependence from  $s$  to  $t$  and  $u$ , in Mandelstam variables, respectively. The full

CHAPTER 2. THE STANDARD MODEL

1-loop amplitude is now:

$$i\mathcal{M} = -i\lambda + (-i\lambda^2)^2 [iF(p_1 + p_2) + iF(p_1 - p_3) + iF(p_1 - p_4)] - i\delta_\lambda. \quad (2.25)$$

From the renormalization conditions in equation (2.24), the constraint on  $\lambda$  at  $s = 4m^2$ ,  $t = u = 0$  requires:

$$\delta_\lambda = -\lambda^2 [F(2m) + 2F(0)].$$

The integral defining  $F(z)$  must be evaluated.

$$F(z) = \frac{i}{2} \int \frac{d^4k}{(2\pi)^2} \frac{1}{((k+z)^2 - m^2)(k^2 - m^2)}$$

Use Feynman parameters to combine denominators.

$$\begin{aligned} &= \frac{i}{2} \int \frac{d^4k}{(2\pi)^2} \int_0^1 dx \frac{1}{[x((k+z)^2 - m^2) + (1-x)(k^2 - m^2)]^2} \\ &= \frac{i}{2} \int_0^1 dx \int \frac{d^4k}{(2\pi)^2} \frac{1}{[k^2 + 2xk \cdot z + xz^2 - m^2]^2} \end{aligned}$$

Complete the square and shift  $\ell = k + xz$ .

$$= \frac{i}{2} \int_0^1 dx \int \frac{d^4\ell}{(2\pi)^2} \frac{1}{[\ell^2 + xz^2 - x^2z^2 - m^2]^2}$$

Wick rotate  $\ell^0$  into  $-i\ell^0$  to Euclidean space.

$$= -\frac{1}{2} \int_0^1 dx \int \frac{d^4\ell}{(2\pi)^2} \frac{1}{[\ell^2 + xz^2 - x^2z^2 - m^2]^2}$$

Shift into  $d$  dimensions.

$$= -\frac{1}{2} \int_0^1 dx \int \frac{d^d\ell}{(2\pi)^d} \frac{1}{[\ell^2 + xz^2 - x^2z^2 - m^2]^2}$$

Evaluate using the  $\Gamma$ -function.

$$= -\frac{1}{2} \int_0^1 dx \frac{\Gamma(2 - \frac{d}{2})}{(4\pi)^{d/2}} \frac{1}{[x^2z^2 - xz^2 + m^2]^{2-d/2}}$$

Let  $\epsilon = 4 - d$ .

$$F(z) = -\frac{1}{2} \int_0^1 dx \frac{1}{(4\pi)^2} \left[ \frac{2}{\epsilon} - \log(x^2z^2 - xz^2 + m^2) - \gamma + \log(4\pi) + \mathcal{O}(\epsilon^2) \right]$$

## CHAPTER 2. THE STANDARD MODEL

This expression diverges as  $\epsilon \rightarrow 0$ . With the condition setting  $\delta_\lambda$ , the counterterm for  $\lambda$  is:

$$\delta_\lambda = \frac{\lambda^2}{2(4\pi)^2} \int_0^1 dx \left[ \frac{6}{\epsilon} - \log((x^2 - x)(4m^2) + m^2) - 2 \log(m^2) - 3\gamma + 3 \log(4\pi) \right].$$

The full  $2 \rightarrow 2$  scattering amplitude at 1-loop is:

$$i\mathcal{M} = -i\lambda - \frac{i\lambda^2}{32\pi^2} \int_0^1 dx \left[ \log \left( \frac{x(x-1)s + m^2}{x(x-1)4m^2 + m^2} \right) + \log \left( \frac{x(x-1)t + m^2}{m^2} \right) + \log \left( \frac{x(x-1)u + m^2}{m^2} \right) \right].$$

This is finite for fixed values of  $m^2$ ,  $s$ ,  $t$ , and  $u$ , and can be numerically evaluated. A similar calculation for the 1-loop propagator with the requirement of a pole at  $p^2 = m^2$  and residue of 1, forces the other counterterms to be:

$$\begin{aligned} \delta_m &= -\frac{\lambda}{32\pi^2} \frac{\Gamma(1 - \frac{d}{2})}{(m^2)^{1-d/2}}, \\ \delta_Z &= 0. \end{aligned}$$

It is somewhat special that  $\delta_Z = 0$  at 1-loop for this theory. At higher orders there are non-zero corrections and most other theories will have non-zero corrections at first order.

### Running Couplings & Scales

The calculation above depended on what renormalization conditions were set on the parameters of the theory. The final result is independent of the choices made, as long as the calculations are done in the same way at every order in the perturbative expansion. A different way to understand the way the renormalized parameters are organized is to understand how they behave at any energy scale. It will turn out that the laboratory measured cou-



## CHAPTER 2. THE STANDARD MODEL

plings in the theory can change or “flow” as a function of the energy scale, called a “running coupling”.

The simplest example is the massless  $\phi^4$  theory, the same theory as above with  $m_0 = 0$ . A mass in the theory introduces an energy scale into the theory. Setting it to 0 and removing that scale helps understand the energy dependence without additional complications. The physical  $n$ -point correlation function uses the renormalized fields, with the renormalization conditions specified at the energy scale  $\mu$ .

$$G^{(n)} = \langle 0 | T \{ \phi_R(x_1) \cdots \phi_R(x_n) \} | 0 \rangle = Z^{-n/2} \langle 0 | T \{ \phi_0(x_1) \cdots \phi_0(x_n) \} | 0 \rangle$$

The renormalized  $G^{(n)}$  is calculated at energy scale  $\mu$ , but could have been calculated at a different scale  $\mu'$ . If a small shift in the scale  $\mu \rightarrow \mu + \delta\mu$  occurs, then the renormalized parameters will have to shift accordingly to absorb the change:

$$\begin{aligned} \mu &\rightarrow \mu + \delta\mu \\ \lambda &\rightarrow \lambda + \delta\lambda \\ \phi &\rightarrow (1 + \delta\phi)\phi \\ G^{(n)} &\rightarrow (1 + n \cdot \delta\phi)G^{(n)}. \end{aligned}$$

The function  $G^{(n)}$  can depend on the energy scale  $\mu$  and coupling  $\lambda$ , so by the chain rule the differential is:

$$\delta G^{(n)} = \frac{\partial G^{(n)}}{\partial \mu} \delta\mu + \frac{\partial G^{(n)}}{\partial \lambda} \delta\lambda = n \cdot \delta\phi G^{(n)}.$$

## CHAPTER 2. THE STANDARD MODEL

This is usually re-written in terms of two dimensionless functions:

$$\begin{aligned}\beta &\equiv \frac{\mu}{\delta\mu}\delta\lambda, \\ \gamma &\equiv -\frac{\mu}{\delta\mu}\delta\phi.\end{aligned}$$

Putting this into the differential for  $G^{(n)}$ , multiplying by  $\frac{\mu}{\delta\mu}$ , and re-arranging gives:

$$\left(\mu\frac{\partial}{\partial\mu} + \beta\frac{\partial}{\partial\lambda} + n\gamma\right)G^{(n)} = 0. \quad (2.26)$$

This is the Callen-Symanzik equation, from Curtis Callen [83] and Kurt Symanzik [84]. It shows that the two functions  $\beta$  and  $\gamma$  can account for any shift in the renormalization scale  $\mu$ .

For the  $\phi^4$  theory calculated earlier, the 4-point vertex correction was calculated to 1-loop in equation (2.25):

$$i\mathcal{M} = -i\lambda + (-i\lambda^2)^2 [iF(p_1 + p_2) + iF(p_1 - p_3) + iF(p_1 - p_4)] - i\delta\lambda.$$

This is not the 4-point correlation function because it does not include the incoming and outgoing fields, but is related to it by factoring in the external propagators for each particle:

$$G^{(4)} = [i\mathcal{M}] \prod_{1,2,3,4} \left(\frac{i}{p_i^2 + i\epsilon}\right).$$

The Callen-Symanzik equation in this case with  $n = 4$  is:

$$\left(\mu\frac{\partial}{\partial\mu} + \beta\frac{\partial}{\partial\lambda} + 4\gamma\right)G^{(4)} = 0.$$

It was asserted earlier that the 1-loop correction to the wavefunction  $\delta Z = 0$  and therefore

CHAPTER 2. THE STANDARD MODEL

the change in the field  $\delta\phi = 0$ . This means the  $\gamma$ -function vanishes at first order, leaving:

$$\left( \mu \frac{\partial}{\partial \mu} + \beta \frac{\partial}{\partial \lambda} \right) G^{(4)} = 0.$$

The renormalization condition used the first time was that the counterterms canceled at  $s = 4m^2, t = u = 0$ . There is no mass-scale in the theory now, so to make this as symmetric as possible the renormalization condition will require the infinities cancel at  $s = t = u = -\mu^2$ . The only term in  $G^{(4)}$  that depends on the renormalization scale is the counterterm  $\delta_\lambda$ :

$$\begin{aligned} \delta_\lambda &= (i\lambda)^2 3F(-\mu^2) \\ &= \frac{3\lambda^2}{2} \int_0^1 dx \frac{\Gamma(2 - \frac{d}{2})}{(4\pi)^{d/2}} \frac{1}{[x(1-x)\mu^2]^{2-d/2}} \\ &= \frac{3\lambda^2}{2(4\pi)^2} \int_0^1 dx \left[ \frac{2}{\epsilon} - \log(\mu^2) - \log(x(1-x)) - \gamma + \log(4\pi) \right]. \end{aligned}$$

The derivative of this with respect to  $\mu$  gives the first term in the Callen-Symanzik equation:

$$\mu \frac{\partial}{\partial \mu} G^{(4)} = -i \frac{3\lambda^2}{2(4\pi)^2} (-2) \prod_{1,2,3,4} \left( \frac{i}{p_i^2 + i\epsilon} \right).$$

The second term can be calculated taking the derivative of  $G^{(4)}$  with respect to  $\lambda$ . The  $\beta$  function is proportional to  $\delta_\lambda$ , which is order  $\lambda^2$ . Matching powers, the only term needed for the  $\beta$  function from the correlation function is the leading  $\lambda$  term:

$$\frac{\partial}{\partial \lambda} G^{(4)} = [-i + \mathcal{O}(\lambda)] \prod_{1,2,3,4} \left( \frac{i}{p_i^2 + i\epsilon} \right)$$

These two results can be inverted to solve for  $\beta$  at the first non-trivial term in  $\lambda$ :

$$\beta = \frac{3\lambda^2}{(4\pi)^2} + \mathcal{O}(\lambda^3). \tag{2.27}$$

CHAPTER 2. THE STANDARD MODEL

In general the first-order correction terms will only depend on the renormalization scale inside a logarithm that must, by dimensional analysis, include the energy scale of the physical process  $-Q^2$ :

$$\mathcal{M} \propto \log \left( \frac{-Q^2}{\mu^2} \right).$$

The Callen-Symanzik equation can be re-written in terms of the physical scale  $Q$  rather than the arbitrary renormalization scale  $\mu$ :

$$\left[ Q^2 \frac{\partial}{\partial Q^2} + D - \beta \frac{\partial}{\partial \lambda} - n\gamma \right] G^{(n)}(Q, \lambda) = 0.$$

$D$  is the number of external powers of  $Q^2$  in the  $n$ -point amplitude. For  $n = 2$  the two-point correlation function, this gives  $D = 1$ ; for  $n = 4$  the scattering amplitude calculated, this is  $D = 4$ , etc. If there is a solution of  $G$  at a fixed value of  $\lambda$  and  $Q^2$ , this is an evolution equation for that solution. Assuming there is a function  $\bar{\lambda}$  that can absorb the energy and coupling constant dependence, this is fixed at the renormalization scale:

$$\bar{\lambda}(-Q^2 = \mu^2, \lambda) = \lambda.$$

The overall energy dependence can be factored out on dimensional grounds:

$$G^{(n)} = \frac{1}{(Q^2)^D} \tilde{G}^{(n)}(\bar{\lambda}) \times \exp \left[ - \int_{-q'^2=\mu}^{-q'^2=-Q^2} d \log \left( \frac{-q'^2}{\mu^2} \right) (D - n\gamma(\bar{\lambda})) \right].$$

This can be inserted back into the Callen-Symanzik equation, and satisfies it if:

$$Q^2 \frac{\partial \bar{\lambda}}{\partial Q^2} = \beta \frac{\partial \bar{\lambda}}{\partial \lambda}.$$

## CHAPTER 2. THE STANDARD MODEL

At first order,  $\frac{\partial \bar{\lambda}}{\partial \lambda} = 1 + \mathcal{O}(\lambda)$  and  $\beta$  can move between  $\bar{\lambda}$  and  $\lambda$  without introducing additional terms. The left hand side can be put back into the log variables to reintroduce the renormalization scale:

$$\frac{d}{d \log \left( \frac{-Q^2}{\mu^2} \right)} \bar{\lambda}(Q, \lambda) = \beta(\bar{\lambda}). \quad (2.28)$$

This is the renormalization group equation, and the new “reduced coupling”  $\bar{\lambda}$  is said to be a running coupling constant. Using the  $\beta$ -function in equation (2.27) and the renormalization condition, the solution is:

$$\begin{aligned} \frac{3\bar{\lambda}^2}{16\pi^2} &= \frac{d\bar{\lambda}}{d \log \left( \frac{-Q^2}{\mu^2} \right)} \\ \Rightarrow \bar{\lambda}(Q, \lambda) &= \frac{\lambda}{1 - \left( \frac{3\lambda}{16\pi^2} \right) \log \left( \frac{-Q^2}{\mu^2} \right)}. \end{aligned}$$

This running coupling organizes the logarithms from the divergent integrals in a very useful way by showing how the coupling behaves as a function of energy. When  $Q \rightarrow 0$ , the reduced coupling vanishes and the perturbative expansion is a reasonable approximation. However, as  $Q \gg \mu$  the denominator will eventually become negative and return unphysical results. At this point the perturbative expansion breaks down and is no longer reasonable. This is due to the  $-$  sign in the denominator; if it were  $+$  then the reverse situation happens where the coupling vanishes at very high energy, called “asymptotic freedom”.

### 2.3 The Standard Model

The Standard Model (SM) is an interacting quantum field theory with gauge invariance including a set of fermions divided into two categories, quarks and leptons. Both categories

## CHAPTER 2. THE STANDARD MODEL

interact under the electroweak gauge theory, while the quarks also interact with an additional color gauge theory. The SM has successfully predicted the outcome of every laboratory test thus far, making it perhaps the most successful theory in the history of humanity. This section will describe some of the specifics of this remarkable theory.

### 2.3.1 A Model of Leptons - $SU(2) \otimes U(1)$

The SM begins by postulating a gauge symmetry that the matter particles must be invariant under. First proposed by Sheldon Glashow [50], the symmetry is  $SU(2) \otimes U(1)$  and is called the Electroweak force. The matter fields transform according to:

$$\chi \rightarrow e^{ig\alpha^a\tau^a} e^{ig'\beta Y} \chi.$$

The  $SU(2)$  transformation has coupling  $g$  and  $\tau^a$  are the generators of  $SU(2)$  algebra. The simplest generators are  $\tau^a = \frac{1}{2}\sigma^a$ , the Pauli spin matrices, and this is the fundamental representation of  $SU(2)$ . This is called “weak isospin”, in analogy to the  $SU(2)$  isospin in nucleons. The  $U(1)$  transformation has a coupling constant  $g'$ , and the  $Y$  is the generator for  $U(1)$  and must be proportional to the identity. This is called “hypercharge”, in analogy to the  $U(1)$  charge of QED. The transformation parameters are  $\alpha^a$  and  $\beta$ . The covariant derivative is:

$$D_\mu = (\partial_\mu - igA_\mu^a\tau^a - ig'B_\mu Y). \quad (2.29)$$

The fields  $A_\mu^a$  and  $B_\mu$  are the gauge fields for the  $SU(2)$  and  $U(1)$  symmetries, respectively. To match the observed phenomena, this should have a spontaneously broken symmetry that leaves a single massless boson (corresponding to QED) and a set of massive bosons (corresponding to the Weak force). This can be done using the Higgs mechanism, breaking

CHAPTER 2. THE STANDARD MODEL

the  $SU(2)_L \otimes U(1)_Y \rightarrow U(1)_{QED}$ . The simplest Higgs sector that transforms under this gauge symmetry is an  $SU(2)$  doublet of complex fields that can change phase under the  $U(1)$ :

$$\text{Higgs} = \phi = \begin{pmatrix} \phi_1 + i\phi_2 \\ \phi_3 + i\phi_4 \end{pmatrix}.$$

There are 4 degrees of freedom in this Higgs sector. The Higgs mechanism requires that this field acquire a VEV due to a non-zero minimum in the potential. One gauge choice that would break three of the symmetries is:

$$\langle \phi \rangle = \frac{1}{\sqrt{2}} \begin{pmatrix} 0 \\ v \end{pmatrix}, \quad v \in \mathbb{R}.$$

This will leave a single massless gauge boson, three massive gauge bosons, and a single massive scalar boson. The masses of the gauge bosons arise in the  $|D_\mu \phi|^2$  term in the Lagrangian, after inserting the VEV for the scalar field. The  $SU(2)$  generators are in the fundamental representation with the Pauli matrices, while the  $U(1)$  generator is proportional to the identity in this representation. To match the normalization of the generators between the  $SU(2)$  and  $U(1)$  transformations, the generator  $Y \propto \frac{1}{2}\mathbb{I}$  under the  $SU(2)$  transformation to preserve  $v \in \mathbb{R}$ . The mass terms for the gauge fields are manifest after symmetry breaking:

$$\begin{aligned} \text{mass terms} &= \frac{1}{2} \begin{pmatrix} 0 & v \end{pmatrix} \left( gA_\mu^{a\dagger} \tau^{a\dagger} + g'B_\mu \frac{1}{2}\mathbb{I} \right) \left( gA_\mu^a \tau^a + g'B_\mu \frac{1}{2}\mathbb{I} \right) \begin{pmatrix} 0 \\ v \end{pmatrix} \\ &= \frac{v^2}{8} [g^2 ((A_\mu^1)^2 + (A_\mu^2)^2) + (gA_\mu^3 - g'B_\mu)^2]. \end{aligned}$$

## CHAPTER 2. THE STANDARD MODEL

The first pair of  $A_\mu^a$  combine together exactly as the raising and lowering operators in the  $SU(2)$  algebra. These are the charged  $W^\pm$  bosons of the Weak force:

$$W_\mu^\pm = \frac{1}{\sqrt{2}}(A_\mu^1 \mp iA_\mu^2), \quad m_W = \frac{1}{2}gv.$$

The second term mixes the  $A_\mu^3$  and  $B_\mu$  gauge fields into another massive gauge boson. This is the neutral  $Z^0$  boson of the Weak force:

$$Z_\mu^0 = \frac{1}{\sqrt{g^2 + g'^2}}(gA_\mu^3 - g'B_\mu), \quad m_Z = \frac{1}{2}\sqrt{g^2 + g'^2}v.$$

The normalization with  $\sqrt{g^2 + g'^2}$  is convenient to describe the mixing between the gauge fields. The remaining massless boson is the  $\gamma$  photon of the Electromagnetic force:

$$A_\mu = \frac{1}{\sqrt{g^2 + g'^2}}(g'A_\mu^3 + gB_\mu), \quad m_A = 0.$$

The mixing between the two fields can be expressed in terms of a  $2 \times 2$  mixing matrix:

$$\begin{pmatrix} Z^0 \\ \gamma \end{pmatrix} = \begin{pmatrix} \frac{g}{\sqrt{g^2 + g'^2}} & \frac{g'}{\sqrt{g^2 + g'^2}} \\ -\frac{g'}{\sqrt{g^2 + g'^2}} & \frac{g}{\sqrt{g^2 + g'^2}} \end{pmatrix} \begin{pmatrix} A^3 \\ B \end{pmatrix}.$$

Treating this as rotation matrix, this defines the weak mixing angle or Weinberg angle:

$$\cos \theta_W = \frac{g}{\sqrt{g^2 + g'^2}}, \quad \sin \theta_W = \frac{g'}{\sqrt{g^2 + g'^2}}, \quad \tan \theta_W = \frac{g'}{g}.$$

The coupling of the fermions to the physical gauge fields is determined by the strength of the gauge transformations and the mixing between the them. The  $SU(2)$  weak isospin couplings is determined entirely by the representation of the fermion and  $g$ . The  $U(1)$  hypercharge, however, can be any real number  $Y$  and leave the overall gauge transformation unchanged.



## CHAPTER 2. THE STANDARD MODEL

Returning to the covariant derivative in (2.29) and using the physical fields of the theory after spontaneous symmetry breaking:

$$D_\mu = \left( \partial_\mu - i \frac{g}{\sqrt{2}} (W_\mu^+ T^+ + W_\mu^- T^-) - i \frac{1}{\sqrt{g^2 + g'^2}} Z_\mu^0 (g^2 T^3 - g'^2 Y) - i \frac{gg'}{\sqrt{g^2 + g'^2}} A_\mu (T^3 + Y) \right).$$

To match the field  $A_\mu$  with the photon after symmetry breaking, the coupling constants and generators must combine to form the electric charge for every particle:

$$\begin{aligned} Q|e| &= \frac{gg'}{\sqrt{g^2 + g'^2}} (T^3 + Y) \\ \Rightarrow |e| &= \frac{gg'}{\sqrt{g^2 + g'^2}}, \\ &\& Q = T^3 + Y. \end{aligned}$$

The value of  $T^3$  is determined by the representation of the fermion under  $SU(2)$ , and is a postulate of the theory. Knowing the charge of the particle then determines the  $U(1)$  coupling  $Y$ .

The relations between the couplings  $g$  and  $g'$ , the charges, and the mixing angle, allows for a simplified covariant derivative in terms of the physical fields and couplings:

$$D_\mu = \left( \partial_\mu - i \frac{e}{\sqrt{2} \sin \theta_W} (W_\mu^+ T^+ + W_\mu^- T^-) - i \frac{e}{\sin \theta_W \cos \theta_W} Z_\mu^0 (T^3 - Q \sin^2 \theta_W) - ieQ A_\mu \right).$$

Massive fermions have both left- and right-handed spinor components, however it is an empirical fact of nature that the charged weak bosons  $W^\pm$  only couple to the left-handed components of fermions. This is not, *a priori* a problem, as the  $L$  and  $R$  components can

## CHAPTER 2. THE STANDARD MODEL

be assigned to different gauge representations. In particular, the left-handed component can be assigned the fundamental representation (doublet) under  $SU(2)$ , while the right-handed component is a singlet and does not transform. The problem comes from the mass terms in the Lagrangian, which when broken into left- and right-handed components are:

$$L_{m_{\text{fermion}}} = -m\bar{\psi}_L\psi_R - m\bar{\psi}_R\psi_L.$$

These terms do not preserve gauge invariance and must be dropped from the theory, which would leave only massless fermions and not describe our world. The way to generate mass for fermions is to again use the Higgs sector. In particular, the terms of the form:

$$-\lambda_\psi\bar{\psi}_R\phi^\dagger\psi_L + \text{conjugate},$$

preserves gauge invariance. After symmetry breaking, the Higgs field acquires a VEV, and these terms become:

$$-\frac{1}{\sqrt{2}}\lambda_\psi v\bar{\psi}_R\psi_L + -\frac{1}{\sqrt{2}}\lambda_\psi v\bar{\psi}_L\psi_R + \text{interactions}.$$

The mass of the fermions are now:

$$m_\psi = \frac{1}{\sqrt{2}}\lambda_\psi v.$$

The single VEV of the scalar field is now responsible for the masses of both the gauge bosons and the fermions. This introduces a new set of Yukawa parameters that controls the masses of the fermions, one for each flavor of quark and lepton.

## CHAPTER 2. THE STANDARD MODEL

The full fermionic matter content is now:

$$E_L = \begin{pmatrix} \nu_e \\ e^- \end{pmatrix}_L, \quad e_R, \quad \nu_{e,R}, \quad Q_L = \begin{pmatrix} u \\ d \end{pmatrix}_L, \quad u_R, \quad d_R.$$

The representation shows that the left-handed lepton doublet has quantum numbers  $T^3 = \pm\frac{1}{2}$  and  $Y = -\frac{1}{2}$ , giving the correct charges to  $e$  and  $\nu_e$ . The left-handed quark doublet has the same  $T^3 = \pm\frac{1}{2}$ , with  $Y = +\frac{1}{6}$  to give the correct charges to the quarks. The right-handed  $SU(2)$  singlets for both quarks and leptons have  $Y = Q$ . The right-handed neutrino is a curious particle needed to generate a mass term for the neutrinos, but has no couplings with the SM particles! These are referred to as “sterile neutrinos” and have been hypothesized to help explain puzzles within the SM such as dark matter and the mass difference between the neutrinos and charged leptons.

### 2.3.2 Quantum Chromodynamics - $SU(3)$

The other gauge symmetry of the SM is a non-Abelian gauge theory called Quantum Chromodynamics or the Strong force. This is an  $SU(3)$  Lie algebra, where all the quarks are postulated to be in the fundamental representation and the leptons do not transform under this gauge group. As a result of this interaction, the quarks will bind together and form the hadronic sector of matter composed of mesons and baryons. The transformation and covariant derivative are:

$$Q \rightarrow e^{ig_S \alpha^a \lambda^a} Q,$$
$$D_\mu = (\partial_\mu - ig_S A_\mu^a \lambda^a).$$

## CHAPTER 2. THE STANDARD MODEL

The Lie algebra  $SU(3)$  is generated by the 8 Gell-Mann matrices  $\lambda^a$ , in exact analogy to the Pauli matrices for  $SU(2)$ . This is not a broken symmetry, therefore the associated 8 gauge bosons remain massless. These are called “gluons”, and are the carriers of the Strong force. The quarks are in the fundamental representation of  $SU(3)$ , which is dimension 3 so there must be 3 different “colors” of each type of quark. The quarks bind together to form  $SU(3)$  invariants. In the fundamental representation, there are only two possible invariant products available:

$$\delta_i^j \bar{Q}^i Q_j \ \& \ \epsilon^{ijk} Q_i Q_j Q_k.$$

The first product forms the mesons from a quark and anti-quark of the same color and anti-color. The second anti-symmetric product forms the baryons out of three quarks (or anti-quarks), one of each color. The existence of a new “color” quantum number resolved some outstanding problems in the observed baryon spectrum where particles were observed to have three of the same flavor of quark and in the same spin states. These should be forbidden by the Pauli Exclusion Principle, but an additional quantum numbers allows the fermions to be in different color states and the same flavor and spin states, evading the theorem.

### Asymptotic Freedom & Confinement

The quarks are bound into  $SU(3)$  invariants because of a special property of the gauge theory. The  $\beta$ -function for this theory is:

$$\beta = - \left( \frac{11}{3} C_2(SU(3)) - \frac{4}{3} N_f C(R_{SU(3)}) \right) \frac{g_S^3}{(4\pi)^2}.$$

## CHAPTER 2. THE STANDARD MODEL

The two constants  $C_2(SU(3))$  and  $C(R_{SU(3)})$  are group theory constants, and only depend on how the gauge fields and interacting fermions transform under the group action. The gauge fields transform in the adjoint  $D^\dagger A_\mu D$  since they are operators in the Hilbert space. The invariant  $C_2$  for the adjoint representation is the dimension of the group,  $C_2(SU(3)) = N_C = 3$ . The fermions are postulated to transform in the fundamental representation,  $\text{Tr}[\lambda^a \lambda^b] = C(R_{SU(3)})\delta^{ab} = \frac{1}{2}\delta^{ab}$ . With these values, the  $\beta$ -function is:

$$\beta = - \left( 11 - \frac{2}{3}N_f \right) \frac{g_S^3}{(4\pi)^2} = -b_0 \frac{g_S^3}{(4\pi)^2}.$$

If  $N_f < 17$ , the  $\beta$ -function is negative unlike the  $\phi^4$  example case result in equation (2.27). When this is put into the running coupling constant evolution equation in equation (2.28), the solution is:

$$\alpha_S(Q^2) = \frac{\alpha_S(\mu^2)}{1 + \alpha_S(\mu^2) \cdot \frac{b_0}{\pi} \log \left( \frac{Q^2}{\mu^2} \right)}.$$

Now as  $Q^2 \rightarrow \infty$  the running coupling constant  $\alpha_S \rightarrow 0$ . This is an example of asymptotic freedom, where at higher energies the quarks behave more and more like a free theory without interactions. At low energies, the coupling constant diverges and the theory becomes strongly interacting. The energy scale where this occurs is labeled  $\Lambda_{QCD}$ :

$$1 \simeq \alpha_S(\mu^2) \cdot \frac{b_0}{\pi} \log \left( \frac{\mu^2}{\Lambda_{QCD}^2} \right).$$

For QCD, this energy scale is  $\Lambda_{QCD} \sim 200$  MeV. Near and below this energy scale, the perturbative treatment breaks down. The color force between quarks inside hadrons is at this scale and leads to a phenomena known as “confinement”. The Strong force keeps the

## CHAPTER 2. THE STANDARD MODEL

quarks “confined” at this scale.

Another consequence of confinement is that there are no “free” quarks. If during a particle scattering process a quark or gluon is emitted, it will “dress” itself or “hadronize” into a color-singlet by pulling in gluons or quark-anti-quark pairs from the vacuum. In high-energy collisions, these particles are observed as “jets”.

### Form Factors & PDFs

A consequence of confinement and the breakdown in perturbation techniques for QCD is that making predictions about how hadrons behave is quite difficult if not impossible. One non-perturbative technique is to put the Lagrangian on a discrete lattice and directly evolve the dynamics using the equations of motion. This is called lattice gauge theory, and is very computationally intensive. Another technique is to parameterize the behavior of the hadrons based on general symmetries of the theory. For example, the proton can interact with a photon following the usual Feynman rules of a massless gauge boson interacting with a fermion. However, the underlying dynamics of how the proton interacts depends on the charged quarks at the confinement scale. Requiring Lorentz invariance, the coupling of the proton must behave as:

$$\begin{array}{c} \text{wavy line} \\ \bullet \\ \begin{array}{l} \nearrow \text{double line} \\ \searrow \text{double line} \end{array} \end{array} = \bar{\psi}_P(p') \left[ \gamma^\mu F_1(Q^2) + \frac{(p-p')_\nu}{4m_P} [\gamma^\mu, \gamma^\nu] F_2(Q^2) \right] \psi_P(p).$$

The two “form factors”  $F_{1,2}(Q^2)$  contain all of the dynamics inside the proton, and by Lorentz invariance can only depend on the momentum transferred  $Q^2$ . The complicated QCD internal dynamics have been reduced to measuring how the proton interacts with a photon as a function of  $Q^2$ .

## CHAPTER 2. THE STANDARD MODEL

A similar problem occurs when trying to determine which quark or gluon will interact. If each quark and gluon inside a hadron carries a fraction  $x_i$  of the total momentum of the hadron, then a set of function  $f_i(x)$  can parameterize the evolution of the various partons depending on their momentum inside the hadron, called “parton distribution functions” (PDFs):

$$\{f_u(x), f_d(x), f_s(x), f_c(x), f_b(x), f_t(x), f_g(x)\}.$$

Baryons are formed from three quarks called “valence” quarks that carry the total quantum numbers. But at energy scales near  $\Lambda_{QCD}$ , many gluons and quark-anti-quark pairs can form from the vacuum called the “sea”. For example, the proton has in total two  $u$  quarks and one  $d$  quark based on the quantum numbers of the proton summed from the valence quarks. The total momentum carried by all the partons must also sum to 1 to conserve momentum. These provide constraints on the PDFs:

$$\begin{aligned} \int_0^1 dx [f_u(x) - f_{\bar{u}}(x)] &= 2, \\ \int_0^1 dx [f_d(x) - f_{\bar{d}}(x)] &= 1, \\ \int_0^1 dx [f_q(x) - f_{\bar{q}}(x)]_{q \neq u, d} &= 0, \\ \int_0^1 dx \sum_i x f_i(x) &= 1. \end{aligned}$$

The PDFs also depend on the energy of the particle that is probing the proton, just as the form factors depended on the  $Q^2$ . PDFs can be measured in various deep-inelastic scattering processes, such as studying  $e^- + p \rightarrow e^- + X$ . By measuring the energy of the electron before and after scattering the total momentum transferred  $Q^2$  is known, and by

CHAPTER 2. THE STANDARD MODEL

measuring the outgoing products  $X$  the parton scattered can be inferred.

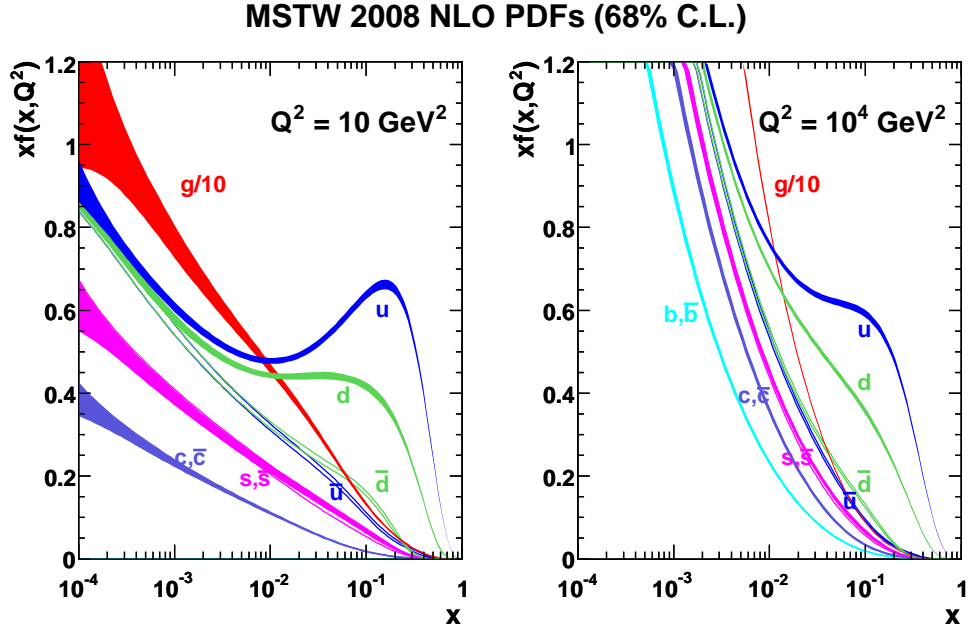


Figure 2.1: An example PDF, the MSTW2008NLO from [85], and the bands are the the 68% C.L. error bars. The left plot is at an energy scale of 3.16 GeV, while the right plot is at an energy scale of 100 GeV or approximately the  $Z^0$  boson mass. The right plot shows the  $u$  quark contribution enhanced at higher  $Q^2$  in the ranges below  $x = 0.1-0.2$ .

PDFs are constructed out of a set of “eigenvectors” of the various functions describing the physical content of the proton. For example, instead of simply using  $f_u(x)$  and  $f_{\bar{d}}(x)$ , the combination  $f_u(x) + f_{\bar{d}}(x)$  can be used to incorporate of these into a separate eigenfunction. These sets of eigenfunctions are designed to be easier to measure and more robust for other applications. Once the PDFs are well-measured, cross sections can be calculated using the underlying quarks in the amplitudes then integrated over  $x$  to find the total cross section.



## CHAPTER 2. THE STANDARD MODEL

For a final state containing particle (or particles)  $S$  and anything else denoted  $X$ :

$$\sigma(p(P_1)p(P_2) \rightarrow S + X) = \int_0^1 dx_1 \int_0^1 dx_2 \sum_{i,j} f_i(x_1) f_j(x_2) \sigma(i(x_1 P_1) + j(x_2 P_2) \rightarrow S),$$

where  $i$  and  $j$  are the partons in the proton involved in the hard scattering process. The cross section on the right involves single particles and can be computed perturbatively, and then integrated using the PDFs such as those in figure 2.1 to get the final result for proton-proton collisions.

### 2.3.3 Features of the Standard Model

There are a wide variety of phenomena described by the SM, and this section has only touched on some of the important features involved in the proton collisions at the Large Hadron Collider. I would just like to mention a few of these fascinating aspects of this remarkable theory. The SM is an anomaly-free theory, due to cancellations between the quark and leptons generation-by-generation. An anomaly is when a symmetry of the theory is not consistent with regularization, and would indicate something fundamentally wrong with the theory. The mass terms generated by the Higgs mechanism for the fermions allows for additional unitary rotations between flavors of quarks. This means that the mass eigenstates and electroweak eigenstates are not the same, leading to mixing between states. This also introduces  $CP$  violation into the SM, which had been an accidental symmetry of the theory. The mixing is captured in the Cabbibo-Kobayashi-Maskawa (CKM) matrix. A similar situation arises in the lepton sector, where the neutrinos mix under the Pontecorvo-Maki-Nakagawa-Sakata (PMNS) matrix. This assumes the leptons acquire a mass in the same manner as the quarks, while for neutrinos it is possible for them to acquire a Majorana mass

## CHAPTER 2. THE STANDARD MODEL

term. In total, there are 25 parameters of the SM, comprising of the coupling constants (3), the masses of the leptons and quarks (12), the fermion mixing angles (8), and the Higgs VEV and mass (2). Measuring these 25 parameters allows, in principle, calculation of all particle interactions measured in nature.

### 2.4 New Physics Beyond the Standard Model

The success of the SM leaves several puzzles remaining. To list a few of these problems:

- Why these 25 parameters and why do they have the values observed?
- Why are the quarks and leptons arranged in generations?
- Why is the charge quantized into  $\{0, \pm\frac{1}{3}, \pm\frac{2}{3}, \pm 1\}$  of  $e$  since the hypercharge could take on any value?
- The SM also allows for a term proportional to  $\theta\epsilon^{\mu\nu\rho\sigma}F_{\mu\nu}F_{\rho\sigma}$  in the  $SU(3)_C$  gauge sector (this can be removed in the  $SU(2)_L$  sector by a chiral rotation and is a total derivative in the  $U(1)_Y$  sector), which violates  $CP$ . This would lead to large  $CP$  violation in the strong sector, but measurements indicate  $\theta \leq 10^{-10}$  [86]. Why is this term not present?
- The Higgs boson, first measured at the LHC [1, 2], appears to have a mass of  $m_h \sim 126$  GeV. However, as a scalar, the quantum corrections to  $\delta_{m_h} \sim \Lambda^2$ , are quadratic in the cutoff. This can be renormalized, but is unlike the cases studied earlier where all the corrections behaved as  $\log(\Lambda^2)$ . This cutoff is expected at the Planck scale,  $\Lambda \sim 10^{19}$  GeV. The quantum corrections must cancel this almost exactly and leave a physical

## CHAPTER 2. THE STANDARD MODEL

mass at the scale of the VEV. The large difference between the Higgs VEV and Planck scale indicates a “Hierarchy problem” in the physical corrections for the Higgs boson.

- Gravity is neglected in the SM, and a truly complete theory should incorporate all known forces.
- The universe appears to be made of matter and not equal parts matter/anti-matter. While the SM does have some CP violation which allows for some matter/anti-matter asymmetry, this effect is not large enough to produce the observed asymmetry. What is the source of the matter/anti-matter asymmetry in the universe?
- Observational astronomy shows that galaxies have much more matter than what is visible in stars, called “dark matter” [87]. Cosmological observations also indicate that the matter composition of the universe requires much more matter than is observed in the visible objects [88]. The favored solution is to introduce a new, stable particle called a “WIMP” (Weakly Interacting Massive Particle). This particle is estimated to have a mass  $\sim 500$  GeV and an interaction strength about the same order as the Weak force, although these are weak bounds. There is no candidate particle in the SM.
- Observing supernovae has shown that the universe’s expansion is accelerating [89, 90]. Cosmological observations also show that the energy budget of the universe must have a “dark energy” component [88]. This can be accounted for in General Relativity by introducing a cosmological constant term, but there is no mechanism in the SM to produce this effect.

There are a variety of possible extensions of the SM that aim to remedy one or more of these problems while maintaining the structure of the theory at the scales that have been measured. This section will discuss some possibilities for physics beyond the SM, generically

called new physics (NP). A nice textbook covering many of these extensions is Michael Dine's *Supersymmetry and String Theory* [91].

### 2.4.1 Gauge Unification

The success of gauge theory to describe particle physics, and in particular the Higgs mechanism for spontaneously breaking symmetry in the Electroweak sector, leads to a natural question if this can be extended. The first such proposal was by Howard Georgi & Sheldon Glashow [92]. The idea is to find a gauge group that contains  $SU(3) \otimes SU(2) \otimes U(1)$ , then use a set of scalar fields with VEVs to spontaneously break the larger gauge symmetry to the SM. This will naturally group the fermions into generations, and, because the  $U(1)$  hypercharge comes from a larger gauge symmetry, explains charge quantization.

#### $SU(5)$ Unification

The smallest gauge group to postulate is  $SU(5)$ , which allows for a very neat representation of all the SM particles. Postulating the fermions to be in the fundamental representation, the generators of  $SU(5)$  in this representation are a set of 24  $5 \times 5$  Hermetian, traceless matrices. After symmetry breaking, these should decompose into:

$$\begin{aligned} T_C^a &= \begin{pmatrix} \lambda^a & 0 \\ 0 & 0 \end{pmatrix}, \\ T_L^i &= \begin{pmatrix} 0 & 0 \\ 0 & \tau^i \end{pmatrix}, \\ T_{\hat{Y}} &= \sqrt{\frac{3}{5}} \begin{pmatrix} -\frac{1}{3}\mathbb{I}_C & 0 \\ 0 & \frac{1}{2}\mathbb{I}_L \end{pmatrix}. \end{aligned}$$

## CHAPTER 2. THE STANDARD MODEL

This preserves the fundamental representation for the  $SU(3)$  and  $SU(2)$  fermions, and because of the traceless generator for  $T_{\tilde{Y}}$  automatically incorporates charge quantization. There are two possible fundamental representations  $\mathbf{5}$  and  $\bar{\mathbf{5}}$ , and the easier choice is the  $\bar{\mathbf{5}}$  representation. The matter content for this representation is:

$$\bar{\mathbf{5}} = \begin{pmatrix} \bar{d}_r \\ \bar{d}_g \\ \bar{d}_b \\ \nu_{e,L} \\ e_L \end{pmatrix}.$$

There are 11 remaining particles that need to be included in the  $SU(5)$ . Another possibility is the 10 representation, the anti-symmetric combination of two  $\mathbf{5}$  representations:

$$10 = \begin{pmatrix} 0 & \bar{u}_b & -\bar{u}_g & U_{L,r} & D_{L,r} \\ -\bar{u}_b & 0 & \bar{u}_r & U_{L,g} & D_{L,g} \\ \bar{u}_g & -\bar{u}_r & 0 & U_{L,b} & D_{L,b} \\ -U_{L,r} & -U_{L,g} & -U_{L,b} & 0 & \bar{e} \\ -D_{L,r} & -D_{L,g} & -D_{L,b} & -\bar{e} & 0 \end{pmatrix}.$$

Lastly there is a singlet for the right-handed neutrinos,  $\nu_{e,R}$ . The full SM particle content is contained in the representations:

$$\text{SM} = \bar{\mathbf{5}} \oplus 10 \oplus 1.$$

The first prediction of this theory is the gauge coupling for  $SU(3)$  and  $SU(2)$  are the same because their couplings come from the same larger gauge group. Next, the relation between the  $U(1)$  and  $SU(2)$  couplings can be studied. The hypercharge  $Y_\ell$  of the lower leptons in the  $\bar{\mathbf{5}}$  that transform under the remaining  $SU(2)$  is related to  $\tilde{Y}$  by  $\tilde{Y} = \sqrt{\frac{3}{5}} \cdot \frac{1}{2} Y$ .

## CHAPTER 2. THE STANDARD MODEL

Defining the coupling  $g'$  for the  $U(1)$ , these are related by:

$$g\tilde{Y} = g'\frac{Y}{2},$$

where the  $\frac{1}{2}$  is the conventional normalization of the generators. The weak mixing angle is:

$$\sin \theta_W = \frac{g'^2}{g^2 + g'^2} = \frac{\left(\frac{2\tilde{Y}}{Y}\right)^2}{1 + \left(\frac{2\tilde{Y}}{Y}\right)^2} = \frac{3}{8}.$$

The Higgs mechanism breaks the 24 symmetry generators of  $SU(5)$  to the  $8 + 3 + 1 = 12$  generators of the SM. This leaves 12 new massive gauge bosons that will generically couple quarks and leptons in the same interaction. These new massive bosons will mediate proton decay, among the many new interactions.

Unfortunately, all of these predictions do not match the observed world. The gauge couplings for  $SU(2)$  and  $SU(3)$  can potentially be the same at a very high energy (the “Unification scale”), then the running couplings allows the two to flow down to their observed values. However, using the observed values of the couplings in the SM at the energy scales measured so far, the 3 couplings for the Strong, Weak, and Electromagnetic forces do not all meet at the same point. The weak mixing angle can also receive large quantum corrections due to the new particle content in the theory and then flow down to lower energies to the observed value of  $\sim 0.23$ , but typically requires new matter fields not observed. The bounds on proton decay also require the mass of the new gauge bosons to be extremely heavy, of order  $M_5 > 10^{12}$  GeV.

## CHAPTER 2. THE STANDARD MODEL

### $E_6$ Unification

Another popular unification gauge group is the “exceptional” Lie algebra  $E_6$ . This gauge group has a 27-dimensional fundamental representation and two maximal sub-algebras,  $SU(6) \times SU(2)$  and  $SU(3) \times SU(3) \times SU(3)$ . One possible example of  $E_6$  unification uses the  $SU(5)$  example from the previous subsection. While  $SU(5)$  is not a maximal sub-algebra it is a regular sub-algebra of  $E_6$ , and under this sub-algebra the fundamental representation transforms as:

$$27 \sim \bar{5} \oplus 10 \oplus 1 \oplus \bar{5} \oplus 5 \oplus 1.$$

The first three representations are precisely the set needed for the SM and can be treated in the same manner as above. The Higgs mechanism for breaking from  $E_6$  can work at a much higher scale and, suitably coupled to the matter content, can give large masses to the matter particles in the  $\bar{5} \oplus 5 \oplus 1$  representations. The higher-scale breaking can leave two  $U(1)$ s from the algebra unbroken:

$$E_6 \rightarrow SU(5) \otimes U(1) \otimes U(1).$$

The particles associated with the  $U(1)$ s are new, heavy gauge bosons which can gain mass through the addition of more Higgs fields and potentially couple to the matter fields of the SM.

$E_6$  is an appealing unification possibility because of the variety of ways of breaking the gauge symmetry down to the SM. Besides the fundamental representation, there is a 78-dimensional adjoint representation that can contain the SM particles and allows for even more combinations of Higgs fields and symmetry breaking. The additional matter content

of the theory also introduces more corrections to the simple  $SU(5)$  breaking done earlier, evading many of the constraints observed in experiment. The  $E_6$  gauge group is also part of one of the maximal sub-algebras of  $E_8$ , which is one of the two possible anomaly-free gauge groups in string theory (see below), and is a way to incorporate the SM into string theory.

## 2.4.2 Supersymmetry

Supersymmetry is the idea that for each particle there are a set of partner particles related by a new class of symmetry generators. All of the symmetries studied so far, such as gauge symmetry, involve bosonic commutation relations:

$$[T^a, T^b] = if^{abc}T^c.$$

Interestingly, Sidney Coleman & Jeffery Mandula [93] proved a no-go theorem stating that the only possible continuous transformations are the product of Lorentz transformations and internal symmetries such as gauge transformations, or else the theory is trivial. Supersymmetry postulates a new “superalgebra” with generators obeying fermionic commutation relations. This mixes the spin indices (derived from Lorentz invariance) and the internal gauge indices (derived from gauge invariance), and evades this no-go theorem due to the anti-commuting structure of the superalgebra:

$$\{Q_a, Q_b\} = 2\sigma_{ab}^\mu P_\mu,$$

where  $P_\mu$  is momentum 4-vector. The inclusion of supersymmetry with the internal gauge and Poincaré symmetries was proved with the HaagLopuszanskiSohnius theorem [94]. These generators can act on fermions and return a bosonic particle with otherwise the same set of interactions. This leads to a very rich phenomenology, including at least one “superpartner”



to every particle in the SM. Because of the explicit connection with Lorentz invariance, the larger symmetries of General Relativity can be incorporated instead of Special Relativity, leading to “Supergravity”. As with gauge unification, experimental searches have not found any superpartners.

### 2.4.3 String Theory

Another avenue of research incorporates both of these concepts on a much larger scale. The basic idea is that particles are not point-particles but rather 1-dimensional strings. A rather interesting feature of this postulate is that these theories automatically contain a massless spin-2 particle, which can be identified as the graviton. Thus string theory is a natural candidate for a complete theory of quantum gravity. Another consequence of string theory is that self-consistency of the algebra requires 26 or 10 space-time dimensions, while anomaly cancellation allows only two gauge groups:  $SO(32)$  and  $E_8 \times E_8$  [95]. The study of string theory led to the discovery of a correspondence between a special class of conformal quantum field theories and a different class of Supergravity theories [96, 97], a powerful new computational technique for quantum field theories. The natural energy scale for quantum theory of gravity is at the Planck scale  $\sim 10^{19}$  GeV, which is well beyond any current testable energy regime. Because string theory naturally lives at such a high scale, the number of possible low-energy solutions has been estimated beyond  $10^{500}$  vacua [98]. Another possibility from string theory is that extra dimensions needed for the consistency of the theory need not be “compact” but at a scale that can help resolve the hierarchy problem. Nima Arkani-Hamed, Savas Dimopoulos, and Gia Dvali proposed using branes in string theory to localize the gauge-theory physics but let gravity propagate in the six other “small” dimensions, changing the Planck scale as the cut-off for the theory [99, 100]. Lisa

Randall and Raman Sundrum proposed using branes separated along one extra dimension to generate the differences in the Planck and Electro-Weak scale to resolve the hierarchy problem, and embed this into a larger string theory [101, 102]. String theory incorporates many different possible extensions to the SM, including gauge unification, supersymmetry, and extra dimensions, but there have been no direct observational evidence for physics beyond the Standard Model.

## 2.5 New Particle Phenomenology

Each of these extensions adds to the possibilities for new physics beyond the Standard Model, typically in the form of new particles. These can come in many varieties, and how they couple to the known SM particles will depend on the details of the theory. To be detected at the LHC, the new particles will have to couple to either quarks or gluons in the proton to be produced in the collisions, then decay either directly or through a chain of decays into observable particles in the detectors. This thesis is a search for new particles in the dilepton channel, either electrons or muons. The dominant backgrounds in this search are the SM processes that have an oppositely-charged lepton pair in the final state. The largest such process is the direct production of two leptons through quark-anti-quark annihilation, the Drell-Yan process [103, 104]. This process has the same initial and final states as the new particle(s) in this search, and is therefore an irreducible background. This section will show the expected background from this process and discuss the other SM backgrounds, as well as how generic new, neutral, heavy gauge bosons would appear in this search.

The Drell-Yan process is a quark and an anti-quark of the same flavor and color annihilating through either a photon or  $Z^0$  boson, which then decays into a lepton pair of either electrons or muons. This calculation will work in the massless limit for both the quarks and

CHAPTER 2. THE STANDARD MODEL

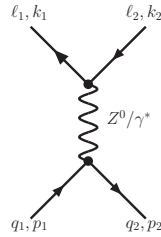
leptons. Corrections due to the finite mass of these particles will be on the order of  $\sim \frac{m^2}{\hat{s}}$ , which is  $\sim 10^{-6}$  for muons (the heaviest incoming/outgoing particle) near the  $Z$ -peak (lowest end of the search region). The incoming quark momenta are in terms of the incoming proton momenta and the fraction of the total energy they carry:

$$\begin{aligned} p_1 &= x_1 P_1 = (x_1 E, 0, 0, x_1 E), \\ p_2 &= x_1 P_2 = (x_1 E, 0, 0, -x_1 E). \end{aligned}$$

The outgoing lepton momenta are  $k_1$  and  $k_2$ . The Mandelstam variables will be of use later:

$$\begin{aligned} \hat{s} &= (k_1 + k_2)^2 = (p_1 + p_2)^2 = q^2 = x_1 x_2 s, \\ \hat{t} &= (k_1 - p_1)^2 = (k_2 - p_2)^2 = -2(k_1 \cdot p_1) = -2(k_2 \cdot p_2), \\ \hat{u} &= (k_1 - p_2)^2 = (k_2 - p_1)^2 = -2(k_1 \cdot p_2) = -2(k_2 \cdot p_1). \end{aligned}$$

In the massless limit the Mandelstam variables sum to zero, so  $\hat{s} + \hat{t} + \hat{u} = 0$ . The matrix element for the photon contribution is:



$$\begin{aligned} i\mathcal{M}_\gamma &= \bar{v}(p_2) [ +ieQ_{in}\gamma^\mu ] u(p_1) \left[ \frac{-i\eta_{\mu\nu}}{q^2+i\epsilon} \right] \bar{u}(k_1) [ +ieQ_{out}\gamma^\nu ] v(k_2) \\ &= -ie^2 \frac{Q_{in}Q_{out}}{q^2} [ \bar{v}(p_2)\gamma^\mu u(p_1) ] [ \bar{u}(k_1)\gamma_\mu v(k_2) ] . \end{aligned}$$

The matrix element for the  $Z^0$  boson is similar, with the intermediate propagator changed

CHAPTER 2. THE STANDARD MODEL

to the massive vector and the vertices with the fermions changed to the  $SU(2)$  couplings:

$$i\mathcal{M}_Z = \bar{v}(p_2) \left[ \frac{+ie}{\cos\theta_w \sin\theta_w} (T_{in}^3 - Q_{in} \sin^2\theta_w) \gamma^\mu \right] u(p_1) \left[ \frac{-i}{q^2 - m_Z^2 + i\epsilon} \left( \eta_{\mu\nu} - \frac{q_\mu q_\nu}{m_Z^2} \right) \right] \\ \times \bar{u}(k_1) \left[ \frac{+ie}{\cos\theta_w \sin\theta_w} (T_{out}^3 - Q_{out} \sin^2\theta_w) \gamma^\nu \right] v(k_2)$$

The  $\not{q}$  operators annihilate the spinors in the massless limit.

$$= -ie^2 \frac{c_{in} c_{out}}{q^2 - m_Z^2} [\bar{v}(p_2) \gamma^\mu u(p_1)] [\bar{u}(k_1) \gamma_\mu v(k_2)].$$

When  $q^2$  is near the mass of the  $Z^0$  boson there will be additional contribution in the denominator due to the finite width of  $Z^0$ . This search is at energies sufficiently past  $m_Z$  these contributions are negligible. The coupling coefficients  $c_{in,out}$  are:

$$c_{in} = \frac{1}{\cos\theta_w \sin\theta_w} (T_{in}^3 - Q_{in} \sin^2\theta_w), \quad T_{in}^3 = \left\{ \pm\frac{1}{2}, 0 \right\}, \quad Q_{in} = \left\{ +\frac{2}{3}, -\frac{1}{3} \right\}, \\ c_{out} = \frac{1}{\cos\theta_w \sin\theta_w} (T_{out}^3 - Q_{out} \sin^2\theta_w), \quad T_{out}^3 = \left\{ -\frac{1}{2}, 0 \right\}, \quad Q_{out} = \{-1\}.$$

These two amplitudes add together, then are squared for the contribution to the cross-section:

$$i\mathcal{M} = i \frac{e^2}{q^2} \left( -Q_{in} Q_{out} + c_{in} c_{out} \frac{q^2}{q^2 - m_Z^2} \right) [\bar{v}(p_2) \gamma^\mu u(p_1)] [\bar{u}(k_1) \gamma_\mu v(k_2)] \\ |\mathcal{M}|^2 = \frac{e^4}{q^4} \left| Q_{in} Q_{out} - c_{in} c_{out} \frac{q^2}{q^2 - m_Z^2} \right|^2 \{ \eta_{\mu\nu} |\bar{v}(p_2) \gamma^\mu u(p_1)|^2 |\bar{u}(k_1) \gamma^\nu v(k_2)|^2 \}.$$

The first factor is designated by  $F(in, out, q^2)$ . The matrix element needs to be averaged over the initial quark states because the incoming protons are not polarized, and summed over all the possible outgoing states. In order to calculate the contributions from the different chiralities, the projection operators  $\frac{1}{2}(1 \pm \gamma^5)$  can be inserted and used. The amplitude for

CHAPTER 2. THE STANDARD MODEL

an incoming left-handed quark pair and outgoing left-handed lepton pair is:

$$|\mathcal{M}_{LL}|^2 = \frac{e^4}{q^4} |F(L, L, q^2)|^2 \times \left\{ \eta_{\mu\nu} \left| \bar{v}(p_2) \gamma^\mu \frac{1}{2} (1 - \gamma^5) u(p_1) \right|^2 \left| \bar{u}(k_1) \gamma^\nu \frac{1}{2} (1 - \gamma^5) v(k_2) \right|^2 \right\}.$$

The first squared set of incoming spinors and gamma matrices can be calculated using the Dirac equation, summing over the spin states, and using the algebra for the  $\gamma^\mu$  matrices:

$$\begin{aligned} \left| \bar{v}(p_2) \gamma^\mu \frac{1}{2} (1 - \gamma^5) u(p_1) \right|^2 &= \frac{1}{2} \frac{1}{2} \sum_{\text{spins}} \bar{v}(p_2) \gamma^\mu \frac{(1 - \gamma^5)}{2} u(p_1) \bar{u}(p_1) \gamma^\nu \frac{(1 - \gamma^5)}{2} v(p_2) \\ &= \frac{1}{2} [(p_1^\mu p_2^\nu + p_1^\nu p_2^\mu) - \eta^{\mu\nu} p_1 \cdot p_2 + i \epsilon^{\mu\nu\rho\sigma} p_{1,\rho} p_{2,\sigma}]. \end{aligned}$$

This calculation is repeated for the other set of outgoing spinors, with the result multiplied by 4 because the outgoing states are summed and not averaged over their spins. The only other difference is exchanging the momenta  $p_1 \rightarrow k_2$  and  $p_2 \rightarrow k_1$ :

$$\left| \bar{u}(k_1) \gamma^\nu \frac{1}{2} (1 - \gamma^5) v(k_2) \right|^2 = 2 [(k_1^\mu k_2^\nu + k_1^\nu k_2^\mu) - \eta^{\mu\nu} k_1 \cdot k_2 + i \epsilon^{\mu\nu\rho\sigma} k_{2,\rho} k_{1,\sigma}].$$

Bringing these together and contracting the indices leaves:

$$\langle |\mathcal{M}_{LL}|^2 \rangle = \frac{e^4}{q^4} |F(L, L, q^2)|^2 [4(p_1 \cdot k_2)(p_2 \cdot k_1)] = \frac{e^4}{\hat{s}^2} |F(L, L, q^2)|^2 [\hat{u}^2].$$

This was for one set of incoming and outgoing states. Summing the contributions from each

CHAPTER 2. THE STANDARD MODEL

chirality contribution gives the final result:

$$\begin{aligned}\langle |\mathcal{M}|^2 \rangle &= |\mathcal{M}_{RR}|^2 + |\mathcal{M}_{LL}|^2 + |\mathcal{M}_{RL}|^2 + |\mathcal{M}_{LR}|^2 \\ &= \frac{e^4}{\hat{s}^2} \left[ \left( |F(L, L, q^2)|^2 + |F(R, R, q^2)|^2 \right) \hat{u}^2 \right. \\ &\quad \left. + \left( |F(L, R, q^2)|^2 + |F(R, L, q^2)|^2 \right) \hat{t}^2 \right].\end{aligned}$$

The differential cross section in the center-of-mass frame for  $2 \rightarrow 2$  scattering is:

$$\begin{aligned}\left( \frac{d\sigma}{d\Omega} \right)_{CM} &= \frac{1}{64\pi^2 \hat{s}} \langle |\mathcal{M}|^2 \rangle \\ &= \frac{\alpha_{EM}^2}{4\hat{s}^3} \left[ \left( |F(L, L, q^2)|^2 + |F(R, R, q^2)|^2 \right) \hat{u}^2 \right. \\ &\quad \left. + \left( |F(L, R, q^2)|^2 + |F(R, L, q^2)|^2 \right) \hat{t}^2 \right].\end{aligned}$$

This can be boosted along the  $z$ -axis and remain invariant; only boosts perpendicular to the beam axis will change the cross section. Because of the boost invariance along the beam axis, this formula is valid for all incoming values of  $x_i$ .

In the CM frame, the variables used are  $\{\theta, \phi\}$ , while this matrix element was calculated with the Mandelstam variables. A change of variables makes this relation a bit clearer:

$$\begin{aligned}\hat{t} &= -2(k_1 \cdot p_1) = -\frac{\hat{s}}{2}(1 - \cos \theta) \\ d\hat{t} &= \frac{\hat{s}}{2}d(\cos \theta).\end{aligned}$$

The matrix element has azimuthal symmetry, so the  $d\phi$  element can be integrated for an additional factor of  $2\pi$ . The relation  $\hat{s} + \hat{t} + \hat{u} = 0$  can be used to eliminate  $\hat{u}$ . The last factor to be included is the incoming quark color, which must be the same for the two quarks to

CHAPTER 2. THE STANDARD MODEL

annihilate. This introduces an additional factor of  $\frac{1}{3}$ :

$$\begin{aligned} \frac{d\sigma}{d\hat{t}}(q\bar{q} \rightarrow \ell\bar{\ell}) &= \frac{\pi\alpha_{EM}^2}{3\hat{s}^2} \left[ -|F(L, L, q^2)|^2 - |F(R, R, q^2)|^2 \right. \\ &\quad + \left( |F(L, R, q^2)|^2 + |F(R, L, q^2)|^2 \right) \frac{\hat{t}^2}{\hat{s}^2} \\ &\quad \left. - \left( |F(L, L, q^2)|^2 + |F(R, R, q^2)|^2 \right) \frac{\hat{t}^2}{\hat{s}^2} \right]. \end{aligned} \quad (2.30)$$

This is the leading-order cross section for the direct production of two leptons by a quark and anti-quark.

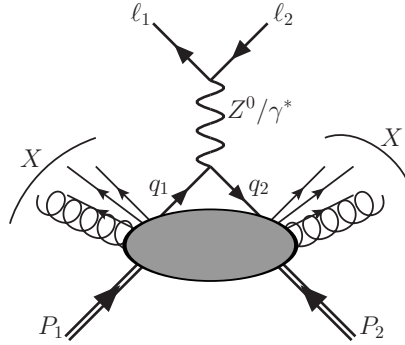


Figure 2.2: The Feynman diagram for the Drell-Yan process of lepton pair production at a hadron collider. The other outgoing particles are labeled  $X$  and can be anything.

To find the pair production of leptons in proton collisions, the parton distribution functions have to be summed over. The Feynman diagram for this is in Figure 2.2. The equation for evaluating this in terms of the differential cross section already calculated for  $q\bar{q} \rightarrow \ell\bar{\ell}$  is:

$$\frac{d\sigma}{dx_1 dx_2 d\hat{t}}(pp \rightarrow \ell\bar{\ell} + X) = \sum_{1,2} f_1(x_1) f_2(x_2) \frac{d\sigma}{d\hat{t}}(q_1\bar{q}_2 \rightarrow \ell\bar{\ell}).$$

Ideally, the cross section should be in terms of the physical variables measured in the detector, rather than ones that cannot be measured directly. Leptons are measured in terms of

CHAPTER 2. THE STANDARD MODEL

$\{p_T, \eta, \phi\}$ , with a four-momentum of:

$$\ell^\mu = (p_T \cosh \eta, p_T \cos \phi, p_T \sin \phi, p_T \sinh \eta).$$

The two Mandelstam variables in terms of the outgoing lepton momenta detector variables:

$$\begin{aligned}\hat{s} &= 2p_T^2 [1 + \cosh(\eta_1 - \eta_2)] = x_1 x_2 E^2, \\ \hat{t} &= -2x_1 E p_T e^{-\eta_1} = -2x_2 E p_T e^{+\eta_2}.\end{aligned}$$

These equations can be inverted to solve for the Jacobian between  $\{x_1, x_2, \hat{t}\}$  and  $\{\eta_1, \eta_2, p_T\}$ :

$$\begin{aligned}x_1^2 &= \frac{2p_T^2}{E^2} [1 + \cosh(\eta_1 - \eta_2)] e^{(\eta_1 + \eta_2)} \\ x_2^2 &= \frac{2p_T^2}{E^2} [1 + \cosh(\eta_1 - \eta_2)] e^{-(\eta_1 + \eta_2)} \\ \hat{t}^2 &= 8p_T^4 [1 + \cosh(\eta_1 - \eta_2)] e^{(\eta_2 - \eta_1)} \\ \frac{\partial(x_1, x_2, \hat{t})}{\partial(\eta_1, \eta_2, p_T)} &= \frac{4p_T^3}{E^2} [1 + \cosh(\eta_1 - \eta_2)].\end{aligned}$$

The differential can be symmetrized between the two leptons. Using azimuthal symmetry the  $p_T$  part can be squared using  $2\pi p_T dp_T = d^2 p_T$ , and because this was calculated in the CM frame the  $p_{T,1} = p_{T,2} = p_T$ . The total cross section is:

$$\frac{d\sigma(pp \rightarrow \ell\bar{\ell} + X)}{d\eta_1 d\eta_2 d^2 p_T} = \sum_{1,2} f_1(x_1) f_2(x_2) \frac{2p_T^2}{\pi E^2} [1 + \cosh(\eta_1 - \eta_2)] \frac{d\sigma}{d\hat{t}}(q_1 \bar{q}_2 \rightarrow \ell\bar{\ell}). \quad (2.31)$$

Where the differential cross section from (2.30) is transformed into the appropriate detector-level variables of the two leptons.

This will receive many corrections such as higher-order Feynman diagrams which contribute to the running of the coupling constants, non-zero transverse momentum for the



## CHAPTER 2. THE STANDARD MODEL

incoming quarks, diagrams that include more out-going particles in the hard scattering process, and other QCD processes described in Section 2.3.2. Besides direct production through an intermediate vector boson, there are two other dominant SM backgrounds that have two opposite-sign leptons in the final state. One is diboson production where two vector bosons are produced in the hard-scattering event and one or both decay leptonically. The other is top quark production, either  $t\bar{t}$  through a QCD process or  $tW$  through an Electro-Weak process, where the top quark decays via a  $W^\pm$  boson, and each  $W^\pm$  decays leptonically. These will each add to the total lepton pair production cross section and must be included in the search.

The search for a new neutral, intermediate vector boson will also add to the Drell-Yan process, giving new channels to produce lepton pairs. The matrix element will look exactly like the Drell-Yan case:

$$i\mathcal{M}_{Z'} = -i \frac{c_{in}c_{out}}{q^2 - m_{Z'}^2} [\bar{v}(p_2)\gamma^\mu u(p_1)] [\bar{u}(k_1)\gamma_\mu v(k_2)].$$

The couplings  $\{c_{in}, c_{out}\}$  to the incoming and outgoing particles will depend on the underlying theory of the new particle. This search looks for excess numbers of lepton pairs beyond what is predicted by the SM. An excess would indicate a new production mechanism, and this is expected to be around the pole mass of the new particle. Such new particles often arise in gauge unification where a second Higgs mechanism breaks the larger symmetry at a higher energy scale and gives rise to new massive vector bosons.

# Chapter 3

## The LHC & ATLAS

The current world leaders in probing the understanding of particle physics at the highest energies are the experiments at the Large Hadron Collider (LHC) [105]. The LHC is an accelerator complex at the Organisation Européenne pour la Recherche Nucléaire (CERN, European Organization for Nuclear Research) colliding two high-energy beams of protons or other nuclei at a variety of experiments. The seven experiments are: A Large Ion Collider Experiment (ALICE) [106], LHC Beauty (LHCb) [107], LHC Forward (LHCf) [108], Monopole and Exotics Detector At the LHC (MoEDAL) [109], Total Elastic and Diffractive Cross Section Measurement (TOTEM) [110], and the two largest, general purpose experiments, the Compact Muon Solenoid (CMS) [111] and A Toroidal LHC Apparatus (ATLAS) [112]. In this chapter I will describe some of the history of experimental particle physics, then detail the LHC complex and ATLAS experiment. Lastly I will discuss how ATLAS reconstructs events and particles inside events used in the analysis of experimental particle physics.

### 3.1 History - From Rutherford to Now

The first modern particle physics experiment was Rutherford's  $\alpha$ -particle on gold nuclei scattering experiment [113] in collaboration with Hans Geiger and Ernest Marsden in 1909-10. This was the first experiment to probe the atomic structure and led to the discovery of the nucleus. Beginning with this experiment and over the next 20 years, the only methods to probe atomic and particle physics had to come from nature, either from radioactive sources or cosmic rays. Cosmic rays would prove to be a bountiful avenue of research. Carl Anderson's study of cosmic rays discovered the positron [114] in 1932, then the muon with collaborator Seth Neddermeyer [115] in 1937. The experiment used a cloud chamber inside a magnetic field to see the tracks of incoming particles, with a lead plate in the middle. As the particle passed through the plate some energy would be lost, and the side of the plate with the less-bent track indicated where the particle came from. By measuring the curvature of the track with a known magnetic field made it possible to estimate the charge-to-mass ratio. Assuming a single-charged object (in units of the proton's charge), the mass did not match a known particle. This new particle was initially identified as the pion, however it was realized it did not have the right properties and was instead called the mu meson and later called simply the muon. In 1947, Cecil Powell and others used cosmic rays to discover the charged pion by looking at emulsion tracks where the new particle decays into a muon [116].

Cosmic rays provide a source for new particles, but this is by passive detection of the not-directly-produced particles. During the 1930s, Robert Van de Graff invented the eponymous electrostatic generator [117], Ernest Lawrence [118] and Leo Szilard independently developed the cyclotron, and John Cockcroft and Ernest Walton developed their own electrostatic generator [119]. The idea of using groups of pulsed magnets synchronized together to form a synchrotron was developed over several steps [120, 121, 122] during and after the war,

### CHAPTER 3. THE LHC & ATLAS

and helped break the “cyclotron barrier” in terms of energy. All of these devices were able to accelerate charged particles, typically protons or electrons, to much higher energies than had been attainable in the laboratory before, and in the post-war era accelerating to higher and higher energies led to many new discoveries. One of the first major accelerators to become operational was the Berkeley Bevatron in 1954, accelerating protons to in excess of 6 GeV, leading to the discovery of the anti-proton by Emilio Segrè and Owen Chamberlain in 1960 [123]. Other experiments used the new, higher-energy protons to discover new particles dubbed the “particle zoo”. Luis Alvarez used a liquid hydrogen target “bubble chamber”, invented earlier by Donald Glaser [124], inside a magnetic field to discover many of these particles [125]. As particles passed through the liquid, they ionize the hydrogen. A piston is used to decrease the pressure and bubbles form, leaving visible tracks where an ionizing particle passed through. A picture is taken, then the piston re-pressurizes the liquid, erasing the previous tracks. Electron scattering off gaseous hydrogen and helium by Robert Hofstadter probed the structure of the nucleon [126] and gave the first true measurement of the proton charge radius [127]. The Alternating Gradient Synchrotron (AGS) installed at Brookhaven National Lab accelerated protons to 33.5 GeV and had much stronger focusing of the output protons. The AGS began operation in 1960 and led to numerous discoveries over its lifetime. Some of the most famous were the discovery of the muon neutrino by Leon Lederman *et al.* [128], the discovery of the  $\Omega^-$  baryon by Barnes *et al.* [129], CP violation in  $K$ -mesons by James Cronin and Val Fitch [70], and the discovery of the  $J/\psi$  meson by Sam Ting *et al.* [130]. The last example aimed the accelerated protons on a Beryllium target, then used a spectrometer to reconstruct pairs of electrons and positrons. The discovery was made when an unexpected “bump” appeared in the reconstructed invariant mass spectrum of the  $e^+e^-$  system, which indicated a new particle.

Besides an avenue for discovering new particles, the new generation of accelerators were

### CHAPTER 3. THE LHC & ATLAS

used to study the nucleons in greater detail than had been done before. At the Stanford Linear Accelerator Center (SLAC), the SLAC-MIT experiment scattering 20 GeV electrons off various targets, in much the same way Rutherford's scattering showed the point-like nucleus, proved that the nucleons were made up of point-like quarks [131]. The scattered electron's energy was measured at fixed angles, and so the total energy imparted to the proton or neutron could be calculated. The number of particles scattered at a given  $Q^2$  matched the expectation of a group of quarks, rather than a diffuse nucleus. At CERN, using the Proton Synchrotron to accelerate protons into a target to produce a pion beam which then decayed to muon-neutrinos, the first evidence of neutral weak currents were observed in the bubble chamber Gargamelle [132, 133].

By the 1970s, a new idea was being developed at CERN that did not use a single beam of high-energy particles. Instead, two beams circulating in a ring in opposite directions are made to collide at designated interaction places. The first such complex, called the Intersecting Storage Rings (ISR) used protons and went online in early 1971. The increase in energy available in the collisions was amazing, and new experiments quickly followed suit. In Germany, the accelerator complex Deutsches Elektronen Synchrotron (DESY) facility, with the Positron-Elektron-Tandem-Ring-Anlage (PETRA, Positron-Electron Tandem Ring Plant) collider, reached energies up to 31.6 GeV. The TASSO experiment and others observed the first evidence of the gluon in 1979 [134, 135, 136, 137] by studying highly-transverse "jets" coming from the interaction point. At CERN, two beams of protons and anti-protons at the Super Proton anti-Proton Synchrotron (Sp $\bar{p}$ S) collided at an energy of 540 GeV. Such high energies were made possible by "Stochastic Cooling" invented by Simon van der Meer, where the field of the accelerated (anti-)protons feeds into a loop that keeps the bunches of (anti-)protons in the storage ring at the same energy and transverse momentum. The two Underground Area experiments (UA1 & UA2) were the first to observe the direct production

### CHAPTER 3. THE LHC & ATLAS

of  $W^\pm$  bosons [138, 139] and then the direct production of the  $Z^0$  boson the following year [140, 141]. By 1986, the Tevatron accelerator at Fermilab reached collision energies of 1.8 TeV using protons and anti-protons. The two experiments, CDF and DØ, co-discovered the top quark in 1995 [142, 143].

Another fruitful area of research has been precision measurements of the Standard Model predictions. In the 1990's there were two  $e^+e^-$  colliders operating at the  $Z^0$ -peak, one at CERN called the Large Electron-Positron collider (LEP), and the other at SLAC called the Stanford Linear Collider (SLC). Experiments at both colliders performed extensive tests on SM parameters and predictions. One interesting measurement looked for so-called “invisible” events where the  $Z^0 \rightarrow \nu\bar{\nu}$ . The neutrinos do not interact and are not observed at all, but by running the collisions slightly above the mass of the  $Z^0$ , a photon is radiated to have the  $Z^0$  be “on-shell”. Counting events with nothing but the single photon, compared to the number of events with the single photon and a lepton pair or two jets, provides an estimate on the number of neutrino species in the SM [144]. At DESY, electrons and protons were accelerated at Hadron-Elektron-Ring-Anlage (Hadron-Electron Ring Plant, HERA) and collided to study the parton distribution functions of the proton over a large kinematic range and search for new physics [145]. At lower energies but higher luminosities, experiments at SLAC and KEK called BaBar and BELLE studied  $B$ -mesons to probe the SM's predictions about CP violation and how different flavors of quarks interact [146, 147].

A common thread throughout these experiments and discoveries is the drive for higher energies. Each step into the “Energy Frontier” [148] has brought rich rewards in understanding how particles interact and what particles there are in the universe. The LHC is the next advancement into that understanding, and already a major discovery has been made with the announcement of the detection of the Higgs Boson made in July 2012 [1, 2].

## 3.2 The Large Hadron Collider

The LHC is a high-energy physics accelerator located at CERN outside Geneva, Switzerland. It is the world's largest machine [149], and is designed to collide bunches of protons at a center-of-mass (CM) energy of 14 TeV and instantaneous luminosity of  $10^{34} \text{ cm}^{-2}\text{s}^{-1}$ , reaching a total of  $\sim 100 \text{ fb}^{-1}$  of integrated luminosity of data per year of operation [105]. To save on construction costs the beams and detectors are placed in the LEP ring, with the construction of two new caverns to accommodate the general purpose experiments ATLAS and CMS, and additional tunnels for upgraded beam transfer and controls.

Construction was completed in 2008 and initial beams were circulated on September 10th, 2008. Due to an electrical fault and subsequent quenching incident on September 19th, 2008 [150], full operations were delayed by more than one year. This also led to the decision to begin operations at a lower CM energy of 7 TeV and lower instantaneous luminosity of  $\sim 10^{32} \text{ cm}^{-2}\text{s}^{-1}$  during the initial data-taking runs in 2010 and 2011 to reduce the strain on the magnets. The data-taking runs during 2012 saw increases in the CM energy to 8 TeV and instantaneous luminosity to  $\sim 7 \times 10^{33} \text{ cm}^{-2}\text{s}^{-1}$ , resulting in over  $20 \text{ fb}^{-1}$  of integrated luminosity recorded by both primary experiments. Further upgrades are expected to have the LHC reach or exceed its design capabilities in terms of CM energy and instantaneous luminosity during future data-taking runs, expected to begin in late 2014. This section will describe how the LHC delivers these proton collisions to the various experiments at CERN. A much fuller account of the LHC design and operation can be found in the LHC Technical Design Report [151, 152, 153].



Figure 3.1: An aerial view of CERN, with the LHC ring superimposed on the surface. The major experiments and other accelerating rings are also shown. “CERN / Aerial view of the CERN”, © Maximilien Brice and Ars Electronica, used under a Creative Commons license.

### 3.2.1 Beam Energy & Luminosity

The performance of the experiments in the search for new physics and the study of the Standard Model depends on two parameters of the LHC proton beams, the energy and the luminosity. The energy of the colliding protons is determined by how strong the magnets must be to keep the beams traveling in a circle. The dipole magnets that are the primary magnets to keep the beam inside the ring have a mean field of 8.33 T, and the LHC ring is 26.7 km in circumference, giving a peak total energy for the protons of 7 TeV. The luminosity



### CHAPTER 3. THE LHC & ATLAS

is determined by several factors such as how many protons are kept together in a bunch, how many bunches there are in the ring, and how small of a bunch can be maintained in the ring. The luminosity formula is:

$$L = \frac{N_b^2 n_b f_{rev} \gamma_r}{4\pi \epsilon_n \beta^*} F,$$

where  $F = \left[ 1 + \left( \frac{\theta_c \sigma_z}{2\sigma^*} \right)^2 \right]^{-1/2}$ .

$N_b$  is the number of protons in the bunch,  $n_b$  is the number of bunches in the ring,  $f_{rev}$  is the revolution frequency,  $\gamma_r$  is the relativistic gamma factor of the particles being collided,  $\epsilon_n$  is the normalized transverse beam emittance,  $\beta^*$  is the beta function at the interaction point (IP), and  $F$  is the geometric factor due to the crossing angle at the IP. The geometric factor's factors are:  $\theta_c$  is the crossing angle,  $\sigma_z$  is the length of the proton bunch, and  $\sigma^*$  the transverse beam size.

For protons at 4 TeV of energy, which were the operating conditions during the 2012 data taking runs, the relativistic gamma factor is  $\gamma_r \sim 4250$  and they travel around the ring at about  $f_{rev} \sim 11,000$  Hz. The bunches were spaced 50 ns apart, with 1755 bunches stored in each beam and each bunch containing  $\sim 10^{11}$  protons, depending on beam conditions during the run. The mechanical size of the LHC magnet apertures limits the beam size to 1.2 mm outside of the IPs, which requires a maximum transverse beam emittance of  $\epsilon_n = 3.75 \mu\text{m}$ , although the typical value during running was  $2.3 \mu\text{m}$ . The other factors all depend on how tightly focused the bunch can be made at the IP. The  $\beta^*$  was adjusted for the 2012 run down to 0.6 m at the ATLAS IP, with a geometric factor of  $F \sim 0.81$ . These combined to give an average instantaneous luminosity of  $\sim 7 \times 10^{33} \text{ cm}^{-2}\text{s}^{-1}$  during the 2012 physics data taking run.

### CHAPTER 3. THE LHC & ATLAS

The integrated luminosity delivered to the experiments for physics analysis is determined by the instantaneous luminosity, which is determined by the beam parameters discussed above. The dominant loss of the beam intensity is due to the collisions at the high-luminosity IPs at ATLAS and CMS. The number of protons lost over time is determined by how many interactions occur between the beams:

$$\frac{dN}{dt} = -\sigma_{tot}L(t)k.$$

Where the factors are:  $\sigma_{tot}$  is the total inelastic nuclear scattering cross section between protons,  $\sigma_{tot} \sim 10^{25} \text{ cm}^2$  (100 mbar),  $L(t)$  is the instantaneous luminosity proportional to  $N(t)^2$ , and  $k$  is the number of high-intensity interaction points,  $k = 2$ . The other experiments such as LHCb are operated at much lower luminosities, in particular maintaining a much larger  $\beta^*$  and smaller  $F$  geometric factor at their interaction points, and do not contribute as much to the beam decay. The initial nuclear decay time be:

$$\tau_{nuc} = \frac{N_0}{2\sigma_{tot}L_0}.$$

Solving these equations, the instantaneous luminosity and beam intensity are:

$$L(t) = \frac{L_0}{\left(1 + \frac{t}{\tau_{nuc}}\right)^2},$$

$$N(t) = \frac{N_0}{1 + \frac{t}{\tau_{nuc}}}.$$

Other effects can cause luminosity loss, such as beam-beam interactions, intrabeam scattering (IBS), scattering from residual particles, and RF noise. The biggest source of IBS is the Touschek effect when charged particles in a bunch scatter off each other, transferring

CHAPTER 3. THE LHC & ATLAS

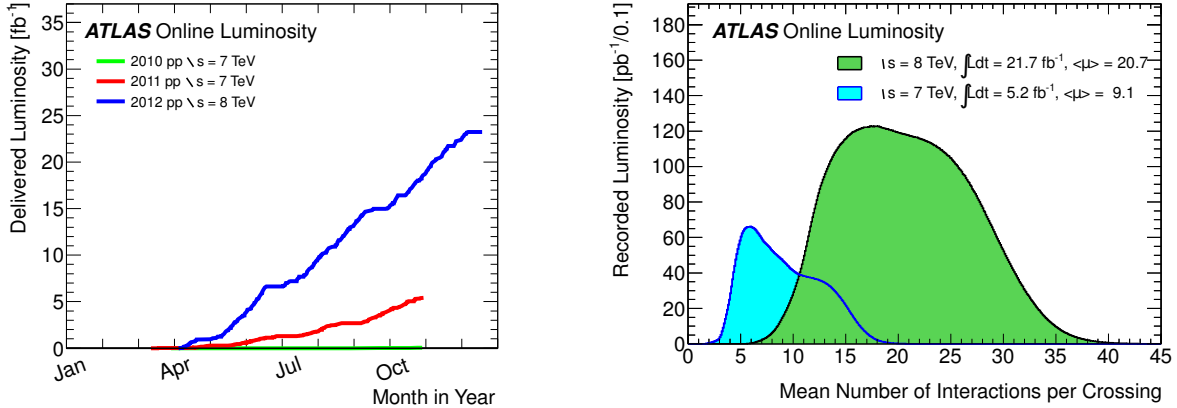


Figure 3.2: Left: Total luminosity delivered to the ATLAS experiment by the LHC during the three data-taking years of Run I. Right: Average number of interactions during a bunch crossing during the 2011 and 2012 data-taking years. From [154].

momentum to the transverse directions and out of the beam aperture. Approximating the various luminosity losses as an exponential decay, the lifetimes add inversely:

$$\frac{1}{\tau_{tot}} = \frac{1}{\tau_{IBS}} + \frac{1}{\tau_{gas}} + \frac{1}{\tau_{nuc,1/e}}.$$

The net estimated luminosity lifetime for the beams in the LHC is:

$$\frac{1}{\tau_{tot}} \sim 15 \text{ hr.}$$

The instantaneous luminosity is monitored at the ATLAS and CMS detectors by Beam Rate of Neutrals (BRAN) detectors [155], placed inside the neutral particle absorbers (TAN) used to protect the insertion and separation dipole magnets which are placed 141 m from the IP on both sides. The BRANs are 10 cm × 10 cm Argon gas ionization chambers, which are radiation hard against the extremely high radiation environment in the forward region. These are flux monitors measuring the incident rate of neutral particles ( $\gamma, n$ ) by

### CHAPTER 3. THE LHC & ATLAS

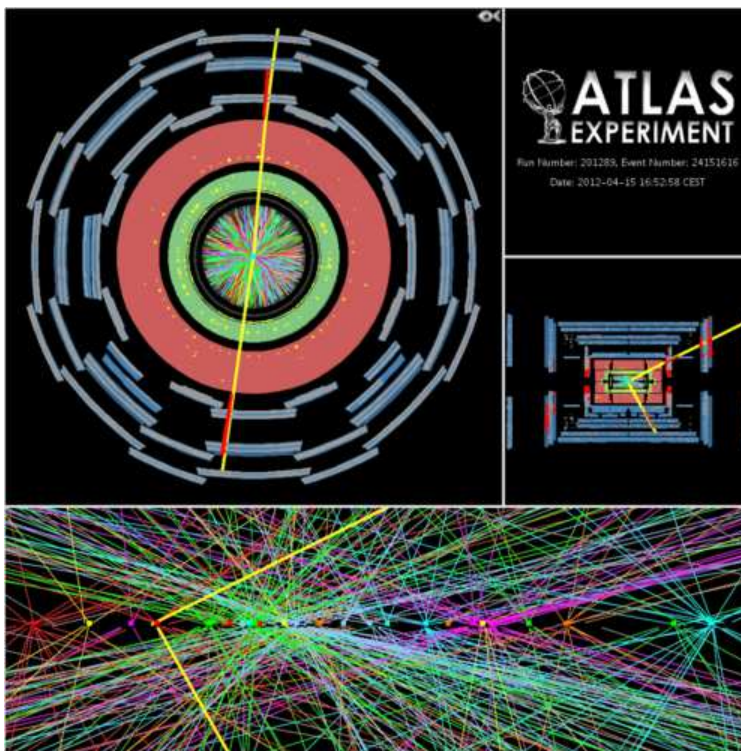


Figure 3.3: A high-pileup event showing  $Z^0 \rightarrow \mu\mu$ . There are 25 reconstructed vertices, where each vertex has at least 3 tracks, and each track has at least 3 Pixel and 6 SCT hits. The track colors correspond to the associated vertex, and the bright yellow tracks are the high- $p_T$  muon pair that form the  $Z^0$  candidate. From [156].

measuring electromagnetic and hadronic showers inside the TAN which is proportional to the  $pp$  collision rate. The readout rate is fast enough for bunch-by-bunch interaction and luminosity estimates and is accurate to better than 1% during normal operations. The total luminosity and average interactions per crossing for ATLAS are shown in Figure 3.2. A typical example of a bunch crossing at ATLAS is shown in Figure 3.3.

### 3.2.2 Accelerator Complex

The beams of protons collided at the LHC require many stages to reach the final collision point at the required energy and luminosity. The full accelerator complex is shown in Figure 3.4. The protons are accelerated initially through the Alvarez Proton Linac (LINAC2) to energies of 50 MeV. The beam then moves to the Proton Synchrotron Booster (PSB) and is accelerated to energies of 1.4 GeV, where it moves to the Proton Synchrotron (PS) and is then accelerated to 25 GeV. From the PS, the beam is put into the Super Proton Synchrotron (SPS), site of the former UA1 and UA2 experiments, and accelerated to 450 GeV. Once at these energies, the beam can finally be placed into the LHC ring and accelerated to the final energy of 4 TeV. Each stage of acceleration requires tight control of the emittance due to the strict requirements of the LHC magnet's aperture limit. During the initial acceleration phases, at low energies, synchrotrons suffer from "space charge" effects due to the Coulomb forces between the low-speed particles, which result in "tune shifts" and can destabilize the beams.

The PSB is fed 50 MeV protons from the Linac, which accelerates them to 1.4 GeV. This is done with up to 4 bunches inside the PSB ring. The bunches are then injected into the PS, which splits the 6 PSB bunches (either 3+3 or 4+2 from the PSB) into the bunches for the LHC. Once these bunches have been split (each bunch is split 12 times, giving 72 total bunches), they are accelerated to 25 GeV and injected into the SPS. The cycling time for the PS is 3.6 seconds. Inside the SPS ring, either 3 or 4 PS batches fill the ring, and then the protons are accelerated to 450 GeV. The cycling time for the SPS is 21.6 seconds, after which the 288 bunches are injected into the LHC ring. This is done 12 times to fill the LHC ring, with a total time of about 4 minutes per beam. Once the LHC ring is filled, it takes  $\sim 20$  minutes for the protons to be accelerated from 450 GeV to 4 TeV.

## CHAPTER 3. THE LHC & ATLAS

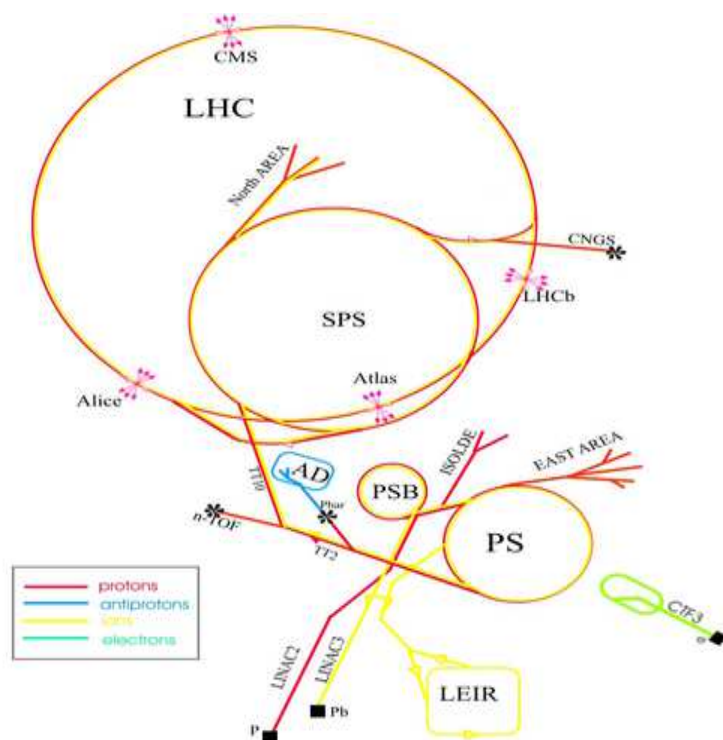


Figure 3.4: The accelerator complex at CERN. From [157].

### 3.2.3 The LHC Magnets & RF System

The LHC proton beams are primarily controlled with 1232 main dipole magnets (MB), using Niobium-Titanium (NbTi) superconducting cables cooled to 1.9 K with a bath of superfluid He-II. These magnets perform the main bending to keep the beams traveling in the ring. 392 main quadrupole magnets (MQ) are also cooled in the same manner as the dipole magnets and are used to keep the beams focused. These magnets are designed with a twin aperture to save space in the LEP tunnel. These two sets of magnets do the main work of keeping the beams in the ring and focused, but many other magnets are needed to fully control the beams. A cross section picture of a standard dipole magnet is shown in Figure 3.5. There are 6028 orbit corrector magnets of dipole (MCBx), sextupole (MCSx), octupole (MCOx),

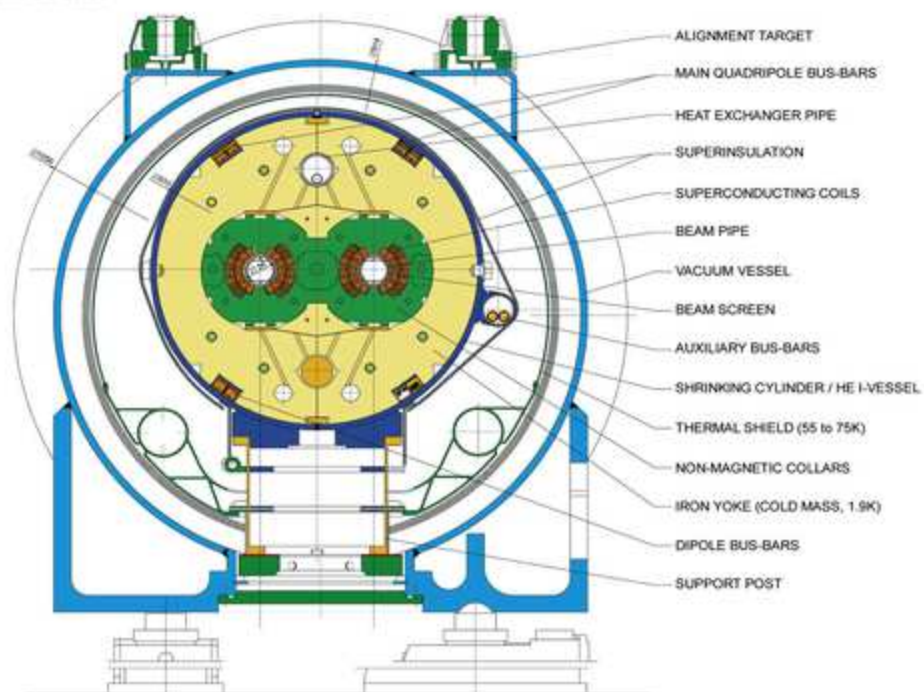
**LHC DIPOLE : STANDARD CROSS-SECTION**

Figure 3.5: A cross section of a dipole magnet for the LHC. From [158].

decapole (MCDx), and dodecapole (MCTx) designs working with the dipole magnets to keep the beams in their arcs. 336 octupole (MO) and 688 + 64 sextupole (MS & MSS) magnets provide lattice corrections in the short straight sections of the ring. Further lattice corrections and beam focusing, as well as final focusing for the IPs, are provided by an additional 702 quadrupole (MQx) magnets. There are 70 dipole (MBx), 42 “kicker” (MKx), and 40 sextupole (MSx) magnets to insert the beams into the ring, bend them to collide at the IPs, separate the beams after a collision point, and eject them for a beam dump. These magnets all work in conjunction to form the LHC magnet system controlling the two proton beams needed for the experiments.

To accelerate the beams to 4 TeV and then maintain that energy due to synchrotron and

## CHAPTER 3. THE LHC & ATLAS

other energy losses, 16 radio frequency (RF) single-cell superconducting cavities are used, 8 per beam [159]. Each cavity operates at 400 MHz, and can deliver up to 2 MV of accelerating voltage per beam at top energy. The acceleration gain during ramp-up of the beams is 485 keV per revolution, which corresponds to 275 kW of power supplied by the RF cavities. The cavities are assembled into cryomodules containing four single cavities. At Point 4 on the LHC ring the four cryomodules are installed, with two before (US45) and two after (UX45) the IP. Each beam is accelerated by one cryomodule per side. Special single aperture dipole magnets (MBRS & MBRB) are used to separate and combine the beams at the RF cryomodules. Each RF cavity is powered by a klystron, which is kept in a separate cavern away from the beam and cavities to prevent possible interference and resonant phenomena. They are coupled with a 3-port junction circulator to prevent reflections from the cavity and fed to the cavities by a  $\sim 22$  m long half- $\lambda$  waveguide. The RF cavities also provide bunch spacing control. When the beams are initially injected from the SPS, the bunch spacing is 1.71 ns. At full energy after 20 minutes of acceleration, the bunch spacing is down to 1.06 ns, and the energy spread for the beams has fallen from  $8.8 \times 10^{-4}$  to  $2.2 \times 10^{-4}$ .

### 3.2.4 Controls

The beams at full energy correspond to  $\sim 250$  MJ of total energy, and the magnet system once fully cooled contains  $\sim 500$  MJ of stored energy. The beams travel in a beam pipe kept at 1.9 or 4.5 K or room temperature for operations, depending on the magnet system the beam is passing through. The vacuum system must maintain  $10^{-10} - 10^{-11}$  mbar at the room temperature sections across more than  $80 \text{ m}^3$  of total beam pipe volume. The temperature and vacuum requirements must be tightly controlled to prevent the beam from nuclear scatterings between the beams and gas molecules in the beam pipe. Image currents



in the beam pipe also generate heat in the cryogenic systems, while electrons stripped from the beam pipe surface can form clouds (SEY, secondary electron yields) that interact with the beams and dissipate energy. All of these sources of energy loss and scattering in the beams leads to instabilities that must be monitored and corrected. The fields of the proton bunches can be measured to correct for deviations from the normal range. The magnets must be monitored to prevent quenching, the rapid energy loss when a superconductor transits to a normal conductor when the material heats up past the critical temperature. A huge number of protections are in place for the vacuum, cryogenic, and power systems for the beams, magnets, and RF components of the LHC.

### 3.3 The ATLAS Detector

The ATLAS detector (A Toroidal LHC Apparatus) was proposed as one of the primary LHC experiments in 1994 and approved in 1995 to begin design and R&D work, and principle construction was completed in 2008. ATLAS is cylindrically shaped, measuring 22 m across by 46 m long and weighing approximately 7000 tons. ATLAS is a general-purpose detector designed to detect all the particles coming from a collision and is comprised of several subsystems. Each subsystem has a specific detection purpose and is designed to handle the high-luminosity environment of the LHC. The general requirements for ATLAS are precision calorimetry for EM and hadronic particles, momentum tracking for muons, efficient particle tracking and identification, with as large acceptance as possible in the azimuthal and polar angles. A large-scale cutaway picture of ATLAS, with annotations of the different subsystems, is shown in Figure 3.6. This section will describe each of the subsystems in the detector, with further detail available in the ATLAS *Technical Design Report* [160, 161].

ATLAS uses a right-handed coordinate system with the beam axis defining the  $z$ -axis,

CHAPTER 3. THE LHC & ATLAS

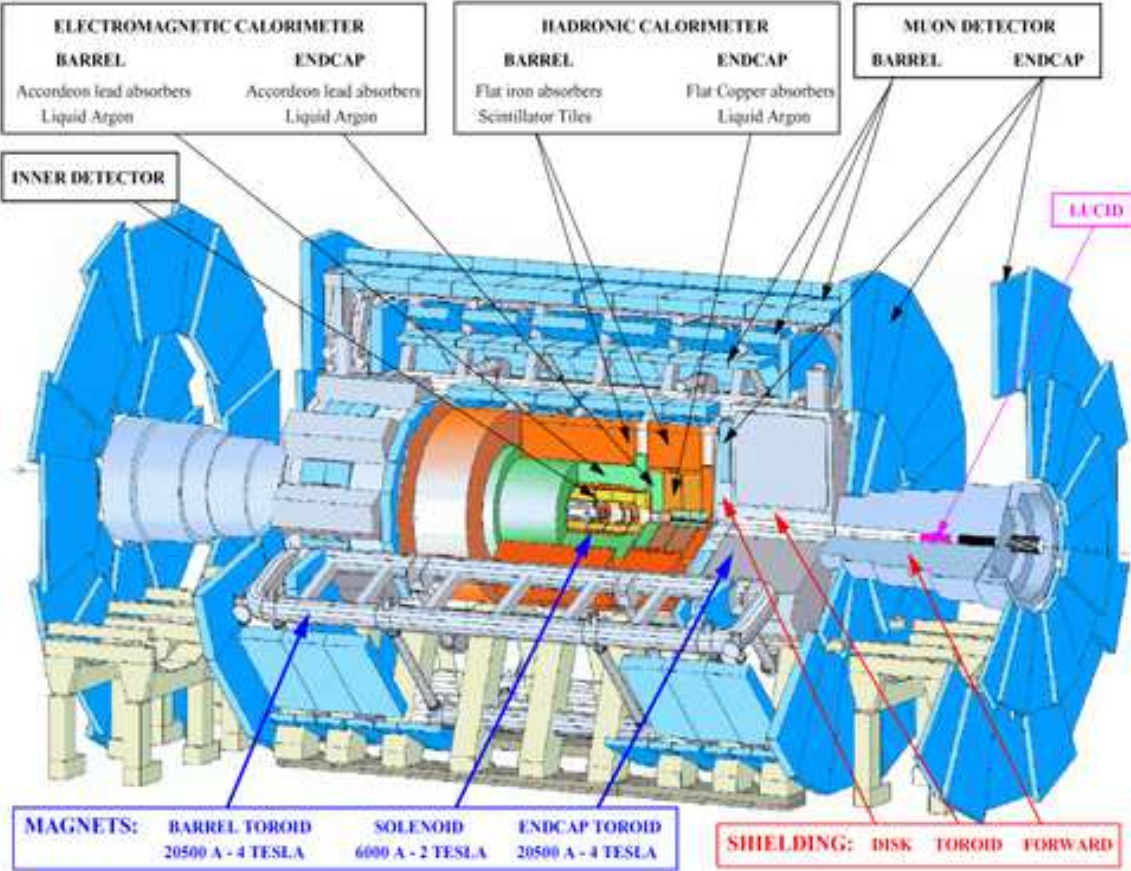


Figure 3.6: An annotated diagram of the full ATLAS detector. From [162].

the positive  $x$ -axis points towards the center of the LHC ring, and the positive  $y$ -axis points upwards away from the center of the earth. The nominal IP is the origin of the coordinate system. Because of the cylindrical geometry of the detector, ATLAS also uses a coordinate

### CHAPTER 3. THE LHC & ATLAS

system with the azimuthal and polar angles defined as:

$$\begin{aligned}\phi &= \arctan\left(\frac{y}{x}\right), \\ \theta &= \arctan\left(\frac{\sqrt{x^2 + y^2}}{z}\right), \\ \eta &= -\ln \tan\left(\frac{\theta}{2}\right).\end{aligned}$$

The pseudo-rapidity ( $\eta$ ) is a common particle physics convention. For cases where the particle is massless or  $E \gg m$  this closely approximates the rapidity, and boosts between Lorentz frames can simply add  $\eta$ . The momenta of particles coming from the collision are split into the transverse plane from the beam axis and along the  $z$ -axis:

$$p_T = \sqrt{p_x^2 + p_y^2}.$$

The transverse energy for a particle is:

$$E_T = \sqrt{m^2 + p_T^2}.$$

The incoming particles have very little initial transverse momenta, and because of the azimuthal symmetry of the collision, the outgoing particles total transverse momenta ( $p_x$  and  $p_y$ ) should sum to zero. Undetected particles such as neutrinos can appear as large “missing transverse energy” (MET), when the vector sum of the transverse momenta does not add to zero. ATLAS has two halves, and these are designated the A side (defined with positive  $z$  or  $\eta$ ) and the C side (defined with negative  $z$  or  $\eta$ ). The “B side” is the plane at  $z = 0$  or  $\eta = 0$ .

The motion of particles is determined by 6 total parameters: the initial position and

## CHAPTER 3. THE LHC & ATLAS

momentum of the particle. Neutral particles will travel in a straight line and charged particles will bend in the magnetic fields, following a fixed trajectory. This path constraint reduces the motion to 5 parameters. In ATLAS, these parameters are:

- $q/p_T$ , this is fit from the path radius of the particle measured passing through the magnetic field;
- $\phi$ , the azimuthal coordinate of the particle, determined by the direction of motion of the particle at the point of closest approach;
- $d_0$ , the impact parameter defined as the transverse distance of closest approach to the beam axis;
- $1/\tan\theta$ , the polar angle of the particle, determined by the direction of motion of the particle at the point of closest approach;
- $z_0$ , the impact parameter defined as the longitudinal distance at the point of closest approach.

Particle separation is defined in terms of the angular variables, using a cone in  $\eta$ - $\phi$  space:

$$\Delta R = \sqrt{(\Delta\eta)^2 + (\Delta\phi)^2}.$$

### 3.3.1 General Detector Strategy

Particles have just a few intrinsic characteristics that can be measured in the lab. Their mass, spin, and parity are from their representation in the Lorentz group (specifically the “Little group” [75]), while their quantum numbers such as charge are from their representation in the various gauge groups. To identify a particle uniquely, the detector needs to measure the

### CHAPTER 3. THE LHC & ATLAS

total energy, the momenta, and the charge of the particle. How the particle interacts with the material in the detector also helps with identification. Different detectors will perform one or more of these tasks, such as measuring the energy, momentum, charge, or separating different particles. The specific sets of detectors will depend on the requirements of the experiment as well as the expected physics output from the collisions.

Generally speaking, there are three time scales for particles created in collisions. Stable or long-lived particles, such as electrons, muons, pions, kaons, protons, neutrons, and photons, will travel into the detector and interact, with typical lifetimes of  $> 10^{-8}$  s. Their decays can only occur through the weak force and are suppressed due to very limited phase space and decay channels. These particles can either come from the collision directly or through the decay of short-lived particles. There are two time scales that determine “short-lived”, and this depends on how the particle decays. If the particle decays through a  $W^\pm$  boson into a limited phase space, for example tau leptons, B mesons, and D mesons, then the typical lifetimes are  $\sim 10^{-13}$ - $10^{-12}$  s. If the particle can decay electromagnetically or through the strong force, for example the  $\pi^0$ ,  $J/\psi$ , and excited B and D mesons, then the lifetimes are  $\leq 10^{-16}$  s. The lifetime of the short-lived particles is important for detection. The particles that decay weakly will travel  $\sim 1$  mm before decay, which is separated enough from the initial collision point that it can be observed as a displaced vertex. Particles with much shorter lifetimes can only be observed through their decay products. A picture of the ATLAS detector showing the different types of SM particles and where and how they interact is shown in Figure 3.7.

Most particles in the SM can be detected either directly or through their decay products, however there is one important exception. Neutrinos do not have any electric charge or color and can only interact through a  $W^\pm$  or  $Z^0$  boson. The cross section for this is extremely small and they will travel straight through the detector (and in fact hundreds of miles through the

## CHAPTER 3. THE LHC & ATLAS

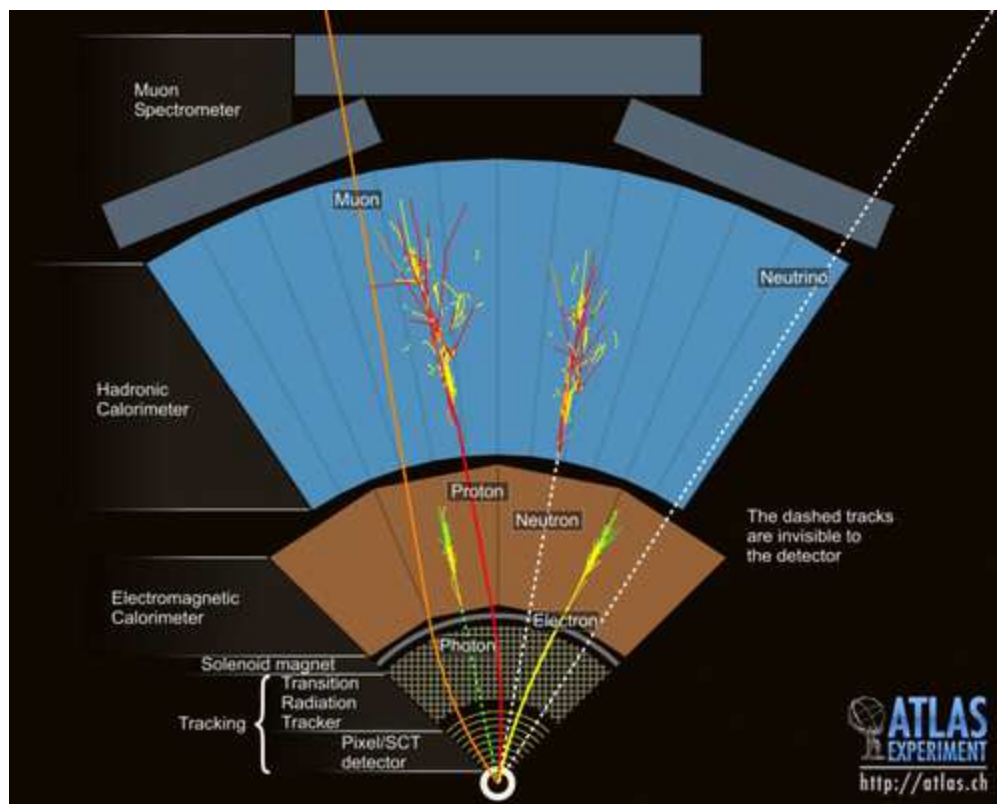


Figure 3.7: A cross section of the ATLAS detector, showing where the different types of particles interact with the various detectors. Each sub-detector performs a function to measure the energy or charge and momentum of a specific class of particles. From [162].

earth) before interacting once. Neutrinos will show up as missing transverse energy after the total transverse momenta of all the other particles has been summed.

Particle charge and momentum can be measured by tracking the trajectory of the particle in a constant magnetic field:

$$p_{\perp} = qBR.$$

The magnetic field orthogonal to the motion is  $B$  and the radius of the path is  $R$ . The direction of bending in the magnetic field indicates the charge  $q$  of the particle. For a

### CHAPTER 3. THE LHC & ATLAS

particle with the same charge as the proton, in typical units measured in an experiment this formula becomes:

$$p_{\perp}[\text{GeV}] = 0.3 B[\text{T}] R[\text{m}].$$

Tracking detectors can use a variety of materials that ionize as the particle passes through the medium. The ionization trail can then be read out to measure the track whose radius measures the particle momentum. Different ionization behavior can also be used in particle identification.

The energy of a particle can be measured by absorbing the particle and adding up the total energy deposited. As a particle passes through material it will interact with the electrons and nuclei inside the material radiating new secondary particles in a “shower”. A typical design is a sampling calorimeter where layers of absorbing material are placed between scintillating material layers that produce light proportional to the amount of ionizing particles passing through. The initial energy of the showering particle is measured by reading out over many layers and adding up the total deposited energy. The sampling also shows the shape of the shower, which is useful for separating between photons and electrons.

Electrons and photons interact with the electrons in the material through Raman and Compton scattering or Bremsstrahlung by emitting additional photons or photons converting into  $e^+e^-$  pairs. The length that determines the size of a shower is called a radiation length  $X_0$ , where one radiation length results in  $\sim 1/e$  of the energy lost through scattering. This depends inversely on the number of electrons per nucleus squared, making high- $Z$  material such as lead useful for shortening this length. Once the electron is below  $\sim 100$  GeV, the process is dominated by ionization. In the ionization regime, the particles interact fewer times and can travel further before losing the same fraction of energy. For particles with a few

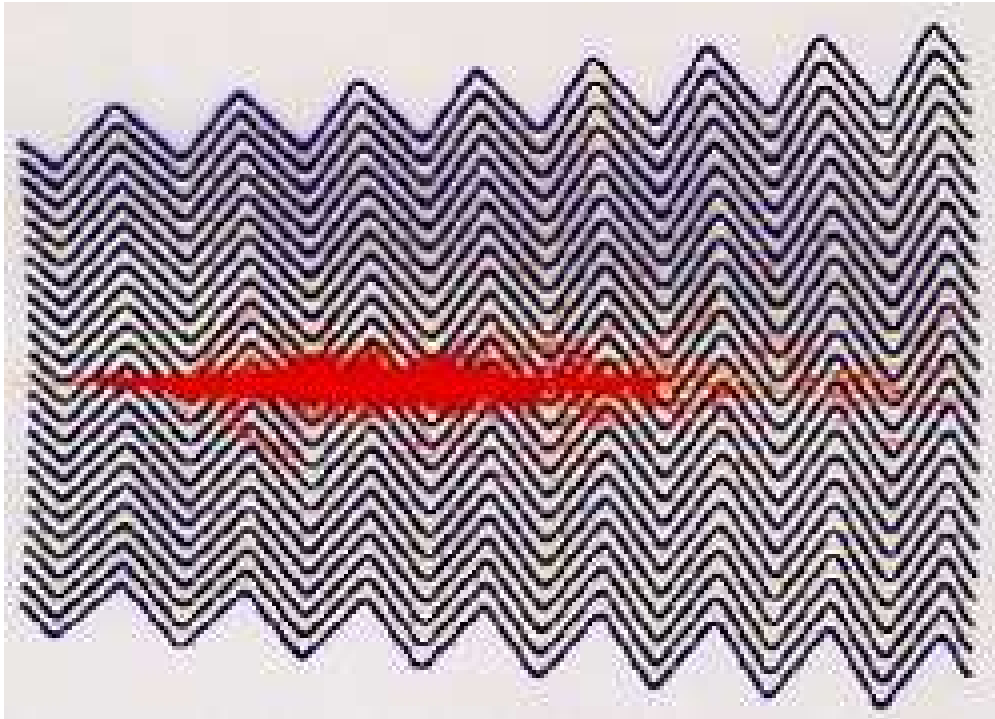


Figure 3.8: An electron shower inside the ATLAS “accordion” electromagnetic calorimeter. From [162].

hundred GeV in energy observed in LHC processes,  $\sim 25 X_0$  is needed for the calorimeter to fully contain an EM shower, with sampling throughout. The ATLAS “accordion” calorimeter is shown in Figure 3.8, with a typical showering electron event.

Hadrons interact via the strong force and will scatter off nuclei, losing energy by radiating pions and other low-energy hadronic particles in a similar fashion to the electromagnetic showering. Because the underlying processes are dominated by very different physics, the length scale is quite different and is called the interaction length  $\lambda_I$ . The interaction length is defined as the distance  $1/e$  particles have not interacted. In this case to make the material as absorbing as possible requires a large nucleus and a lattice layout with the smallest inter-nuclear spacing. The interaction length scales with density, so higher density materials are



the most useful. The shape of hadronic showers are much more spread out than EM showers. Due to the size needed to contain these showers, cheaper elements such as iron, or common alloys like brass are typically used. A hadronic calorimeter will usually have  $10 - 12 \lambda_I$  with sampling material to contain and measure jets coming from the collisions.

### 3.3.2 Magnets

The magnet system is extremely important for charged particle identification and measuring the momentum of charged particles. ATLAS uses two different magnet systems [163], a central solenoid and an outer toroid system. The solenoid surrounds the inner detector and produces a uniform magnetic field for tracking all charged particles from the collision. The outer toroid has three components, a barrel toroid and two endcap toroids. The toroid magnets are outside the calorimeters and are in place to help track muons.

#### Solenoid

The ATLAS Central Solenoid [164] (CS) provides a uniform axial magnetic field for the inner detector tracking. The CS is a cylinder with an inner diameter of 2.44 m and outer diameter of 2.63 m, and 5.3 m long centered about the IP. It is placed between the tracking system of the inner detector and the electromagnetic calorimeters. The placement before the calorimeters requires the CS to use a minimal amount of materials to ensure less interference with the calorimetry. Outside of the calorimeters, an iron yoke is in place to return the magnetic flux of the solenoid and limit interference with the outer toroid system.

The CS uses NbTi/Cu Rutherford cables as the superconducting material to carry the currents generating the magnetic field, surrounded by pure Al to support the cables. The superconducting cables are indirectly cooled by liquid helium, operating at a temperature of

## CHAPTER 3. THE LHC & ATLAS

4.5 K. Each cable contains 12 superconducting strands, and the cables are pitched 4.5 mm center-to-center. There are 1173 total turns along the length of the CS, corresponding to 9.1 km total length of superconducting cable. The operational load of 7600 A provides 2 T of magnetic field strength throughout the central volume, with a peak field of 2.6 T at the boundary of the CS and a total energy stored in the magnetic field of 38 MJ.

### **Toroid**

The ATLAS toroid system has three components: a barrel toroid [165] (BT) and two endcap toroids [166] (ECTs), to provide the muon spectrometer with a magnetic field for tracking. Each toroid is built of 8 coils using NbTi/Cu superconducting cables, as in the CS. The cables are in a “flat pancake” layout and arrayed in a “race track” configuration winding through the coils. To accommodate the muon spectrometer and give maximum coverage, the toroids feature an open-air design to allow detector chambers to be placed between and inside the coils. The air-core toroids also have much smaller energy loss and multiple scattering for the muons compared to an iron-core magnet system, allowing for a more precise measurement of their momenta.

The BT has an inner radius of 4.72 m and outer radius of 10.04 m with a length of 25.26 m. There are 8 coils, pitched at  $45^\circ$  azimuthally about the beam axis. The BT is shown in Figure 3.9 with the 8-fold symmetry design. Inside the coils there are two “pancakes” of superconducting cables and each pancake contains 2 layers of cables. These cables use the same technology as the CS, surrounding the superconductor with pure Al and indirectly cooling with liquid He down to an operating temperature of 4.5 K. Each pancake wraps 30 times around the racetrack, giving 120 total turns in the coil and 56 km of total length of the superconducting cables. The operating current is 20.5 kA giving a peak field of 3.85 T at the inner surface of the coils. Due to the spacing between the coils, the average

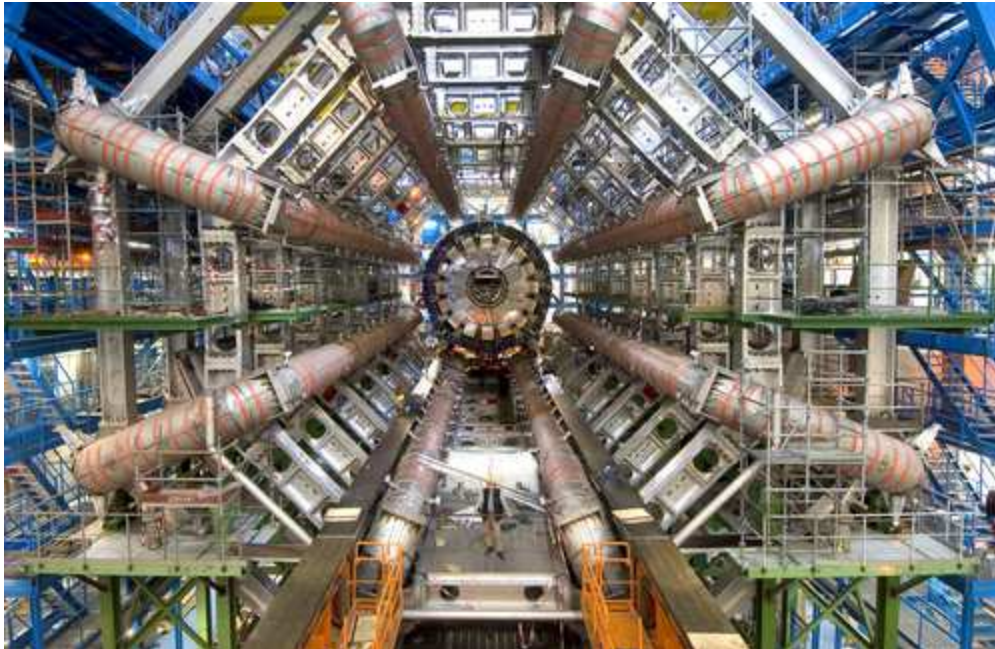


Figure 3.9: The iconic view of the ATLAS detector. This shows the 8-fold azimuthal symmetry of the toroid magnet system, where the 8 coils have orange tape. This also shows the size of the ATLAS detector. ©CERN, from [162].

field throughout the BT is  $\sim 0.6$  T. The figure of merit that determines the total bending of a charged particle, and therefore the resolution of the momentum measurement, is  $\int \vec{B} \times d\vec{\ell}$ . This averages  $\sim 2\text{-}4$  T·m in the barrel. During normal operation the BT has a total stored energy of 1 GJ.

The two ECTs are designed similar to the BT, with 8 coils pitched at  $45^\circ$  azimuthally about the beam axis. The ECTs coils are rotated by  $22.5^\circ$  from the BT coils to allow them to fit between the BT at the ends, and have overlapping magnetic field. The ECTs could have been integrated with the BT for greater uniformity of the field, however for construction purposes and ease-of-access to the inner components of the detector a separate design was adopted. A single ECT has an inner radius of 0.825 m and outer radius of 5.35 m with an axial length of 5 m. Inside the coils the ECTs follows a similar design and operating

procedure as the BT, with two pancakes of superconducting cables, each pancake containing 2 layers of cables, wrapping 29 times around the coil for 116 total turns. At the operating current of 20 kA, the peak field is 4.1 T and this produces an average field of  $\sim 1$  T throughout the ECT. The field integral  $\int \vec{B} \times d\vec{\ell}$  averages  $\sim 4-8$  T·m in the end caps. During normal operation each ECT has a total stored energy of 200 MJ.

### 3.3.3 Inner Detector

The ATLAS Inner Detector [167, 168] (ID) contains three subsystems of high-resolution tracking detectors placed inside the 2 T magnetic field of the central solenoid. The resolution requirements are designed to provide excellent measurements of the momentum of charged particles as well as the positions of the (many) vertices in the LHC environment. The inner two subsystems, a silicon pixel detector and a silicon microstrip detector, use semiconductor technology to achieve the high-granularity needed for these measurements. The innermost subsystem is the Pixel detector with 3 layers in the barrel region. The middle subsystem is the silicon microstrip detector (SCT) with 4 layers in the barrel region. The outer subsystem of the ID is a straw tube tracker (TRT) where charged particles radiate when transitioning between the plastic of the tube and the gas inside. The relatively economical design of the straws allows for a large number of tubes and high hit multiplicity, typically 36 hits per track. The ID must fit inside the CS and LAr cryostat, limiting the size to a maximum outer radius of 1.15 m. The ID is placed inside the calorimeters, so the material budget is minimized to allow for more precise calorimetry and to minimize photon conversions. The ID has a central barrel and two identical endcaps. The barrel is 1.6 m long and is centered at the IP, the endcaps extend the ID to  $\pm 3.5$  m. A schematic of the ID and the three subsystems is shown in Figure 3.10.

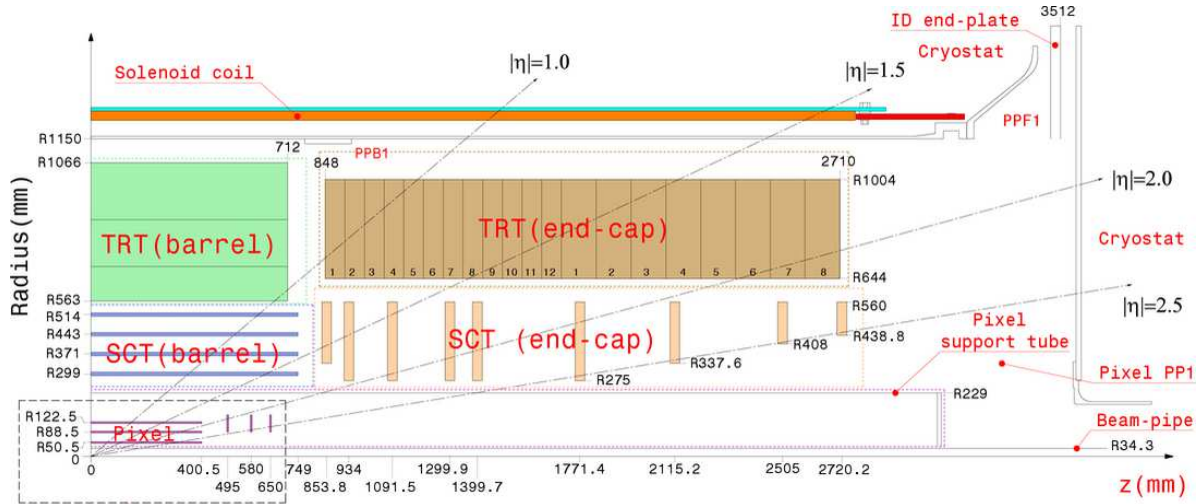


Figure 3.10: The layout of the ATLAS inner detector. From [169].

### Pixel Detector

The Pixel detector [170] is the silicon-based detector that is the closest to the IP. The barrel section has one removable innermost barrel layer 4 cm from the nominal beam axis and two additional barrel layers 10 and 13 cm from the beam axis. The Pixel barrel extends  $\pm 0.4$  m about the nominal IP, giving an  $\eta$  coverage up to  $\pm 1.7$ . The endcap is a set of five disks in the azimuthal plane orthogonal to the beam with an inner radius 11 cm and outer radius 20 cm. The five disks are placed between  $\pm 0.4$  m and  $\pm 0.78$  m, extending the  $\eta$  coverage to 1.7-2.5. The complete Pixel detector totals to 140 million detector elements and  $2.3 \text{ m}^2$  of pixel surface area. Each pixel is  $50 \text{ }\mu\text{m}$  in the  $R\phi$  direction and  $300 \text{ }\mu\text{m}$  in the  $z$  direction. Most tracks will have 3 or 4 pixel layer hits, and the resolution for each layer is  $12 \text{ }\mu\text{m}$  in the  $R\phi$  direction and  $66 \text{ }\mu\text{m}$  in the  $z$  direction. The three layers of the Pixel detector are the dominant contribution to the resolution of the track impact parameters for outgoing particles and their performance is crucial in tagging separated vertices for  $b$ - and  $\tau$ -physics.

The Pixel detector is modular, with 1500 barrel modules and 700 endcap modules using

## CHAPTER 3. THE LHC & ATLAS

similar layouts and identical readout chips. Each readout chip contains the amplifier and buffering for the trigger readout, serving  $24 \times 160$  pixels, and each is directly bump-bonded onto the substrate. A single barrel module is 62.4 mm long by 22.4 mm wide and has 61440 pixel elements with 16 readout chips. The support structure and readout electronics constitute only  $\sim 0.1$ - $0.2$  radiation lengths of material except in the services region around  $\eta \sim \pm 1.7$ . Due to the proximity to the IP, the Pixel detector must be radiation hard. The readout chips are the most susceptible to the high-radiation environment. At peak luminosity operations they are expected to receive 30 kGy of ionizing radiation and  $5 \times 10^{13}$  neutrons per  $\text{cm}^2$  per year. Special design and materials are needed to ensure proper operations.

### Semiconductor Tracker

The Semiconductor Tracker (SCT) is a silicon microstrip-based detector and is the middle subsystem of the ID. The central part of the SCT consists of 4 barrel layers placed at radii of 30.0, 37.3, 44.7, and 52.0 cm from the nominal beam axis, extending  $\pm 80$  cm in  $z$  giving an  $\eta$  coverage of  $\pm 1.4$ . The two identical endcaps of the SCT have 9 disks in the azimuthal plane perpendicular to the beam axis, placed from 80 to 280 cm along the beam axis. The disks have an outer radius of 56.0 cm and inner radii varying from 26.0 cm for the disks closest to the IP to 43.9 cm for the disk furthest from the IP. The  $\eta$  coverage for the SCT endcaps extends from 1.4-2.5. Figure 3.10 show the barrel layers aligned with the beam axis and the endcap disks surrounding the beam facing the IP. Each microstrip detector is 6.36 cm  $\times$  6.40 cm, and the strips have a pitch width of 80  $\mu\text{m}$ . The SCT totals to 61.1  $\text{m}^2$  of silicon surface area and 6.2 million readout channels. A typical track will have  $\sim 8$  SCT layer hits, and the resolution for each layer is 16  $\mu\text{m}$  in the  $R\phi$  direction and 580  $\mu\text{m}$  in the  $z$  direction.

An SCT barrel module has four microstrip detectors joined together. Two individual microstrip detectors are bonded together to form a 12.8 cm long device, and these are glued

## CHAPTER 3. THE LHC & ATLAS

back-to-back to a heat sink and support plate. The strips are glued at a 40 mrad pitch angle to allow for separation in the  $z$  direction. The endcaps use strips arranged both azimuthally and radially, and feature a tapered strip size to accommodate the geometry of the disks. The modules are mounted on a carbon-fiber support frame to limit the total material budget, which adds up to  $\sim 0.1$ - $0.2$  radiation lengths. With the additional separation from the IP, the radiation doses for the detectors and readout electronics is reduced by a factor of 3-5.

### Transition Radiation Tracker

The Transition Radiation Tracker (TRT) is the outer subsystem of the ID and uses many gas-filled straw tubes to provide a near-continuous tracking measurement. The plastic straw tubes and gas mixture allow for a high number of track hit measurements at a relatively lower cost. The TRT uses small-diameter tubes to reduce occupancy and handle the high rates in the LHC environment. Each straw is 4 mm in diameter and has a  $30\ \mu\text{m}$  wire to readout tracking hits. The straws are filled with a gas mixture of 70% Xe, 27%  $\text{CO}_2$ , and 3%  $\text{O}_2$ . For each straw there are two read out hits from a passing charged particle: the low-threshold drift time of the ionized charged passing through the gas and the high-threshold hit associated with the transition radiation (TR) of a charged particle passing between the plastic straw and gas mixture. The low-threshold ionization hits typically deposit  $\sim$ few-hundred eV of energy, while a high-threshold TR hit deposits  $\sim$ few keV of energy. The drift time allows for a spatial resolution of  $170\ \mu\text{m}$  per straw, while the TR hits allows for particle identification. Straws with hits that do not match the expected TR for the track are called “outliers”.

The barrel of the TRT has an inner radius of 0.56 m and outer radius of 1.07 m and extends to  $\pm 0.8$  m along the beam axis, giving an  $\eta$  coverage up to  $\pm 0.7$ . In the barrel there are 50000 straws each split in two at the middle plane  $\eta = 0$  to reduce occupancy. The

## CHAPTER 3. THE LHC & ATLAS

tubes are arranged parallel to the beam in layers of constant radii with between 329 and 793 straw tubes per layer, and a typical barrel track will have 36 tube hits. The endcaps have 18 wheels of tubes, with the tubes arranged radially. The endcap extends the axial coverage from 0.8 m to 3.4 m, increasing the  $\eta$  coverage to 0.7-2.5. The first 14 endcap wheels have an inner radius of 0.64 m and outer radius of 1.03 m, with the first 7 wheels have twice as many straw tubes as the second 7 wheels to keep the number of tube hits approximately constant as a function of  $\eta$ . The last 4 wheels have an inner radius of 0.48 m to extend the endcap  $\eta$  coverage. See Figure 3.10 for the layout of the TRT with respect to the beam and other ID components.

The rates at which the straws can be readout depends on the type of hit. The standard low-threshold drift time can be measured at a rate of 20 MHz, although the efficiency of a single tube falls to 60% at this high rate. The high-threshold TR hit deposits much more energy and can be measured at a rate of 1 MHz. The readout times lead to high straw hit occupancy of  $\sim 0.4$  for the inner barrel layers at the nominal luminosity. The high occupancy require special gating for the readout electronics to allow for more efficient tube operations.

### 3.3.4 Electromagnetic Calorimeter

The electromagnetic calorimeter [171, 172] (ECAL) is designed to measure the energy of electrons and photons coming from the collisions and decaying particles. It is a sampling calorimeter covering the pseudo-rapidity range  $|\eta| < 3.2$ , split into a barrel and two identical endcaps. The ECAL uses lead as the absorbing material and liquid argon (LAr) as the ionizing detector in an accordion structure for full azimuthal coverage and high granularity. The readouts only need to be placed at the front and back of the detector. The ECAL is placed outside the central solenoid, with an inner radius of 1.15 m and outer radius of



## CHAPTER 3. THE LHC & ATLAS

2.25 m. The layout and placement of the ECAL is shown in Figure 3.11. Because of the detectors, support structure, and electronics totaling to  $\sim 2.3X_0$  between the ECAL and the IP, a presampler is placed after the central solenoid to estimate the energy loss due to this material. Due to the large amount of material for the cooling, vacuum, and electronic readouts for the ID and calorimeter services, the space around  $z = \pm 3.4$  m is not usable for physics analysis, corresponding to a “crack” in coverage at  $1.37 < |\eta| < 1.52$ .

### Barrel

The ECAL barrel is 6.8 m long split into two identical half-barrels, centered about the IP with a small gap of 6 mm at  $\eta = 0$ , and has pseudo-rapidity coverage up to  $|\eta| < 1.475$ . The presampler at a radius of 1.15 m covers up to  $|\eta| < 1.5$ . The barrel accordion shape radiates outward from the beam axis. The accordion design is shown in Figure 3.11. The lead absorber plates have a thickness of 1.5 or 1.1 mm for  $|\eta| < 0.8$  or  $|\eta| > 0.8$ , with a constant LAr gap of 2.1 mm. Between layers is a Cu/kapton electrode with high voltage to read out the ionization from the showering particles, with 101,760 channels total plus 7808 channels for the presampler. The granularity of the ECAL in the different  $\eta$  regions is listed in Table 3.1. The design is to ensure a consistent amount of material crossed by the incoming particles as a function of  $\eta$ . The barrel has 3 sampling layers plus the presampler. At  $\eta = 0$ , the first layer is  $4.3 X_0$ , the second layer is  $16 X_0$ , and the third layer is  $2.0 X_0$ . The presampler is a single layer of LAr and electrodes. The total amount of material for the ECAL barrel is  $24 - 35 X_0$ , growing with  $\eta$ .

### Endcap

The ECAL endcaps are split into two parts: a precision physics outer wheel with coverage  $1.375 < |\eta| < 2.5$  and a more coarsely grained inner wheel (forward calorimeter) between

CHAPTER 3. THE LHC & ATLAS

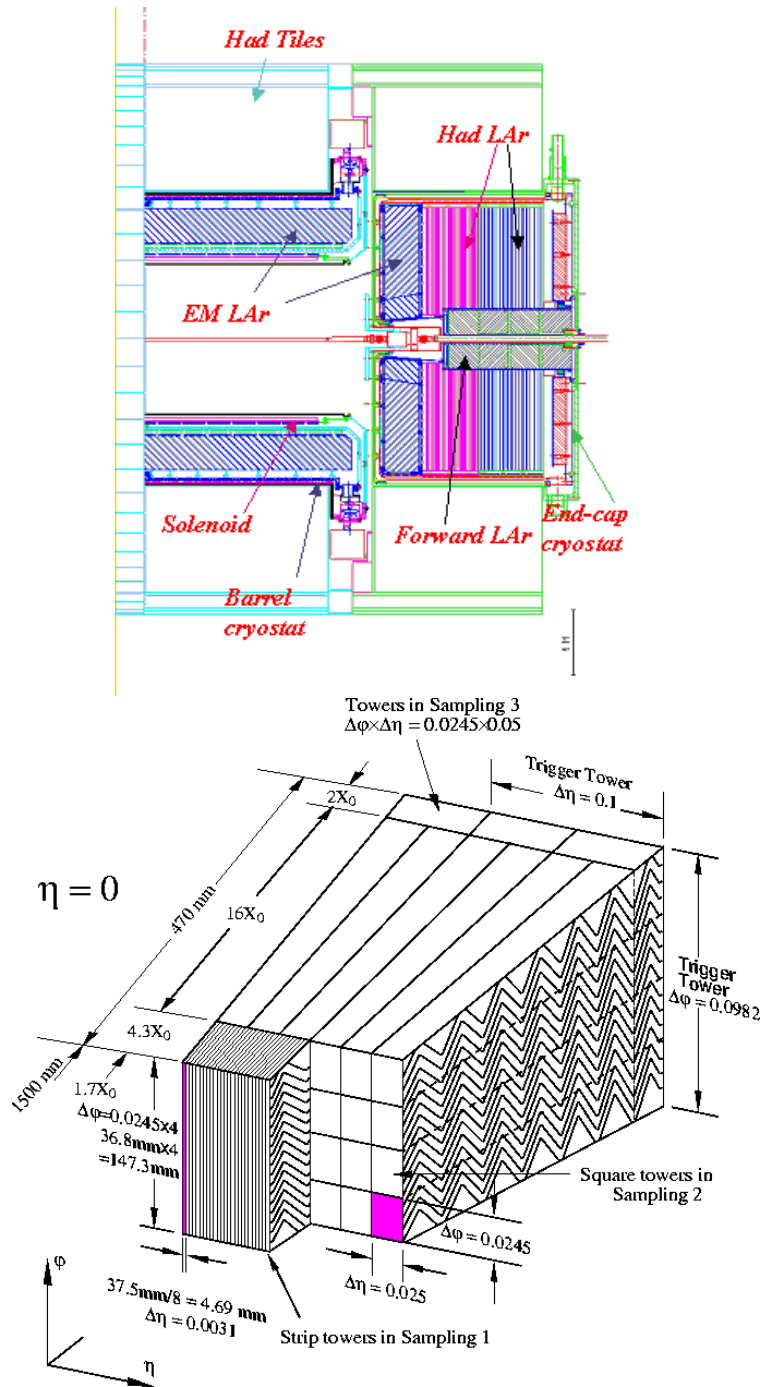


Figure 3.11: Top: layout of the ATLAS Liquid Argon calorimeter. Bottom: the sampling tower structure of the barrel ECAL. The strip towers show the granularity of the three layers in the ECAL. From [173].

CHAPTER 3. THE LHC & ATLAS

EM Calorimeter	Barrel	Endcap
Coverage	$ \eta  < 1.475$	$1.375 <  \eta  < 3.2$
Longitudinal segmentation	3 samplings	2 samplings      1.375 < $ \eta $ < 1.5
		3 samplings      1.5 < $ \eta $ < 2.5
		2 samplings      2.5 < $ \eta $ < 3.2
Granularity	$(\Delta\eta \times \Delta\phi)$	$(\Delta\eta \times \Delta\phi)$
Sampling 1	$0.003 \times 0.1$	$0.025 \times 0.1$ 1.375 < $ \eta $ < 1.5
		$0.003 \times 0.1$ 1.5 < $ \eta $ < 1.8
		$0.004 \times 0.1$ 1.8 < $ \eta $ < 2.0
		$0.006 \times 0.1$ 2.0 < $ \eta $ < 2.5
		$0.1 \times 0.1$ 2.5 < $ \eta $ < 3.2
		$0.1 \times 0.1$ 2.5 < $ \eta $ < 3.2
Sampling 2	$0.025 \times 0.025$	$0.025 \times 0.025$ 1.375 < $ \eta $ < 2.5
		$0.1 \times 0.1$ 2.5 < $ \eta $ < 3.2
Sampling 2	$0.05 \times 0.025$	$0.05 \times 0.025$ 1.375 < $ \eta $ < 2.5
Presampler	Barrel	Endcap
Coverage	$ \eta  < 1.52$	$1.5 <  \eta  < 1.8$
Longitudinal segmentation	3 samplings	2 samplings
Granularity	$0.025 \times 0.1$	$0.025 \times 0.1$

Table 3.1: Pseudo-rapidity coverage, granularity, and longitudinal segmentation of the ECAL and Presampler. From [160], Table 1-3.

$2.5 < |\eta| < 3.2$ . The geometry of the accordion design is more complicated to ensure uniformity of material crossed. The lead absorber plates have a thickness of 1.7 or 2.2 mm for  $1.375 < |\eta| < 2.5$  or  $2.5 < |\eta| < 3.2$ . The amplitude of the accordion waves increases with radius, so the LAr gap increases in depth from 0.9 to 2.8 mm and 1.8 to 3.1 mm. There are 62,208 channels to read out for both endcaps, with an additional 1536 channels for the presampler before  $|\eta| < 1.8$ . The total amount of material for an ECAL endcap is 26 - 38  $X_0$ , growing with  $\eta$ . See Figure 3.11 for the endcap layout and Table 3.1 for the coverage and granularity of the calorimeter.

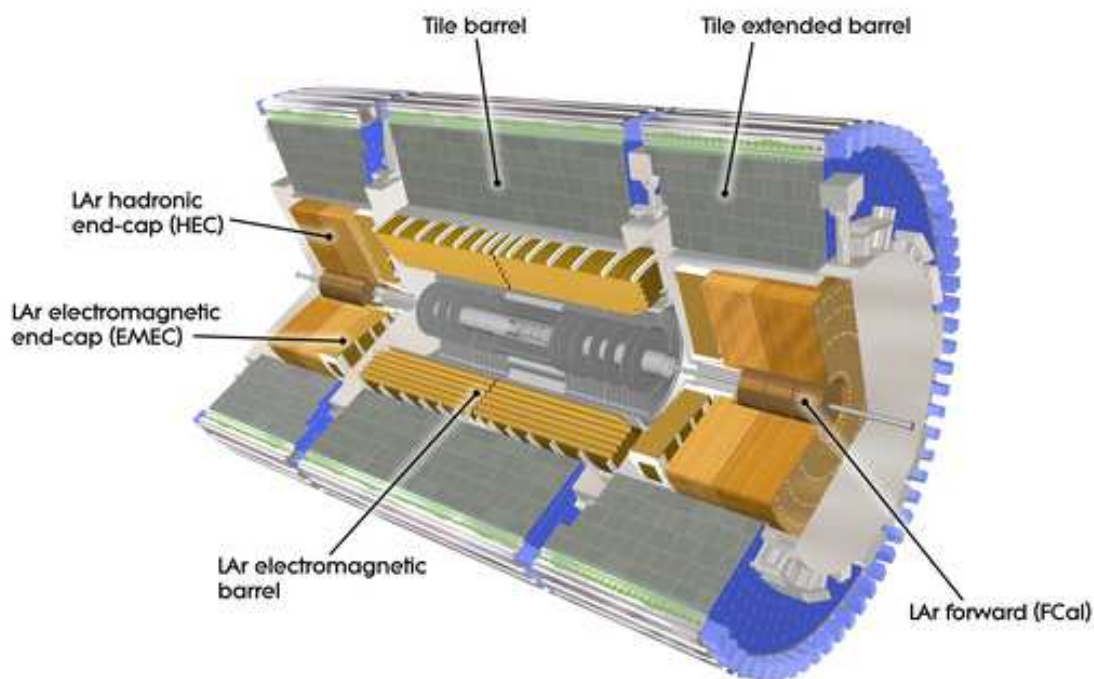


Figure 3.12: The ATLAS calorimeters including the hadronic tile calorimeter barrel and extended barrel sections, and the endcap and forward LAr calorimeters. From [162], ©CERN.

### 3.3.5 Hadronic Calorimeter

The hadronic calorimeter [171, 174] (HCAL) is designed to measure the energy of particles that are bound states of quarks and gluons. Because these particles interact with the strong force, they behave differently than the electrons and photons that shower in the ECAL. The HCAL is a sampling calorimeter covering the pseudo-rapidity range  $|\eta| < 4.9$ , split into a barrel, an extended barrel, two endcaps, and two forward calorimeters. In the barrel, the HCAL uses a tile design with iron absorbing plates and scintillating tiles. The endcap and forward calorimeters use either a copper or lead absorbing material with LAr as the scintillating material.

## Barrel

The HCAL barrel has two parts: a central barrel with  $\eta$  range up to  $|\eta| < 1.0$  and two extended barrels up to  $0.8 < |\eta| < 1.7$ . These extend from an inner radius of 2.28 m to an outer radius of 4.23 m. Figure 3.12 shows the layout of the HCAL barrel and endcaps with respect to the ID and ECAL. The materials used are iron tiles as the absorber and scintillating tiles. Both sets of tiles are 3 mm thick, stacked perpendicular to the beam axis and staggered over the three sampling regions. The structure is periodic in  $z$ , with the staggering increasing with  $z$  to scale with  $\eta$ . The scintillating tiles are read out by a wavelength shifting (WLS) guide into photo-multiplier tubes (PMTs). The three segmented layers are 1.4, 4.0, and 1.8  $\lambda_I$  deep at  $\eta = 0$  and growing with  $\eta$ . The total amount of material before the HCAL grows with  $\eta$  from 1.8 to 2.5  $\lambda_I$ , and the total amount of material before the muon spectrometer increases with  $\eta$  but is always greater than 11  $\lambda_I$ . The larger granularity in the HCAL means fewer channels to be read out compared to the ECAL, with 10,000 channels in the barrel.

There is a gap of 68 cm between the barrel and the extended barrel to allow for cabling, cooling, vacuum, and other ID or CS services. The extended barrel has the same segmentation structure as the barrel in the azimuthal direction, but varies in the radial direction to maintain uniform granularity in  $\eta$ - $\phi$ . See Table 3.2 for the coverage and granularity of the HCAL. To compensate for the gap between the two barrel components, an Intermediate Tile Calorimeter (ITC) is fit between them. The ITC has 2 sampling sections, starting at the outer radius moving inwards. The outer section is 31 cm thick and extends 45 cm toward the interior. The inner section is 9 cm thick and extends an additional 45 cm toward the beam axis. In addition to these two sampling sections, a scintillating tile is extended down the rest of the face of the extended barrel calorimeter to measure the losses due to the material

CHAPTER 3. THE LHC & ATLAS

Hadronic Calorimeter	Barrel	Extended Barrel
Coverage	$ \eta  < 1.0$	$0.8 <  \eta  < 1.7$
Longitudinal segmentation	3 samplings	3 samplings
Granularity ( $\Delta\eta \times \Delta\phi$ )		
Samplings 1 and 2	$0.1 \times 0.1$	$0.1 \times 0.1$
Sampling 3	$0.2 \times 0.1$	$0.2 \times 0.1$
Hadronic LAr		Endcap
Coverage		$1.5 <  \eta  < 3.2$
Longitudinal segmentation		3 samplings
Granularity ( $\Delta\eta \times \Delta\phi$ )		
		$0.1 \times 0.1$ $1.5 <  \eta  < 2.5$
		$0.2 \times 0.2$ $2.5 <  \eta  < 3.2$
Forward Calorimeter		Endcap
Coverage		$3.1 <  \eta  < 4.9$
Longitudinal segmentation		3 samplings
Granularity ( $\Delta\eta \times \Delta\phi$ )		$\sim 0.2 \times 0.2$

Table 3.2: Pseudo-rapidity coverage, granularity, and longitudinal segmentation of the Hadronic calorimeters. From [160], Table 1-3.

in the services region. The total  $\eta$  coverage of the ITC is from  $1.0 < |\eta| < 1.6$ . The total material in the extended barrel region ranges from 10-15  $\lambda_I$ .

### Endcap

The HCAL endcaps have two parts: a standard LAr calorimeter between  $1.5 < |\eta| < 3.2$  and a high-density forward LAr calorimeter (FCAL) from  $3.2 < |\eta| < 4.9$ . Their coverage and granularity is listed in Table 3.2. The LAr endcaps are divided into two wheels that are stacked back-to-back in  $z$ . The inner wheel uses 25 mm thick copper plates with a LAr gap of 8.5 mm. This is divided into two readout segments of 8 and 16 layers deep. The outer wheel has 50 mm thick copper plates and a LAr gap of 8.5 mm in one readout segment of 16 layers. This makes up about 12  $\lambda_I$  of material, and is quite uniform in  $\eta$ .

The FCAL starts at  $z = 4.6$  m from the nominal IP, and is just 8 cm from the beam axis. This is a very high-radiation environment, but is required to find far-forward jets and fully account for all the energy in a collision. This is segmented into three sections: the first uses copper absorbing plates and the other two use tungsten plates. The plates are drilled with holes and have slightly smaller diameter copper rods inserted and set at positive high voltage. The channels between the absorbing medium and rods are filled with LAr and are spaced just 250, 375, and 500  $\mu\text{m}$  for the first, second, and third layers. As there are no detectors behind the FCAL the total absorbing material is less important than the other parts of the HCAL, and the total material is about  $9 \lambda_I$ . In total, there are 3,584 channels to be read out from both FCALs.

### 3.3.6 Muon Spectrometer

The ATLAS Muon Spectrometer [175] has two parts: a barrel region for the central region  $|\eta| < 1.0$  and two endcap regions extending from  $1.0 < |\eta| < 2.7$ . The detector design is to track muons passing from the inner detectors and calorimeters through the outer toroidal field. Using two types of precision chambers, the bending of the tracks can be measured to determine the muon's momenta. The chambers are placed into layers (also called stations), and the 8-fold azimuthal symmetry of the toroids dictates a 16-fold symmetry of the chambers in each layer, half that line up azimuthally with the coils and half that are spaced between the coils. The chambers lined up with the coils are small chambers (S chambers), and the chambers lined up between the coils are large chambers (L chambers). Chambers are designated Barrel (B chambers) and Endcap (E chambers), and placed either Inner (I chambers), Middle (M chambers), or Outer (O chambers). The layout of the barrel chambers in this pattern is shown in the upper portion of Figure 3.13. The lower part of Figure 3.13

### CHAPTER 3. THE LHC & ATLAS

shows the layer structure in both the barrel and endcaps for the large and small sectors. There are also trigger chambers used to accept both low- and high-energy muon events as well as to measure the non-bending ( $\phi$ ) coordinate.

In the barrel region the precision measurements are done by monitored drift tubes (MDTs), arranged in three layers in concentric cylinders about beam axis. The first layer is placed inside the barrel toroid coils (BIS/BIL chambers) at a radius of  $\sim 5$  m; the second is placed in the middle of the coils (BMS/BML chambers) at a radius of  $\sim 7.5$  m; and the third is placed outside the coils (BOS/BOL chambers) at a radius of  $\sim 10$  m. In the region about the “feet” of the ATLAS detector where the support structure for the inner detectors and calorimeters is placed, special chambers (BIM,BIR chambers) are put in to ensure full coverage. This arrangement provides three precision tracking points along the  $z$  coordinate to fit the bending of the measured muon track. The groups of chambers that a muon would pass through coming from the IP form a projective tower. They are aligned using an optical system with lasers and CCD cameras with video pixel targets and readouts to measure the relative positions of the chambers in a tower to a precision of  $50 \mu\text{m}$ . The alignment precision determines how well the muon track’s bending radius is measured. The total bending depends on the total magnetic field a muon travels through, which is shown in Figure 3.14.

The endcap regions have two types of precision chambers arranged into wheels in the  $r$ - $\phi$  plane. They are principally covered by MDTs, except in the region  $|\eta| > 2.0$  for the inner layer where cathode strip chambers (CSCs) are used due the higher particle rates. The occupancy of MDTs would be unacceptably high. The inner layer or “small wheel” is placed inside the endcap toroid (EIS,EIL chambers) at  $z = \pm 7$  m; the middle layer or “large wheel” is placed outside the endcap toroid (EMS,EML chambers) at  $z = \pm 14$  m; and the outer layer or “outer wheel” is placed on the cavern walls (EOS,EOL chambers) at  $z = \pm 21$ - $23$  m. These stations provide the typical three precision tracking points in the  $\eta$ -region  $1.3 < |\eta| < 2.7$ ,



CHAPTER 3. THE LHC & ATLAS

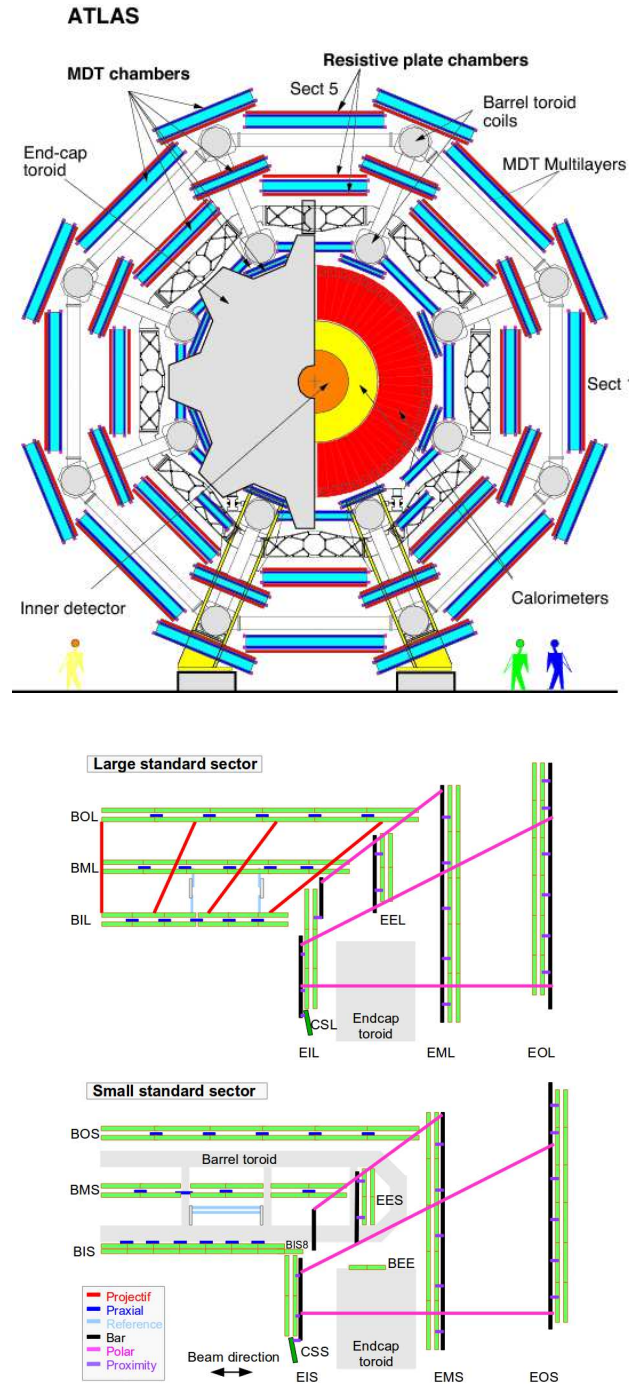


Figure 3.13: The ATLAS muon spectrometer. Top: Azimuthal view showing the 8-fold symmetry and Large/Small sector differences. Bottom: “Quarters” view in the  $r$ - $z$  plane for both the Large and Small sectors. From [175].

## CHAPTER 3. THE LHC & ATLAS

measuring the muon  $r$  coordinate. Due to the size limitation of the outer wheel, extra endcap chambers (EES,EEL chambers) are placed about the endcap toroids at  $z = \pm 10$  m. These chambers provide coverage in the “transition region”  $1.0 < |\eta| < 1.4$  between the barrel toroid and endcap toroid’s magnetic fields. The relative alignment is also done by an optical system.

The trigger chambers perform three functions: high-speed timing to assist in bunch-crossing identification, simple triggering methods with well-defined  $p_T$  cutoffs, and measuring the second coordinate  $\phi$ . In the barrel region, three layers of resistive plate chambers (RPCs) are arranged with one layer attached to the inside and one outside of the BM chambers and the third layer attached to the inside of the BO chambers. In the endcap regions, three layers of thin-gap chambers (TGCs) are arranged with one layer attached inside the EM chambers and two layers spaced outside the EM chambers.

### Monitored Drift Tubes

The largest number of precision chambers in the muon spectrometer are monitored drift tubes. These are aluminum tubes with  $400 \mu\text{m}$  thick walls, 30 mm diameter, with a  $50 \mu\text{m}$  diameter tungsten-rhenium wire at the center. The single-tube position resolution is  $\sim 80 \mu\text{m}$  based on drift-time readout. The tubes are grouped into chambers. Each chamber is formed from monolayers of tubes glued together and stacked up into multilayers. The inner chambers (BI,EI) have  $4 \times 2$  monolayers glued together, while the middle and outer chambers have  $3 \times 2$  monolayers. The two sets of multilayers are mounted on opposite sides of a rigid support structure. The glueing and structure support can accurately position the tubes in a single chamber up to  $\sim 10\text{-}15 \mu\text{m}$  depending on the size of the structure. Each chamber has a set of optical alignment equipment to monitor any deformations of the chamber itself with respect to normal. The gas mixture is 93% Ar and 7%  $\text{CO}_2$ , at 3 bar of pressure. The tubes

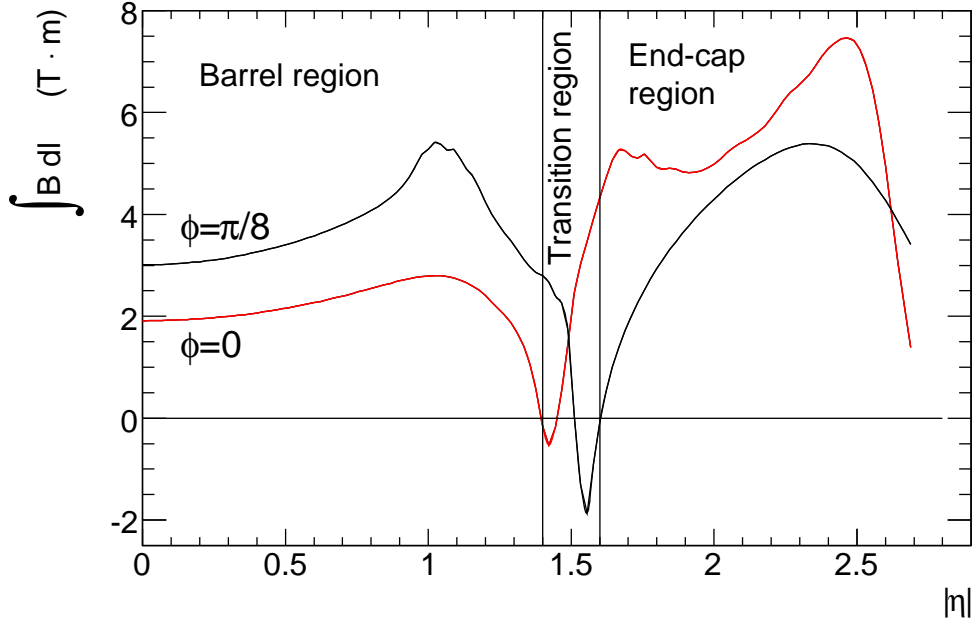


Figure 3.14: The total bending power of the ATLAS muon spectrometer toroidal field in the different  $\eta$  regions. In the barrel ( $|\eta| < 1.05$ ), the red curve corresponds to the Large sectors and the black curve to the Small sectors. In the endcaps ( $|\eta| > 1.05$ ), the red curve corresponds to the Small sectors and the black curve to the Large sectors. From [175].

are read out from one end with a current-sensitive preamplifier, followed by a differential amplifier, shaping amplifier and discriminator. The shaping amplifier also corrects the drift-time measurement using the integrated signal. There are 1194 total MDT chambers and 370,000 total readout channels, covering 5500 m<sup>2</sup> of area and containing 800 m<sup>3</sup> of gas.

### Cathode Strip Chambers

The other precision chambers are cathode strip chambers in the inner layer of the endcaps. These are multi-wire proportional chambers with cathode strip readout. The cathode-anode strip spacing is equal to the anode wire pitch. The readout strips are aligned orthogonal to the anode wires. Position is measured from the charge induced on the cathode strips due

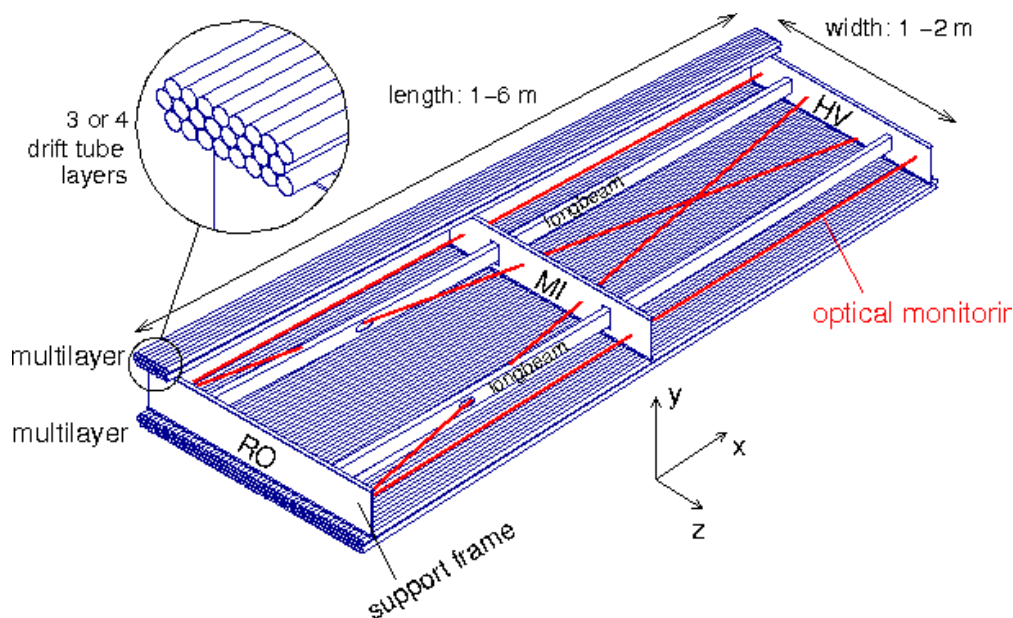


Figure 3.15: A layout of a typical MDT chamber for the muon system showing the layers of tubes, support structure, and alignment sensors. From [176].

to the charge avalanche formed by the ionization trail of a muon on the anode wire. The spatial resolution is improved by interpolating the charge sharing between cathode strips. The anode wire pitch is 2.54 mm and the cathode readout strips are 5.08 mm apart. The second coordinate is measured from cathode strips aligned parallel to the anode wires, which also form the second anode of the chamber. The chambers are arranged in  $4 \times 2$  layers, the same as the other EI MDT chambers. The gas mixture used is 30% argon, 50% carbon dioxide, and 20% carbon tetrafluoride. The fast drift times of the CSC (30 ns) allow for them to be used as part of the trigger system. The readout is a charge preamplifier into analog storage, which is used in the level-1 trigger. There are 32 total CSC chambers and 67,000 total readout channels, covering 27 m<sup>2</sup> of area and containing 1.1 m<sup>3</sup> of gas.

### Resistive Plate Chambers

The barrel trigger chambers are resistive plate chambers (RPC) with timing resolution of 1.5 ns. They are placed around the MDT chambers in the barrel, as shown in Figure 3.16. There are two parallel high-resistance bakelite plates 2 mm thick, separated by 2 mm with insulating polycarbonate spacers. There is a gas mixture of tetrafluoroethane between the plates, with some sulfur hexafluoride to allow for lower operating voltages. There are no wires in the design, which allows for a simple structure and manufacture. Between the two plates, a 4.5 kV/mm uniform electric field is applied via graphite electrodes painted onto the backs of the plates. Ionizing electrons form avalanches between the plates, which is detected by capacitively-coupled strips outside the two plates. There are two sets of strips: one set of  $\eta$  strips in the bending plane, and one set of  $\phi$  strips pitched between 30.0 and 39.5 mm. A complete chamber has two detector layers and four sets of readout strips. There are 596 RPC chambers and 355,000 total readout channels covering 3650 m<sup>2</sup> of area. The geometrical coverage of the barrel is about 80% of the total area.

### Thin Gap Chambers

The endcap trigger chambers are thin gap multiwire proportional chambers (TGCs). They are placed around the MDT and CSC chambers in the endcap, as shown in Figure 3.16. The anode wires are pitched 1.8 mm apart, further than the spacing between the cathode strips of 2.8 mm. The anode wires are arranged parallel to the MDT wires in the bending plane and provide the readout for the trigger information. The cathode strips are arrayed orthogonally to the wires and measure the second  $\phi$  coordinate. The gas mixture used is 55% carbon dioxide and 45% *n*-pentane ( $n\text{-C}_5\text{H}_{12}$ ), which is highly quenching to prevent streamers but is also flammable and demands adequate safety precautions. The applied voltage is 3.1 kV,

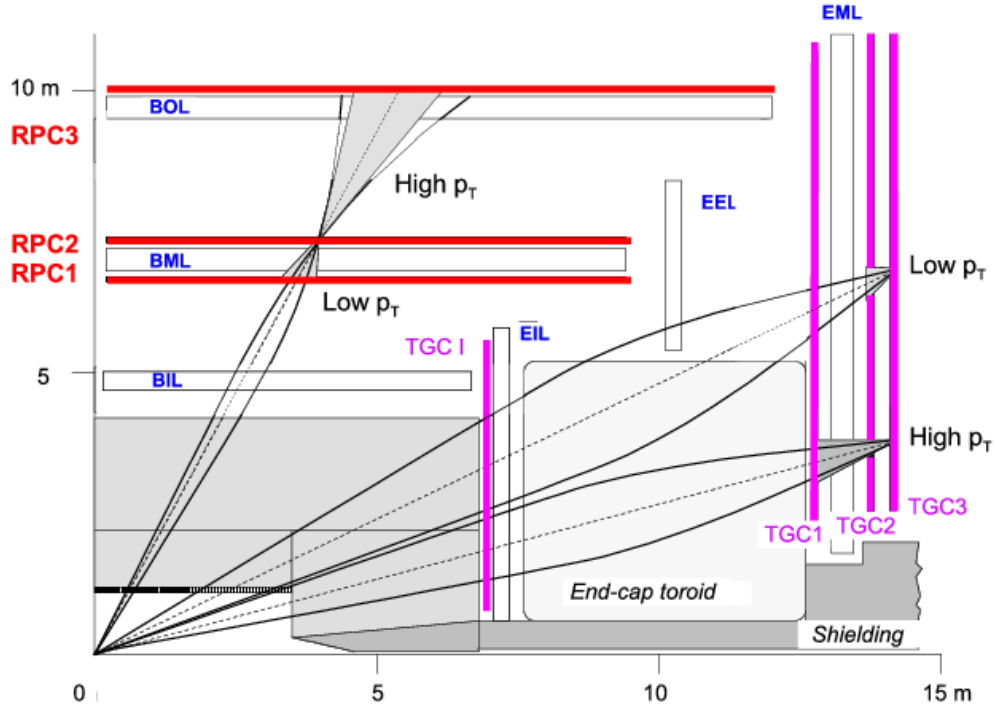


Figure 3.16: ATLAS muon trigger chambers, showing the typical trajectories of low- and high- $p_T$  muons. From [177].

with a uniform electric field and small wire spacing to ensure short drift times. The TGCs are formed in doublets and triplets, with either two or three anode wire sets sandwiched between 20 mm thick honeycomb spacers and graphite cathode strips. There are 192 TGC chambers and 440,000 total readout channels covering 2900 m<sup>2</sup> of area. The geometrical coverage of the endcap is about 99% of the total area.

### 3.4 Acceptance & Reconstruction at ATLAS

The detectors described above work together to reconstruct all the outgoing stable particles produced after the initial collision. A trigger is employed to select events that pass certain

criteria and then save those events for later analysis. After the event has been saved to long-term data storage, offline reconstruction begins. Offline reconstruction employs a variety of algorithms to reconstruct what types of particles and their the energy and momenta were produced in an event as precisely as possible. This “reprocessed” data is then used for analyses. This section covers how the events are selected with a trigger menu, then discusses how electrons and muons, the two objects used in the search for new physics in this thesis, are reconstructed from the detector information.

### 3.4.1 Trigger

The trigger system is based on three levels to perform event selection for long-term data storage and analysis [178]. The total nuclear cross section is  $\sim 100$  mbarn at LHC energies [179]. At the LHC luminosity there are  $\sim 7 \times 10^8$  interactions per second. Each event uses 1.5 MB of information to store the hit information from all the sub-detectors. The total data acquisition rate can only accept about 600 MB/s, or  $\sim 400$  Hz of events from the different detectors, and therefore a rejection factor of  $\sim 2 \times 10^6$  is needed. Most of the interactions are ‘minimum-bias’ events, either elastic scattering or soft QCD processes, which can be ignored in the search for new physics and other less-common SM processes. The three levels of the trigger are the level-1, level-2, and event filter, where the level-2 and event filter are together called the high-level trigger. A trigger chain is one selection sequence from level-1 through the event filter triggers. The trigger menu is the full set of trigger chains, including their pre-scaling factors. A typical trigger menu has  $\sim 500$  chains and is decided before data taking begins. The most common sets of triggers for the 2012 data taking runs are shown in Table 3.3. Approximately 35% of the readout bandwidth is used by the electron/photon triggers, and an additional 25% is used by the muon triggers.

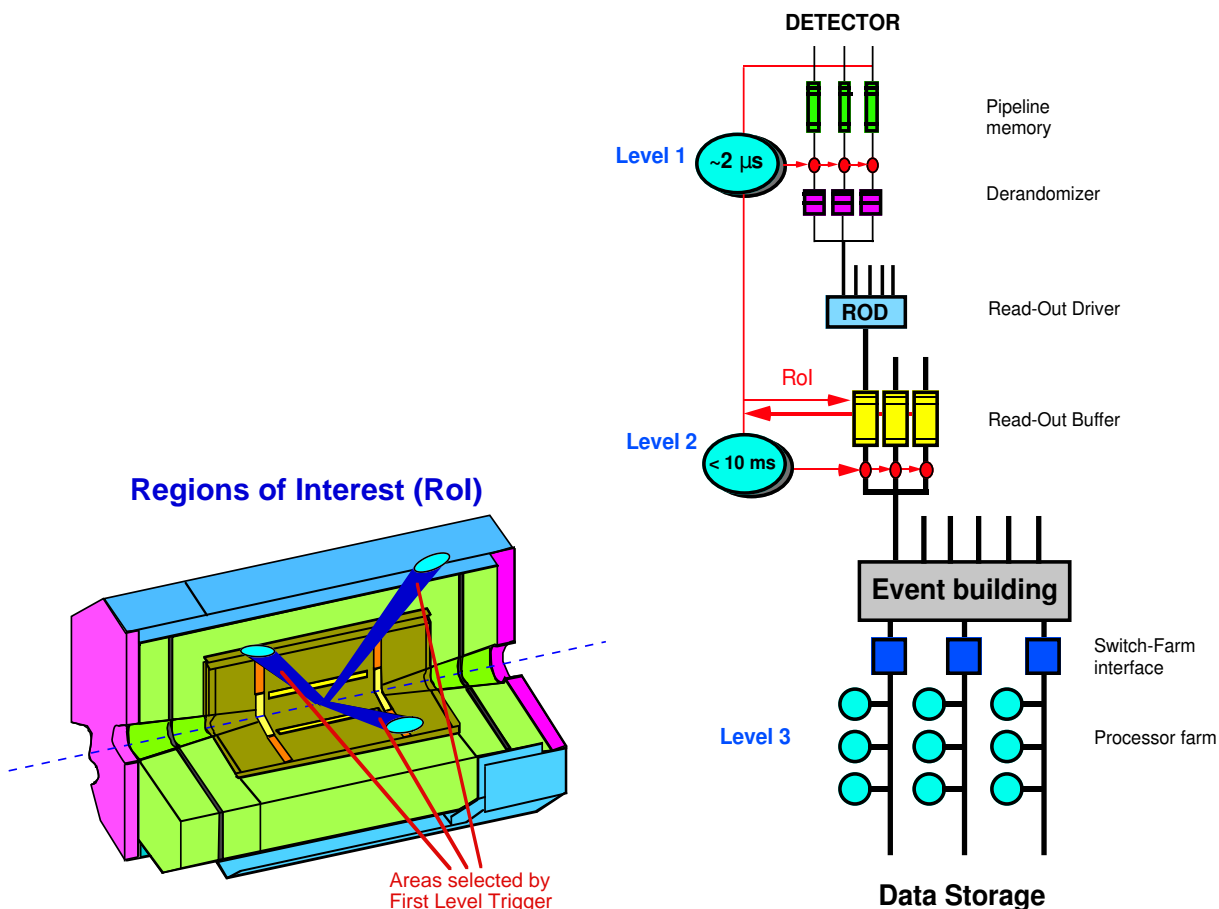


Figure 3.17: Left: How the trigger determines the Regions of Interest in an event, by singling out the region(s) that meet the LVL1 trigger threshold in the calorimeters or muon spectrometer. Right: Data acquisition at ATLAS, showing the data flow through the three trigger stages and event readout. Level 3 is the event filter stage described in the text. From [178].

The remaining 40% use hadronic triggers in some fashion, such as jets, MET, taus,  $b$ -physics, etc.

The level-1 trigger (LVL1) makes a course-grained initial selection after finding one or more Region-of-Interest (RoI), shown in Figure 3.17, in an  $\eta$ - $\phi$  cone within the calorimeters or muon spectrometer. The RoI can come from energy deposited in the ECAL or HCAL,



Trigger Type	Offline Selection	LVL1	EF	LVL1 Peak (kHz)	EF Ave (Hz)
Single Lepton	Single Muon, $p_T > 25$ GeV	15 GeV	24 GeV + Iso	8	45
	Single Electron, $p_T > 25$ GeV	18 GeV	24 GeV	17	70
Two Leptons	Di-Muon, $2 \times p_T > 15$ GeV	$2 \times 10$ GeV	$2 \times 13$ GeV	1	5
	Di-Muon, $p_T > 20, 10$ GeV	15 GeV	18,8 GeV	8	8
	Di-Electron, $2 \times p_T > 15$ GeV	$2 \times 10$ GeV	$2 \times 12$ GeV	6	8
	Di-Tau, $p_T > 45, 30$ GeV	15,11 GeV	29,20 GeV	12	12
Two Photons	Di-Photon, $2 \times p_T > 25$ GeV	$2 \times 10$ GeV	$2 \times 20$ GeV	6	10
	Di-Photon (loose), $p_T > 40, 30$ GeV	16,12 GeV	35,25 GeV	6	7
Single Jet	Jet, $E_T > 360$ GeV	75 GeV	360 GeV	2	5
Multi-Jet	5 jets, $5 \times E_T > 55$ GeV	$4 \times 15$ GeV	$5 \times 55$ GeV	1	8
<i>b</i> -Jets	<i>b</i> tag + 3 jets, $3 \times E_T > 45$ GeV	$4 \times 15$ GeV	$4 \times 45$ GeV + <i>b</i> -tag	1	4
MET	MET $> 360$ GeV	40 GeV	80 GeV	2	17
TOTAL				$< 75$	$\sim 400$

Table 3.3: The most common unprescaled trigger menu chains for 2012 data taking. From [178], Slide 19.

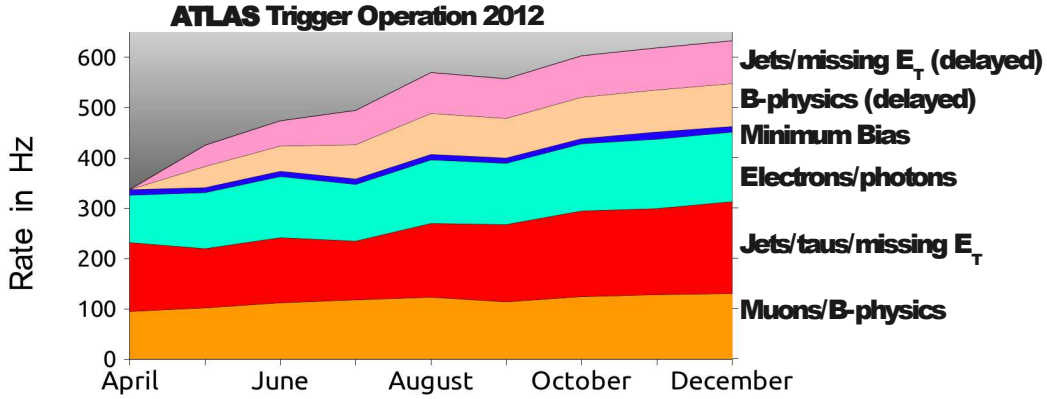


Figure 3.18: ATLAS Trigger stream rates for 2012 data taking, showing the total event-writing rate due to the various triggers. From [180].

or from the muon trigger chambers in the MS. This reduces the event rate from a peak of  $\sim 30$  MHz to  $\sim 65$  kHz, and reduces the data output to  $\sim 100$  GB/s. The detectors are continuously operating and being monitored in the front-end (FE) electronics. A LVL1 trigger decision is made using course-grained information from the calorimeters (both ECAL and HCAL) and the muon trigger system. The LVL1 trigger can be a single object, such as a high- $p_T$  muon or large energy deposit in the calorimeters, or more generic multi-object events such as two photons or multi-jets. The LVL1 trigger is hard-wired into the electronics to reduce latency between collision and trigger decision, with  $\sim 2.0 \mu\text{s}$  as the total time for reading in detectors, trigger decision, and readout to the next level. When a trigger decision is made for an event, the FEs of the detectors are read out to readout drivers (RODs), then into readout buffers (ROBs) for the level-2 trigger. Between the RODs and ROBs there are intermediate buffers called ‘derandomizers’ that average out the data rate from the LVL1 trigger to match the total bandwidth of the RODs.

The level-2 trigger (LVL2) uses the RoI defined in the LVL1, and uses the full granularity

## CHAPTER 3. THE LHC & ATLAS

of the triggered detector systems as well as the other detectors in the same RoI. The LVL2 trigger uses some fast software algorithms to do track matching or calorimeter clustering, and tightens the physics requirements on the objects in the event. The latency for the LVL2 trigger is about 60 ms. The LVL2 trigger reduces the event rate from  $\sim 65$  kHz to  $\sim 5$  kHz, and reduces the data output to  $\sim 7.5$  GB/s. The full detector data is kept in the ROBs until a LVL2 decision is made, then either discarded or moved to the third and final trigger stage.

The event filter (EF) is the last level of the trigger and uses the full event information from all the detectors. After the LVL2 acceptance, the data is moved to the sub-farm input (SFI) then to the event filter network. The EF builds the full event and applies offline software to perform tracking, electron selection, and calorimeter clustering. The EF trigger requirements are very close or the same as the final physics requirements for the objects in the event filter network. The latency for the EF is about 1 second, and it reduces the event rate from  $\sim 5$  kHz to  $\sim 400$  Hz and data output to  $\sim 600$  MB/s. The 2012 trigger stream rates for ATLAS are shown in Figure 3.18, and this is the data-flow to the ATLAS permanent data storage for use in analyses.

### 3.4.2 Reconstructing Electrons

The electron and photon (E/gamma) triggers are based on energy deposited in the ECAL. For the LVL1 trigger, the single-electron requirement is 18 GeV in a cluster in the ECAL, while the di-electron or di-photon requires  $2 \times 10$  GeV in two isolated clusters in the ECAL. At LVL2 trigger, track matching between the calorimeter energy deposit and the inner detector in the RoI provides rejection of electron events, while the cluster shape in the calorimeter also provides discrimination for photons and electrons from jets. The ratio between the

### CHAPTER 3. THE LHC & ATLAS

energy deposited in the ECAL compared to the HCAL in the RoI can reject jets. At the EF level, full cluster-shape algorithms can be applied as well as simple track reconstruction for electrons. The single-electron reconstruction efficiency varies from 95-99% depending on the  $\eta$  and  $p_T$  of the electron. The efficiency is best in the barrel region ( $|\eta| < 1.3$ ) and improves with increasing  $p_T$ .

There are three electron reconstruction algorithms: the standard electron algorithm for isolated, high- $p_T$  electrons; the soft electron algorithm for low- $p_T$  electrons and electrons in jets; and a forward-electron algorithm for tracks with  $|\eta| > 2.5$  where the inner detector does not provide tracking information. The remaining parts of this section will only discuss the standard electron algorithm as these are the only electrons used in this analysis.

The first step in electron reconstruction is electron identification [181]. A variety of discriminating variables are used to both identify E/gamma objects and discriminate between electrons and photons. Figure 3.19 shows what photon and  $\pi^0$  events look like in the ECAL. Hadronic leakage, the amount of transverse energy deposited in the same  $\eta$ - $\phi$  region in the HCAL compared to the ECAL, discriminates E/gamma from jets. Most of the energy from EM showers are deposited in the second compartment of the ECAL, where the bulk of the material is located. The lateral shower width and shape in the second compartment also discriminates from softer jets, as EM showers are more narrow than hadronic showers. The more finely-grained first compartment of the ECAL discriminates between two collimated photons coming from  $\pi^0$  or  $\eta$  particles, which can fake electrons. These calorimeter cuts provide a strong rejection of hadronic objects faking as electrons. After the calorimeter cuts, track matching discriminates between electrons and photons. Track matching has several parts. Track quality cuts are applied to the ID tracks to reject noise and converted photons. The track in the ID must be in the same  $\eta$ - $\phi$  cone as the ECAL. The measured momenta in the ID must also match the deposited energy in the ECAL. The number of TRT straw hits

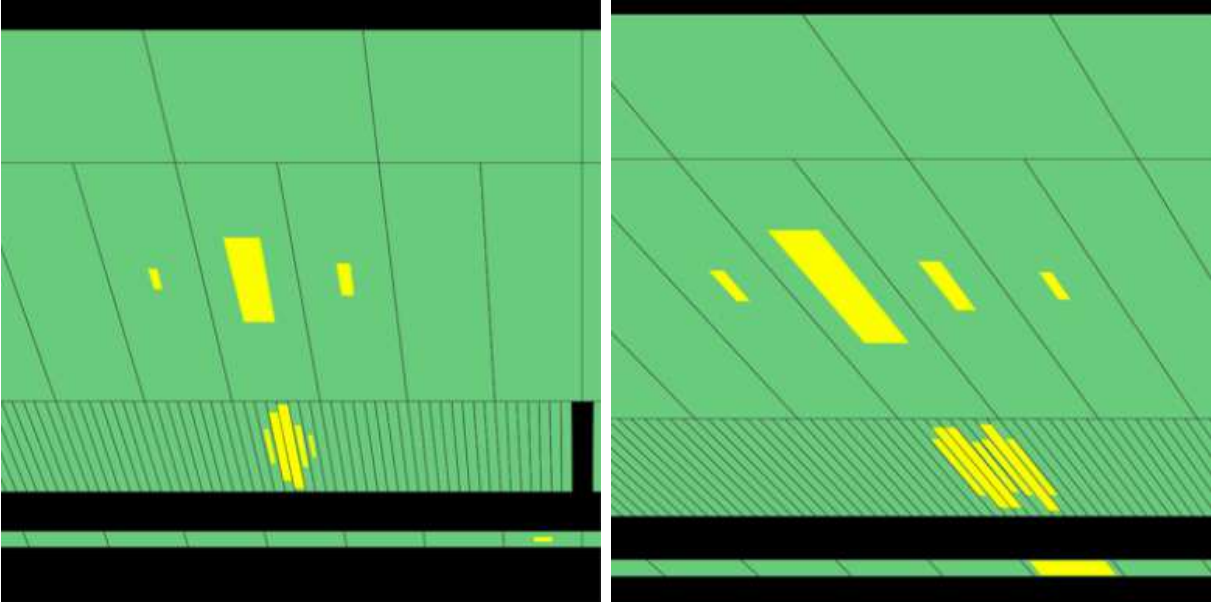


Figure 3.19: Two E/gamma events in the ECAL. Left: A single, isolated photon. Right: A  $\pi^0$  event showing the double peak from the decay to two photons. Electron identification needs to discriminate between these types of events in the ECAL, using clustering (to remove  $\pi^0$  or non-prompt conversions), track matching (to remove prompt photons), and hadronic leakage (to remove  $\pi^\pm$  and jets). From [182].

can reduce the mis-identification of charged pions and kaons as electrons as well. Finally, an isolation requirement is applied so that the electron is the only object in the  $\eta$ - $\phi$  cone  $\Delta R < 0.2$ .

After identification, the standard electron reconstruction begins with clusterization [183]. This uses a sliding window clusterization algorithm, which works in three steps. The first step is tower building, where the ECAL is divided into a grid of  $N_\eta$ - $N_\phi$  elements ( $200 \times 256$ ). This segments the  $\eta$ - $\phi$  grid into squares of  $0.025 \times 0.025$ . A window built from a fixed number of towers ( $5 \times 5$ ) is then slid about the grid, and if the  $E_T^{window}$  is above the threshold  $E_T^{thresh}$  (3 GeV) the position is saved. The size of the window and threshold energy have been optimized from simulations of the detector for the best efficiency while limiting fake pre-

### CHAPTER 3. THE LHC & ATLAS

clusters due to noise. With this initial window position, the second step is to form the pre-clusters. A smaller position window is scanned with  $N_{\eta}^{pos}-N_{\phi}^{pos}$  ( $3 \times 3$ ). These position windows form the pre-clusters. If two pre-clusters are within  $2 \eta$  or  $2 \phi$  towers, the pre-cluster with the largest  $E_T$  is kept. The pre-clusters then seed the final clusters for the final step. The final clusters are filled with towers of size  $3 \times 5$ ,  $3 \times 7$ ,  $5 \times 5$ ,  $7 \times 7$ . After the clusters are filled, they are corrected based on electron or photon identification.

Inside the final clusters, the full electron reconstruction is performed using the ECAL shower shape and track matching with the ID. These are similar to the procedure in electron identification, but more finely-grained and applied to find the electron track parameters. The energy in the ECAL is corrected based on the shower shape, using the track matching data as well. Electrons traversing the ID must cross  $\sim 1-2 X_0$  of material before the ECAL and can lose a significant fraction of their energy due to bremsstrahlung. A Gaussian sum filter approach is applied to the entire electron reconstruction to correct for the bremsstrahlung [184], refitting every electron track parameter. These corrected and refitted parameters are the final track parameters used for physics analysis.

Electrons are classified based on their identification and reconstruction, and are called “loose”, “medium”, and “tight”. The efficiency for reconstructing loose electrons as a function of  $\eta$  and  $E_T$  is shown in Figure 3.20, and is better than 95% in the range used for this analysis. Loose electrons only use the hadronic leakage and coarse shower shape variables to pass the electron definition. Medium electrons use the fine-grained information in the first compartment of the ECAL for the shower shape to further reject jets and  $\pi^0$ . In addition, a track in the ID with in the same  $\eta$  range with Pixel and SCT hits and transverse impact parameter  $d_0$  must match the ECAL. Tight electrons have additional track matching requirements. The matched track must be in the same  $\Delta\phi$  range, with tighter restrictions on  $\Delta\eta$  and  $d_0$ . The track hit requirements in the Pixel, SCT, and TRT subsystems of the

CHAPTER 3. THE LHC & ATLAS

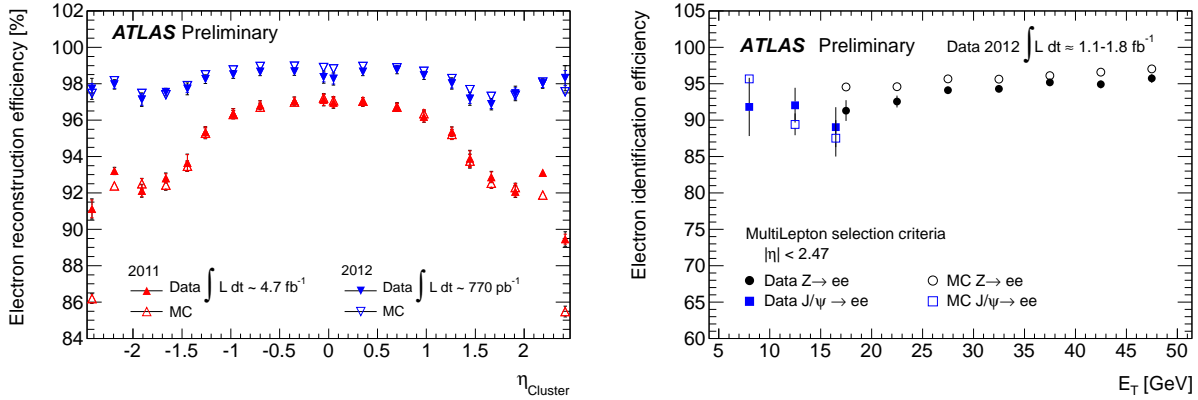


Figure 3.20: Left: Electron reconstruction efficiency vs. the measured  $\eta$  of the electron, comparing the early 2012 data results to the 2011 data. The efficiency is best in the barrel, and decreases in the endcaps. Right: Electron reconstruction efficiency vs. the measured  $E_T$  of the electron, using two different 2012 datasets to compare low- and high- $E_T$ . Electron reconstruction efficiency improves with  $E_T$ . From [182].

ID are all tightened. Lastly, the measured momentum in the ID must match the energy deposited in the ECAL.

The energy resolution of the sampling ECAL has been measured in a test beam [185], and found to be:

$$\frac{\sigma_E}{E} = \frac{a}{\sqrt{E}} \oplus b, \quad a = 10.1 \pm 0.1\% \sqrt{\text{GeV}} \quad \text{and} \quad b = 0.17 \pm 0.04\%.$$

This is the dominant source of uncertainty for the measurement of high energy electrons in the ATLAS detector. There are a set of prescriptions [186] for the measured electrons to adjust the measured energy to the correct, calibrated energy scale.

### 3.4.3 Reconstructing Muons

The muon trigger is based on a coincidence between the trigger chambers in the MS, working from the inside-out [187]. The trigger chamber layout is shown in Figure 3.16, with the general shape of a high- $p_T$  muon path in the different regions. The angle between the line formed by the hits in the trigger chambers and the IP is a fast measure of the  $p_T$  and is the primary LVL1 muon trigger, requiring  $p_T > 15$  GeV. The LVL2 trigger has a fast reconstruction algorithm for muons in the RoI identified by the LVL1 trigger, and tightens the  $p_T$  requirement. At the EF level, an additional isolation requirement is applied to the single muon trigger. First, the sum of the  $p_T$  of the tracks in an  $\eta$ - $\phi$  cone  $\Delta R < 0.2$  is calculated. A track is included in the sum if it has  $p_T > 1$  GeV and  $|z_0(\text{track}) - z_0(\text{muon})| < 6$  mm. The isolation requirement is  $(\sum p_{T,\text{tracks}}/p_{T,\mu}) < 0.12$ , and the final  $p_T$  requirement is 24 GeV. Muon trigger efficiency during the 2012 data taking is shown in Figure 3.21. The primary single-muon trigger is  $\sim 70\%$  efficient in the barrel and  $\sim 90\%$  efficient in the endcaps, including geometric acceptance.

Muon reconstruction in ATLAS begins in the muon spectrometer. There are two standard muon reconstruction algorithms, called “chains”, for muon tracks in the MS: Muonboy [189] and MOORE [190]. There are also two low- $p_T$  reconstruction algorithms for muons based on ID tracks which do not use the spectrometer, called MuGirl [191] and MuTag [189]. Muons in ATLAS are classified by how much reconstruction information is used. The most robust muons are “combined” (CB) muons, which uses both MS track information and ID track information that have been matched together. There are two algorithms that can do this combination: STACO [189] paired with the Muonboy MS reconstruction and MUID [192] paired with the MOORE MS reconstruction. “Standalone” (SA) muons are STACO or MUID MS tracks, done with Muonboy or MOORE respectively, without a matched ID track.



CHAPTER 3. THE LHC & ATLAS

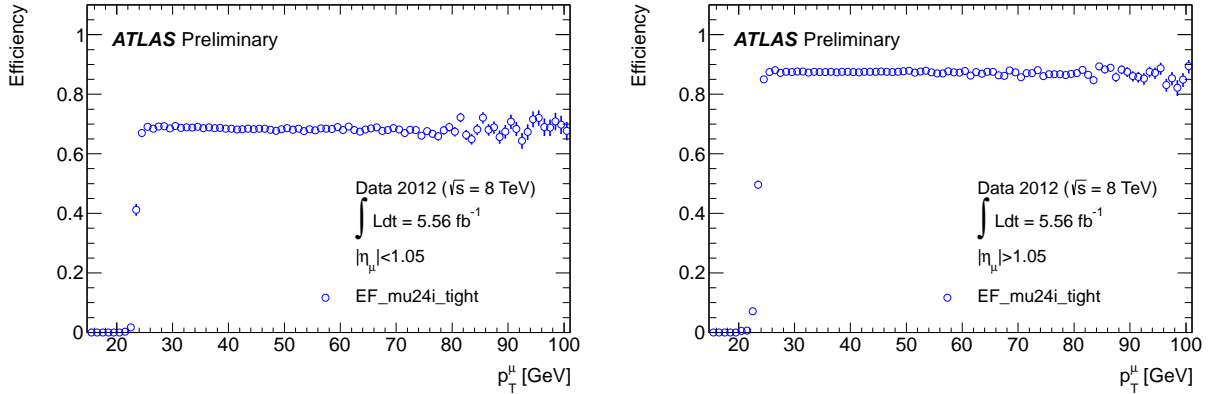


Figure 3.21: Left: Muon trigger efficiency in the barrel ( $|\eta| < 1.05$ ) for the mu24i\_tight trigger. Right: Muon trigger efficiency in the endcap ( $|\eta| > 1.05$ ) for the mu24i\_tight trigger. This is seeded by the L1\_MU15 trigger. Both use a tag-and-probe method for  $Z^0 \rightarrow \mu\mu$  decays to calculate the efficiencies. The efficiencies also include the geometric acceptance of the trigger chambers in their respective regions. From [188].

“Segment-Tagged” (ST) muons use either MuGirl or MuTag with some segments in the MS where the Muonboy or MOORE algorithms fail to fully reconstruct the track. These are used to recover inefficiencies where the MS has only 1 or 2 layers to reconstruct the muon track, particularly in the region  $|\eta| > 2.5$ . “Calorimeter-Tagged” (Calo) muons use either MuGirl or MuTag without any MS information, instead using the energy deposited in the calorimeters parameterized as a minimum ionizing particle (MIP). These are used to recover inefficiencies where there is no MS coverage, especially in the services region at  $|\eta| < 0.1$ . The remaining parts of this section will only discuss the MOORE and MUID algorithms, as this is the method used for muon reconstruction and combination for this analysis.

Muons are identified in the MS based on the hit patterns in the various subsystems. Muons are MIPs in the gas detectors with small multiple scattering, while hadronic particles such as pions or kaons that have passed through the calorimeters will shower much more and have a larger average multiple scattering angle. Once a muon has been identified, the track

CHAPTER 3. THE LHC & ATLAS

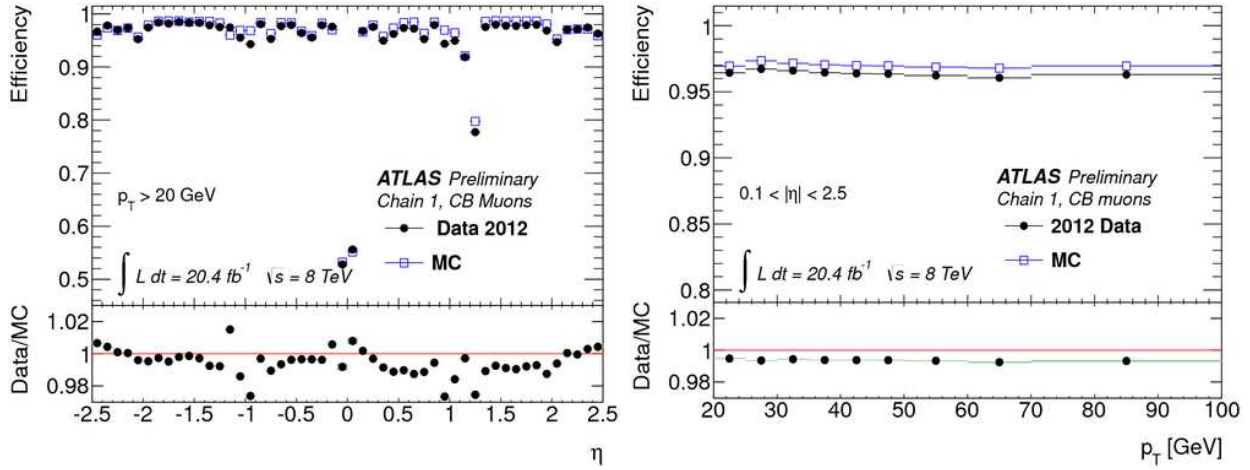


Figure 3.22: Left: Muon reconstruction efficiency vs.  $\eta$ . Right: Muon reconstruction efficiency vs.  $p_T$ . These are for combined muons only, and show the high reconstruction efficiency for muons in the dataset. From [188].

reconstruction can begin. The event information is broken up into different levels of data objects, beginning with hits, then segments, roads, and finally tracks. The final output is stored in a “container”. The combined muon reconstruction efficiency for a triggered muon object is shown in Figure 3.22, and past the trigger threshold is better than 95%.

The MOORE algorithm first processes hits in the  $\phi$ -plane. The toroid has minimal bending in the  $\phi$  direction and the track can be approximated as a straight line. The RPC, TGC, and CSC  $\phi$  hits build up the PhiSegments. The toroidal field bends in the  $Rz$ -plane; however, over the distance of a single precision layer in the MS, such as one MDT or CSC chamber, the bending power is negligible and can be approximated as a straight line. The tubes that have hits reconstruct a straight line, and the pattern recognition uses the hits inside a single layer to define a  $\theta$  coordinate with respect to the straight line for each tube center. These straight lines form CrudeRZSegments. With the two segments filled for the event, MOORE loops over all PhiSegments, then over each CrudeRZSegment within the same region as the chamber with the PhiSegments. The CrudeRZSegments are analyzed with a

### CHAPTER 3. THE LHC & ATLAS

different pattern recognition algorithm to produce “fine” RZSegments. The RZSegments and PhiSegments are then grouped into a road. If a road contains segments from more than one layer, a fit is attempted to merge them together. If successful, the road is accepted for further processing, otherwise the one-layer roads are used. The roads are then passed on for further processing. The last phase is to make tracks. This loops over all the roads, assigning all the hits from the precision chambers without trigger chambers (the inner and outer layers) to that road. A correction is applied to account for the material inside the MS which results in multiple scattering and energy loss. Each hit assigned to the road is then accepted or rejected based on how much it contributes to  $\chi^2$  of the track pattern recognition. The tracks are the roads after rejecting high-residual hits and corrections due to material. The tracks are filled based on their first measured point in the MS, with the parameters  $d_0$ ,  $z_0$ ,  $\phi$ ,  $\cot \theta$ , and  $q/p_T$ .

MUID uses the MOORE reconstructed muons in the MS, and matches them to the IP and tracks in the ID. The first step uses the MOORE track, then extrapolates it back to the IP through the magnetic field and detectors. Moving backwards through the calorimeters, the energy loss is corrected as a parameterized function of  $\eta$  and  $p_T$  and uses the energy deposited in the calorimeters in the same  $\eta$ - $\phi$  region. It then finds the point of closest approach to the IP and uses that point for basis of the track parameters. This is saved in the MUID SA track container. If an ID track is in the same  $\eta$ - $\phi$  region, then a match is attempted. Tracks are combined using hits from the sub-detectors of the ID, as MUID attempts to rebuild the roads using the ID hit information. If the combined fit satisfies the  $\chi^2$  probability cutoff, the result is kept in the MUID CB track container. All of the information for the ID tracks are also kept in their own container.

The resolution of the reconstructed muon tracks is discussed in Appendix E.

# Chapter 4

## Analysis Event Selection

One of the goals of ATLAS and the LHC is to search for, and hopefully find, new physics beyond the Standard Model. There are a wide variety of models that describe possible new physics, with hundreds of different analyses being performed at the experiments at the LHC testing various examples. This thesis will describe one such search,  $Z' \rightarrow \ell\ell$ . This search reconstructs the dilepton invariant mass spectrum in both the electron and muon channels, then tests it for peaks deviating from the SM prediction which would indicate the presence of a new particle. The dilepton channel has traditionally been a fruitful avenue for discovering new physics, such as the  $J/\psi$  meson and  $Z^0$  boson. The advantage of this search is that the system is fully reconstructed with a well known and simulated SM background. This search uses the 2012 data taking run of 8 TeV  $pp$  collisions at the LHC, with an integrated luminosity of approximately  $21 \text{ fb}^{-1}$ . This chapter describes how events are selected from the ATLAS data set, and how the SM expectation is simulated and produced to compare to the observed data.

## 4.1 Data & Monte Carlo Samples

There are two types of input files analyzed: data from the ATLAS detectors and Monte Carlo (MC) samples that simulate the expected SM background and  $Z'$  signals. The data collected at ATLAS undergoes several stages of processing to move from the individual hit information for each event inside the sub-detectors to the final files that are analyzed in this thesis. The MC samples involve several stages of simulation and processing before being analyzed. This section will describe the simulation steps for MC samples, and the processing stages for both Data and MC. The analysis is done using ROOT, a C++ based object-oriented data analysis framework [193, 194, 195]. The Data and MC processing for ATLAS are done in the Athena framework [196].

### 4.1.1 Processing Data

Processing the event information from the ATLAS detector into files usable for analysis involves a huge amount of computing and networking, detailed in the ATLAS Computing TDR [197] and the report on analysis computing for 2012 [198]. The output from the event filter farm (the final stage of the trigger, see Section 3.4.1) raw data stream is saved to both tape and disk storage at CERN (Tier-0), as well as distributed to the 12 Tier-1 sites around the world so that two copies of the full raw dataset are maintained. The raw data contains the hit information from each channel in the sub-detectors and is approximately 0.8 MB/event in size. The raw data is reprocessed at the Tier-0 into Event Summary Data (ESD) files, after reconstruction of the objects in the event. The size is approximately 0.5 MB/event and these are also distributed to the Tier-1 sites. The ESD is designed so that direct access to the raw files is not necessary. The format of ESDs are ROOT POOL (Pool Of persistent Objects for LHC) files, intended for long-term storage. The ESDs are reprocessed into

## CHAPTER 4. ANALYSIS EVENT SELECTION

Analysis Object Data (AOD) files, which are reduced event representations with extraneous information filtered out. This format contains physics objects such as electrons and muons as well as event-level information such as trigger data. AODs are approximately 250 kB/event and are also stored in ROOT POOL format. A full set of AODs are distributed to each Tier-1 site. In addition to these data formats, there are TAG files that contain the metadata information for each event, such as trigger information and identification of objects of interest for analyses within an event. These files are only 1 kB/event and are designed for fast event selection from analysis queries.

The AOD files are still quite large, have the entire dataset stored, and contain the full event information. Most analyses are only interested in a subset of the full dataset and only need some of the event information; for example this thesis requires two high-energy leptons and only needs the information associated with those leptons. The AODs are further processed into Derived Physics Data (DPD) files, now in their third iteration of formatting called D3PDs. These files are only filled with physics objects and event-level information with very limited detector-level information, for example the  $\eta$  value for each identified muon or number of interaction vertices in the event. Analysis groups determine what information should be stored in their set of D3PDs, with a large variety of D3PDs being processed from the AODs. The D3PDs can range from 5-260 kB/event and are ROOT-readable files using the TTree structure called *ntuples*. The data files used for this analysis are:

- data12\_8TeV.*run-number*.physics\_Egamma.merge.NTUP\_ZPRIMEEEE.\*
- data12\_8TeV.*run-number*.physics\_Muons.merge.NTUP\_ZPRIMEMM.\*

The run numbers for 2012 range from 00200804-00216432. The “\*” designates the merging and reprocessing tags; the reprocessing tags used for this analysis are p1344-p1345 corresponding to Athena release 17.2.7.x.

## CHAPTER 4. ANALYSIS EVENT SELECTION

A Good Runs List (GRL) is used to monitor the ATLAS detector's status and remove events when the relevant sub-detectors were not operational. For example if the cryostat for the ECAL experienced a problem causing a portion to be off-line for part of a run, events using the ECAL will not be included in the analysis. The GRLs used for the electron and muon analyses are:

- data12.8TeV.periodAllYear\_DetStatus-v61-pro14-02\_DQDefects-00-01-00\_PHYS\_StandardGRL\_All\_Good.xml,
- data12.8TeV.periodAllYear\_DetStatus-v61-pro14-02\_DQDefects-00-01-00\_PHYS\_CombinedPerf\_Muon\_Muon.xml.

### 4.1.2 Monte Carlo Generation

The simulated data is produced over several stages and then reprocessed using the same reconstruction algorithms as in the data samples. There are a variety of MC event generators that can perform these simulations in general, with different generators specializing in different types of physics processes. The MC generators have as inputs the physics process being simulated, the various parameters for the LHC environment such as the proton beam energies, the PDF set being used, the QCD parameters for both the PDF and matrix amplitude calculation, and other phenomenological parameters. The MC generation begins by calculating the cross section of the physics process being simulated by calculating the matrix element, evaluating the PDF, estimating the phase space, etc. If the matrix elements are already known, they can be input as well. The generation then simulates the hard process that takes the incoming particles from the protons through the physics process being simulated. The physics process inputs will specify a set of intermediate particle(s), and, depending on the samples being generated, will also specify the outgoing particles as well.

## CHAPTER 4. ANALYSIS EVENT SELECTION

The output of the generator is the four-momenta of the stable and semi-stable particles outgoing from the simulated process. These are the particles that will be simulated passing through the detector. The initial hard process will have just a few particles such as quarks, gluons, leptons, or photons. The event generator will take these “bare” particles and evolve them through parton-showers, hadronization, and decays of very short-lived particles. For example, if the underlying process being simulated is top-quark pair-production ( $t\bar{t}$ ), the initial top quarks will decay into b-quarks which hadronize into B mesons. The  $W$  bosons from the initial top decay will themselves decay, and there can also be gluons radiated which shower into soft jets. All of these particles are processed during the generator simulation; the generator has the masses, lifetimes, and branching ratios of all the SM particles as well as hypothesized particles from beyond the SM. The longer-lived particles with lifetimes  $\sim 10^{-12-13}$  s, such as  $B$  mesons,  $D$  mesons, and  $\tau$  leptons, can be simulated with either the same generator or a special, separate generator that is interfaced with the initial generator. In addition to the hard process, a varying number of other, softer interactions are simulated to account for the multiple interactions that occur during one bunch crossing. The final output includes all of the information about the underlying events as well as the stable and long-lived particles that will interact with the detector.

The long-lived particles are then simulated passing through the detector. This is done using GEANT4 (GEometry ANd Tracking) [199, 200, 201], an object-oriented, C++-based software that is “a toolkit for the simulation of the passage of particles through matter”. A team of physicists and programmers have input the entire ATLAS detector into GEANT4 [202], including all of the detectors, services, and inert materials. The behavior of the particles such as multiple scattering, ionization, and photon conversion is done in GEANT4, and the detector response is output. The simulated detector response is then digitized into hits, and the trigger decisions are done using the same set of algorithms coded into the



## CHAPTER 4. ANALYSIS EVENT SELECTION

trigger menu. Customized digitization and triggering for MC event generation in ATLAS is available in the Athena framework. After simulation of the detector response to an event, the digitized hits undergo the same reprocessing as the data hits, from ESDs to AODs to D3PDs for use in analyses. The output for MC files is typically  $\sim 20\%$  larger than the output for standard data files due to keeping the “truth” information of the underlying simulated event.

This analysis makes use of several MC generators for simulating the SM backgrounds and expected  $Z'$  signals. PYTHIA [203] is a leading-order (LO) event generator, where the matrix elements for the hard process are evaluated at LO and the parton-showers and hadronization are done using a leading-log approximation that is estimated from empirical data. PYTHIA can be interfaced with PHOTOS [204] to more accurately simulate final state radiation (FSR), which is the emission of a photon by a charged particle similar to the parton-shower in QCD. PYTHIA is noted for being more accurate when simulating electro-weak processes. POWHEG [205] is a next-to-leading-order (NLO) event generator, where the hard process is evaluated at NLO in QCD using the input PDF. While POWHEG event generator does have parton-shower and hadronization algorithms, it can be interfaced with PYTHIA for this stage of the simulation [206]. MC@NLO [207] is another next-to-leading-order event generator interfaced with HERWIG [208, 209] for parton-showering and hadronization. The multiple parton interactions simulation of the underlying event can be made more accurate by including the JIMMY library [210]. HERWIG also contains a LO event generator which has been tuned to the ATLAS operating conditions [211].

## 4.2 $Z'$ Search Requirements

This search for a new particle in the dilepton spectrum interprets the possible finding as a new, neutral, heavy, spin-1 gauge boson. Generically, this new particle will couple to all the fermions in the SM in a vector/axial-vector coupling:

$$L_{Z'} \subset Z'_\mu \sum_i \bar{f}_i (g_{V,i} - g_{A,i} \gamma^5) \gamma^\mu f_i,$$

where the index  $i$  covers both quarks and leptons, and includes all the colors, flavors, and chiralities (L & R) for each generation. The  $Z'$  can induce flavor-changing  $Z'$  currents with non-diagonal fermion terms, although the bounds on this for charged fermions are very strict [212]. There can also be mixing between a new  $Z'$  particle and the  $Z^0$  boson; however, this has been measured in LEP I [213] and found to be quite small, with the mixing angle limited to  $\Theta_{Z-Z'} < 0.01$  depending on the model analyzed. The values of  $g_i$  will depend on the theory from which the  $Z'$  is derived. For a  $Z'$  directly produced at a collider (through the  $s$ -channel), the decay width into a fermion pair (when  $M_{Z'} \gg m_f$ ) is given by:

$$\Gamma(Z' \rightarrow \ell\ell) = \left[ \sum_j (g_{\ell,V,j}^2 + g_{\ell,A,j}^2) \right] \frac{M_{Z'}}{12\pi},$$

where the index  $j$  is the sum over colors and chiralities for the fermion flavor. This can also be used to calculate the expected production cross section from the colliding quarks at tree level by including the color factor and integrating over the PDF. Once the  $g_i$  are known, the production and decay of the  $Z'$  can be calculated and compared to experimental data.

The benchmark signal searched for is the Sequential Standard Model (SSM)  $Z'$ . This model has all of the same couplings to the fermions (both leptons and quarks) as the SM  $Z^0$  boson. Because the couplings are the same, the width of the new particle as a function of

## CHAPTER 4. ANALYSIS EVENT SELECTION

its mass is very similar to the  $Z^0$  boson,  $\sim 3\%$ . This is not a theoretically motivated model; instead the limits placed on this model serve as a way to compare results from different experiments. In addition to the SSM  $Z'$ , limits are placed on a set of possible new particles based on the  $E_6$  gauge group [214, 215]. The  $E_6$  gauge group is a possible GUT discussed in Section 2.4.1. Labeling the two quantum charges associated with the two  $U(1)$ s  $\psi$  and  $\chi$ , the two heavy, neutral gauge bosons can mix under their interactions with the SM particle:

$$Z' = Z'_\psi \cos \theta_{\psi-\chi} + Z'_\chi \sin \theta_{\psi-\chi}.$$

The  $Z'$  candidate is the lowest-mass mixed particle. The mixing angle  $\theta_{\psi-\chi}$  can range from  $-\pi/2$  to  $\pi/2$ , with 0 corresponding to  $Z' = Z'_\psi$  and  $\pi/2$  corresponding to  $Z' = Z'_\chi$ . Limits are also placed on four other models with varying mixing angles,  $\theta = \{-0.29\pi, 0.129\pi, 0.21\pi, 0.42\pi\}$  and labeled  $Z'_\eta, Z'_S, Z'_I, Z'_N$  respectively. Each model couples differently to the quarks and leptons in the SM and has a different width as a function of mass, ranging from 0.5% for  $Z'_\psi$  to 1.2% for  $Z'_\chi$  or  $Z'_S$ .

The expectation for new physics from GUTs is that new particles will appear at a scale higher than the electro-weak scale, therefore this search for  $Z'$  particles is in the high-mass region above the  $Z^0$  peak. The search method uses the  $Z^0$  boson peak to calibrate and normalize the SM background and analyses in the mass region from 130 GeV and above, with an event selection optimized for acceptance and resolution of these high-energy leptons.

### 4.2.1 Expected $Z'$ Signal

The  $Z'$  signal templates are derived from the Drell-Yan (DY) process simulated in PYTHIA8 with the MSTW2008LO PDF (Martin-Stirling-Thorne-Watt Parton Distribution Functions, see Section 2.3.2) [85, 216]. The PYTHIA8 DY spectrum is generated in mass bins from 75 to

## CHAPTER 4. ANALYSIS EVENT SELECTION

>3000 GeV, with 16 samples in total with mass ranges {75-120, 120-250, 250-400, 400-600, 600-800, 800-1000, 1000-1250, 1250-1500, 1500-1750, 1750-2000, 2000-2250, 2250-2500, 2500-2750, 2750-3000, 3000+}. Each sample contains  $\sim 100,000$  events, except the first sample from 75-120 GeV which has  $\sim 300,000$  events. Each sample is produced separately, and is called a “run” in the same terminology as the data taking of the real detector. The MC runs for the PYTHIA8 samples are:

- mc12\_8TeV.run-number.Pythia8\_AUMSTW2008LO\_DYee\_mass.merge.  
NTUP\_SMWZ.\*
- mc12\_8TeV.run-number.Pythia8\_AUMSTW2008LO\_DYmumu\_mass.merge.  
NTUP\_SMWZ.\*

The run numbers range from 145963-145978 for the electron samples and 145979-145994 for the muon samples. The reconstruction and processing tags are r3542\_r3549\_p1328. The high statistics throughout the spectrum ensures accurate representation of the expected signal.

The signal templates are made by reweighting the DY spectrum from the  $Z^0/\gamma^*$  cross section to the  $Z'$  cross section for each model. This is done with a 2-dimensional weighting function:

$$\mathcal{W}(m_{\ell\ell}, q_{in}) = \frac{|\mathcal{M}_{Z'}|^2}{|\mathcal{M}_{DY}|^2}. \quad (4.1)$$

The inputs are the truth dilepton invariant mass  $m_{\ell\ell}$  and flavor of the incoming quark  $q_{in}$  that annihilates to form the  $Z'$ . The couplings for the  $Z'$  are assumed to be universal across different generations. The phase space and spin-dependence is expected to be the same for both DY and  $Z'$ . This weighting ignores the quantum mechanical interference that will take place between two processes with the same incoming and outgoing states. The effects of

## CHAPTER 4. ANALYSIS EVENT SELECTION

interference are expected to be small for masses much larger than  $m_Z$ . After specifying a pole mass for the given  $Z'$  template, this weight can be calculated and applied event-by-event for all the DY samples to form the expected signal. The signal template is the entire dilepton mass spectrum being measured in the search, filled with what the  $Z'$  would appear as in the mass plot. The signal templates are generated for the SSM  $Z'$  over the pole mass range from 150-3500 GeV in steps of 50 GeV, for 68 mass points total. Some representative signal templates for the SSM  $Z'$  can be seen in their respective channel sections below. The electron signal templates are found in Figure 4.3, and the muon signal templates are found in Figures 4.6.

The signal templates are used for the search and limit setting. In addition there are also some smaller, dedicated samples of  $Z'_{SSM}$  at fixed mass generated for validation, signal studies, and visualization. These are generated with PYTHIA8 and the same MSTW2008LO PDF, at mass points of {500, 1000, 1500, 2000, 2500, 3000} GeV and  $\sim 20,000$  events per sample. The dedicated samples are:

- `mc12_8TeV.run-number.Pythia8_AUMSTW2008LO_Zprime_ee_SSMmass.merge.NTUP_SMWZ.*`
- `mc12_8TeV.run-number.Pythia8_AUMSTW2008LO_Zprime_mumu_SSMmass.merge.NTUP_SMWZ.*`

The run numbers range from 158019-158024 for the electron samples and 158025-158030 for the muon samples, and the same reprocessing tags as the DY samples. These samples are generated with interference with the SM DY process included, and have a cut-off at half the pole mass to prevent the DY events from dominating the spectrum. To weight these events

## CHAPTER 4. ANALYSIS EVENT SELECTION

with respect to the standard  $Z'$  signals, Equation (4.1) becomes

$$\mathcal{W}(m_{\ell\ell}, q_{in}) = \frac{|\mathcal{M}_{DY+Z'}|^2}{|\mathcal{M}_{DY}|^2}.$$

By including the effects of interference, small discrepancies can be seen at the point of maximal interference between the reweighted signal templates at a given pole mass and the generated fixed-mass samples. See Figure 4.1 for the mass spectrum plot of these dedicated signal samples compared to the reweighted template signal samples described above. This could be recovered by including the angular information from the decay leptons ( $\cos\theta^*$ ) in the weighting function, but this effect has been ignored due to the negligible impact on the analysis.

The production of the  $Z'$  must come from the partons inside the proton, therefore the PDF choice made will have an effect on the expected cross section for the signal as a function of  $m_{\ell\ell}$ . The eigenvectors for the PDF are each varied at the 90% C.L., as well as  $\alpha_S(m_Z)$ , and the resulting change in expected cross section is measured. The  $Z'$  signal samples are generated using the MSTW20008LO PDF set, which has 20 eigenvectors and their 68% and 90% C.L. values and the  $\alpha_S(m_Z)$  variation. The nominal cross section value is calculated by generating 100 K events using PYTHIA, then each eigenvector and  $\alpha_S$  is varied at their  $\pm 90\%$  values and the cross section is again estimated by generating 100 K events for each variation, giving 42 total varied cross sections at each mass point. The asymmetric uncertainty is:

$$\begin{aligned} \Delta\sigma^+ &= \sqrt{\sum_{i=1}^{21} (\text{Max}(\sigma_i^+ - \sigma_0, \sigma_i^- - \sigma_0, 0))^2}, \\ \Delta\sigma^- &= \sqrt{\sum_{i=1}^{21} (\text{Max}(\sigma_0 - \sigma_i^+, \sigma_0 - \sigma_i^-, 0))^2}. \end{aligned}$$

CHAPTER 4. ANALYSIS EVENT SELECTION

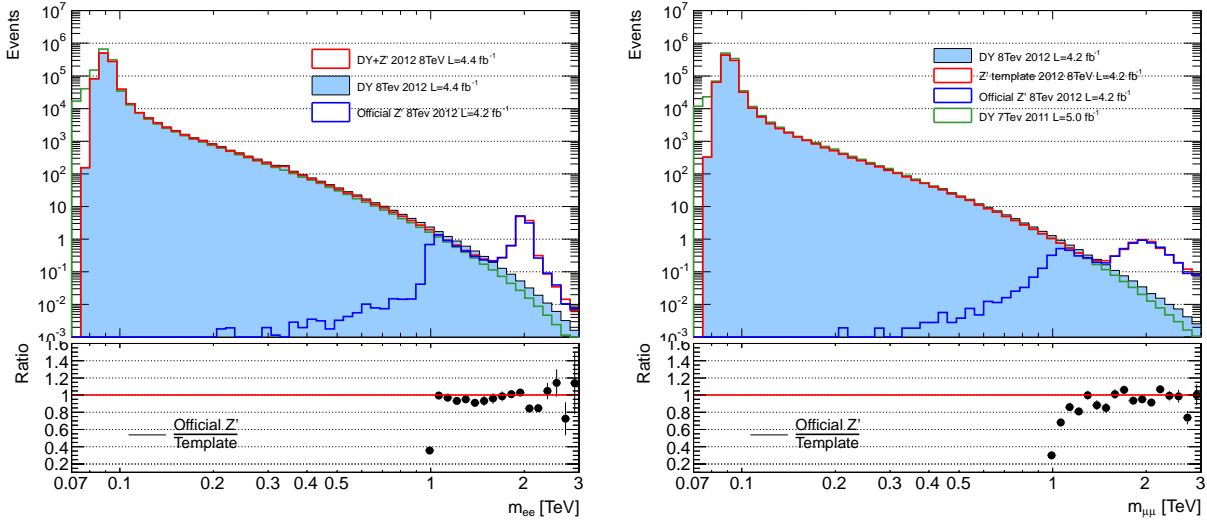


Figure 4.1: Left: Dielectron invariant mass overlaid with dedicated 2000 GeV SSM sample and reweighted signal template. Right: Dimuon invariant mass with the same histograms. This shows the reweighting procedure reproduces the expected signal in the same way as the dedicated samples. In both cases the interference with the SM DY background is included, and both sets of samples follow the SM background in the 1000-1500 GeV range. For the dedicated samples (the dark blue histogram), the production is cut-off at half the pole mass value, 1000 GeV, leaving low mass tails below this value. From [217], Appendix I, Figure 99.

The values  $\sigma_i^+$  and  $\sigma_i^-$  are the cross sections from varying the  $i^{\text{th}}$  parameter up or down, and  $\sigma_0$  is the nominal value. The resulting variation is shown in Table 4.1. The PDF variation could have potentially affected the signal acceptance as well, but variation in acceptance was found to be  $< 0.2\%$  for the 3000 GeV  $Z'$  signal and has been neglected. The PDF uncertainty on the signal is not used in the search or limit-setting because it is already included in the Drell-Yan systematic uncertainties, but it is included in the visualization to denote the theoretical uncertainties on the  $Z'$  signal.

### 4.2.2 Standard Model Backgrounds

The dominant backgrounds in the search for new physics in the dilepton channel are processes with two real leptons in the final state. The largest such background is the Drell-Yan process, the direct production of leptons through a  $Z^0/\gamma^*$ . This process is described in detail in Section 2.5. This background has the same initial and final states and therefore is an irreducible background. The peak at the  $Z^0$  mass is used to normalize the MC estimated background. There are also reducible backgrounds from top-quark and diboson production, where one or both of the gauge bosons decay leptonically. All of these backgrounds are simulated with other interaction vertices in the underlying event, due to other protons in the bunches colliding. These other vertices contribute many soft particles to the event which must be reconstructed and included, which is referred to as “pileup”. Figure 3.3 shows a typical pileup situation with more than 20 vertices during a  $Z^0$  event. The detector response, trigger efficiency, and reconstruction precision can all potentially depend on the pileup. The MC events are re-weighted using a tool to ensure the pileup for each type of event is the

$Z'$ mass [GeV]	Uncertainty using MSTW2008LO	
200	+5.6%	-4.7%
500	+4.0%	-5.0%
1000	+6.8%	-6.7%
1500	+11.0%	-10.6%
2000	+17.6%	-18.3%
2500	+30.1%	-29.7%
3000	+42.5%	-42.3%
3500	+51.6%	-52.8%
4000	+62.1%	-60.5%
4500	+71.1%	-71.9%

Table 4.1: Uncertainty on  $Z'$  cross sections due to PDF and  $\alpha_s$  variations at the 90% C.L. From Appendix F, Table 37 in [217].



## CHAPTER 4. ANALYSIS EVENT SELECTION

same as seen in data.

### Drell-Yan

The Drell-Yan (DY) background is simulated with POWHEG interfaced with PYTHIA8 for parton-showering and hadronization, and uses the CT10 PDF (The Coordinated Theoretical-Experimental Project on QCD Parton Distribution Function) [218]. The DY spectrum is generated with 18 different samples over different bins in the invariant mass between 60 and  $>3000$  GeV, similar to the PYTHIA8 samples used for the signal generation. The mass ranges are  $\{60+, 110-120, 120-180, 180-250, 250-400, 400-600, 600-800, 800-1000, 1000-1250, 1250-1500, 1500-1750, 1750-2000, 2000-2250, 2250-2500, 2500-2750, 2750-3000, 3000+\}$ . The first sample is an “unbinned”, inclusive simulation of  $pp \rightarrow Z^0/\gamma^* + X \rightarrow \ell\bar{\ell} + X$ , with a cutoff of the dilepton invariant mass at 60 GeV and contains  $\sim 30$  million events. The samples are:

- mc12\_8TeV.147806.PowhegPythia8\_AU2CT10\_Zee.merge.NTUP\_SMWZ.\*
- mc12\_8TeV.run-number.PowhegPythia8\_AU2CT10\_DYee\_mass.merge.NTUP\_SMWZ.\*
- mc12\_8TeV.147807.PowhegPythia8\_AU2CT10\_Zmumu.merge.NTUP\_SMWZ.\*
- mc12\_8TeV.run-number.PowhegPythia8\_AU2CT10\_DYmumu\_mass.merge.NTUP\_SMWZ.\*

The run numbers range from 129503-129518 for the mass-binned electron samples and 129522-129538 for the mass-binned muon samples. The reconstruction and processing tags are r3549\_p1328. The 110-120 GeV samples contain  $\sim 2.2$  million events, the 120-180 GeV samples contain  $\sim 3.3$  million events, and the rest of the samples all contain  $\sim 100,000$  events each. The high statistics throughout the mass range ensures accurate simulation of the

CHAPTER 4. ANALYSIS EVENT SELECTION

$m_{\ell\ell}$ [GeV]	250	500	1000	1500	2000	2500	3000	3500	4000	4500
$K_{NNLO} = \frac{\sigma_{NNLO}}{\sigma_{NLO}}$	1.049	1.065	1.071	1.076	1.096	1.121	1.136	1.149	1.189	1.238

Table 4.2:  $K$ -factors obtained for POWHEG DY samples from FEWZ. From [217], Table 2.

spectrum. When joining the samples together to form the complete spectrum, a cut is applied to the unbinned sample on the truth-level dilepton invariant mass at 110 GeV to avoid double-counting events in the range above this point.

The matrix elements for the events generated in POWHEG are at NLO in QCD, therefore the production cross section used to scale the MC to data is also at NLO. NNLO generators are not yet available for this process, instead the NNLO QCD calculation for  $Z^0/\gamma^*$  production is calculated using FEWZ (Fully Exclusive  $W$  and  $Z$  Production) [219] in the LHC environment. The resulting cross section as a function of  $Q^2$  momentum transfer, or truth dilepton invariant mass, is used to weight the generated events to NNLO. The ratio of the NNLO to NLO cross sections are the weights used and are called mass-dependent  $K$ -factors. The FEWZ corrections include NNLO QCD effects, NLO EW effects, real weak-boson emission, and photon-induced corrections. Final state radiation of a real photon (FSR) is already accounted for using PHOTOS; other corrections such as initial and final state photon virtual photon emission which interferes with the amplitudes and real initial state radiation (ISR) must be included. A table showing some of the  $K$ -factor weights is shown in Table 4.2. See Appendix A for further details. The total cross section for  $Z^0/\gamma^*$  production has been calculated to NNLO precision in the mass range above 60 GeV. The uncertainty on the cross section 4% and is treated as a systematic error. The other systematic uncertainties for the DY process associated with the PDFs are discussed in Appendix B.

## CHAPTER 4. ANALYSIS EVENT SELECTION

### Top

The background due to top quark production is simulated using the MC@NLO event generator with the CT10 PDF set, with both  $t\bar{t}$  events and single-top  $t + W$  events included. The generated events are interfaced with JIMMY to describe the multiple parton interactions and HERWIG to describe the parton-showering and hadronization. The samples are:

- mc12\_8TeV.105200.McAtNloJimmy\_CT10\_ttbar\_LeptonFilter.merge.NTUP\_SMWZ.\*
- mc12\_8TeV.108346.McAtNloJimmy\_AUET2CT10\_SingleTopWtChanIncl.merge.NTUP\_SMWZ.\*

The reconstruction and processing tags are r3549\_p1328. These are inclusive samples with final states that have both electrons and muons, and are used in both analysis channels. The samples are added together to form the total “Top” background.

The cross sections calculated in MC@NLO for the  $t\bar{t}$  process is 208.13 pb and for the single-top process is 20.67 pb. These processes have been calculated to NNLO in QCD in the LHC environment with a top quark mass of 172.5 GeV with the top++ 2.0 program [220, 221, 222, 223, 224, 225], and includes the resummation of the NNLO leading-logarithmic terms due to soft gluon radiation. The uncertainties due to the PDF set eigenvectors, variations between PDF sets, value of  $\alpha_S(m_Z)$ , and renormalization and factorization scales are included in the systematic uncertainty. The top quark mass is also varied by  $\pm 1$  GeV, and the resulting change in cross section is added in quadrature with the other systematic uncertainties. The computed cross sections are  $253 \pm 15$  pb for  $t\bar{t}$  and  $22.4 \pm 1.5$  pb for  $tW$ . The computed cross sections are used to scale the Top backgrounds from the generated NLO cross section values to the NNLO values and an overall systematic uncertainty of 6% is assigned to the Top background.

## CHAPTER 4. ANALYSIS EVENT SELECTION

The generated MC samples for the Top background have no events at high dilepton invariant mass due to the limited phase space. To fill the entire mass range with an estimate of the Top background, a binned  $\chi^2$  fit is used over the low-to-mid mass range and extrapolated to the full mass range. The primary fitting function used is the “dijet” function:

$$f_{\text{dijet}}(x) = a \cdot x^b \cdot x^{c \cdot \ln(x)}.$$

The fit range is varied over the range from 150 to 1000 GeV until the  $\chi^2$  probability is closest to 0.5, ensuring the errors from the fit parameters are similar to the statistical errors of the Top distribution. The fit range is 191.5-733.9 GeV, and the fit is used from 561 GeV (the stitching point) and beyond, see Figure 4.2. The fit is converted into a binned histogram, and extended to the full mass range, then stitched onto the MC distribution. The parameter errors from the fit are used to calculate “statistical” errors for the distribution using ROOT’s built-in `TH1:IntegralError()` function. Two systematic errors are calculated for the fit extrapolations. The first varies the starting and ending bins of the fit range, each changed by  $\pm 2$  bins, resulting in 25 different fits. The systematic error assigned is the maximum difference between the central values of the nominal fit used and the 25 different varied fits. The second systematic error is evaluated by using a different fit function, an “inverse monomial” function:

$$f_{\text{mono}}(x) = \frac{a}{(x + b)^c}.$$

This function is used to fit the Top distribution over the same range, and varied over the same 25 bins. Again, the maximum difference between the central values and the nominal fit is used as the systematic error. The two sources of error are added in quadrature to form the full systematic error from the fits. This is combined with the systematic uncertainty due

## CHAPTER 4. ANALYSIS EVENT SELECTION

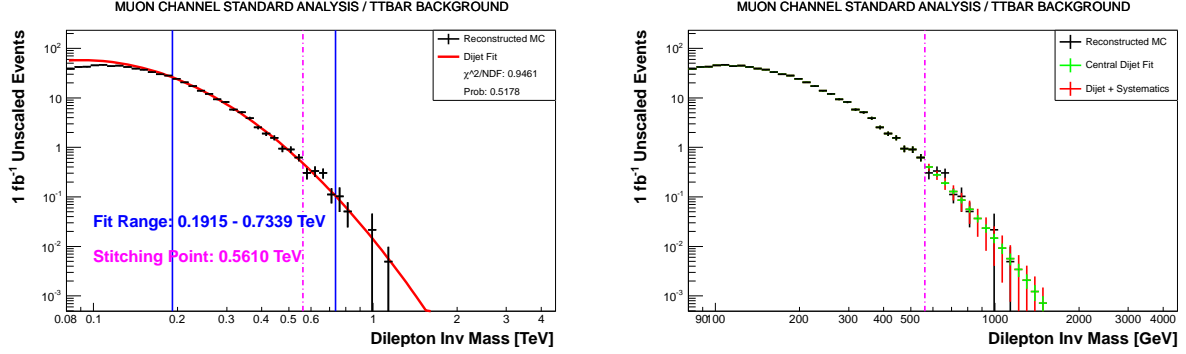


Figure 4.2: Left: The nominal fit for the Top background in the muon channel. The black histogram is the Top background and statistical errors, the blue lines show the fit range, and the pink dashed line is the stitching point. Right: The resulting final distribution is shown, with the “statistical” errors in green and the combined errors in red.

to the Top cross section after the stitching point.

### Diboson

The background due to diboson production is simulated using the HERWIG event generator with the CTEQ6L1 PDF set, at LO in QCD. There are three processes simulated,  $WW$ ,  $WZ$ , and  $ZZ$ , with 2.5 M, 1 M, and 250 K events each, respectively. The samples are:

- mc12\_8TeV.105985.Herwig\_AUET2CTEQ6L1\_WW.merge.NTUP\_SMWZ.\*
- mc12\_8TeV.105986.Herwig\_AUET2CTEQ6L1\_ZZ.merge.NTUP\_SMWZ.\*
- mc12\_8TeV.105987.Herwig\_AUET2CTEQ6L1\_WZ.merge.NTUP\_SMWZ.\*

The reconstruction and processing tags are r3549\_p1328. These are inclusive, unbinned samples with final states that have both electrons and muons and are used in both analysis channels.

Again due to limited phase space at high dilepton invariant mass, these samples are inadequate for the full mass range. Instead, dedicated samples with 10000 events each are

## CHAPTER 4. ANALYSIS EVENT SELECTION

created for each diboson channel and each lepton flavor covering the dilepton invariant mass over the ranges 400-1000 GeV and 1000+ GeV, resulting in 12 new samples:

- mc12\_8TeV.run-number.Herwig\_AUET2CTEQ6L1\_diboson\_filter\_lepton\_mass-range.merge.NTUP\_SMWZ.\*

The run numbers are from 180451-180462, diboson can be  $WW$ ,  $WZ$ , or  $ZZ$ , lepton flavor can be  $ee$  or  $mm$ , and the mass range can be 400M1000 or 1000M. The reconstruction and processing tags are r3549\_p1328. When stitching the binned samples with the unbinned samples, a cut is placed on the truth dilepton invariant mass in the unbinned samples to only keep events below 400 GeV.

The diboson production cross section was calculated in HERWIG at LO in QCD, however these cross sections have all be computed to NLO [226]. The inclusive diboson cross sections at NLO are 21.7 pb, 6.6 pb, and 1.6 pb for  $WW$ ,  $WZ$ , and  $ZZ$ , respectively. These values are used to scale the individual samples, then the samples are added together and treated as a single “Diboson” background. The theoretical uncertainty is 5% for the cross section values and is treated as a systematic uncertainty.

### 4.3 Electron Channel

The electron channel event selection and resulting invariant mass spectrum used in the search for a  $Z'$  are detailed here. This includes the event selection, corrections applied to events, the estimated backgrounds, and comparisons between the data and Monte Carlo background.

### 4.3.1 Electron Event Selection

The events with a dielectron pair are selected using the following criteria, applied in the order listed. “Flags” are simple TRUE/FALSE Boolean variables that indicate if an event experienced an error during operations. The event-level cuts are applied first.

1. Event is in the Physics All Good Standard Good Runs List - ensures the detector is in good working order.
2. Event passes trigger *EF\_g35\_loose\_g25\_loose* - ensures an electron/photon triggered the event.
3. Event passes “incomplete event” flag, *coreFlags* - removes events with a trigger or readout error.
4. Event has at least 2 electrons - only use events with at least one dielectron pair to analyze.
5. Event has at least 1 primary vertex with at least 3 tracks - ensures a “hard process” was recorded.
6. Event passes LAr Calorimeter error flag - removes events with an ECAL error or noise burst.
7. Event passes Tile Calorimeter error flag - removes events with an HCAL error or noise burst.

After the event-level cuts, the electron-level cuts are applied. The analysis loops over all the electrons stored in an event, and there must be at least two electrons that pass the listed cuts.

## CHAPTER 4. ANALYSIS EVENT SELECTION

8. Both electrons must be 1 or 3 - the algorithms used to reconstruct the electrons, these are the standard E/gamma algorithms.
9. Both electrons  $\eta$  must be in the barrel or endcap and not in the forward endcap or the “crack” region:  $|\eta| < 2.47$  and  $1.37 < |\eta| < 1.52$  - ensures electrons are in the “best” regions of the detector.
10. Both electrons pass electron object quality in the calorimeter flag - removes electrons with bad cluster/shower shapes.
11. The leading electron must have  $p_T > 40$  GeV and the subleading electron must have  $p_T > 30$  GeV - matches with trigger event filter requirements and removes low-energy events.
12. Both electrons pass isEM *medium++* identification - hit and shower shape variables for electron identification.
13. The electron transverse energy is isolated in a cone of  $\Delta R < 0.2$ . The total corrected transverse energy of all other particles in this cone must be less than  $0.007 \times E_T + 5.0$  GeV for the leading electron. For subleading electrons, the total must be less than  $0.022 \times E_T + 6.0$  GeV. The values have been tuned studying MC samples to remove electrons from hadronic decays in flight while maximizing signal to noise in the search region.

After the electron-level cuts, the dielectron cuts are applied.

14. At least 2 electrons must pass the above cuts; if more than 2 pass the cuts, use the event with the two electrons with the highest scalar summed  $p_T$ . This ensures at most one candidate per event, which is assumed as part of the search and limit-setting framework.



## CHAPTER 4. ANALYSIS EVENT SELECTION

15. Invariant mass of final electron pair must have  $m_{ee} > 80$  GeV - dielectron event is in the normalization or search region.

There is not an explicit opposite-charge requirement due to the unknown charge misidentification rate for electrons at high momenta. The diphoton trigger *EF\_g35\_loose\_g25\_loose* is used as it is based solely on ECAL information and does not require any hits in the ID. This is to prevent any inefficiencies due to track matching at the Trigger or Event Filter stages. The isEM *medium++* requirement on both electrons includes the required hit information in the ID and ECAL, see [227].

### 4.3.2 Electron Event Corrections

For data samples, the only correction applied is to the measured energy scale. A tool is provided by the ATLAS E/gamma performance group to perform this correction [186]. The tool uses the electron energy and  $\eta$  to rescale the measured value. The rescaling values are calibrated using  $Z^0$  peak data.

In Monte Carlo samples, four different corrections are applied. The first is a smearing of the MC electron energy to obtain the same energy resolution observed in data [186]. This is done with the same tool as the data energy rescaling. The second is a reweighting of the MC event based on the  $E_T$  and  $\eta$  of the two electrons in the event. Small differences in the electron reconstruction and identification efficiency between data and MC as a function of  $\eta$  and  $E_T$  have been measured. The E/gamma performance group provides a tool to apply scale factors [228] to bring them into better agreement. The third and fourth corrections are two other scale factors, one for the isolation requirement and one for the trigger item used in event selection. Both are consistent with 1.00 to within 1%. A full discussion of the scale factors can be found in Appendix C.

### 4.3.3 Electron $Z'$ Signal

The electron channel expected  $Z'$  signal templates are in Figure 4.3. These are created by the procedure outlined in Section 4.2.1. The global acceptance for the SSM  $Z'$  over the mass range between 150 and 3500 GeV is also shown.

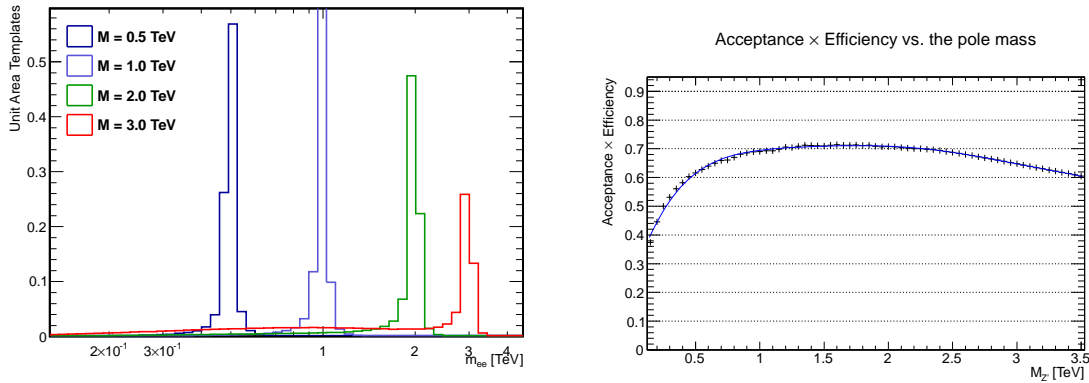


Figure 4.3:  $Z'$  signal templates at representative mass points for the dielectron selection (left), and the detector acceptance times efficiency for the expected signal (right).

### 4.3.4 Electron Background Estimation

The total SM background estimation for the electron channel is done in two parts. The first part is the “real” background due to two real electrons being produced in the event. This is estimated using generated Monte Carlo samples. The second part is the “fake” background due to one or more jets in an event “faking” the signal of an electron. This is estimated using a data-driven method. The two parts are then added together to form the expected total background that will be compared to the data.

### Real Dielectron Backgrounds

The SM background due to two real electrons is dominated by the three processes discussed in Section 4.2.2: Drell-Yan, Top, and Diboson. These are MC events, where a truth-level cut is applied to only keep events with at least two true electrons in order to prevent double-counting with the fake dielectron background. After scaling the different backgrounds by their calculated cross sections to a nominal integrated luminosity of  $1 \text{ fb}^{-1}$ , the samples are added together and scaled to the expected luminosity. In both the total MC and the data (after including the events due to fake electrons, see below), the number of events in the invariant mass window from 80-110 GeV are added up, and the full MC mass distribution is rescaled to match the data. The scaling is found to be 1.021, within the luminosity uncertainty of 2.8%.

### Fake Dielectron Backgrounds

The background due to at least one electron being misidentified from a jet in the calorimeter is estimated using the “fake factor” or “matrix” method. The idea is to loosen some of the electron identification criteria and estimate the rate at which the looser objects are reconstructed as electrons. This is a data-driven method and uses the full 2012 data set of  $\sim 21 \text{ fb}^{-1}$ . The details for this estimation can be found in Appendix D.

### 4.3.5 Electron Data - Monte Carlo Comparison

The dielectron invariant mass spectrum after event selection is shown in Figure 4.4. This includes the data and expected SM background, and shows the ratio between the two with the systematic errors included. In addition, the SSM  $Z'$  model at two mass points are overlaid to demonstrate possible signal shape. The  $p_T$  distributions for the leading and

## CHAPTER 4. ANALYSIS EVENT SELECTION

subleading electrons are shown in Figure 4.5. The electron event selection numbers over 7 mass bins is listed in Table 4.3, including statistical, systematic, and combined errors for each background.

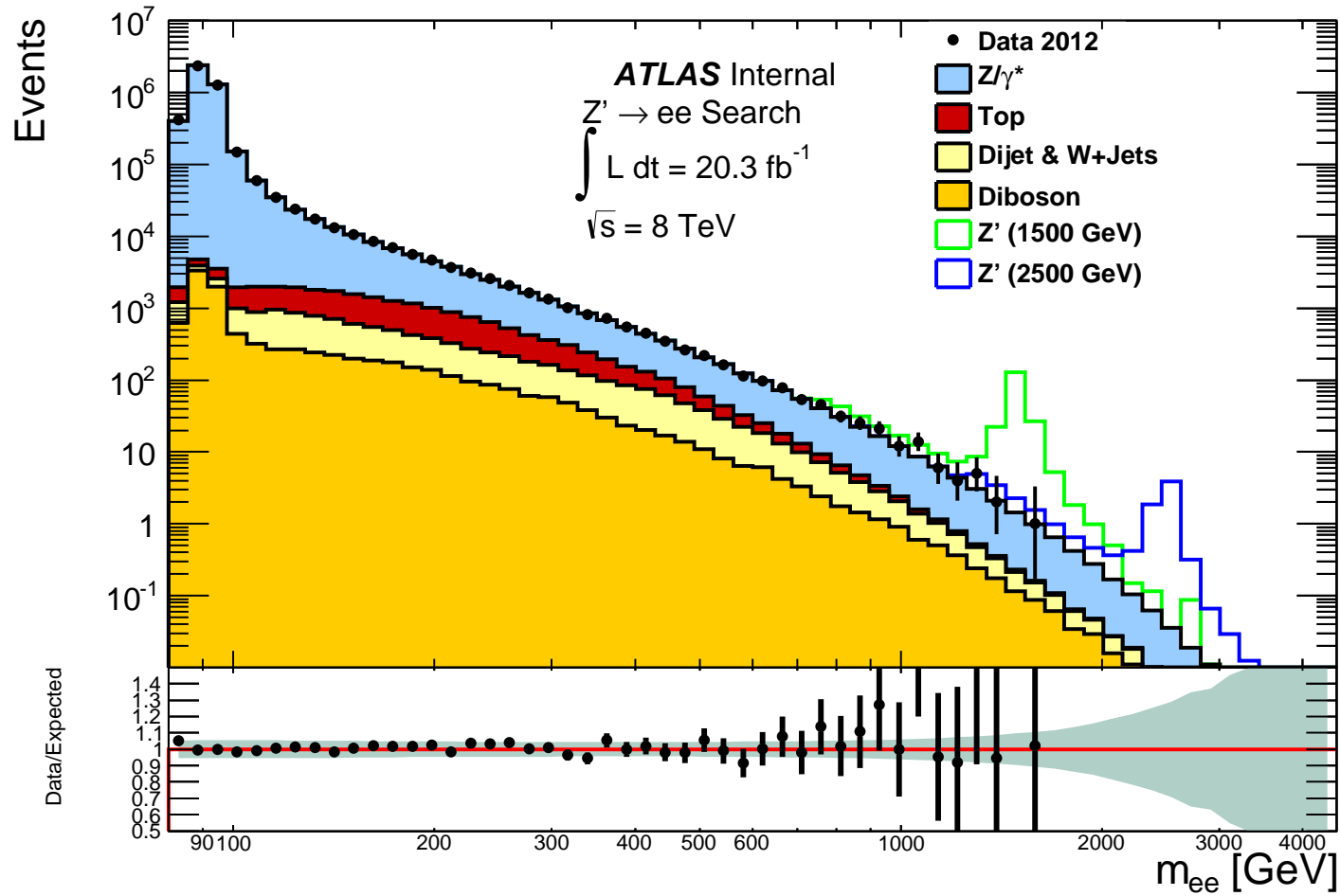


Figure 4.4: The dielectron invariant mass spectrum after event selection. The binning is constant in  $\log(m_{ee})$ . The Top and Dijet &  $W$ +jets backgrounds have been fit and extrapolated to cover the full mass range. Two representative  $Z'$  signals have been overlaid. The ratio in the lower plot shows the agreement between the observed and expected distributions. The error bars on the data points are statistical and the band in the ratio plot is the combined systematic error.

$m_{ee}$ [GeV]	80 - 110	110 - 200	200 - 400	400 - 800	800 - 1200	1200 - 3000	3000 - 4500
$Z^0/\gamma^*$	$4243000 \pm 4000$	$121600 \pm 400$	$13980 \pm 70$	$1322 \pm 7$	$70.03 \pm 0.27$	$10.01 \pm 0.04$	$0.00823 \pm 0.00004$
Top	$4330 \pm 240$	$8200 \pm 600$	$2900 \pm 500$	$200 \pm 80$	$3.1 \pm 0$	$0.16 \pm 0$	$0.00005 \pm 0$
Diboson	$6650 \pm 40$	$1880 \pm 21$	$680 \pm 13$	$94.4 \pm 1.8$	$5.90 \pm 0.21$	$1.035 \pm 0.024$	$0.00006 \pm 0.00005$
Dijet, $W$ +jet	$1300 \pm 600$	$3930 \pm 230$	$1290 \pm 190$	$230 \pm 50$	$9 \pm 0$	$0.9 \pm 0$	$0.0022 \pm 0$
Total	$4256000 \pm 4000$	$135600 \pm 700$	$18800 \pm 500$	$1850 \pm 90$	$87.99 \pm 0.35$	$12.10 \pm 0.05$	$0.01051 \pm 0.00006$
Data	4257744	136200	18986	1862	99	9	0

$m_{ee}$ [GeV]	80 - 110	110 - 200	200 - 400	400 - 800	800 - 1200	1200 - 3000	3000 - 4500
$Z^0/\gamma^*$	$4240000 \pm 230000$	$122000 \pm 7000$	$14000 \pm 800$	$1320 \pm 70$	$70 \pm 5$	$10.0 \pm 1.0$	$0.008 \pm 0.004$
Top	$4330 \pm 260$	$8200 \pm 500$	$2850 \pm 170$	$198 \pm 13$	$3.1 \pm 0.8$	$0.16 \pm 0.08$	$0.00005 \pm 0.00009$
Diboson	$6650 \pm 330$	$1880 \pm 90$	$680 \pm 33$	$94 \pm 5$	$5.90 \pm 0.29$	$1.03 \pm 0.05$	$0.00006 \pm 0.00003$
Dijet, $W$ +jet	$1260 \pm 240$	$3900 \pm 800$	$1290 \pm 260$	$230 \pm 50$	$9.0 \pm 2.3$	$0.9 \pm 0.5$	$0.002 \pm 0.004$
Total	$4260000 \pm 230000$	$136000 \pm 7000$	$18800 \pm 800$	$1850 \pm 80$	$88 \pm 5$	$12.1 \pm 1.1$	$0.011 \pm 0.005$
Data	4257744	136200	18986	1862	99	9	0

$m_{ee}$ [GeV]	80 - 110	110 - 200	200 - 400	400 - 800	800 - 1200	1200 - 3000	3000 - 4500
$Z^0/\gamma^*$	$4240000 \pm 230000$	$122000 \pm 7000$	$14000 \pm 800$	$1320 \pm 70$	$70 \pm 5$	$10.0 \pm 1.0$	$0.008 \pm 0.004$
Top	$4300 \pm 400$	$8200 \pm 700$	$2900 \pm 500$	$200 \pm 80$	$3.1 \pm 0.8$	$0.16 \pm 0.08$	$0.00005 \pm 0.00009$
Diboson	$6650 \pm 330$	$1880 \pm 90$	$680 \pm 40$	$94 \pm 5$	$5.9 \pm 0.4$	$1.03 \pm 0.06$	$0.00006 \pm 0.00005$
Dijet, $W$ +jet	$1300 \pm 700$	$3900 \pm 800$	$1290 \pm 320$	$230 \pm 70$	$9.0 \pm 2.3$	$0.9 \pm 0.5$	$0.002 \pm 0.004$
Total	$4260000 \pm 230000$	$136000 \pm 7000$	$18800 \pm 1000$	$1850 \pm 120$	$88 \pm 5$	$12.1 \pm 1.1$	$0.011 \pm 0.005$
Data	4257744	136200	18986	1862	99	9	0

Table 4.3: Dielectron event yield tables with statistical (top), systematic (middle) and total (bottom) uncertainties. The first column is used to normalize the MC total to the observed data total.

CHAPTER 4. ANALYSIS EVENT SELECTION

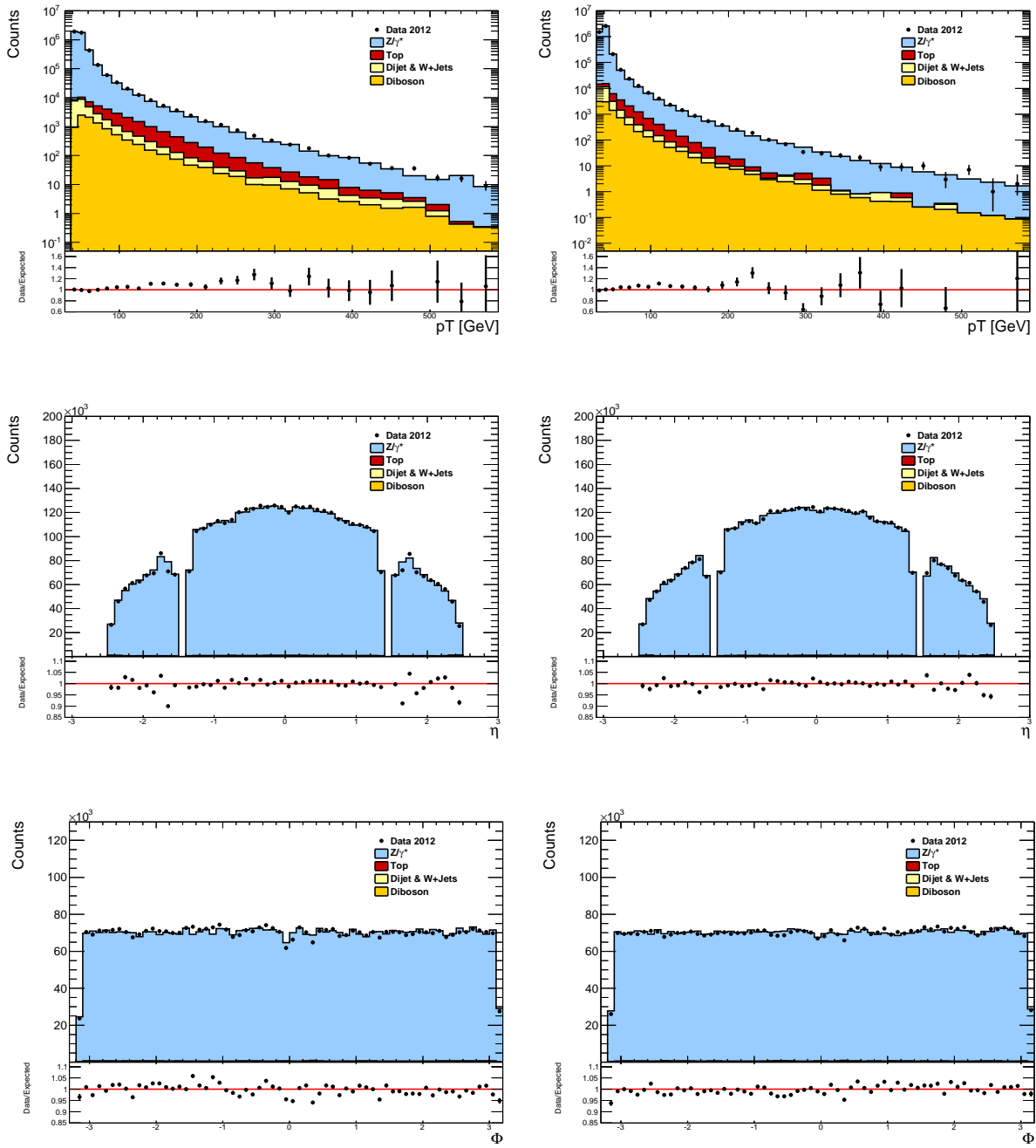


Figure 4.5: Leading (left) and subleading (right) electron kinematic distributions after event selection. The top row are the  $p_T$  distributions, the middle row are the  $\eta$  distributions, and the bottom row are the  $\phi$  distributions.

## 4.4 Muon Channel

The muon channel event selection and resulting invariant mass spectrum used in the search for a  $Z'$  are detailed here. This includes the event selection, corrections applied to events, the estimated backgrounds, and comparisons between the data and Monte Carlo background.

### 4.4.1 Muon Event Selection

The events with a dimuon pair are selected using the following criteria, applied in the order listed. The event-level cuts are applied first.

1. Event is in the Muon Combined Performance Good Runs List - ensures the muon tracking portion of the detector is in good working order.
2. Event passes “incomplete event” flag, *coreFlags* - removes events with a trigger error.
3. Event passes trigger *EF\_mu24i\_tight* OR *EF\_mu36\_tight* - ensures a muon triggered the event.
4. Event has at least 1 primary vertex with at least 3 tracks - ensures a “hard process” was recorded.

After the event-level cuts, the muon-level cuts are applied. In each event there must be at least two muons that pass the listed cuts.

5. Muons must be MUID combined - reconstruction with tracks in both the MS and ID.
6. Muons must have  $p_T > 25$  GeV - matches with trigger event filter requirements and removes low-energy events.
7. Muons must pass hit requirements in the ID - ensures well-measured track in the ID.



## CHAPTER 4. ANALYSIS EVENT SELECTION

8. Muons must have a transverse impact parameter  $d_0$  within 0.2 mm of the primary vertex - ensures muons come from the hard process and reduces cosmic ray background.
9. Muons must have a longitudinal impact parameter  $z_0$  within 1.0 mm of the primary vertex - ensures muons come from the hard process and reduces cosmic ray background.
10. Muons must be isolated in a cone of  $\Delta R < 0.3$  with the transverse momenta of all other particles in the cone totaling less than 5% of the muon  $p_T$  - reduces background from hadronic decays.
11. Muons must pass hit requirements in the MS - ensures well-measured track in the MS.

After the muon-level cuts, the dimuon cuts are applied.

12. At least 2 muons must pass the above cuts.
13. Dimuon pairs are formed from opposite-sign muons; if more than one pair can be formed, use the pair with the highest summed  $p_T$ . This ensures at most one candidates per event, which is assumed as part of the search and limit-setting framework.
14. Invariant mass of final muon pair must have  $m_{\mu\mu} > 80$  GeV - the dimuon event is in the normalization or search region.

Details about the ID and MS hit requirements are listed below, based on the recommendation of the Muon Combined Performance group (MCP). There are two different selection criteria for the MS hits with different resolutions for the expected  $Z'$  signal, resulting in two muon channels used in this search. The “tight” muon channel uses the standard selection for both muons labeled the “tight” muon channel. The “loose” muon channel uses a modified selection in the MS only for the second muon to increase the detector acceptance. These selections are described below, with further details found in Appendix E.

### Inner Detector Hit Requirements

The hit requirements in the ID as recommended by the MCP are required by all muons in the event selection. These are:

- At least 1 BLayer hit, ignoring dead sensors.
- At least 1 Pixel hit, including dead sensors.
- At least 5 SCT hits, including dead sensors.
- No more than 2 dead sensors crossed in Pixel or SCT.
- If  $0.1 < |\eta| < 1.9$ , at least 6 TRT hits including TRT outliers, and outlier fraction  $< 0.9$ .
- If  $|\eta| < 0.1$  OR  $|\eta| > 1.9$ , if there are at least 6 TRT hits including TRT outliers, require outlier fraction  $< 0.9$ . Otherwise, no TRT requirement.

### Standard Muon Spectrometer Hit Requirements

The standard hit requirements in the MS as recommended by the MCP are:

- Three-station hit requirements must satisfy one of the following:
  - At least 3 hits in each layer of BI, BM, BO drift chambers.
  - At least 3 hits in each layer of EI, EE, EM drift chambers.
  - At least 3 hits in each layer of EI, EM, EO drift chambers.
  - At least 3 hits in each layer of EM, EO drift chambers AND at least 2 “unspoiled” eta hits in the CSC chambers.

## CHAPTER 4. ANALYSIS EVENT SELECTION

- At least 1  $\phi$  hit in 2 layers of RPC/TGC/CSC chambers.
- No hits in the BIS7/8 or BEE chambers.
- The significance between the  $p_T$  measured in the ID standalone track and the MS standalone track must be less than 5.0. The error used is the estimated track fit covariance.

$$\text{significance} = \frac{p_T^{ID} - p_T^{MS}}{\sqrt{\sigma_{p_T^{ID}}^2 + \sigma_{p_T^{MS}}^2}} < 5.0. \quad (4.2)$$

These requirements are used for both muons in the tight channel and one muon in the loose channel. Between 2011 and 2012 data taking at ATLAS, one complete side of EE chambers was installed on the C side and 3 large EE chambers were installed on the A side, which led to a 15% gain in relative acceptance for the expected  $Z'$  signal. Details of these chambers' performance can be found in Appendix E.

### Two-Station Muon Spectrometer Hit Requirements

The two-station hit requirements in the MS are:

- At least 5 hits in the BI and BO drift chambers.
- At least 1  $\phi$  hit in 1 layer of RPCs.
- No hits in the BIS7/8 or any endcap chambers.
- No hits in the following barrel towers, which are excluded due to residual misalignment:
  - Sectors 4 or 6, with  $|\eta| > 0.85$ .
  - Sector 9, with  $0.2 < |\eta| < 0.35$ .

## CHAPTER 4. ANALYSIS EVENT SELECTION

– Sector 13, with  $0.0 < |\eta| < 0.2$ .

- The significance, defined above in Equation 4.2, between the  $p_T$  measured in the ID standalone track and the MS standalone track must be less than 3.0. The error used is the estimated track fit covariance.

In this analysis, the loose channel requires a selected two-station muon must be paired with a three-station muon of the opposite charge. The higher hit requirement in the BI and BO chambers allows for a better measurement of the angle of the track segment with respect to the primary vertex. The BI and BO chambers requirement allows for the maximum amount of total bending between measurements due to the magnetic field. This improves the two-station performance, although the resolution remains worse than for three-station selection muons. See Appendix E for details. There is an 8% gain in relative acceptance for the expected  $Z'$  signal by including these muons.

### 4.4.2 Muon Event Corrections

No corrections are applied to muons in the data. In the Monte Carlo events, a correction is applied to the  $p_T$  to obtain the same momentum resolution observed in data. A tool is provided by the Muon Combined Performance group to perform this correction [229]. This correction “smears” the simulated muon momentum in both the ID and MS based on the  $p_T$  and  $\eta$  of the muon. The smearing parameters are calibrated using  $Z^0 \rightarrow \mu\mu$  peak data. A full discussion of muon resolution and smearing can be found in Appendix E.

### 4.4.3 Muon $Z'$ Signal

The muon channel expected  $Z'$  signal templates for the tight and loose channel are in Figure 4.6. These are created by the procedure outlined in Section 4.2.1. The global acceptances

## CHAPTER 4. ANALYSIS EVENT SELECTION

for the SSM  $Z'$  over the mass range between 150 and 3500 GeV are also shown for the two channels.

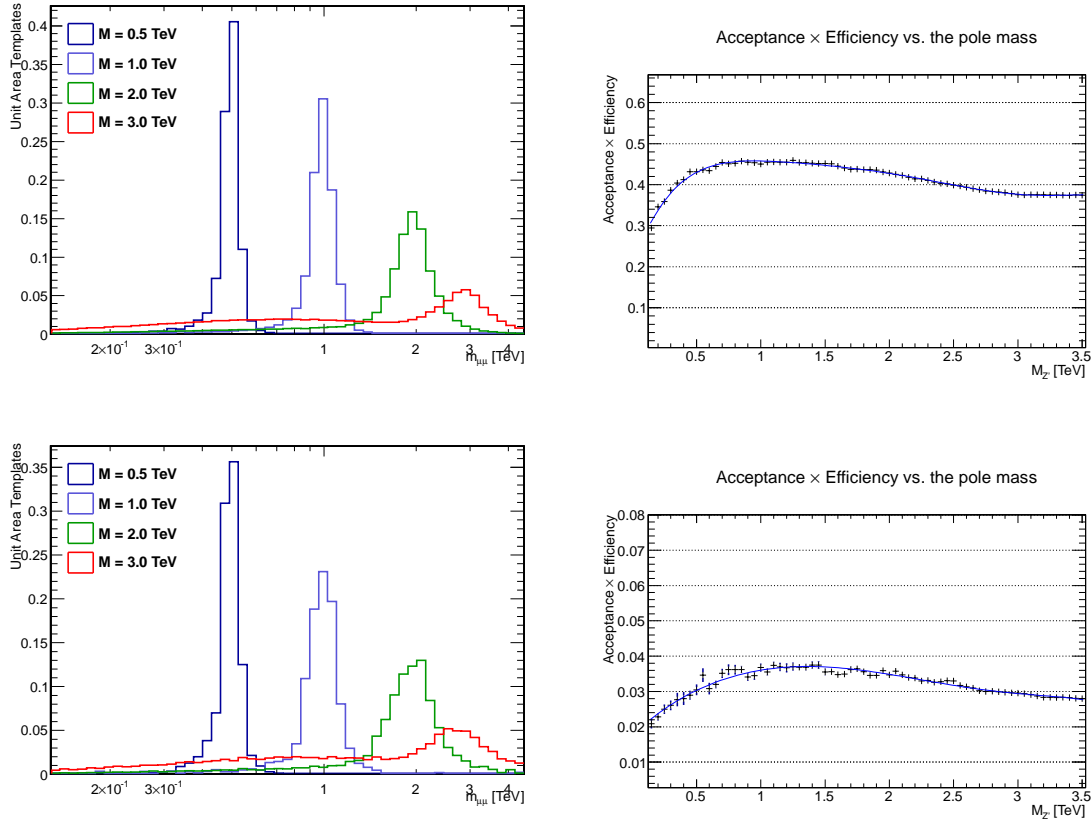


Figure 4.6: Left:  $Z'$  signal templates at representative mass points. Right: The detector acceptance times efficiency for the expected signal. Top: Tight channel. Bottom: Loose channel.

### 4.4.4 Muon Background Estimation

The total background estimation for the muon channel is done solely through generated Monte Carlo samples. The “fake” rate for single muons has been estimated to be less than 1 part in  $5 \times 10^{-4}$  at  $p_T = 20$  GeV, and improves with  $p_T$ . This is a negligible effect for this

analysis.

### Real Dimuon Backgrounds

The Standard Model background due to two real muons is dominated by the three processes discussed in Section 4.2.2: Drell-Yan, Top, and Diboson. After scaling the different backgrounds by their cross sections to a nominal luminosity of  $1 \text{ fb}^{-1}$ , the samples are added together and scaled to the expected luminosity. In both the total MC and the data, the number of events in the invariant mass window from 80-110 GeV are added up, and the full MC mass distribution is rescaled to match the data. The scaling is found to be 0.976 in the tight channel, within the luminosity uncertainty of 2.8%. The scaling is found to be 0.921 in the loose channel, with more limited statistics in both data and MC.

#### 4.4.5 Muon Data - Monte Carlo Comparison

The dimuon invariant mass spectrum after event selection for the tight selection channel is shown in Figure 4.7 and for the loose selection channel in Figure 4.9. This includes the data and expected SM background and shows the ratio between the two with the systematic errors included. In addition, the SSM  $Z'$  model at two mass points are overlaid to demonstrate possible signal shape. The  $p_T$ ,  $\eta$ , and  $\phi$  distributions for the leading and subleading muons for the tight selection channel are shown in Figure 4.8 and for the loose selection channel in Figure 4.10. The muon event yields over 7 mass bins in the tight channel are listed in Table 4.4 and for the loose channel in Table 4.5, including statistical, systematic, and combined errors for each background.

The total muon channel, the sum of the tight and loose channels, is included for visual purposes but is not used in the search or limit setting. The invariant mass spectrum is in

## CHAPTER 4. ANALYSIS EVENT SELECTION

Figure 4.11, the leading and subleading  $p_T$  distributions are in Figure 4.12, and the event totals are listed in Table 4.6.

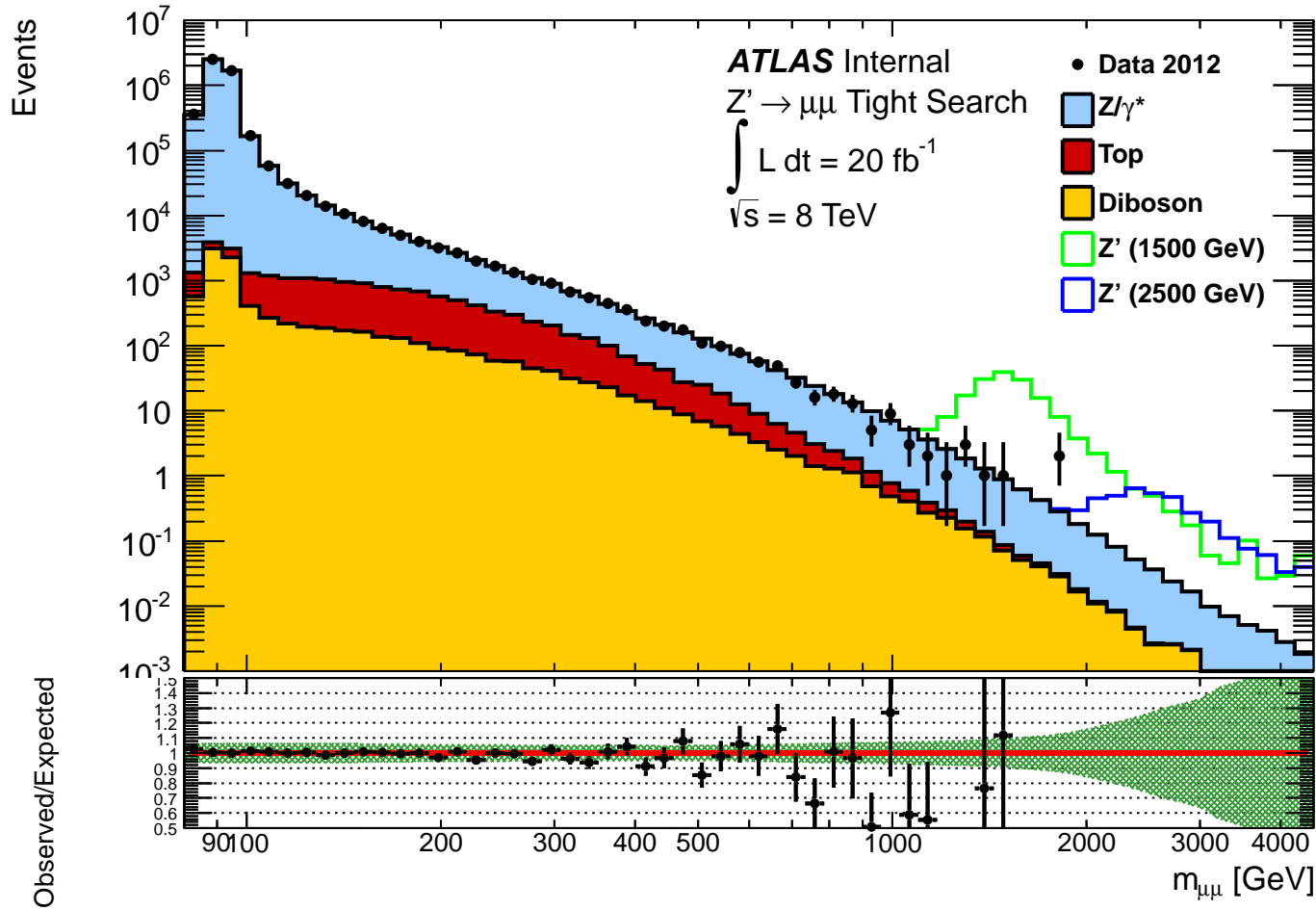


Figure 4.7: The dimuon invariant mass spectrum in the **tight channel** after event selection. The binning is constant in  $\log(m_{\mu\mu})$ . The Top background has been fit and extrapolated to cover the full mass range. Two representative  $Z'$  signals have been overlaid. The ratio in the lower plot shows the agreement between the observed and expected distributions. The error bars on the data points are statistical and the band in the ratio plot is the combined systematic error.



$m_{\mu\mu}[\text{GeV}]$	80 - 110	110 - 200	200 - 400	400 - 800	800 - 1200	1200 - 3000	3000 - 4500
$Z^0/\gamma^*$	$4762000 \pm 9000$	$105000 \pm 1000$	$10200 \pm 600$	$900 \pm 70$	$46 \pm 4$	$6.7 \pm 0.8$	$0.029 \pm 0.015$
Top	$4100 \pm 200$	$6600 \pm 500$	$2100 \pm 400$	$140 \pm 80$	$2.6 \pm 0.5$	$0.14 \pm 0.05$	$0 \pm 0$
Diboson	$6600 \pm 200$	$1430 \pm 160$	$490 \pm 130$	$61 \pm 15$	$4.0 \pm 2.1$	$0.65 \pm 0.30$	$0.0018 \pm 0.0018$
Total	$4773000 \pm 9400$	$113000 \pm 1100$	$12900 \pm 700$	$1110 \pm 120$	$52 \pm 5$	$7.5 \pm 0.9$	$0.031 \pm 0.016$
Data	4772951	112913	12681	1065	45	8	0

$m_{\mu\mu}[\text{GeV}]$	80 - 110	110 - 200	200 - 400	400 - 800	800 - 1200	1200 - 3000	3000 - 4500
$Z^0/\gamma^*$	$4760000 \pm 320000$	$105000 \pm 7000$	$10200 \pm 700$	$900 \pm 60$	$45.7 \pm 3.5$	$6.7 \pm 0.8$	$0.029 \pm 0.016$
Top	$4050 \pm 240$	$6600 \pm 400$	$2140 \pm 130$	$145 \pm 13$	$2.6 \pm 1.5$	$0.14 \pm 0.13$	$0 \pm 0$
Diboson	$6560 \pm 330$	$1430 \pm 70$	$492 \pm 25$	$61 \pm 3$	$3.95 \pm 0.20$	$0.646 \pm 0.032$	$0.0018 \pm 0.0001$
Total	$4770000 \pm 320000$	$113000 \pm 7000$	$12900 \pm 700$	$1110 \pm 60$	$52 \pm 4$	$7.5 \pm 0.8$	$0.031 \pm 0.016$
Data	4772951	112913	12681	1065	45	8	0

$m_{\mu\mu}[\text{GeV}]$	80 - 110	110 - 200	200 - 400	400 - 800	800 - 1200	1200 - 3000	3000 - 4500
$Z^0/\gamma^*$	$4760000 \pm 320000$	$105000 \pm 7000$	$10200 \pm 1000$	$900 \pm 100$	$46 \pm 5$	$6.7 \pm 1.1$	$0.029 \pm 0.022$
Top	$4050 \pm 320$	$6600 \pm 600$	$2100 \pm 400$	$140 \pm 80$	$2.6 \pm 1.6$	$0.14 \pm 0.14$	$0 \pm 0$
Diboson	$6560 \pm 370$	$1430 \pm 170$	$490 \pm 130$	$61 \pm 16$	$4.0 \pm 2.1$	$0.65 \pm 0.30$	$0.0018 \pm 0.0018$
Total	$4770000 \pm 320000$	$113000 \pm 8000$	$12900 \pm 1000$	$1110 \pm 130$	$52 \pm 6$	$7.5 \pm 1.2$	$0.031 \pm 0.023$
Data	4772951	112913	12681	1065	45	8	0

Table 4.4: Dimuon event yield tables for the **tight channel** with statistical (top), systematic (middle) and total (bottom) uncertainties. The first column is used to normalize the MC total to the observed data total.

## CHAPTER 4. ANALYSIS EVENT SELECTION

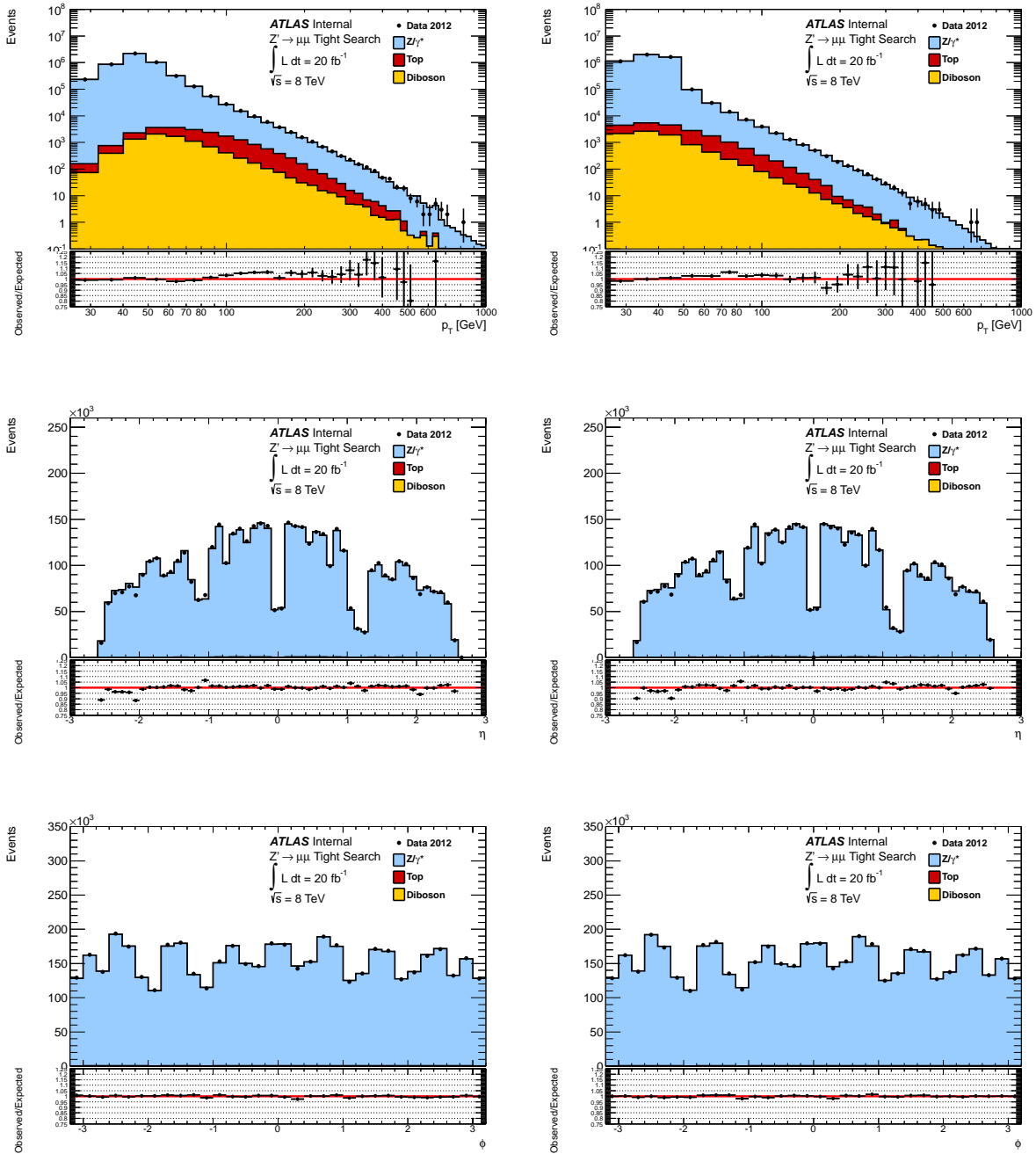


Figure 4.8: Leading (left) and subleading (right) distributions in the muon **tight channel** after event selection. The top row are the  $p_T$  distributions, the middle row are the  $\eta$  distributions, and the bottom row are the  $\phi$  distributions.

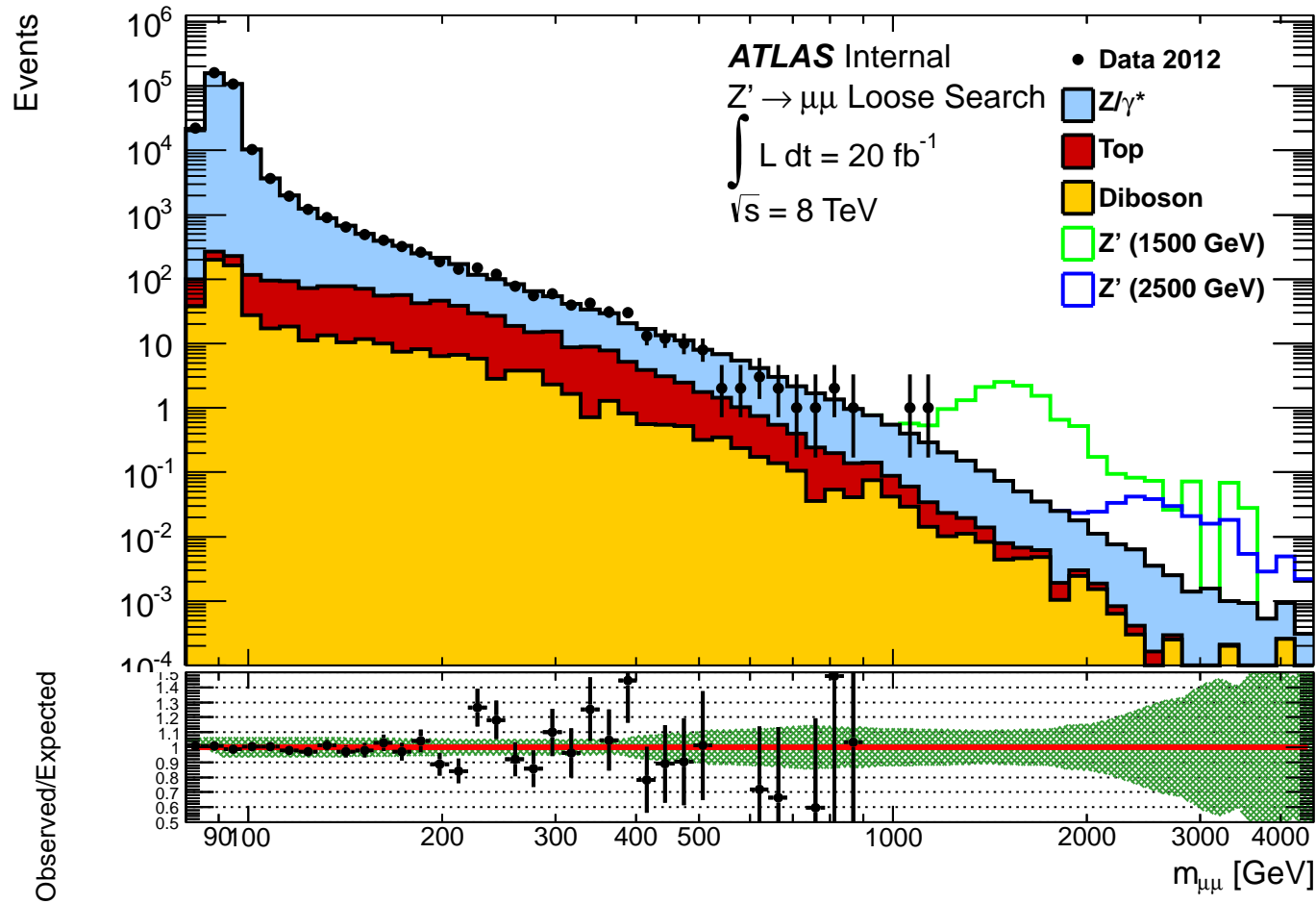


Figure 4.9: The dimuon invariant mass spectrum in the **loose channel** after event selection. The binning is constant in  $\log(m_{\mu\mu})$ . The Top background has been fit and extrapolated to cover the full mass range. Two representative  $Z'$  signals have been overlaid. The ratio in the lower plot shows the agreement between the observed and expected distributions. The error bars on the data points are statistical and the band in the ratio plot is the combined systematic error.

$m_{\mu\mu}[\text{GeV}]$	80 - 110	110 - 200	200 - 400	400 - 800	800 - 1200	1200 - 3000	3000 - 4500
$Z^0/\gamma^*$	$302000 \pm 2300$	$6510 \pm 230$	$600 \pm 150$	$58 \pm 18$	$3.4 \pm 1.1$	$0.55 \pm 0.23$	$0.005 \pm 0.004$
Top	$340 \pm 60$	$500 \pm 120$	$160 \pm 80$	$12.9 \pm 2.9$	$0.37 \pm 0.25$	$0.03 \pm 0.04$	$0 \pm 0$
Diboson	$440 \pm 40$	$100 \pm 40$	$33 \pm 24$	$3.0 \pm 2.2$	$0.24 \pm 0.22$	$0.05 \pm 0.04$	$0.0006 \pm 0.0006$
Total	$302800 \pm 2300$	$7110 \pm 270$	$790 \pm 170$	$74 \pm 18$	$4.0 \pm 1.2$	$0.63 \pm 0.25$	$0.005 \pm 0.005$
Data	302788	7098	798	57	4	0	0
$m_{\mu\mu}[\text{GeV}]$	80 - 110	110 - 200	200 - 400	400 - 800	800 - 1200	1200 - 3000	3000 - 4500
$Z^0/\gamma^*$	$302000 \pm 20000$	$6500 \pm 500$	$600 \pm 40$	$58 \pm 4$	$3.36 \pm 0.26$	$0.55 \pm 0.06$	$0.0046 \pm 0.0025$
Top	$344 \pm 21$	$500 \pm 30$	$158 \pm 11$	$13 \pm 7$	$0.4 \pm 0.4$	$0.03 \pm 0.04$	$0 \pm 0$
Diboson	$444 \pm 22$	$98 \pm 5$	$32.6 \pm 1.6$	$3.00 \pm 0.15$	$0.243 \pm 0.012$	$0.0471 \pm 0.0024$	$0.00059 \pm 0.00003$
Total	$303000 \pm 20000$	$7100 \pm 500$	$790 \pm 40$	$74 \pm 8$	$4.0 \pm 0.5$	$0.63 \pm 0.08$	$0.0052 \pm 0.0026$
Data	302788	7098	798	57	4	0	0
$m_{\mu\mu}[\text{GeV}]$	80 - 110	110 - 200	200 - 400	400 - 800	800 - 1200	1200 - 3000	3000 - 4500
$Z^0/\gamma^*$	$302000 \pm 21000$	$6500 \pm 500$	$600 \pm 150$	$58 \pm 18$	$3.4 \pm 1.1$	$0.55 \pm 0.23$	$0.005 \pm 0.005$
Top	$340 \pm 60$	$500 \pm 120$	$160 \pm 80$	$13 \pm 8$	$0.4 \pm 0.5$	$0.03 \pm 0.06$	$0 \pm 0$
Diboson	$440 \pm 50$	$100 \pm 40$	$33 \pm 24$	$3.0 \pm 2.2$	$0.24 \pm 0.22$	$0.05 \pm 0.04$	$0.0006 \pm 0.0006$
Total	$303000 \pm 21000$	$7100 \pm 500$	$790 \pm 180$	$74 \pm 20$	$4.0 \pm 1.3$	$0.63 \pm 0.26$	$0.0053 \pm 0.0053$
Data	302788	7098	798	57	4	0	0

Table 4.5: Dimuon event yield tables for the **loose channel** with statistical (top), systematic (middle) and total (bottom) uncertainties. The first column is used to normalize the MC total to the observed data total.

## CHAPTER 4. ANALYSIS EVENT SELECTION

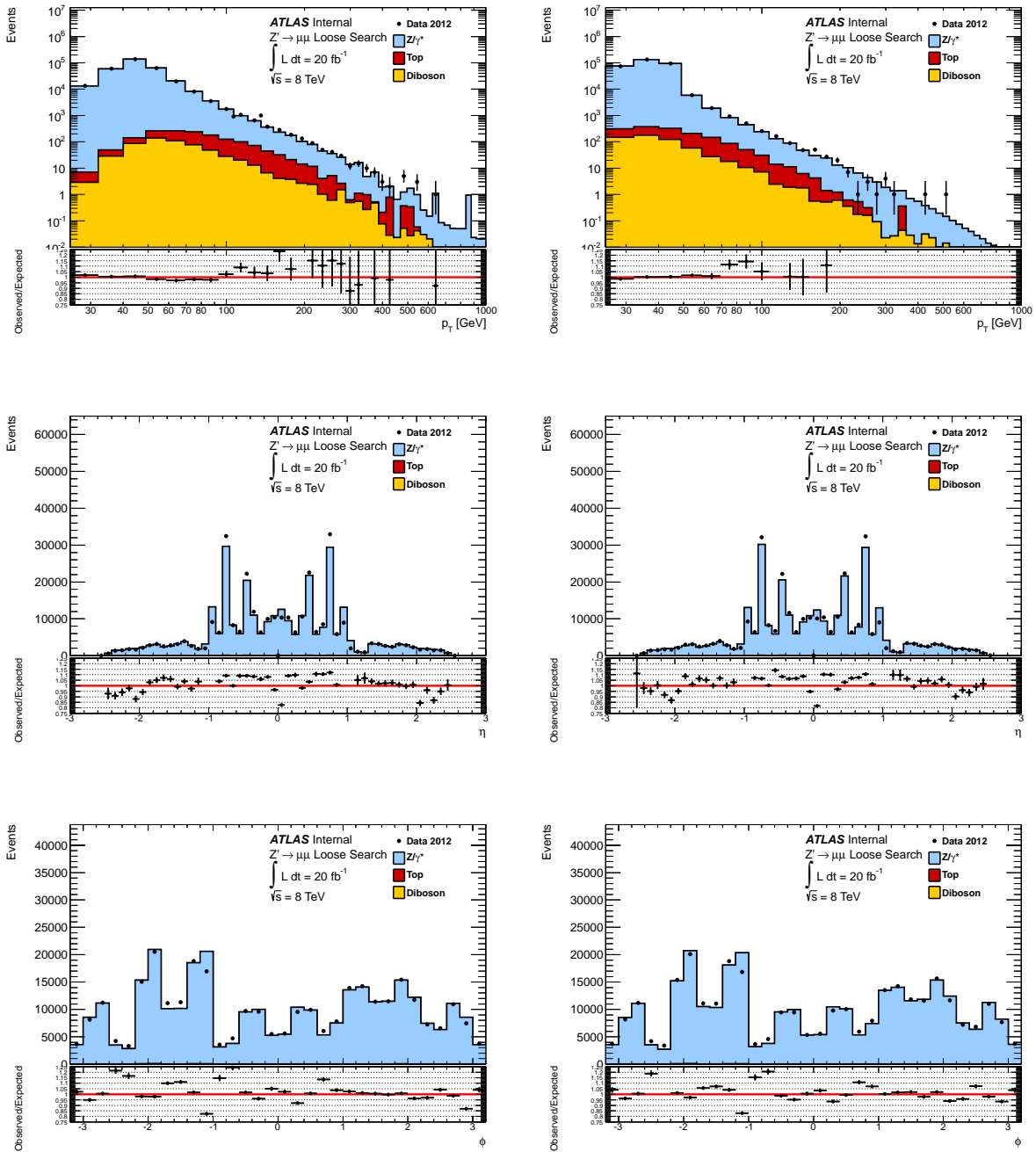


Figure 4.10: Leading (left) and subleading (right) distributions in the muon **loose channel** after event selection. The top row are the  $p_T$  distributions, the middle row are the  $\eta$  distributions, and the bottom row are the  $\phi$  distributions.

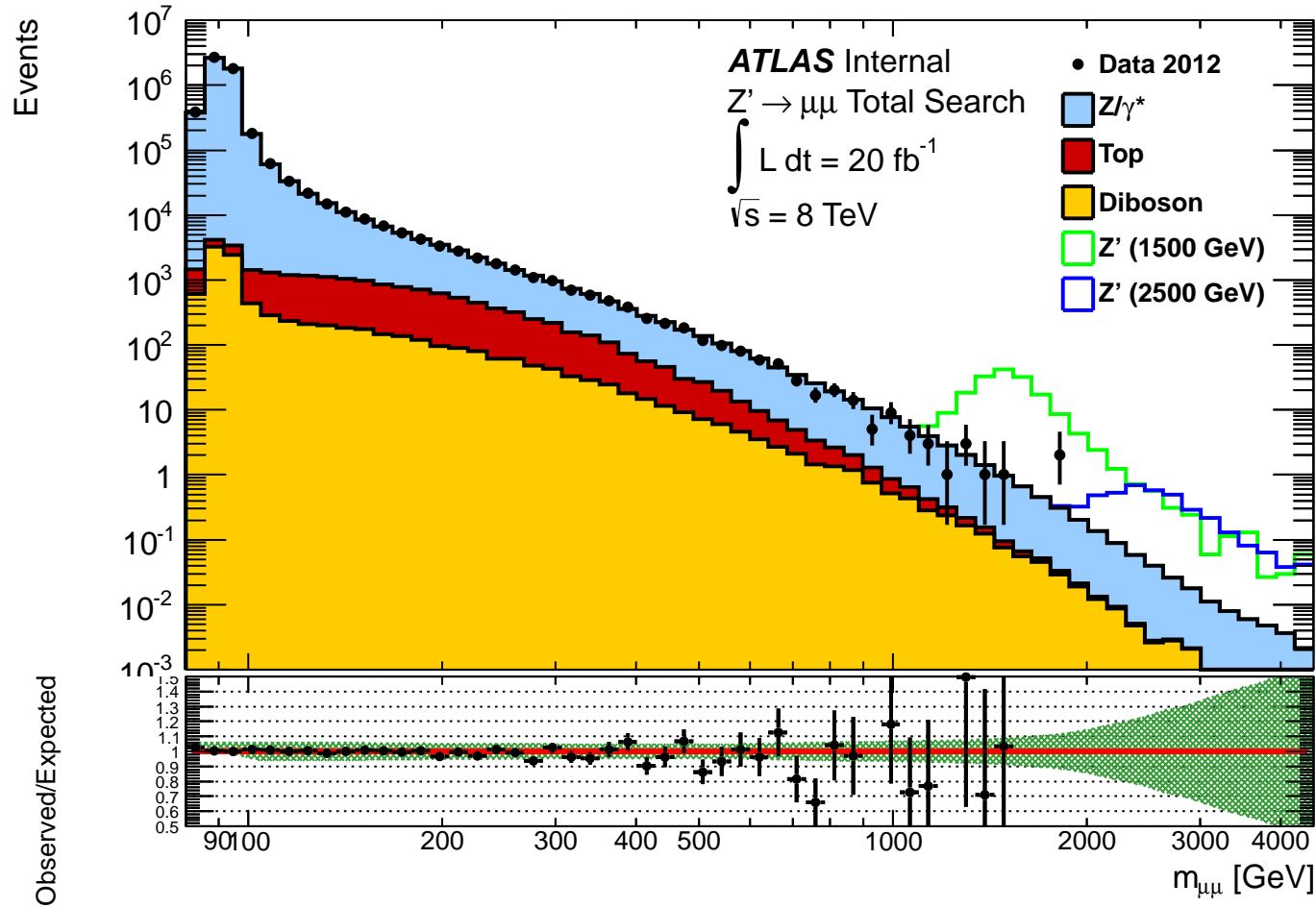


Figure 4.11: The dimuon invariant mass spectrum in the **tight + loose channel** after event selection. The binning is constant in  $\log(m_{\mu\mu})$ . The Top background has been fit and extrapolated to cover the full mass range. Two representative  $Z'$  signals have been overlaid. The ratio in the lower plot shows the agreement between the observed and expected distributions. The error bars on the data points are statistical and the band in the ratio plot is the combined systematic error.

$m_{\mu\mu}[\text{GeV}]$	80 - 110	110 - 200	200 - 400	400 - 800	800 - 1200	1200 - 3000	3000 - 4500
$Z^0/\gamma^*$	$5064300 \pm 9700$	$111500 \pm 1000$	$10800 \pm 600$	$960 \pm 80$	$49 \pm 4$	$7.3 \pm 0.8$	$0.034 \pm 0.015$
Top	$4400 \pm 220$	$7070 \pm 470$	$2300 \pm 400$	$160 \pm 80$	$3.0 \pm 0.5$	$0.18 \pm 0.06$	$0 \pm 0$
Diboson	$7010 \pm 170$	$1530 \pm 160$	$520 \pm 130$	$64 \pm 15$	$4.2 \pm 2.1$	$0.69 \pm 0.30$	$0.0024 \pm 0.0019$
Total	$5075700 \pm 9700$	$120100 \pm 1100$	$13700 \pm 800$	$1180 \pm 120$	$56 \pm 5$	$8.2 \pm 0.9$	$0.036 \pm 0.017$
Data	5075739	120011	13479	1122	49	8	0

$m_{\mu\mu}[\text{GeV}]$	80 - 110	110 - 200	200 - 400	400 - 800	800 - 1200	1200 - 3000	3000 - 4500
$Z^0/\gamma^*$	$5060000 \pm 320000$	$111000 \pm 7000$	$10800 \pm 700$	$960 \pm 60$	$49 \pm 3$	$7.3 \pm 0.8$	$0.034 \pm 0.012$
Top	$4400 \pm 240$	$7100 \pm 400$	$2300 \pm 130$	$158 \pm 14$	$3.0 \pm 1.6$	$0.18 \pm 0.14$	$0 \pm 0$
Diboson	$7010 \pm 330$	$1530 \pm 70$	$524 \pm 25$	$64.0 \pm 3.0$	$4.20 \pm 0.20$	$0.693 \pm 0.032$	$0.0024 \pm 0.0001$
Total	$5080000 \pm 320000$	$120000 \pm 7000$	$13700 \pm 700$	$1180 \pm 60$	$56 \pm 4$	$8.2 \pm 0.8$	$0.036 \pm 0.016$
Data	5075739	120011	13479	1122	49	8	0

$m_{\mu\mu}[\text{GeV}]$	80 - 110	110 - 200	200 - 400	400 - 800	800 - 1200	1200 - 3000	3000 - 4500
$Z^0/\gamma^*$	$5060000 \pm 320000$	$111000 \pm 8000$	$11000 \pm 1000$	$1000 \pm 100$	$49 \pm 5$	$7.3 \pm 1.1$	$0.034 \pm 0.022$
Top	$4400 \pm 330$	$7100 \pm 600$	$2300 \pm 400$	$160 \pm 80$	$3.0 \pm 1.7$	$0.18 \pm 0.15$	$0 \pm 0$
Diboson	$7010 \pm 370$	$1530 \pm 180$	$520 \pm 130$	$64 \pm 16$	$4.2 \pm 2.1$	$0.69 \pm 0.30$	$0.0024 \pm 0.0019$
Total	$5080000 \pm 320000$	$120000 \pm 8000$	$13700 \pm 1100$	$1180 \pm 130$	$56 \pm 6$	$8.2 \pm 1.2$	$0.036 \pm 0.023$
Data	5075739	120011	13479	1122	49	8	0

Table 4.6: Dimuon event yield tables for the **tight + loose channel** with statistical (top), systematic (middle) and total (bottom) uncertainties. The first column is used to normalize the MC total to the observed data total.

## CHAPTER 4. ANALYSIS EVENT SELECTION

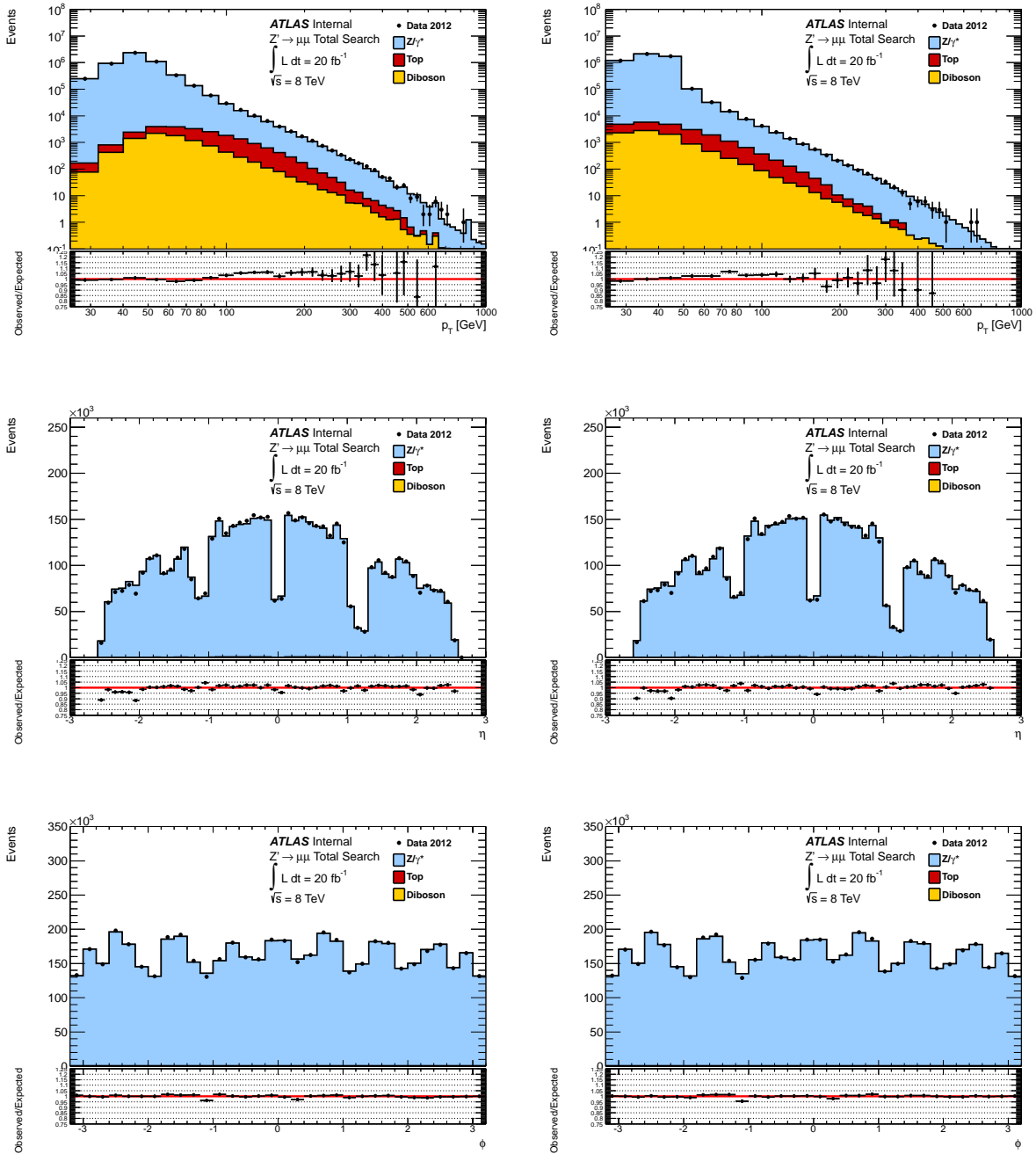


Figure 4.12: Leading (left) and subleading (right) distributions in the muon **tight + loose channel** after event selection. The top row are the  $p_T$  distributions, the middle row are the  $\eta$  distributions, and the bottom row are the  $\phi$  distributions.



## 4.5 Systematic Uncertainties

The MC is normalized to the data in the  $Z^0$  peak region which cancels all mass-independent systematic errors such as the total luminosity error. However, there are still mass-dependent systematic uncertainties which must be accounted for. These are typically small in the low-mass range and grow at higher mass. The systematics are incorporated using nuisance parameters in the likelihood function. Systematic uncertainties with an error less than 3% of the total background at 3 TeV are ignored. This is to limit the amount of computation needed and because of the negligible effect small systematics have on the search and limit setting.

The different sources of uncertainty are broken into groups between theoretical and experimental errors. The theoretical systematic uncertainties were discussed in Section 4.2.2. The dominant theoretical uncertainties come from the PDF used in calculating the various processes, and this is discussed in detail in Appendix B. The list of theoretical systematic uncertainties considered is:

- $Z^0/\gamma^*$  total cross section uncertainty, estimated at 4% of the total DY contribution.
- PDF uncertainty, propagated from the eigenvector set errors, using MSTW2008NNLO as the nominal PDF. This is split into 4 groups based on their behavior as a function of invariant mass.
- PDF choice uncertainty, envelope comparing central values of different PDFs to the nominal PDF.
- PDF scale uncertainty, calculated by varying the factorization and renormalization scale in the nominal PDF.

## CHAPTER 4. ANALYSIS EVENT SELECTION

- PDF  $\alpha_S(m_Z)$  uncertainty, calculated by varying  $\alpha_S$  in the nominal PDF.
- Electro-Weak uncertainty, propagated from the errors in the rescaling of the DY MC to include the additional EW effects. This is split into 2 groups based on their origin: higher-order and photon-induced corrections.
- Top total cross section uncertainty, estimated at 6% of the total Top contribution.
- Diboson total cross section uncertainty, estimated at 5% of the total Diboson contribution.

All of these have been evaluated as a function of the true invariant mass of the system. When including the systematics in the search and limit setting, they should be applied as a function of the reconstructed invariant mass. Each event in the MC has saved the true and reconstructed invariant mass, so the proper systematic error can be evaluated event-by-event. The cumulative effect of the systematic variation on the expected background can then be estimated. This is done by using three histograms. The first histogram is the nominal reconstructed invariant mass spectrum of the expected background. The second and third histograms are the reconstructed invariant mass spectra after varying one of the systematics up and down as a function of the true mass of the MC simulation. Calculating the ratios of the second and third histograms to the first, evaluated bin-by-bin in the reconstructed invariant mass and keeping the largest % change, is the systematic error as a function of the reconstructed invariant mass. See Figure 4.13 for a comparison between the systematic error evaluated as a function of the true and reconstructed invariant mass.

The experimental systematic uncertainties come from a variety of sources and are listed here:

- Beam energy uncertainty, estimated at 0.65% of 4 TeV/beam [230]. This is propagated

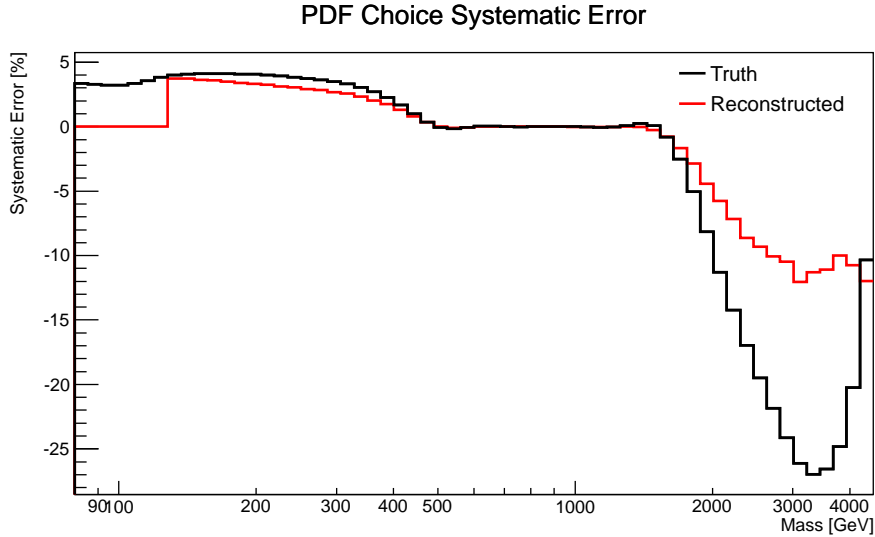


Figure 4.13: PDF Choice systematic uncertainty as a function of invariant mass in the tight dimuon channel. This shows the difference between the systematic error evaluated as a function of the true and reconstructed invariant mass. The black histogram is the % systematic error evaluated at the true invariant mass. The red histogram is the % systematic error evaluated at the reconstructed invariant mass, using the procedure outlined in the text. The red histogram is “smeared” due to the worsening resolution of the high- $p_T$  muons from the larger invariant mass events. Before the start of the search region at 130 GeV the reconstructed systematic error is not needed (red histogram) and is set to zero. The reconstructed systematic error histograms are computed for each systematic error in each channel.

to the DY background using VRAP with the MSTW2008NNLO PDF to compute the change in nominal DY production and is treated like a theoretical systematic. See Appendix B.

- Electron fake rates uncertainty from QCD multi-jets and  $W$ +jets, extrapolated to high invariant mass from fits by increasing the background by  $+1\sigma$ . See Appendix D.
- Muon resolution is measured at the  $Z^0$  peak and the uncertainties are extrapolated to high- $p_T$  and invariant mass. See Appendix E.

CHAPTER 4. ANALYSIS EVENT SELECTION

- Top background uncertainty, calculated by systematically varying the Top background fits to high invariant mass.

These are known in terms of the reconstructed invariant mass and apply to the total background.

The systematic uncertainties are only applied to the expected SM background, with the exception of the overall normalization (the DY cross section), in a procedure described in Section 5.2. The values of the systematic errors at the benchmark invariant mass points of 1, 2, and 3 TeV are listed in Table 4.7. In particular, due to the small contribution of the Diboson and Top backgrounds to the overall background, even though their systematics are relatively large, their contribution to the total systematic uncertainty is considered negligible.

Source	1 TeV		2 TeV		3 TeV	
	Electron	Muon	Electron	Muon	Electron	Muon
DY Cross Section	4%	4%	4%	4%	4%	4%
PDF Variation	5%	5%	11%	12%	30%	17%
PDF Choice	—	—	7%	6%	22%	12%
$\alpha_S$	—	—	3%	3%	5%	4%
Electro-Weak	—	—	—	3%	4%	3%
Photon-Induced	—	—	3%	3%	6%	4%
Beam Energy	—	—	—	3%	5%	3%
Fake Jets	3%	N/A	5%	N/A	21%	N/A
Resolution	N/A	3%	N/A	3% (7%)	N/A	8% (13%)
Diboson	—	—	—	—	—	—
Top	—	—	—	—	—	—
Total	7%	7%	15%	15% (16%)	44%	24% (26%)

Table 4.7: A summary of the systematic uncertainties in the electron and muon channels at three mass points. A “-” indicates the uncertainty is negligible (below 3%), while an “N/A” indicates the uncertainty does not apply to that channel. For the muon channel the listed terms are for the tight channel and the terms in parentheses are for the loose analysis, if it differs.

# Chapter 5

## $Z'$ Search & Limit Setting

The search for new physics begins with the expected background from the Standard Model and tests the observed data for deviations from that expectation. The SM expectations were calculated in the previous chapter, as well as possible signals for new  $Z'$  particles. This chapter will describe how the input invariant mass spectra from the expected SM background,  $Z'$  signal templates, and observed data are analyzed to perform this search as well as the results.

### 5.1 History - Prior $Z'$ Searches to Now

The dilepton channel has been a common search mode for new physics for decades, with the successful searches contributing to the completion and understanding of the SM. After the direct production and observed decay of the  $Z^0$  boson in the dilepton channel at UA1 and UA2 [140, 141], many experiments have searched for new  $Z'$  particles in this channel at higher energies. Some of these results are shown in Table 5.1 at the end of this section.

The most recent and stringent results come from the LHC experiments ATLAS and CMS.

## CHAPTER 5. $Z'$ SEARCH & LIMIT SETTING

The ATLAS direct search  $Z' \rightarrow \ell\ell$  used the 2011 data set, and combined both the  $ee$  and  $\mu\mu$  channels with  $5.0 \text{ fb}^{-1}$  of data in both channels collected at  $\sqrt{s} = 7 \text{ TeV}$ . The lower mass limit on an SSM  $Z'$  was set at 2220 GeV at the 95% C.L. [8]. CMS has also performed this direct search,  $Z' \rightarrow \ell\ell$  combining the  $ee$  and  $\mu\mu$  channels. Their most recent results combined the  $5 \text{ fb}^{-1}$  at  $\sqrt{s} = 7 \text{ TeV}$  2011 data with  $4 \text{ fb}^{-1}$  at  $\sqrt{s} = 8 \text{ TeV}$  2012 data. The lower mass limit on an SSM  $Z'$  was set at 2590 GeV at the 95% C.L. [9].

The previous set of direct searches was performed by DØ and CDF, the two primary experiments at the Tevatron. Each performed a direct search in both the  $e^+e^-$  and  $\mu^+\mu^-$  channels. The DØ search in the  $ee$  channel put a lower mass limit of 1023 GeV limit on an SSM  $Z'$  at the 95% C.L. [4], and in the  $\mu\mu$  channel a lower mass limit of 680 GeV [5]. The CDF search in the  $ee$  channel found a lower mass limit of 963 GeV [6] and in the  $\mu\mu$  channel a lower mass limit of 1071 GeV [7], both for an SSM  $Z'$ .

Besides direct searches such as those at the Tevatron, there have been indirect searches for new particles coupling to lepton pairs. At LEP II, four different experiments (ALEPH, DELPHI, L3, and OPAL) performed measurements of the  $e^+e^- \rightarrow f\bar{f}$  differential cross section, where the fermions can be quarks or leptons. This search used the Forward-Backward asymmetry ( $A_{FB}$ ), which compares the outgoing fermion/anti-fermion directions to the incoming electron/positron directions ( $\cos\theta$ , the polar angle between the incoming electron and outgoing fermion). The SM is a chiral theory with different couplings for the left- and right-handed particles, so that after averaging over both chiralities the different couplings determine the preferred directions for the outgoing fermion/anti-fermion compared to the incoming electron/positron. A new particle such as a  $Z'$  would change the cross section behavior as a function of  $\cos\theta$  at high energies. For example, by measuring the asymmetry at an energy of  $\sqrt{s} = 33.5 \text{ GeV}$  in the  $e^+e^- \rightarrow \mu^+\mu^-$  channel, this type of analysis was used with the JADE experiment data at the PETRA collider to constrain the mass of the

## CHAPTER 5. $Z'$ SEARCH & LIMIT SETTING

$Z^0$  boson before its direct production and measurement [231]. The LEP II result scans over a larger energy range and combines many channels ( $ee$  after subtracting out Bhabha scattering, with  $\mu\mu$  &  $\tau\tau$  in the lepton channel, and  $c\bar{c}$  &  $b\bar{b}$  in the heavy quark channel) and measures the  $A_{FB}$  for each one. These are all combined using the ZFITTER [232, 233, 234] package and compared to the SM expectation. Any deviations in the asymmetry can be interpreted as due to a new particle interfering with the  $Z^0/\gamma^*$  process. The constraints on an SSM  $Z'$  from this search gives a lower mass limit of 1787 GeV [3].

In addition to the direct and indirect searches, there are searches for  $Z'$  particles in other channels at both the Tevatron and the LHC experiments. Due to the lower precision reconstructing the non-leptonic channels, these all have weaker mass limits than the dilepton searches. In the leptonic channel,  $Z' \rightarrow \tau\tau$  has been searched for at CDF [235] and CMS [236], but due to the  $\tau$  decays having neutrinos, the limits are weaker. The hadronic decay channel  $Z' \rightarrow t\bar{t}$  has been studied at DØ [237], CDF [238], ATLAS [239], and CMS [240]. Decays to light quarks observed as jets have also been studied at CDF [241] and CMS [242]. The new  $Z'$  could also couple to the bosons in the EW theory, and searches for resonances in the diboson channel  $Z' \rightarrow W^+W^-$  have been performed at DØ [243] and CDF [244].

Experiment	$\sqrt{s}$ [TeV]	Channel	Data [ $\text{fb}^{-1}$ ]	$Z'$ Model Mass Limit [GeV]						
				$\psi$	$N$	$\eta$	$I$	$S$	$\chi$	SSM
LEP II	0.130-0.209	Indirect	$\sim 2.8$	481	—	434	—	—	673	1787
DØ	1.96	$Z' \rightarrow e\bar{e}$	5.4	891	874	923	772	822	903	1023
DØ	1.96	$Z' \rightarrow \mu\bar{\mu}$	0.25	—	—	—	—	—	—	680
CDF	1.96	$Z' \rightarrow e\bar{e}$	2.5	851	837	877	735	792	862	963
CDF	1.96	$Z' \rightarrow \mu\bar{\mu}$	4.6	917	900	938	817	858	930	1071
ATLAS	7.0	$Z' \rightarrow \ell\bar{\ell}$	5.0	1790	1790	1870	1860	1910	1970	2220
CMS	7.0 & 8.0	$Z' \rightarrow \ell\bar{\ell}$	5.3 & 4.1	2270	—	—	—	—	—	2590

Table 5.1: The observed 95% C.L. mass limits for a variety of  $Z'$  models from various experiments. The LEP II results combine the output from the four experiments, each with an integrated luminosity of  $\sim 700 \text{ pb}^{-1}$ . The full combination and result is from Table 3.15 in [3]. The DØ results in the  $ee$  channel are from Table III in [4] and  $\mu\mu$  channel from [5]. The CDF results in the  $ee$  channel are from Table II in [6] and  $\mu\mu$  channel from Table I in [7]. The ATLAS results combined the  $ee$  and  $\mu\mu$  channels and are from Tables 5 & 6 in [8]. The CMS results combined data from  $\sqrt{s} = 7$  and 8 TeV and the  $ee$  and  $\mu\mu$  channels, the results are from Table 2 in [9].



## 5.2 Bayesian Search & Limit Setting

This search takes a Bayesian approach to determining whether or not a signal has been observed, and in the absence of a signal, the lower limits placed on the signal mass. A note on the search and limit setting procedures written for the ATLAS Exotics group can be found here [245].

Bayes' theorem states [246]:

$$P(A|B) = \frac{P(B|A)P(A)}{P(B)},$$

where  $P(A|B)$  is the conditional probability of  $A$  occurring given  $B$ . This can heuristically be derived from the probability of both  $A$  and  $B$  occurring and the definition of the conditional probability:

$$P(A \text{ and } B) = P(A|B)P(B) = P(B|A)P(A).$$

A note by Louis Lyons on Bayesian and Frequentist interpretations in particle physics and how they differ can be found in [247]. In this search, we observe a distribution of measured data and would like to know what this says about a parameter hypothesized from some new physics, for example the production and decay of a  $Z'$  to leptons  $(\sigma B)_{Z'}$ , given the couplings from a particular model. Bayes' theorem cast in this form reads:

$$p((\sigma B)_{Z'}|\text{data}) = \mathcal{L}(\text{data}|(\sigma B)_{Z'}) \times \pi((\sigma B)_{Z'}). \quad (5.1)$$

This is the form of Bayes' theorem used in this analysis. The second term on the right-hand side is prior probability density for this hypothesis and essentially contains what we do (or don't) know about this parameter before the measurement. The first term on the right is

## CHAPTER 5. $Z'$ SEARCH & LIMIT SETTING

the likelihood function of observing this particular accumulation of data given the value of the parameter (hypothesis). The term on the left is the posterior probability distribution and contains the probabilistic distribution of the parameter value, taking into account the measured data and prior information of the parameter. In this analysis, since there is no previous sign of new physics, a uniform (flat) prior is used throughout the search region.

The search is based on Poisson statistics both within each bin and across all the bins in the search region. The likelihood to observe  $n_{obs}$  events with an expectation of  $N$  events in Poisson statistics is:

$$\mathcal{L}(n_{obs}|N) = \frac{N^{n_{obs}} e^{-N}}{n_{obs}!}.$$

This is maximized at  $n_{obs} = N$ . To include multiple bins, the product for each set of observations is taken bin-by-bin and maximized. The total likelihood is computed by taking the Poisson distribution for each bin in the search region, and the systematics are included by using a nuisance parameter  $\theta$ . These are assumed to have Gaussian priors, and included by spreading out the  $N$  expected events in each bin:

$$\begin{aligned} \mathcal{L}(\text{data} | (\sigma B)_{Z'}, \theta_i) &= \prod_{k=1}^{N_{bin}} \frac{\mu_k^{n_k} e^{-\mu_k}}{n_k!} \prod_i^{N_{sys}} \text{Gaus}(\theta_i, 0, 1), \\ \mu_k &= \sum_{j=1,2} N_j T_{j,k} (1 + \theta_i \epsilon_{ijk}). \end{aligned}$$

In each bin  $k$  there are an observed number of entries  $n_k$  in the data. For the parameter  $\mu_k$ ,  $j = 1$  is the hypothesized signal contribution and  $j = 2$  is the expected background contribution. The  $N_j$  are the total number of events in signal and background and  $T_{j,k}$  are

CHAPTER 5.  $Z'$  SEARCH & LIMIT SETTING

the fraction of the total events expected in the  $k^{\text{th}}$  bin:

$$\begin{aligned} N_1 &= (\mathcal{A} \cdot \varepsilon)_{Z'} \times (\sigma B)_{Z'} \times \text{Luminosity}, \\ N_2 &= N_{\text{Bkg}}, \\ \sum_{k=1}^{N_{\text{bin}}} T_{j,k} &= 1. \end{aligned}$$

For each nuisance parameter  $\theta_i$ ,  $\epsilon_{ijk}$  is the systematic uncertainty on the template  $j$  in the  $k^{\text{th}}$  bin. The likelihood is a function of  $N_1$ , which in turn can be converted into the parameter  $(\sigma B)_{Z'}$ . The systematic errors are only applied to the background template, except for the overall normalization error due to the DY cross section uncertainty, and all are assumed to be Gaussian.

The template functions  $T_{j,k}$  allow for more detailed tests of the expected SM background by including the shape information of the  $Z'$ . This avoids the simple “bump-hunting” and allows for a more directed search of new physics by using different templates. The template shape fitting can also help avoid false signals due to fluctuations or possible experimental errors such as poor MC background modeling. The template shapes are more robust and more sensitive for searches for new physics compared to the simple counting experiments because they can include several bins in a range of the invariant mass. By including multiple bins in the template, each with different Signal to Background ratios, the likelihood can better help constrain or enhance a signal contribution in the observed data.

The number of signal events  $N_1$  depends on the luminosity, which would require incorporating the uncertainty associated with the total data taken. Instead, this analysis uses the normalization about the  $Z^0$  peak to determine the number of signal events  $N_{Z'}$  and in turn,

CHAPTER 5.  $Z'$  SEARCH & LIMIT SETTING

the production and decay rate  $(\sigma B)_{Z'}$ .

$$(\sigma B)_{Z'} = (\sigma B)_{Z^0} \frac{N_{Z'} \times (\mathcal{A} \cdot \varepsilon)_{Z^0}}{N_{Z^0} \times (\mathcal{A} \cdot \varepsilon)_{Z'}} \quad (5.2)$$

The normalization about the  $Z^0$  peak has a systematic uncertainty of 4% due to the DY cross section uncertainty. However, since the expected background was scaled to the observed data, this is only applied to the signal templates and not the expected background. This uses the formula for the event count for any given scattering process:

$$N = \mathcal{L} \times (\sigma B) \times (\mathcal{A} \cdot \varepsilon).$$

This normalization procedure allows for a simple conversion between the signal events count and the physics quantity  $(\sigma B)_{Z'}$ .

The likelihoods are computed using Markov Chain Monte Carlo (MCMC) with the Bayesian Analysis Toolkit (BAT) [248]. This is a software framework designed to take in observed data, expected backgrounds, and hypothesized signals for a variety of models in particle physics and perform various Bayesian analyses. BAT treats the parameters of interest and nuisance parameters in the appropriate way and uses MCMC to sample the parameter spaces for maximization or integration.

To combine the analysis channels, combined likelihood is defined as the product of the two channel's Poisson probabilities bin-by-bin. Both are written in terms of the same parameter of interest, and this allows for systematics that are correlated across channels to be taken

care of in a consistent way.

$$\mathcal{L}(\text{data} | (\sigma B)_{Z'}, \theta_i) = \prod_{l=1}^{N_{chan}} \prod_{k=1}^{N_{bin}} \frac{\mu_{l,k}^{n_{l,k}} e^{-\mu_{l,k}}}{n_{l,k}!} \prod_i^{N_{sys}} \text{Gaus}(\theta_i, 0, 1)$$

$$\mu_{l,k} = \sum_{j=1,2} N_{l,j} T_{l,j,k} (1 + \theta_i \epsilon_{ijkl})$$

The search and limits will be performed for all the channels separately as well as combined together.

### 5.2.1 Bayesian Search

Two different tests are done during the search for a  $Z'$  signal, one is a global search for a  $Z'$  signal and the other is a local search for deviations from the expected SM background. The global search looks for the values of mass  $m_{Z'}$  and event rate  $N_{Z'}$  that are most like that observed in data. The local search looks for large deviations from the expected SM background bin-by-bin.

The global search looks across all the bins in the search region and finds the best possible values for the new physics parameters of interest. This is a counting experiment for each bin in the invariant mass spectrum across the full set of bins because the full likelihood function is the product of each single bin likelihood. The likelihood is calculated two times, once assuming a signal in addition to the expected background ( $S + B$ ) and once assuming only the SM background ( $B$ ). The significance is rated using a  $p$ -value, which is the probability of observing an outcome that is at least as signal-like as what was actually measured, assuming no signal is actually present. The significance is calculated from a log-likelihood ratio (LLR)

CHAPTER 5.  $Z'$  SEARCH & LIMIT SETTING

test based on the Neyman-Pearson lemma [249]:

$$LLR = -2 \ln \frac{\mathcal{L}'(\text{data}|S + B, \hat{\theta}_i)}{\mathcal{L}'(\text{data}|B, \tilde{\theta}_i)}.$$

This corresponds to a  $\chi^2$  difference between the background and signal+background hypotheses. The signal templates assume a shape for the  $Z'$  and have two degrees of freedom:  $m_{Z'}$  and  $N_{Z'}$ . Because the details of a possible  $Z'$  signal are *a priori* unknown, the likelihood is maximized to find the best-fitting  $m_{Z'}$  and  $N_{Z'}$  in the observed data and the  $p$ -value is then computed for this signal point. A common convention in particle physics is that a  $p$ -value less than  $1.35 \times 10^{-3}$  is considered “evidence” for a signal and a  $p$ -value less than  $2.87 \times 10^{-7}$  is considered “discovery” of a signal. These values are the one-sided integrals of a unit Gaussian beyond  $+3\sigma$  and  $+5\sigma$ , respectively.

The two likelihoods used in the LLR are computed in different ways using BAT. The  $S+B$  likelihood is maximized over the  $\hat{\theta}_i$  using the observed data and finding the best-fit values of the parameters of interest  $m_{Z'}$  and  $N_{Z'}$ . The background-only likelihood is maximized over the  $\tilde{\theta}_i$  by performing 1,000 pseudo-experiments (PE) with the expected background only and assuming no  $Z'$  signal. Each PE samples 10,000 variations in the nuisance parameters using MCMC to generate a set of pseudo-data, and selects the peak value. The LLR distribution is computed for each PE, with the resulting  $p$ -value:

$$p = P(LLR_{PE} > LLR_{obs} | \text{SM only}).$$

The best-fit  $N_{Z'}$  is converted to  $(\sigma B)_{Z'}$  for ease of comparison using Equation (5.2). As this scans the full available parameter space, it automatically takes into account the “look-elsewhere” effect.

The second search is a simple local significance test for each bin in the search region.

This is implemented using a tool developed by Choudalakis and Casadei [250]. The tool uses the statistical and systematic errors in each bin to compute a local significance for the observed data deviation from the expected SM background.

## 5.2.2 Bayesian Limit Setting

In the absence of a  $Z'$  signal, an upper limit is set on the cross section times branching fraction and lower limit is set on the mass. In this case, rather than maximizing the likelihood, the likelihood can be reduced from a function of both the parameter of interest and the systematic nuisance parameters to just a function of the parameter of interest, through the marginalization procedure. This is essentially “integrating out” the uncertainty by including all the variations weighted by their respective Gaussian error:

$$\mathcal{L}'(\text{data} | (\sigma B)_{Z'}) = \int \cdots \int \mathcal{L}(\text{data} | (\sigma B)_{Z'}, \theta_i) \prod_i^{N_{sys}} d\theta_i.$$

The marginalization is computed using MCMC with BAT. This can work two ways, depending on the inclusion of the observed data or not. When including the observed data, the marginalization in BAT works to maximize the the reduced likelihood with respect to the parameter of interest. When not including the observed data, instead a series of pseudo-data distributions are generated. These called pseudo-experiments (PE) and are generated by using the expected signal and background distribution and varying all the sources of systematic uncertainties across the distribution. The systematic variations are sampled to produce 10,000 pseudo-data distributions (ensembles) for each PE to ensure statistical accuracy. 1,000 PE in total are generated, and the resulting likelihood values for each PE is used to estimate the maximum reduced likelihood.

The marginalization is performed in both data and with PE for each of the 68 signal

## CHAPTER 5. $Z'$ SEARCH & LIMIT SETTING

templates generated, discussed in Section 4.2.1. Each of the signal templates was generated at a fixed mass  $m_{Z'}$  with a computed template shape  $T_{l,j,k}$ . This leaves the only remaining signal parameter  $N_{Z'}$ , or using Equation (5.2) and transforming this into a physics quantity,  $(\sigma B)_{Z'}$ . For each signal template, a 95% C.L. upper bound is placed on  $(\sigma B)_{Z'}$ . This is done by transforming the reduced likelihood into a posterior probability using Bayes' theorem, as seen in Equation 5.1. To do this, we assume a uniform (flat) prior in  $(\sigma B)_{Z'}$ , *i.e.*  $\pi((\sigma B)_{Z'}) = \text{constant}$ . The 95% C.L. upper limit is at the point where 95% of the posterior probability is covered, and this value is the upper limit  $(\sigma B)_{Z'}^{95}$ :

$$0.95 = \frac{\int_0^{(\sigma B)_{Z'}^{95}} \mathcal{L}'(\text{data} | (\sigma B)_{Z'}) \times \pi((\sigma B)_{Z'}) d(\sigma B)_{Z'}}{\int_0^{\infty} \mathcal{L}'(\text{data} | (\sigma B)_{Z'}) \times \pi((\sigma B)_{Z'}) d(\sigma B)_{Z'}}.$$

The “data” can be both the observed data and the generated pseudo-data from the PE. The limits on  $(\sigma B)_{Z'}$  are then interpolated between the template mass points. Each  $Z'$  model has a defined  $(\sigma B)_{Z'}$  as a function of  $m_{Z'}$  curve, and where this curve intersects the interpolated limit curve of  $(\sigma B)_{Z'}^{95}$  is the corresponding mass limit for that model.

### 5.3 ATLAS Search for a $Z'$

This section describes the results of the ATLAS search for a new, neutral heavy gauge boson using the dilepton invariant mass distributions. The inputs are the observed data using the ATLAS detector, simulated MC events for the expected Standard Model background, and simulated MC signal expectation templates using the SSM  $Z'$  as the model.



### 5.3.1 The Global $\sigma B$ and $M_{Z'}$ Search

The observed invariant mass distributions are scanned to find the most signal-like  $M_{Z'}$  and  $\sigma_{Z'}$  by comparing the background-only and signal+background hypothesis using a log-likelihood ratio. A set of 1000 PE invariant mass distributions are generated from the expected SM background distributions only, taking into account the systematic variations. These are scanned for the most signal-like point in the pseudo-data with the same LLR method as the observed data. The observed LLR is compared to the distribution of LLR values from the 1000 PE and assigned a  $p$ -value. The observed  $p$ -values are 12% in the dielectron channel, 98% in the dimuon channel (combining the tight and loose selections), and 48% in the combined dilepton channel. The 2D scanning “heat map” for the various channels are shown in Figure 5.1. No statistically significant signal is observed in the data.

CHAPTER 5.  $Z'$  SEARCH & LIMIT SETTING

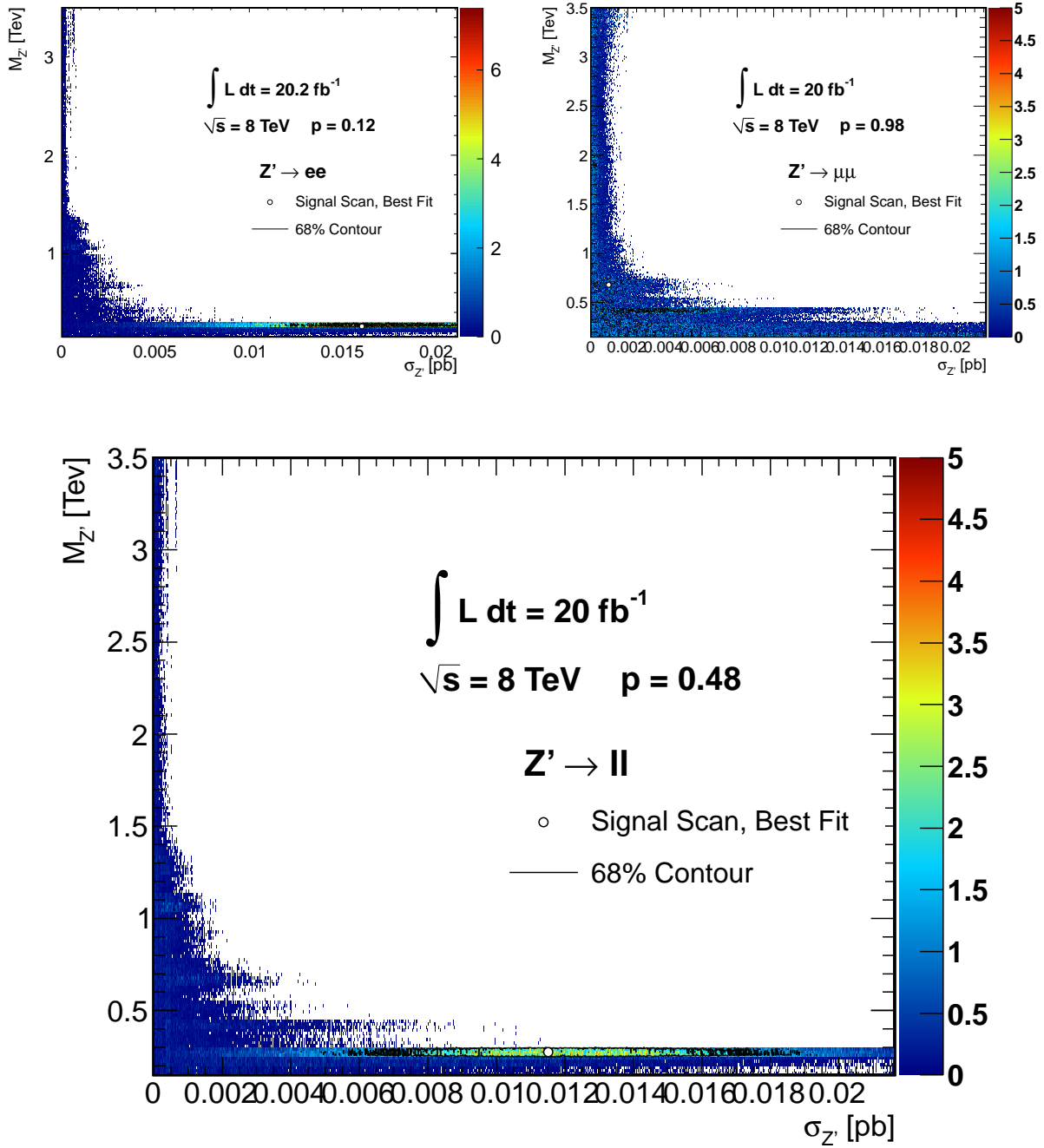


Figure 5.1: The LLR search for a  $Z'$  signal in the various dilepton invariant mass histograms. Upper Left: Dielectron channel. Upper Right: Dimuon channel, combining the tight and loose selections. Bottom: Combined dilepton channel. The circles represent the “most-signal-like” points and the  $p$ -value is the global probability to observe such a deviation in the data assuming background-only.

### 5.3.2 Local Significance Search

The local significance is calculated for each mass bin across the search region for each analysis channel. This includes both the statistical and systematic errors for the observed data and expected MC background. A table of the largest significance deviations are listed in Table 5.2. The histograms with uncertainties and significance insets are shown in Figure 5.2. No statistically significant deviation is seen in the data.

Channel	+ Significance		- Significance	
	$\sigma$	$m_{\ell\ell}$	$\sigma$	$m_{\ell\ell}$
$ee$	+1.3	1060	-1.1	340
$\mu\mu$ Loose	+1.2	227	-1.9	543
$\mu\mu$ Tight	+0.7	1820	-1.8	930
$\mu\mu$ Total	+0.6	1820	-2.0	930

Table 5.2: Largest positive and negative local significance deviations in all analysis channels. The total muon channel is dominated by the tight muon channel.

CHAPTER 5.  $Z'$  SEARCH & LIMIT SETTING

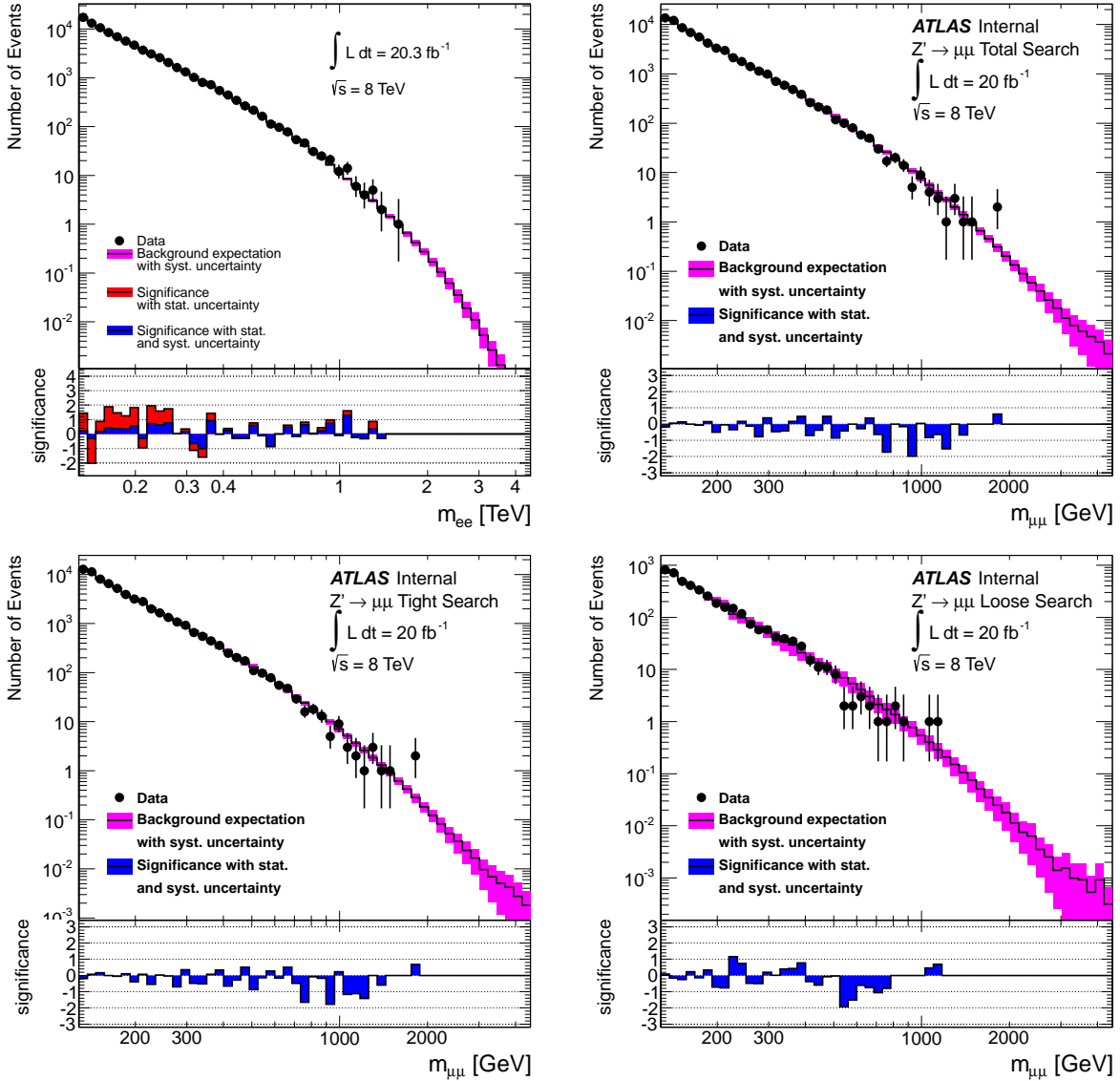


Figure 5.2: Local significance of deviations including statistical and systematic uncertainties between data and the expected SM background for each bin in the search region from 128 to 4500 GeV. These are for the separate channels, with dielectron (top left), dimuon tight + loose (top right), dimuon tight (lower left), and dimuon loose (lower right) selections.

## 5.4 ATLAS Limits on a $Z'$

No statistically significant deviation is observed in the data to indicate a possible  $Z'$  signal. Instead, 95% C.L. limits are placed on the benchmark SSM  $Z'$  model and six  $Z'$  models from an  $E_6$ -derived gauge unification model. The limits are calculated for three channels, the dielectron, the dimuon, and the combined channel. The dimuon channel combines the tight and loose channels as two independent channels for the likelihood, and the combined channel combines the electron, tight muon, and loose muon channels as three independent channels in the likelihood. The lower mass limit from these three channels for the benchmark SSM  $Z'$  and the limits from the combined channel for the various  $E_6$  models are listed in Table 5.3. The interpolated observed and expected  $(\sigma B)_{Z'}$  as a function of  $m_{Z'}$  for these channels are shown in Figure 5.3. The width of the SSM  $Z'$  curve corresponds to the theoretical uncertainty on the parameters of the model. The two other models shown are the  $Z'_\chi$  and  $Z'_\psi$ , which have the largest and smallest  $(\sigma B)_{Z'}$  vs.  $m_{Z'}$  of the  $E_6$  models. The mass point where the limit curve intersects the theoretical model curve is the lower mass limit on that model.

	$ee$	$\mu\mu$	$\ell\ell$
Observed Limit [TeV]	2.79	2.53	2.90
Expected Limit [TeV]	2.76	2.53	2.87

Combined Channel	$Z'_\psi$	$Z'_N$	$Z'_\eta$	$Z'_I$	$Z'_{SQ}$	$Z'_\chi$
Observed Limit [TeV]	2.43	2.43	2.49	2.46	2.51	2.58
Expected Limit [TeV]	2.38	2.38	2.45	2.41	2.47	2.55

Table 5.3: Upper Table: The 95% C.L. mass limits for the SSM  $Z'$  in the three analysis channels. The  $\mu\mu$  limit is the combination of the tight and loose muon channels. Lower Table: The 95% C.L. mass limits for the  $E_6$ -derived  $Z'$  in the combined channel.

CHAPTER 5.  $Z'$  SEARCH & LIMIT SETTING

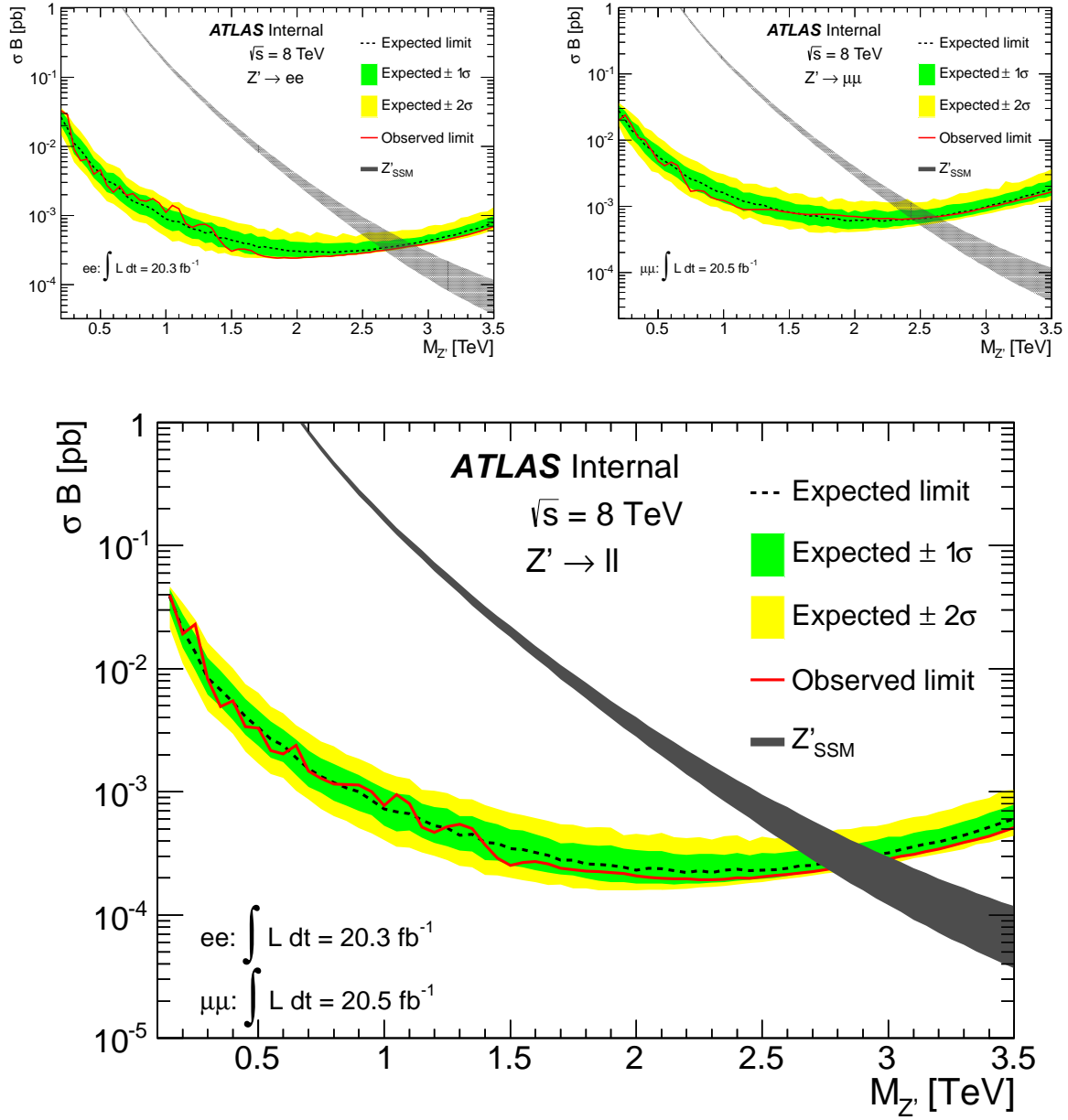


Figure 5.3: Expected and observed 95% C.L. limits on  $(\sigma B)_{Z'}$  as a function of  $m_{Z'}$  in the various analysis channels. Upper Left: Dielectron channel. Upper Right: Dimuon channel, combining the Tight and Loose selections. Bottom: Combined dilepton channel. The green and yellow bands show the  $\pm 1\sigma$  and  $\pm 2\sigma$  posterior errors on the expected  $(\sigma B)_{Z'}$  limit. The thickness of the SSM  $Z'$  band indicates the theoretical uncertainty on the model parameters, and applies to the other theory curves as well.

# Chapter 6

## Conclusion

During the 2012 year of operation of the LHC at  $\sqrt{s} = 8$  TeV, the ATLAS detector recorded over  $20 \text{ fb}^{-1}$  of data. This data was used to perform a search for new, neutral heavy gauge bosons as signal for physics beyond the Standard Model. The search looked in the dilepton decay channel,  $Z' \rightarrow \ell\ell$ , in the invariant mass region above the  $Z^0$  boson peak. The dilepton channel is able to fully reconstruct the intermediate particle, allowing for a precise measurement of its properties.

The analysis was split into three different channels: an electron channel, a tight muon channel, and a loose muon channel. Several corrections have been applied to the simulated expected Standard Model background in the various channels to more accurately model the known physics processes. In addition, a variety of systematic errors from both theoretical and experimental sources were evaluated and used in the search. The channels were searched both independently and in combination. The search scanned the dilepton invariant mass distribution searching for the largest deviations from the expected Standard Model background. The search returned the most signal-like  $Z'$  point in the combined channel at  $M_{Z'} = 280$  GeV and  $\sigma_{Z'} = 11.5$  nb, with a  $p$ -value of 0.48.

## CHAPTER 6. CONCLUSION

None of the searches yielded a statistically significant result and in the absence of a signal of new physics, limits were placed on a variety of  $Z'$  models. The limits are a Bayesian 95% C.L. lower limit on the mass of the  $Z'$ . In the benchmark model of the Sequential Standard Model, where the  $Z'$  has identical couplings as the Standard Model  $Z^0$  boson, the combined limit from the three channels is:

$$M_{Z'_{SSM}} > 2.90 \text{ TeV}.$$

Lower mass limits were also placed on a variety of  $E_6$ -motivated  $Z'$  boson, ranging from 2.38-2.54 TeV. Previous limits on the SSM  $Z'$  from LEP II are 1.79 TeV, from the Tevatron range from 0.68-1.07 TeV, from CMS are 2.59 TeV, and from ATLAS are 2.22 TeV. These new limits are the strongest on this class of models in the world.

Discovery of new physics is ATLAS's primary goal. The discovery of the Higgs boson has been a triumph for the physics program at the LHC and CERN, but it only fills in the final piece of the Standard Model puzzle. The LHC is expected to operate for approximately 20 more years at a higher center-of-mass energy and higher instantaneous luminosity, and the various experiments will periodically receive detector upgrades. While so far Nature has shown herself to be very "Standard", the hope is that continued work by the ATLAS Collaboration, the LHC operators, and all of the personnel at CERN can help resolve some of the unanswered questions in physics or maybe even discover a new puzzle to solve!



# Appendix A

## Drell-Yan Cross Section Corrections

The Drell-Yan production of lepton pairs is the dominant background in this search for new particles. Therefore, correctly modeling this to the best available precision is of the utmost importance. The MC generated is up to NLO in QCD and LO in EW, and includes real photon FSR using PHOTOS. The production cross section for  $Z^0/\gamma^*$  has been calculated up to NNLO in QCD and NLO in EW, and should be used to correct the MC to this order. The NLO EW corrections include real weak-boson emission, initial and final state photon virtual photon emission which interferes with the amplitudes, and real photon initial state radiation (ISR). A full description of the corrections describe here can be found in the Dilepton Search Support Note [217], and all figures and tables are taken from there.

The motivation for these corrections, aside from working at higher-order in the SM backgrounds, is that it allows for a well-defined and consistent choice of schemes between QCD and EW. A comparison of the FEWZ program at NLO using the same PDF set as the MC generators is shown in Table A.1. This shows the difference due to the parameter schemes. To avoid tuning between the external calculations in QCD and different MC EW schemes,

## APPENDIX A. DRELL-YAN CROSS SECTION CORRECTIONS

the mass-dependent  $K$ -factor is defined as:

$$\begin{aligned}\sigma_{best}(m_{\ell\ell}) &= K(m_{\ell\ell}) \times \sigma_{MC}(m_{\ell\ell}), \\ K(m_{\ell\ell}) &= \frac{\sigma_{best}(m_{\ell\ell})}{\sigma_{MC}(m_{\ell\ell})}.\end{aligned}$$

The “best” cross section is the highest-order consistent calculation possible, using NNLO QCD calculations with the MSTW2008NNLO PDF set and NLO EW corrections excluding FSR. This requires the MC samples to be re-weighted to the best-possible theory values. As a cross-check, this correction method is run for both the POWHEG (NLO) and PYTHIA (LO) DY samples throughout.

### A.1 QCD NNLO Corrections

The mass-dependent cross sections are calculated to NNLO in QCD using FEWZ [219] and VRAP [251]. Both interface with the LHAPDF library [252, 253] to utilize the large variety of PDF sets to study systematic differences. The comparisons to various PDFs are made in Figure A.1. In the mass range from 10 to 1500 GeV, the QCD  $K$ -factor is  $\sim +10\%$  across all PDF sets. Above 1500 GeV, there is a larger variation due to the lack of constraint on the PDFs at high Bjorken- $x$ . This shows that there is no preferred PDF set, so a choice is made to obtain a “nominal”  $K$ -factor and uncertainties will be centered about this choice. The nominal choice made is to use the MSTWNNLO PDF [85]. The nominal QCD  $K$ -factors are the first part of the overall  $K$ -factor applied.

The uncertainties associated with the NNLO QCD predictions derive from the uncertainties (90% CL) taken from the set of eigenvectors of the nominal PDF. There is also the uncertainty due to the QCD coupling  $\alpha_S$ , again using the 90% CL, covering the range

APPENDIX A. DRELL-YAN CROSS SECTION CORRECTIONS

$m_{\ell\ell}^{\text{lower}}$	$m_{\ell\ell}^{\text{upper}}$	$\frac{d\sigma_{\text{NLO,FEWZ}}}{dm_{\ell\ell}}$	$\frac{d\sigma_{\text{NLO,Powheg}}}{dm_{\ell\ell}}$	$\Delta_{\text{stat}}$ [%]	$\Delta_{\text{match}}$ [%]	$\Delta_{\text{stat,match}}$ [%]
66	116	2.17e+01	2.16e+01	0.0	0.3	0.0
116	140	3.53e-01	3.54e-01	0.2	-0.4	0.2
140	169	1.07e-01	1.08e-01	0.2	-1.1	0.2
169	204	4.02e-02	4.11e-02	0.3	-2.2	0.3
204	246	1.63e-02	1.65e-02	0.5	-1.4	0.5
246	297	6.76e-03	6.94e-03	0.4	-2.5	0.4
297	359	2.80e-03	2.88e-03	0.6	-2.6	0.5
359	433	1.15e-03	1.18e-03	0.7	-1.8	0.7
433	522	4.70e-04	4.82e-04	0.5	-2.6	0.4
522	631	1.86e-04	1.94e-04	0.6	-3.9	0.6
631	761	7.11e-05	7.32e-05	0.4	-3.0	0.4
761	919	2.61e-05	2.70e-05	0.4	-3.4	0.4
919	1110	9.03e-06	9.28e-06	0.4	-2.7	0.4
1110	1339	2.91e-06	3.01e-06	0.4	-3.1	0.4
1339	1617	8.62e-07	8.91e-07	0.3	-3.3	0.3
1617	1951	2.26e-07	2.34e-07	0.3	-3.1	0.3
1951	2355	5.13e-08	5.31e-08	0.3	-3.3	0.3
2355	2843	9.52e-09	9.87e-09	0.3	-3.5	0.3
2843	3432	1.33e-09	1.39e-09	0.3	-4.0	0.3
3432	4142	1.23e-10	1.28e-10	0.8	-3.9	0.7
4142	5000	5.76e-12	5.83e-12	3.2	-1.2	3.1

Table A.1: NLO NC Drell-Yan production differential cross sections using the CT10 PDF set calculated with FEWZ ( $G_\mu$  scheme) and the POWHEG generated cross section for the given invariant mass bins. The masses are in GeV, and the cross sections are in pb/GeV. The statistical error  $\Delta_{\text{stat}}$  is fully dominated by POWHEG. The deviation between external and MC cross sections is evaluated per mass bin with  $\Delta_{\text{match}} = 100 \times (1 - \sigma_{\text{FEWZ}}/\sigma_{\text{Powheg}})$ , and the statistical MC error is propagated to  $\Delta_{\text{stat,match}}$ . From [217], Appendix E, Table 36.

APPENDIX A. DRELL-YAN CROSS SECTION CORRECTIONS

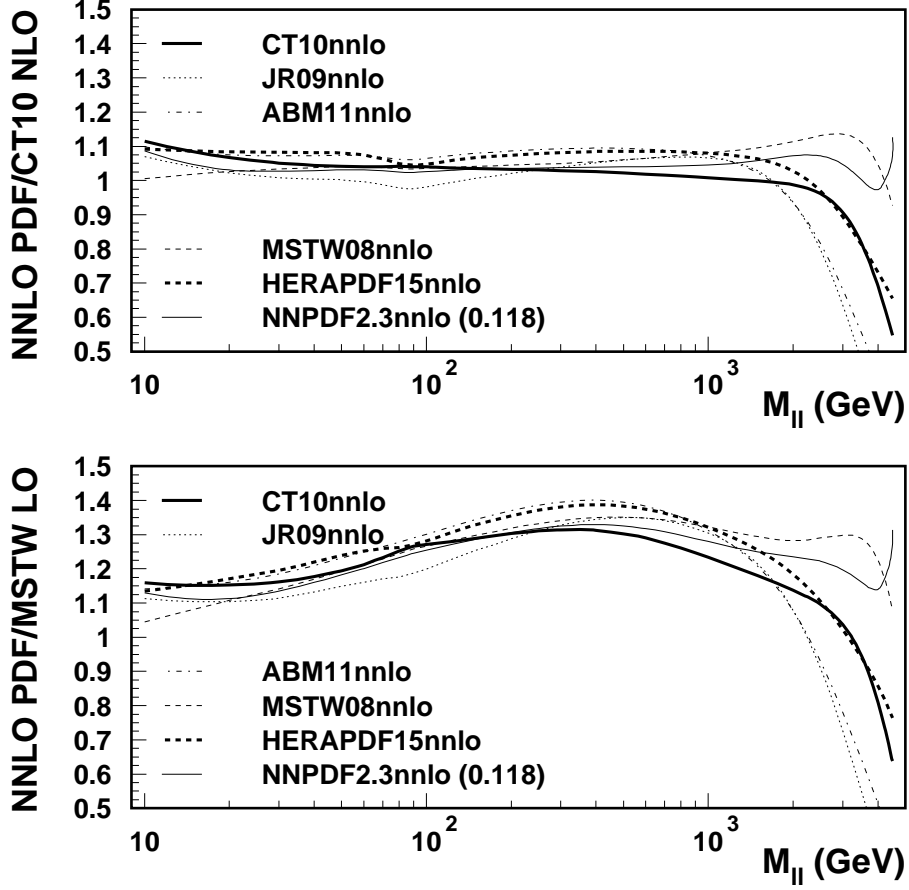


Figure A.1: Higher-order QCD corrections for the two MC DY samples, using NNLO PDF sets. The upper plot shows the ratio of six NNLO QCD prediction to CT10 NLO used in POWHEG, the lower plot uses the same PDF sets compared to MSTW LO used in PYTHIA. From [217], Appendix E, Figure 85.

$0.11365 \leq \alpha_S(M_Z) \leq 0.12044$ , with nominal value  $\alpha_S(M_Z) = 0.11707$ . Due to the larger variation of the different PDF sets, an additional uncertainty was assigned to the PDF choice. The 90% variation of the nominal PDF with the eigenvectors covered four of the PDF set choices central values. The ABM11 PDF was not covered by this variation, so a systematic is assigned between the central value of this PDF and the 90% variation of the nominal

## APPENDIX A. DRELL-YAN CROSS SECTION CORRECTIONS

PDF. This PDF Choice systematic is only non-zero above 1500 GeV and below 500 GeV. Lastly, VRAP allows the variation in the renormalization and factorization scales. The scale variations take into account further higher-order QCD effects and differences between the conventions used by the PDF sets. The scales were varied by factors of 1/2 and 2, due to the uncertainty ranging as high as 100%.

### A.2 EW NLO Corrections

The higher-order EW corrections are calculated separately at LO in QCD, and then applied additively to the higher-order QCD values. The EW correction total cross section is assumed to be the same for all orders in QCD. The additional EW correction factor is calculated using the HORACE event generator [254]. These are then added as a constant additional cross section to the QCD total, independent of the order of the QCD corrections. This approach was checked using the SANC MC generator [255, 256] up to 1500 GeV. The comparisons between the higher-order EW corrections at LO and NNLO in QCD are shown in Figure A.2. The resulting systematic uncertainty from this correction as a function of truth dilepton invariant mass is also shown. The additive approach is also used in the FEWZ package, however the subtraction schemes differ between the two programs. Varying the schemes and comparing the results from the two packages for the inclusion of higher-order EW corrections, show excellent agreement of 0.2-0.3%.

The largest EW correction is the photon-induced dilepton cross section, coming from lepton pair production due to emission of virtual photons. This is calculated at LO in QCD using the MRST2004QED PDF [257]. This includes higher-order QED corrections, and the additive factor is again assumed independent of QCD order. The uncertainties are mostly due to the effective quark masses used, either a constituent or current quark model, and

APPENDIX A. DRELL-YAN CROSS SECTION CORRECTIONS

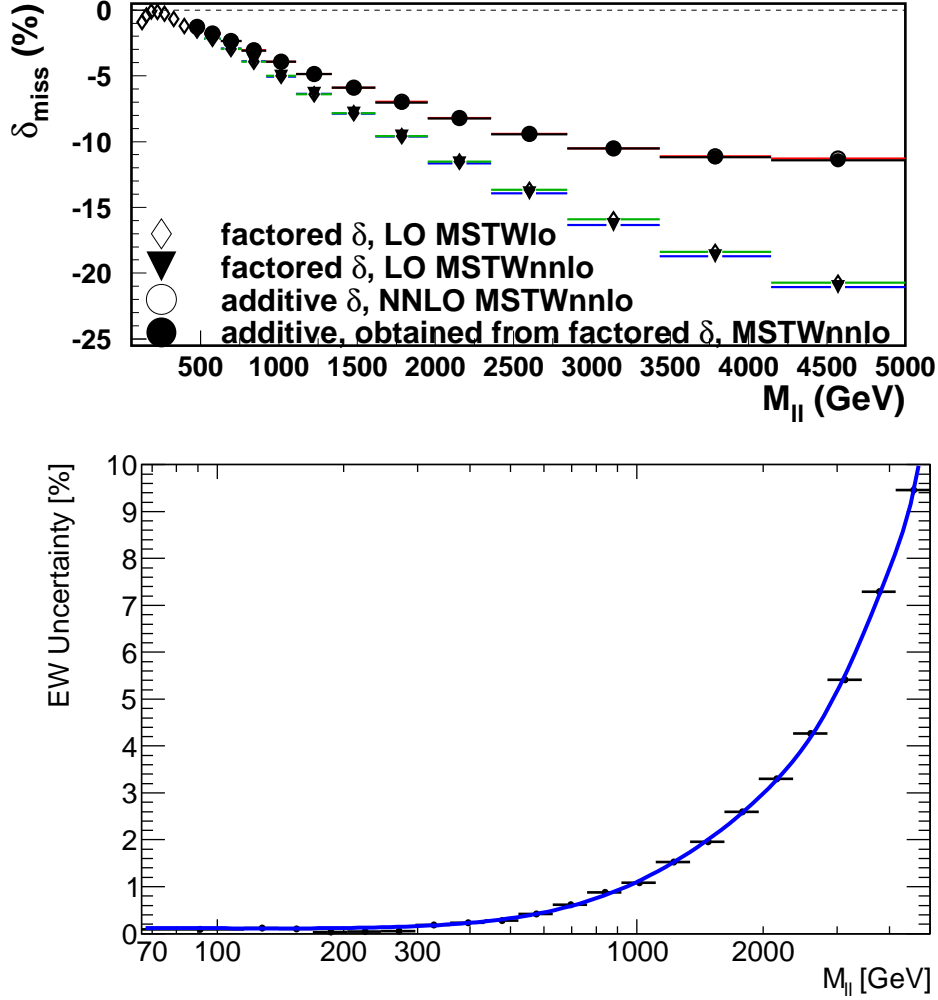


Figure A.2: Upper plot: Higher-order EW corrections across LO and NNLO QCD orders, comparing the factored and additive results. This shows the additive results, obtained from factoring at a lower order, is consistent across QCD orders. Lower plot: Systematic uncertainty due to the additional EW corrections as a function of  $m_{\ell\ell}$ . From [217], Appendix E, Figure 87.

the photon contribution to the PDF. The total uncertainty can be seen in Figure A.3. The photon-induced cross section contribution is found to be lepton-flavor independent over the mass ranges being studied. The corrections were again cross-checked in SANC.

APPENDIX A. DRELL-YAN CROSS SECTION CORRECTIONS

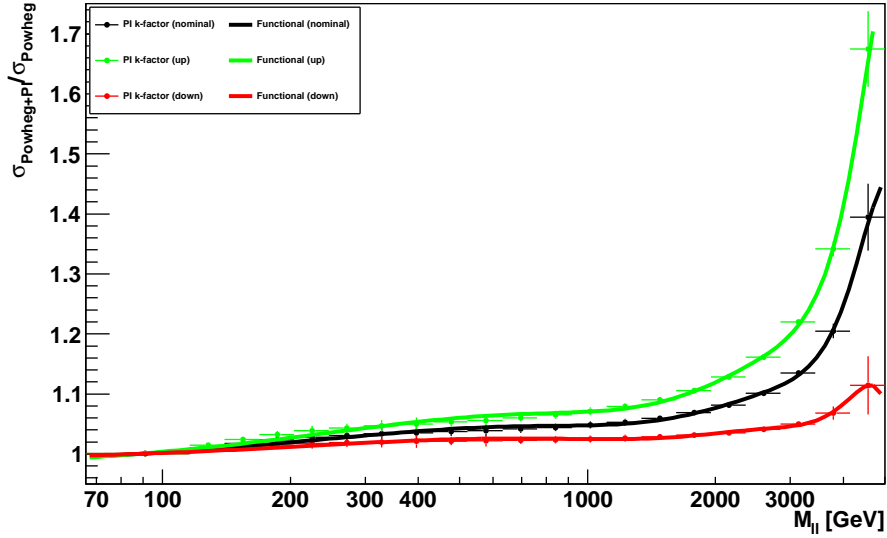


Figure A.3: Uncertainty due to the photon-induced cross section as a function of  $m_{\ell\ell}$ . The nominal value is calculated in FEWZ using POWHEG with MSTWNNLO and includes the higher-order EW corrections. The correction and upper and lower uncertainty bands come from the LO corrections added to the nominal value, based on the different quark mass schemes. From [217], Appendix E, Figure 89.

Another source of EW corrections comes from the emission of real  $W^\pm$  or  $Z^0$  bosons, in the same manner as photon emission in QED. This process is not included in the HERWIG diboson samples, which only simulates the direct production of two real EW bosons. Using MadGraph 5.4 [258], the EW boson radiation is calculated with respect to the DY process at LO in QCD, using the method described in [259]. Again, the input PDF set, the  $\alpha_S(m_Z)$  value, and renormalization and factorization scales are all varied and added as a systematic uncertainty.

### A.3 Total Corrections

The total mass-dependent  $K$ -factors calculated for the POWHEG samples are shown in Figure A.4. The samples are reweighted to the overall “best” theory available (MSTWNNLO PDF,  $G_\mu$  scheme) before FSR (which is included after interfacing with PHOTOS). The  $K$ -factor is fit with a smooth function over the full mass range, and the resulting fit values are used in the analysis. The reweighting was repeated for the PYTHIA LO DY samples as a cross check, and the results for the cross sections are compared between the two sets of samples in Figure A.5. The agreement shows the consistency of this reweighting approach.



APPENDIX A. DRELL-YAN CROSS SECTION CORRECTIONS

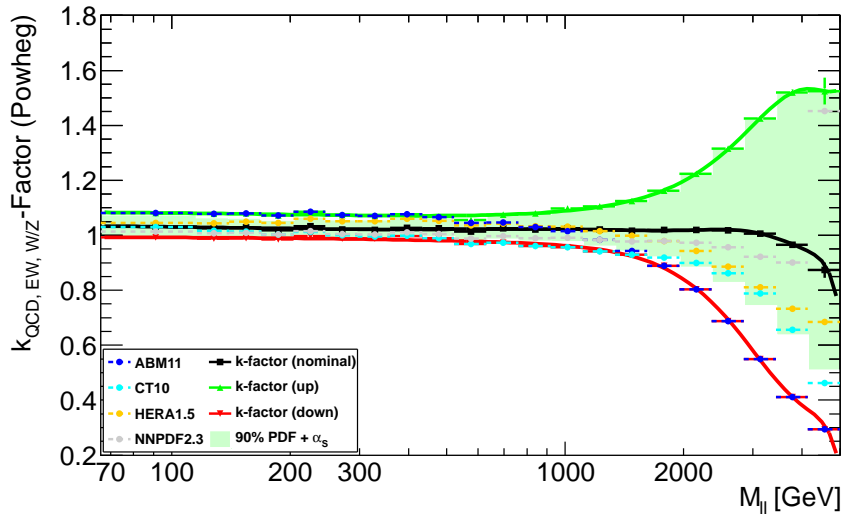


Figure A.4: The total  $K$ -factor for the POWHEG samples to reweight them to the “best” theory. This includes NNLO QCD and higher-order EW effects. The upper and lower limits at the 90% error envelope are shown shaded, the lower  $K$ -factor value at higher  $m_{\ell\ell}$  is due to the difference in PDF value using the ABM11 PDF set compared to the nominal MSTWNNLO PDF set. From [217], Appendix E, Figure 90.

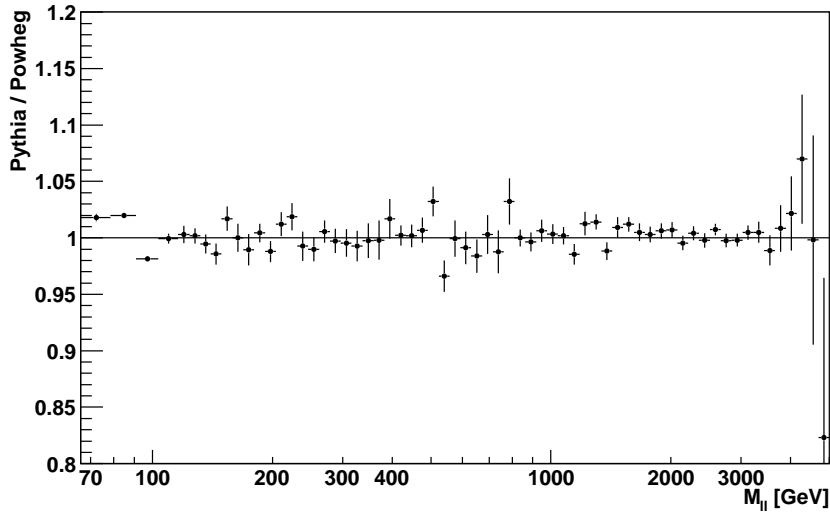


Figure A.5: The resulting cross sections after reweighting both PYTHIA LO DY samples and POWHEG NLO DY samples are compared across the full mass range. The error bars are the statistical uncertainty only. This shows excellent agreement between the two, and validates this as a consistent reweighting scheme. From [217], Appendix E, Figure 92.

# Appendix B

## Drell-Yan Systematics

The Drell-Yan component is the largest background in the dilepton search for new physics, and the understanding of that background is crucial to determining if a signal is present. Appendix A discussed how the simulated Monte Carlo samples are scaled to the most up-to-date theoretical predictions. This appendix will discuss the uncertainties associated with the Drell-Yan process. This is separated into PDF uncertainty, other QCD uncertainties, higher-order Electro-Weak uncertainties, and the LHC beam energy uncertainty. A complete description can be found in the Dilepton Search Support Note [217], and all figures and tables are taken from there.

### B.1 PDF Uncertainty

Each PDF has a set of eigenvectors in the parton function space, with errors from the measurements and theoretical uncertainties used to create the PDF. An example PDF is shown in Figure 2.1. Varying the value of the eigenvectors can systematically change the expected amount of Drell-Yan events observed in a hadronic collider environment, and this

## APPENDIX B. DRELL-YAN SYSTEMATICS

must be accounted for in the systematic errors. The nominal PDF used to calculate the Drell-Yan cross section is the MSTW 2008 NNLO [85], which contains 20 eigenvectors. In [85] Table 5 on page 52 shows the contributions to the errors for the eigenvectors from the individual parton functions.

The eigenvectors are varied at the 90% C.L. errors, and the change to the Drell-Yan cross section as a function of  $Q^2$  (or invariant mass,  $m_{\ell\ell}$ ) is calculated using VRAP [251]. Ideally, each eigenvector should be given its own systematic nuisance parameter in the search and limit setting procedure described in Section 5.2. However, this would involve a huge amount of computing power in the statistical framework and is impractical. The simplest option would be to sum in quadrature all of the errors for the 20 eigenvectors into a single systematic nuisance parameter, which was done in the previous iteration of this analysis [8]. This treats the uncertainties on the eigenvectors at low and high invariant mass as uncorrelated, but this leads to an over-constraint due to the different behaviors over the mass range.

Instead, the PDF eigenvectors are grouped into bundles corresponding to their uncertainty behavior as a function of  $Q^2$ . Four groups are used, corresponding to the eigenvectors dominant in the low mass range ( $m_{\ell\ell} < 400$  GeV), a middle mass range ( $400 < m_{\ell\ell} < 1500$  GeV), a high mass range ( $m_{\ell\ell} > 1500$  GeV), and a group that is not dominant anywhere but still has a non-negligible contribution. The eigenvectors for each group are listed below, and the sign associated with each eigenvector indicates whether the errors are inverted or not to follow the behavior of the group as a whole. A  $(-)$  sign indicates the down variation has been exchanged with the up variation and vice-versa, while a  $(+)$  sign preserves the up/down variation.

- Group A. Eigenvectors 2(+), 13(+), 14(-), 17(-), 18(+), and 20(+). It is not domi-

## APPENDIX B. DRELL-YAN SYSTEMATICS

nant anywhere, but has a non-negligible contribution.

- Group B. Eigenvectors 3(-), 4(-), 9(+), and 11(+). It is dominant in the mass range  $m_{\ell\ell} < 400$  GeV.
- Group C. Eigenvectors 1(+), 5(+), 7(+), and 8(-). It is dominant in the mass range  $400 < m_{\ell\ell} < 1500$  GeV.
- Group D. Eigenvectors 10(+), 12(+), 15(-), 16(-), and 19(+). It is dominant in the mass range  $m_{\ell\ell} > 1500$  GeV.

Eigenvector 6 does not match any of the groups; it corresponds principally to the  $s - \bar{s}$  sea contributions to the PDF and has a negligible impact on the overall Drell-Yan uncertainty, so it is ignored in these systematic errors. The largest single uncertainty in the high mass range comes from eigenvector 12 in Group D, which corresponds to the  $d - \bar{u}$  contribution to the PDF.

For each group, the total asymmetric uncertainty from the eigenvectors is calculated at each mass point as:

$$\begin{aligned}\Delta\sigma_G^+ &= \text{sgn}_G \sqrt{\left| \sum_{i=1}^{N_G} \text{sgn}(\sigma_i^+ - \sigma_0) \cdot (\sigma_i^+ - \sigma_0)^2 \right|}, \\ \Delta\sigma_G^- &= \text{sgn}_G \sqrt{\left| \sum_{i=1}^{N_G} \text{sgn}(\sigma_i^- - \sigma_0) \cdot (\sigma_i^- - \sigma_0)^2 \right|}.\end{aligned}$$

The sum is over the PDF eigenvectors for the group,  $\sigma_0$  is the cross section from the central value of the nominal PDF, and  $\sigma_i^\pm$  is the cross section from the upward (downward) variation of the  $i^{\text{th}}$  eigenvector, or downward (upward) if that eigenvector error is inverted. The overall sign  $\text{sgn}_G$  is the sign of the sum inside the square root. The asymmetric uncertainties are

## APPENDIX B. DRELL-YAN SYSTEMATICS

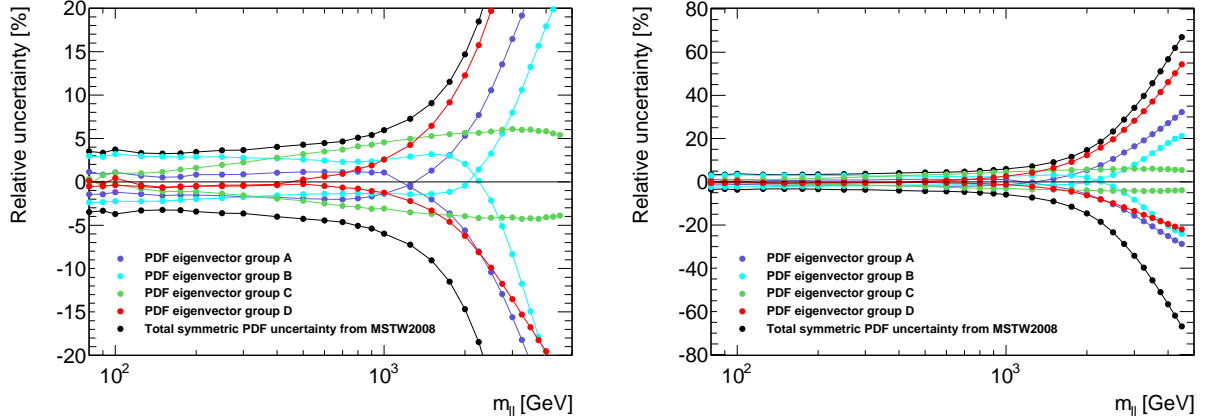


Figure B.1: The total asymmetric uncertainty on the Drell-Yan cross section as a function of invariant mass  $m_{\ell\ell}$ . The four eigenvector groups are shown in color, and the black is the total symmetric uncertainty following the MSTW2008 prescription. The left plot shows the lower mass range below  $m_{\ell\ell} < 1500$  GeV, and the right plot shows the full mass range. From [217], Appendix G, Figure 98.

plotted in Figure B.1, along with the total symmetric uncertainty following the MSTW2008 prescription which includes all the eigenvectors.

A cross check was performed comparing the symmetric sum in quadrature of the calculated uncertainties using FEWZ [219]. This showed good agreement with the total uncertainty as calculated with VRAP above, after symmetrizing and summing in quadrature. Below 3500 GeV the two methods agreed to within 0.35%, and are within 1% below 4500 GeV.

## B.2 PDF Choice, Scale, and $\alpha_S$ Uncertainty

The PDF set has the eigenvectors corresponding to the parton contributions to the proton, however there are additional inputs to a PDF that should be taken into account. The strength of the QCD coupling ( $\alpha_S(m_Z)$ ) and the scale at which the theoretical inputs are renormalized

## APPENDIX B. DRELL-YAN SYSTEMATICS

( $\mu_R$ ) and factorized ( $\mu_F$ ) can change the PDF outputs. There are other PDF sets available besides the one chosen as the nominal central value, and a systematic comparison between PDF sets is included. In Appendix A, the inclusion of higher-order electro-weak and photon-induced also introduced systematic errors from the theoretical inputs.

The systematic uncertainty due to  $\alpha_S$  is measured by varying the input value between 0.11365 and 0.12044, the 90% C.L.  $\alpha_S(m_Z)$  limits used in MSTW 2008. The difference in the cross section value computed in VRAP from the nominal value is the asymmetric uncertainty.

The systematic uncertainty due to  $\mu_R$  and  $\mu_F$  is measured by varying them both simultaneously up by a factor of two and down by a factor of half. The maximum difference between the cross sections computed in VRAP and the nominal value is the symmetric uncertainty.

The systematic uncertainty due to varying which PDF set is used in the calculations is measured by changing the input PDF set in the VRAP calculations, leaving the input coupling  $\alpha_S$  and scales  $\mu_R$  and  $\mu_F$  the same. Four other PDF sets were considered:

- CT10NNLO [218].
- NNPDF2.3 [260].
- ABM11 [261].
- HERAPDF1.5 [262].

The difference in the cross section calculated between central value of these PDF sets and the nominal MSTW2008NNLO is compared to the 90% C.L. values from the nominal MSTW2008NNLO PDF set. Three out of four had nominal values within the 90% C.L. variation throughout the mass range; the only PDF set showing larger deviations is ABM11.

## APPENDIX B. DRELL-YAN SYSTEMATICS

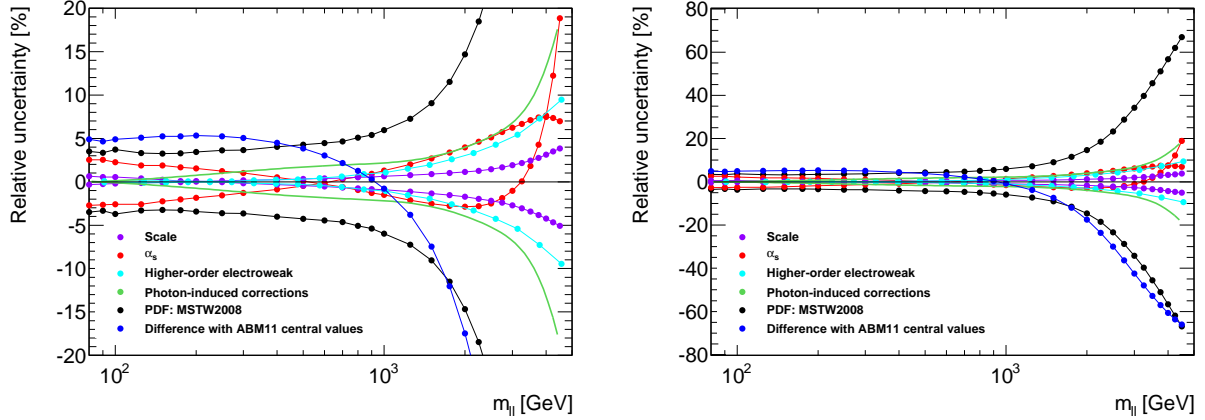


Figure B.2: The total asymmetric uncertainty on the Drell-Yan cross section as a function of invariant mass  $m_{\ell\ell}$ . The colors correspond to each source as calculated in this Appendix. The black curve is the total symmetric uncertainty following the MSTW2008 prescription, for comparison with the PDF eigenvector uncertainties in Figure B.1. The left plot shows the lower mass range below  $m_{\ell\ell} < 1500$  GeV, and the right plot shows the full mass range. From [217], Appendix G, Figure 100.

The difference is included as an additional uncertainty, to account for different theoretical modeling between the PDF collaborations.

The Monte Carlo has been scaled to include higher-order electro-weak processes in the Drell-Yan process, as described in Section A.2. This scaling also includes the errors from the underlying theoretical inputs, and these are included as systematics. The systematic uncertainties can be seen in Figure A.2 and Figure A.3. The uncertainty due to HO EW loops is very small until 1500 GeV, while the uncertainty due to the photon-induced corrections are larger.

Each of these systematics are plotted together in Figure B.2, with the MSTW2008 PDF 90% C.L. to show their relative systematic contribution with respect to the PDF set uncertainties.

### B.3 Beam Energy Uncertainty

One additional systematic uncertainty is applied to the Drell-Yan process, which comes from an experimental rather than theoretical source. The beam energy at the LHC was measured to be  $P_{beam} = 3988 \pm 5(\text{stat}) \pm 26(\text{sys})$  GeV [230]. The production cross section was calculated in VRAP using the MSTW2008NNLO PDF, varying the two input beam energies up and down from their nominal values. See Figure B.3 for the behavior as a function of the invariant mass of the dilepton system. The ratio from the nominal value is the systematic uncertainty quoted for the search and limit setting.

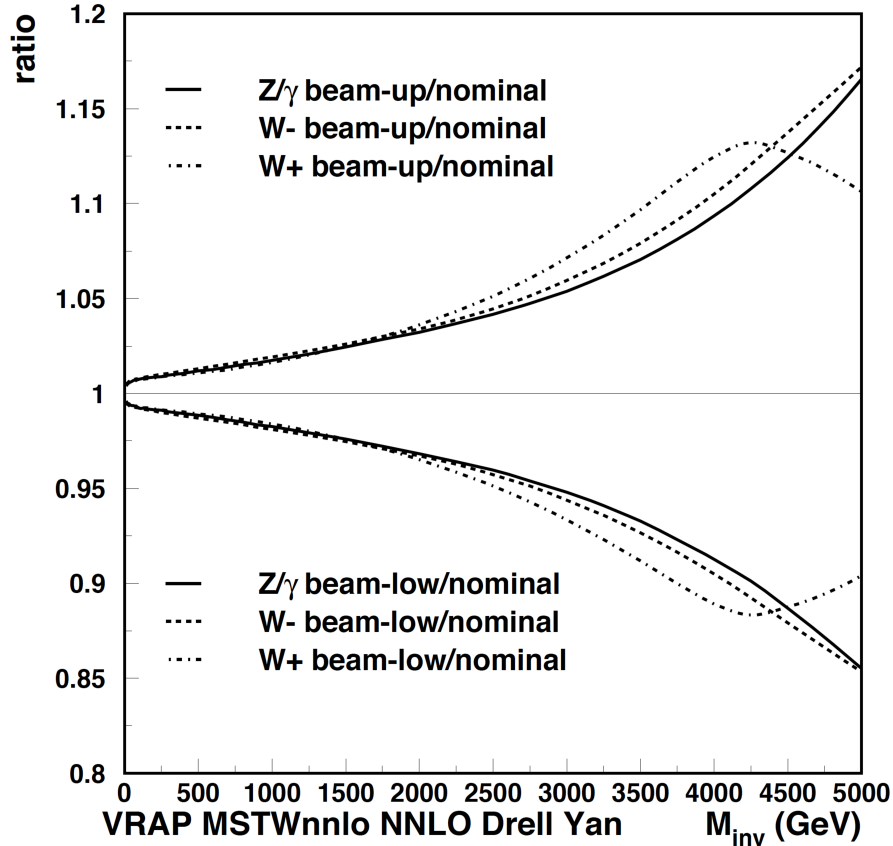


Figure B.3: The relative uncertainty on the Drell-Yan and  $W^\pm$  production cross section due to the input beam energy, as calculated in VRAP. From [263].



# Appendix C

## Electron Scale Factors

Scale factors are applied to the electron events to better match the simulated Monte Carlo with the observed data. This is done to prevent any mis-modeling in the simulations of the trigger or showering from affecting the expected data. The scale factors are calculated by studying the efficiency in the data and MC in the same way, and the scale factor is defined as:

$$\text{SF} = \frac{\varepsilon_{DATA}}{\varepsilon_{MC}}.$$

The efficiencies are calculated using the “Tag & Probe” method, where a sample of dielectron events are used from  $Z^0 \rightarrow e^+e^-$  decays. If the sample has an appropriate “Tag” electron, the efficiency is calculated for the “Probe” electrons by computing the ratio between the passing probe electrons ( $N_P$ ) and all possible probe electrons ( $N_0$ ):

$$\varepsilon = \frac{N_P}{N_0}.$$

## APPENDIX C. ELECTRON SCALE FACTORS

The errors on the efficiencies are calculated following [264], Equation 14:

$$(\delta_\varepsilon)^2 = \frac{(1 - 2\varepsilon)\delta_P^2 + \varepsilon^2\delta_0^2}{N_0^2}.$$

The  $\delta_{P,0}^2$  factors are the Poisson errors on the  $N_{P,0}$ .

Because the selection is asymmetric between the leading and sub-leading electrons, the scale factors will be different between them. In the two cases studied, the trigger event-level cut and the isolation electron-level cut, each case has its own event, tag, and probe selection to study the scale factors.

### C.1 Trigger Scale Factors

The electron event selection uses the *EF\_g35\_loose\_g25\_loose* diphoton trigger. The leading electron should fire the first leg and the sub-leading electron should fire the second leg, however the event filter does not store which object fired which leg of the trigger. Instead, single-photon triggers are looked at separately for the leading and sub-leading electron cases. There is no *EF\_g25\_loose* (or *EF\_g35\_loose*) trigger, and the closest single-photon trigger is the *EF\_g20\_loose* trigger. This trigger was operating in “RERUN-RESURRECTED” mode, which means the trigger is re-evaluated over the whole trigger chain if any unprescaled photon trigger was fired. To approximate the single triggers *EF\_g25\_loose* (or *EF\_g35\_loose*), the electron must be matched to the *EF\_g20\_loose* trigger and the LVL1 triggers *L1\_EM12* (or *L1\_EM16V*), with a cut on the uncorrected  $E_T$  in the ECAL cluster at 25 (35) GeV.

The sample of  $Z^0 \rightarrow e^+e^-$  decays used for the tag & probe study must pass the following selection:

- Event passes a single-electron trigger *EF\_e24vhi\_medium1* or *EF\_e60\_medium1*. The

### APPENDIX C. ELECTRON SCALE FACTORS

first trigger applies an isolation cut and a hadronic leakage cut; the second trigger does not in order to regain some lost high- $E_T$  electrons.

- Event has no data errors from Calorimeters or coreFlags.
- Event has a good primary vertex with at least 3 tracks.
- Event has at least 2 electrons with author 1 or 3, and in the standard acceptable  $\eta$  range.

Pileup and  $z$ -vertex reweighting are also applied to the MC. In this sample, one tag electron is required. The tag electron must satisfy the following:

- Tag electron must pass object quality in the calorimeters.
- Tag electron  $E_T > 25$  GeV.
- Tag electron must pass isEM *tight++*.
- Tag electron must match the trigger object.

If a tag electron is found, all other electrons in the event are checked for probe status with the following criteria:

- Probe electron  $E_T > 15$  GeV.
- Probe electron must pass isEM identification.
- Probe electron track in the ID must have at least 7 Silicon hits and at least 1 Pixel hit.
- Probe electron charge must be opposite to the tag electron.

### APPENDIX C. ELECTRON SCALE FACTORS

- Probe electron must be loosely matched to a truth electron (in MC only).
- The invariant mass of the tag & probe pair should be in the mass window about the  $Z^0$  peak.

All tag & probe pair combinations are considered. The trigger efficiencies are calculated in data and MC as the ratio between the number of probe electrons that are matched to the approximated trigger object and the total number of probe electrons. These are divided up into  $E_T$  and  $\eta$  bins, and leading and sub-leading electrons. The scale factors are the average efficiency in data divided by the average efficiency in MC, for each bin and leading/sub-leading electrons.

Systematics uncertainties for the efficiencies are calculated by varying the selection on the probe electrons in the following ways:

- The invariant mass window of the tag & probe pair is varied over three windows:
  - 75-105 GeV, 80-100 GeV, 85-95 GeV
- The probe electron isEM identification is varied between *medium++* and *tight++*.

There are six combinations of efficiencies in data and MC, and six SFs calculated. The average over the six values is the nominal central value of the SF applied in this analysis. The statistical error is the average over the statistical errors in each calculation. The systematic error is the RMS from the six values SF values. The SFs over  $E_T$  and  $\eta$  bins for the leading and sub-leading electrons are shown in Figure C.1, and listed in Table C.1. The  $\eta$  region corresponding to the “crack” ( $1.37 < |\eta| < 1.52$ ) is shown in the SF calculation, but is excluded in the analysis.

APPENDIX C. ELECTRON SCALE FACTORS

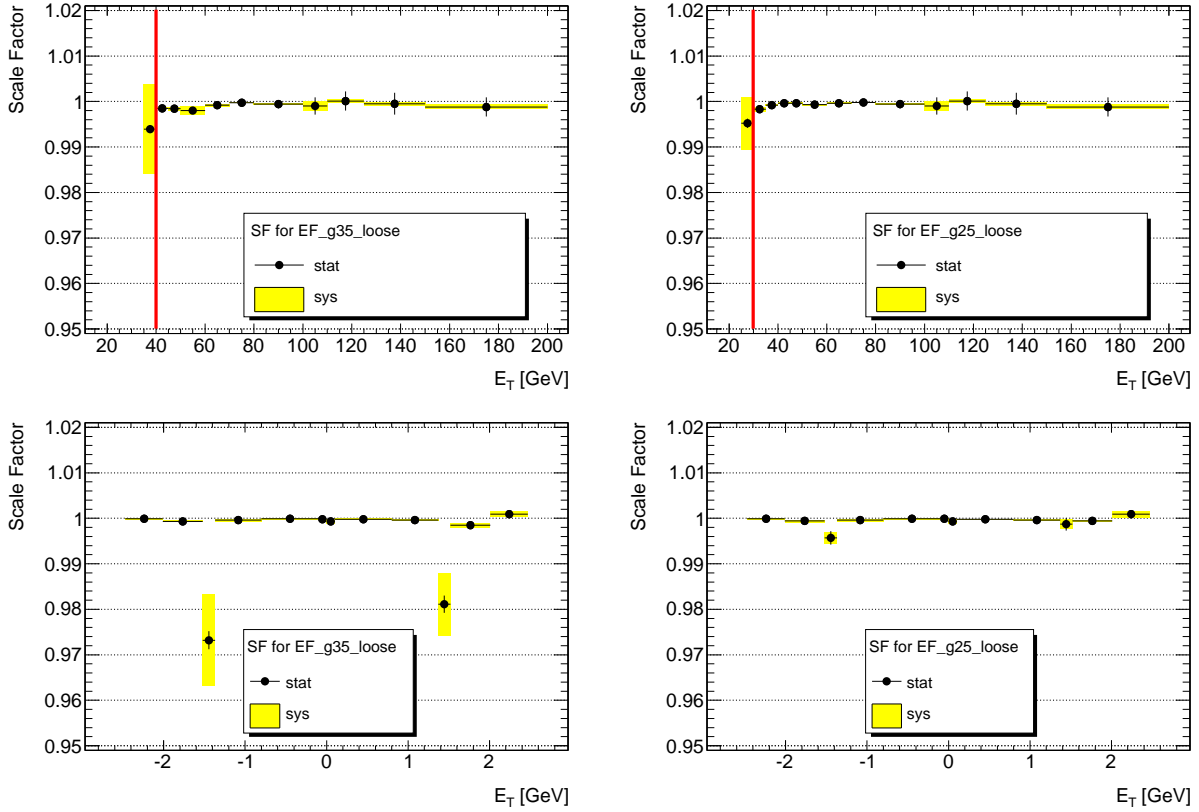


Figure C.1: Upper Left: Leading electron ( $\sim EF_{g35\_loose}$ ) SFs as a function of  $E_T$ . Upper Right: Sub-leading electron ( $\sim EF_{g25\_loose}$ ) SFs as a function of  $E_T$ . Lower plots are the same, as a function of  $\eta$ . From [217], Appendix L, Figures 119,120.

APPENDIX C. ELECTRON SCALE FACTORS

$E_T[GeV]$	Subleading electron( $EF\_g25\_loose$ )	Leading electron( $EF\_g35\_loose$ )
30 - 35	$0.9983 \pm 0.0002 \pm 0.0005$	
35 - 40	$0.9992 \pm 0.0001 \pm 0.0002$	$0.9939 \pm 0.0003 \pm 0.0098$
40 - 45	$0.9996 \pm 0.0001 \pm 0.0002$	$0.9985 \pm 0.0001 \pm 0.0002$
45 - 50	$0.9996 \pm 0.0001 \pm 0.0001$	$0.9984 \pm 0.0001 \pm 0.0004$
50 - 60	$0.9993 \pm 0.0001 \pm 0.0002$	$0.9980 \pm 0.0002 \pm 0.0009$
60 - 70	$0.9996 \pm 0.0002 \pm 0.0001$	$0.9992 \pm 0.0002 \pm 0.0003$
70 - 80	$0.9998 \pm 0.0003 \pm 0.0001$	$0.9997 \pm 0.0003 \pm 0.0001$
80 - 100	$0.9994 \pm 0.0004 \pm 0.0002$	$0.9994 \pm 0.0004 \pm 0.0002$
100 - 110	$0.9990 \pm 0.0008 \pm 0.0010$	$0.9990 \pm 0.0008 \pm 0.0010$
110 - 125	$1.0001 \pm 0.0008 \pm 0.0004$	$1.0001 \pm 0.0008 \pm 0.0004$
125 - 150	$0.9995 \pm 0.0010 \pm 0.0004$	$0.9995 \pm 0.0010 \pm 0.0004$
150 - 200	$0.9988 \pm 0.0009 \pm 0.0005$	$0.9988 \pm 0.0009 \pm 0.0005$
200 - 400	$0.9990 \pm 0.0010 \pm 0.0005$	$0.9990 \pm 0.0010 \pm 0.0005$
400 - 1000	$0.9939 \pm 0.0061 \pm 0.0043$	$0.9939 \pm 0.0061 \pm 0.0043$
$\eta$	Subleading electron( $EF\_g25\_loose$ )	Leading electron( $EF\_g35\_loose$ )
-2.47, -2.01	$0.9999 \pm 0.0002 \pm 0.0001$	$0.9999 \pm 0.0002 \pm 0.0001$
-2.01, -1.52	$0.9994 \pm 0.0001 \pm 0.0003$	$0.9993 \pm 0.0002 \pm 0.0001$
-1.52, -1.37	$0.9957 \pm 0.0015 \pm 0.0013$	$0.9732 \pm 0.0020 \pm 0.0101$
-1.37, -0.8	$0.9996 \pm 0.0000 \pm 0.0003$	$0.9996 \pm 0.0000 \pm 0.0003$
-0.8, -0.1	$0.9999 \pm 0.0000 \pm 0.0001$	$0.9999 \pm 0.0000 \pm 0.0001$
-0.1, 0	$0.9999 \pm 0.0001 \pm 0.0001$	$0.9998 \pm 0.0001 \pm 0.0001$
0, 0.1	$0.9993 \pm 0.0001 \pm 0.0005$	$0.9993 \pm 0.0001 \pm 0.0005$
0.1, 0.8	$0.9998 \pm 0.0000 \pm 0.0001$	$0.9998 \pm 0.0000 \pm 0.0002$
0.8, 1.37	$0.9996 \pm 0.0000 \pm 0.0002$	$0.9996 \pm 0.0000 \pm 0.0002$
1.37, 1.52	$0.9987 \pm 0.0014 \pm 0.0011$	$0.9811 \pm 0.0019 \pm 0.0069$
1.52, 2.01	$0.9994 \pm 0.0001 \pm 0.0002$	$0.9985 \pm 0.0002 \pm 0.0005$
2.01, 2.47	$1.0009 \pm 0.0002 \pm 0.0007$	$1.0009 \pm 0.0002 \pm 0.0006$

Table C.1: Trigger SFs for leading and subleading electrons vs  $E_T$  and  $\eta$  with statistical and systematic errors. From [217], Appendix L, Tables 45,46.

## C.2 Isolation Scale Factors

A similar procedure is followed for the isolation scale factors, with the criteria for the tag and probe electrons modified for this selection. The isolation cut is designed to eliminate QCD and  $W$ +jets backgrounds, but the scale factors should only be applied to the real electron background. The non-electron background is subtracted from the total probe background for the scale factors and will be considered in Appendix D.

Most of the selection from Section C.1 is applied to this tag & probe selection, and the tag electron selection is identical. Previously, the probe electron leading and sub-leading difference was the trigger selection, now this is modified to the  $E_T$  and isolation cuts. The probe electron selection criteria are:

- Probe electron is *medium++*.
- Probe electron (leading)  $E_T > 40$  GeV.
- Probe electron (leading)  $el\_Etcone20\_pt\_corrected > 0.007E_T + 5$  GeV.
- Probe electron (sub-leading)  $E_T > 30$  GeV.
- Probe electron (sub-leading)  $el\_Etcone20\_pt\_corrected > 0.022E_T + 6$  GeV.

The variations of the selection for the systematic uncertainty and to determine the central SF value are also modified from the previous selection.

- The probe electron isEM identification is varied between *medium++* and *tight++*.
- The invariant mass window of the tag & probe pair is varied over three windows.

– 75-105 GeV, 80-100 GeV, 85-95 GeV

### APPENDIX C. ELECTRON SCALE FACTORS

- The templates used for background subtraction for the probe electron are varied between three choices:
  - Same-sign electron pair failed *loose++*.
  - Opposite-sign electron pair failed TRT and  $W_{stot}$  cuts.
  - Probe electron fails  $p_T$  dependent track isolation cut:  $\frac{el\_ptcone40}{p_T} > 0.05$ .

There are 18 combinations of efficiencies in data and MC, and six SFs are calculated. The central value of the SF is used as the nominal SF applied, and is the average over the six values. The statistical error is the average over the statistical errors in each calculation. The systematic error is the RMS from the SF values. The SFs over  $E_T$  and  $\eta$  bins for the leading and sub-leading electrons are shown in Figure C.2, and listed in Table C.2. The  $\eta$  region corresponding to the “crack” ( $1.37 < |\eta| < 1.52$ ) is shown in the SF calculation, but is excluded in the analysis.



APPENDIX C. ELECTRON SCALE FACTORS

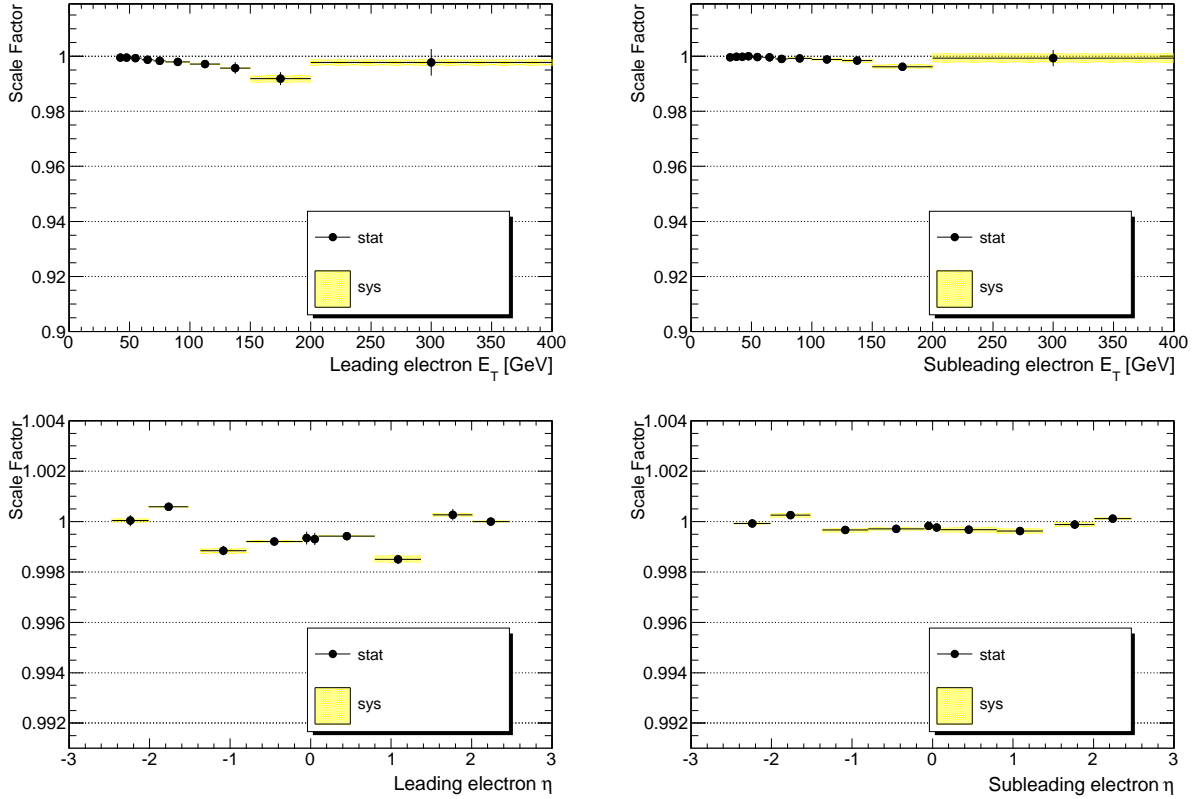


Figure C.2: Upper Left: Leading electron isolation SFs as a function of  $E_T$ . Upper Right: Sub-leading electron isolation SFs as a function of  $E_T$ . Lower plots are the same, but as a function of  $\eta$ . From [217], Appendix M, Figures 122,123.

APPENDIX C. ELECTRON SCALE FACTORS

$E_T$ [GeV]	Subleading electron SF	Leading electron SF
30 - 35	$0.9996 \pm 0.0001 \pm 0.0002$	
35 - 40	$0.9998 \pm 0.0001 \pm 0.0001$	
40 - 45	$0.9998 \pm 0.0000 \pm 0.0000$	$0.9995 \pm 0.0001 \pm 0.0001$
45 - 50	$1.0000 \pm 0.0000 \pm 0.0000$	$0.9995 \pm 0.0001 \pm 0.0000$
50 - 60	$0.9997 \pm 0.0001 \pm 0.0000$	$0.9993 \pm 0.0001 \pm 0.0000$
60 - 70	$0.9996 \pm 0.0001 \pm 0.0001$	$0.9988 \pm 0.0003 \pm 0.0001$
70 - 80	$0.9990 \pm 0.0003 \pm 0.0001$	$0.9983 \pm 0.0004 \pm 0.0002$
80 - 100	$0.9992 \pm 0.0007 \pm 0.0002$	$0.9979 \pm 0.0008 \pm 0.0002$
100 - 125	$0.9989 \pm 0.0007 \pm 0.0003$	$0.9972 \pm 0.0012 \pm 0.0003$
125 - 150	$0.9984 \pm 0.0012 \pm 0.0005$	$0.9957 \pm 0.0021 \pm 0.0003$
150 - 200	$0.9962 \pm 0.0011 \pm 0.0007$	$0.9919 \pm 0.0023 \pm 0.0012$
200 - 400	$0.9993 \pm 0.0029 \pm 0.0016$	$0.9978 \pm 0.0048 \pm 0.0010$
400 - 1000	$1.0184 \pm 0.0207 \pm 0.0021$	$0.9931 \pm 0.0248 \pm 0.0014$
$\eta$	Subleading electron SF	Leading electron SF
-2.47, -2.01	$0.9999 \pm 0.0001 \pm 0.0000$	$1.0000 \pm 0.0002 \pm 0.0001$
-2.01, -1.52	$1.0003 \pm 0.0001 \pm 0.0001$	$1.0006 \pm 0.0002 \pm 0.0000$
-1.52, -1.37	$0.0000 \pm 0.0000 \pm 0.0000$	$0.0000 \pm 0.0000 \pm 0.0000$
-1.37, -0.80	$0.9997 \pm 0.0001 \pm 0.0001$	$0.9988 \pm 0.0002 \pm 0.0001$
-0.80, -0.10	$0.9997 \pm 0.0001 \pm 0.0001$	$0.9992 \pm 0.0001 \pm 0.0001$
-0.10, 0.00	$0.9998 \pm 0.0001 \pm 0.0001$	$0.9993 \pm 0.0003 \pm 0.0000$
0.00, 0.10	$0.9998 \pm 0.0001 \pm 0.0001$	$0.9993 \pm 0.0002 \pm 0.0000$
0.10, 0.80	$0.9997 \pm 0.0001 \pm 0.0001$	$0.9994 \pm 0.0001 \pm 0.0000$
0.80, 1.37	$0.9996 \pm 0.0001 \pm 0.0001$	$0.9985 \pm 0.0002 \pm 0.0001$
1.37, 1.52	$0.0000 \pm 0.0000 \pm 0.0000$	$0.0000 \pm 0.0000 \pm 0.0000$
1.52, 2.01	$0.9999 \pm 0.0002 \pm 0.0001$	$1.0003 \pm 0.0002 \pm 0.0001$
2.01, 2.47	$1.0001 \pm 0.0001 \pm 0.0001$	$1.0000 \pm 0.0001 \pm 0.0000$

Table C.2: Isolation SFs for leading and subleading electrons vs  $E_T$  and  $\eta$  with statistical and systematic errors. From [217], Appendix L, Tables 47,48.

# Appendix D

## Electron Fake Factors

The background for electrons where one or both are mis-identified from a jet in the EM calorimeter (“fakes”) is estimated using the “fake factor” or “matrix” method. The idea is to loosen some of the electron identification criteria from the standard tight criteria and compare the rate looser objects pass as electrons to the tight selection, and use that comparison to estimate the rate tight selected non-electron objects pass electron identification. Several variations are performed to evaluate statistical and systematic uncertainties. This is a data-driven method, using the full 2012 ATLAS data set of about  $21 \text{ fb}^{-1}$ .

### D.1 Matrix Method

The matrix method looks at electrons that either pass the tight or loose selections  $N_{T/L}$ . These are measurable, and can be related to the “true” quantities of the real or fake electrons  $N_{R/F}$ . The matrix method analyzes the ratios between real/fake ( $R/F$ ) and tight/loose ( $T/L$ ) selections. The probability that a true fake in the loose selection also passes the tight selection is the “fake rate” and the probability that a true real electron in the loose selection

## APPENDIX D. ELECTRON FAKE FACTORS

also passes the tight selection is the “real rate”.

$$f_i = \frac{N_{T,i}^F}{N_{L,i}^F}, \quad r_i = \frac{N_{T,i}^R}{N_{L,i}^R}.$$

The  $i$  designates the leading or sub-leading electron, and the  $N_{T/L}^{R/F}$  are the number of tight/loose objects coming from real/fake electrons. Ideally, the fake rate should be 0 and the real rate should be 1, independent of the loose selection. In this analysis the leading and sub-leading electron selections are different and they will have different fake and real rates.

The selection comes in pairs, so there are four total choices for the measurable quantities:  $N_{TT}$ ,  $N_{TL}$ ,  $N_{LT}$ , and  $N_{LL}$ , and four choices for the true quantities:  $N_{RR}$ ,  $N_{RF}$ ,  $N_{FR}$ , and  $N_{FF}$ . The two sets of four are related by a matrix equation:

$$\begin{pmatrix} N_{TT} \\ N_{TL} \\ N_{LT} \\ N_{LL} \end{pmatrix} = \begin{pmatrix} r_1 r_2 & r_1 f_2 & f_1 r_2 & f_1 f_2 \\ r_1(1-r_2) & r_1(1-f_2) & f_1(1-r_2) & f_1(1-f_2) \\ (1-r_1)r_2 & (1-r_1)f_2 & (1-f_1)r_2 & (1-f_1)f_2 \\ (1-r_1)(1-r_2) & (1-r_1)(1-f_2) & (1-f_1)(1-r_2) & (1-f_1)(1-f_2) \end{pmatrix} \begin{pmatrix} N_{RR} \\ N_{RF} \\ N_{FR} \\ N_{FF} \end{pmatrix}$$

The part of concern for the analysis is the number of tight-tight pairs  $N_{TT}$  that come from fake objects. The top row of the matrix gives:

$$N_{TT}^{\text{fakes}} = \underbrace{r_1 f_2 N_{RF} + f_1 r_2 N_{FR}}_{N_{TT}^{\ell+\text{jets}}} + \underbrace{f_1 f_2 N_{FF}}_{N_{TT}^{\text{dijet}}}. \quad (\text{D.1})$$

The matrix can be inverted to solve for the real and fake quantities in terms of the measured

APPENDIX D. ELECTRON FAKE FACTORS

tight and loose selections.

$$\begin{pmatrix} N_{RR} \\ N_{RF} \\ N_{FR} \\ N_{FF} \end{pmatrix} = \frac{1}{(r_1 - f_1)(r_2 - f_2)} \begin{pmatrix} (f_1 - 1)(f_2 - 1) & (f_1 - 1)f_2 & f_1(f_2 - 1) & f_1f_2 \\ (f_1 - 1)(1 - r_2) & (1 - f_1)r_2 & f_1(1 - r_2) & -f_1r_2 \\ (r_1 - 1)(1 - f_2) & (1 - r_1)f_2 & r_1(1 - f_2) & -r_1f_2 \\ (1 - r_1)(1 - r_2) & (r_1 - 1)r_2 & r_1(r_2 - 1) & r_1r_2 \end{pmatrix} \begin{pmatrix} N_{TT} \\ N_{TL} \\ N_{LT} \\ N_{LL} \end{pmatrix}$$

Define the lead factor  $\alpha \equiv \frac{1}{(r_1 - f_1)(r_2 - f_2)}$ . Inserting the measured quantities for the true quantities, the number of fake tight-tight objects reconstructed in Equation (D.1) is now:

$$\begin{aligned} N_{TT}^{\text{fakes}} &= \alpha [f_1f_2(1 - r_1r_2) - r_1f_2(1 - r_2) - f_1r_2(1 - r_1)] N_{TT} \\ &\quad + \alpha [r_1r_2f_2(1 - f_1)] N_{TL} \\ &\quad + \alpha [r_1f_1r_2(1 - f_2)] N_{LT} \\ &\quad - \alpha [r_1f_1r_2f_2] N_{LL}. \end{aligned} \tag{D.2}$$

The problem is reduced to measured quantities, provided there are reasonable estimates of the fake rates  $f_i$  and real rates  $r_i$  for the leading and sub-leading electrons.

Equation D.2 can be further simplified with an approximation that the real electron contribution to the tight selection is ideal ( $r_i = 1$ ). Simplifying Equation (D.2) with this approximation:

$$N_{TT}^{\text{fakes}} = \frac{f_2}{1 - f_2} N_{TL} + \frac{f_1}{1 - f_1} N_{LT} - \frac{f_2}{1 - f_2} \frac{f_1}{1 - f_1} N_{LL}.$$

The coefficients are called the ‘‘fake factors’’. Using the definition of the fake rate, this can be simplified in terms of the number of objects in the tight and loose selections:

$$F_i = \frac{f_i}{1 - f_i} = \frac{N_{T,i}^F / N_{L,i}^F}{1 - N_{T,i}^F / N_{L,i}^F} = \frac{N_{T,i}^F}{N_{L,i}^F - N_{T,i}^F}.$$

## APPENDIX D. ELECTRON FAKE FACTORS

The tight selection is a subset of the loose selection so the difference is the number of objects that fail the tight selection. In the denominator, this becomes:

$$N_{L,i}^F - N_{T,i}^F = N_{\text{fail T},i}^F. \quad (\text{D.3})$$

The fake factor is now the ratio of the two sets of fake objects in the dataset, those that pass the tight selection to those that fail.

$$F_i^{\text{fail T}} = \frac{N_{T,i}^F}{N_{\text{fail T},i}^F} \quad (\text{D.4})$$

$$N_{TT}^{\text{fakes}} = F_2^{\text{fail T}} N_{TL} + F_1^{\text{fail T}} N_{LT} - F_1^{\text{fail T}} F_2^{\text{fail T}} N_{LL} \quad (\text{D.5})$$

The fake factor is derived from the fake rate, and to evaluate it depends on finding a sample that contains a large amount of true fakes.

The tight selection is the standard signal selection used in the analysis, including the  $p_T$  and isolation cuts for the leading and sub-leading electrons as well as the electron identification isEM *medium++*. This identification includes shower shape and track matching requirements. The loose selection must satisfy the  $p_T$  cuts, but not the isolation cuts, and the electron identification requirement used isEM *loose++* without track matching. A second loose selection, designed to give a cleaner sample of fake objects and provide a systematic check, changes the electron identification requirement to isEM *medium++* but fails the track matching requirement. The fake factor from Equation (D.4) for this selection is designated:

$$F_i^{\text{fail track}} = \frac{N_{T,i}^F}{N_{\text{fail track},i}^F}. \quad (\text{D.6})$$

The loose selection is changed and must be applied to all the  $N_{T/L}$  in Equation (D.5).

## D.2 Real Electron Rates

The real electron rates  $r_i$  are the rates that a true leading and sub-leading electron are correctly identified in the tight selection as an electron. This requires a sample of true electrons, either in data or Monte Carlo. This is estimated in MC, where the objects can be matched to the truth electrons in the simulation. The MC samples of leading and sub-leading electrons are the mass-binned Drell-Yan MC described in Section 4.2.2. The tight and loose selections follow the requirements described above.

The real electron rates estimated from the MC, including applying the appropriate scale factors, for the leading and sub-leading electrons are shown in Figure D.1. The rates are binned in  $p_T$  and split into three  $\eta$  regions in the barrel and two endcap regions. The rates vary for the leading electron from  $r_1 \simeq 0.92 - 0.96$  and for the sub-leading electron from  $r_2 \simeq 0.90 - 0.96$ .

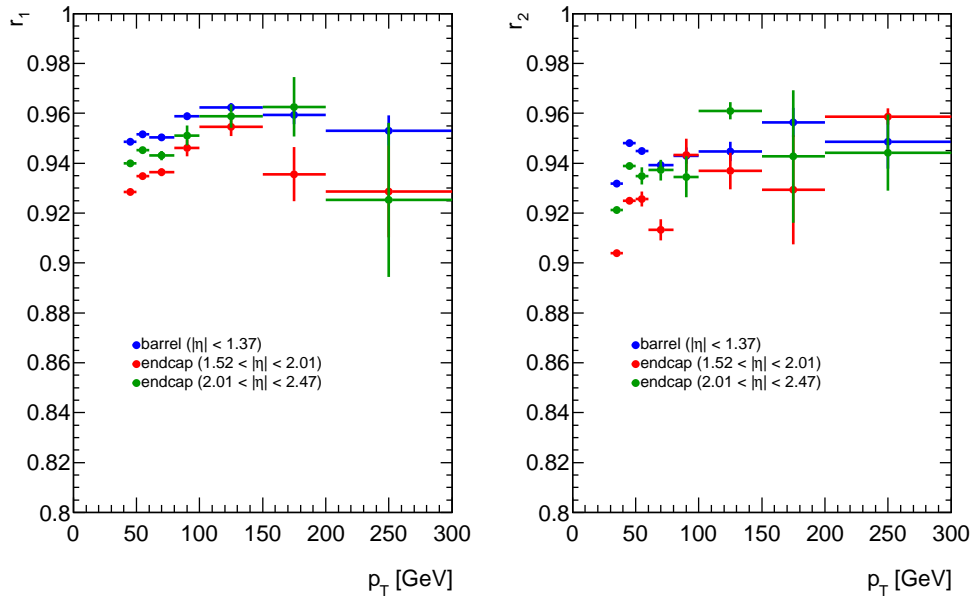


Figure D.1: The real electron rates estimated from the Drell-Yan Monte Carlo. Left: Leading electron. Right: Sub-leading electron. These are binned in  $p_T$  and split into three  $\eta$  regions, excluding the crack region. From [217], Figure 2.

### D.3 Fake Electron Rates

The fake electron rates  $f_i$  and fake factors  $F_i$  must be calculated from a sample of true fake electrons. This requires finding a fake-enriched sample in the data, either from the E/gamma stream or the Jet stream. The estimations use three different methods and/or samples: the first two use an “inverse” Tag & Probe method with the E/gamma stream and Jet stream separately, and the third is a single object method from the Jet stream. Systematic variations for each method are also studied for uncertainty estimations.

#### Tag & Probe - E/gamma Stream

This method for estimating the fake electron rates uses an inverse tag and probe on the E/gamma data stream where the tag electron candidate has a high probability of being a jet faking. Events are required to pass the *EF\_g35\_loose\_g25\_loose* diphoton trigger and all other event level requirements. The tag candidate must pass the standard data quality and  $\eta$  cuts, but the other requirements are loosened to  $p_T > 25$  GeV and *loose++* without track matching. To maximize the jet-like nature of the tag candidate it must fail the track matching and isEM *medium++* requirements. If an event has a tag candidate, all other electron candidates are considered probes. If an event has multiple tag candidates, the probes are only used once. The fake rates  $f_i$  and fake factors  $F_i$  are determined from the number of probes satisfying the loose and tight selections  $N_L^F$  and  $N_T^F$ . The alternate loose selection of *medium++* and fail track match  $N_{\text{fail track},i}^F$  is also calculated.

To further reduce the number of real electrons in the probe samples, cuts are applied on the tag and probe pairs. For the background due to  $W$ +jets, the missing transverse energy for the event is required  $MET < 25$  GeV. For the background due to  $Z^0$  dielectron events, the tag and probe pair invariant mass must not be near the  $Z^0$  peak,  $|m_{\text{tag and probe}} - 91| > 20$  GeV.



## APPENDIX D. ELECTRON FAKE FACTORS

No lower cut is applied to the invariant mass. Both tag and probe candidates are required to have the same sign. The final probe selection is corrected for real electron contamination using the MC for the Drell-Yan, Top, Diboson, and  $W$ +jets, using a dilution factor estimated from their contribution.

### Tag & Probe - Jet Stream

This method is similar to the previous selection, but applied to objects from the Jet data stream instead of the E/gamma data stream. In principle these objects should be more jet-like and have less contamination from real electrons. Events must satisfy the single jet triggers  $EF\_jX\_a4tchad$ , where  $X = \{25, 35, 45, 55, 80, 110, 145, 180, 220, 280, 360\}$ . Events passing multiple triggers are kept with the lowest trigger threshold. Due to the more jet-like nature of the candidates, the tag requirement is loosened to fail *loose++* to accumulate more statistics. The probe and pair requirements are the same as before to count  $N_L^F$ ,  $N_T^F$ , and  $N_{\text{fail track},i}^F$ . For each trigger a fake rate is calculated, and the final fake rate used is the weighted average over all the different triggers.

### Single Object - Jet Stream

A final method is used by selecting single objects from the Jet data stream. Events are selected satisfying the single jet trigger  $EF\_jX\_a4tchad$ , where  $X = \{25, 35, 45, 55, 80, 110, 145, 180, 220, 280, 360\}$ . Events passing multiple triggers are kept with the lowest trigger threshold. All objects in the jet container *AntiKt4TopoEMJets* are matched to objects in the electron container with an  $\eta$ - $\phi$  requirement  $\Delta R < 0.1$ . The jets must also pass the medium jet-cleaning criteria. Electrons matched with these jets are then used for the  $N_L^F$ ,  $N_T^F$ , and  $N_{\text{fail track},i}^F$  selection. Because of the single jet triggers, the fake rates and fake factors are calculated with prescale factors, and the trigger and isolation scale factors are also applied.

## APPENDIX D. ELECTRON FAKE FACTORS

Again, to reduce real electron contamination from  $W^\pm$  and  $Z^0$  decays, the event missing transverse energy must have  $MET < 25$  GeV and events with two *loose++* electrons must be away from the  $Z^0$  peak  $|m_{\text{pair}} - 91| > 20$  GeV.

### Systematics

A variety of changes are made to the different methods to estimate the systematic uncertainty on the fake rates and fake factors. The event level cuts on the missing  $E_T$  and the invariant mass window value are changed over three different values. For the tag and probe method, the requirement on the tag  $p_T$  is also varied. The tag is also allowed to fail the *medium++* track matching or isolation cuts. The variations lead to a systematic uncertainty on the  $f_i$  of about 20% for the tag and probe selection, and about 15% for the single object selection.

### Comparison

The fake rates and fake factors are calculated from  $N_L^F$ ,  $N_T^F$ , and  $N_{\text{fail track},i}^F$  for both the leading and sub-leading electron. The fake rates are largest at high  $|\eta|$ , and are stable with respect to the object  $p_T$ . They are about 10% for the leading electron and slightly higher for the sub-leading electron due to the looser isolation requirement. Figure D.2 shows the estimated fake rates for the leading and sub-leading electrons with respect to  $p_T$  in different  $\eta$  regions of the detector.

## APPENDIX D. ELECTRON FAKE FACTORS

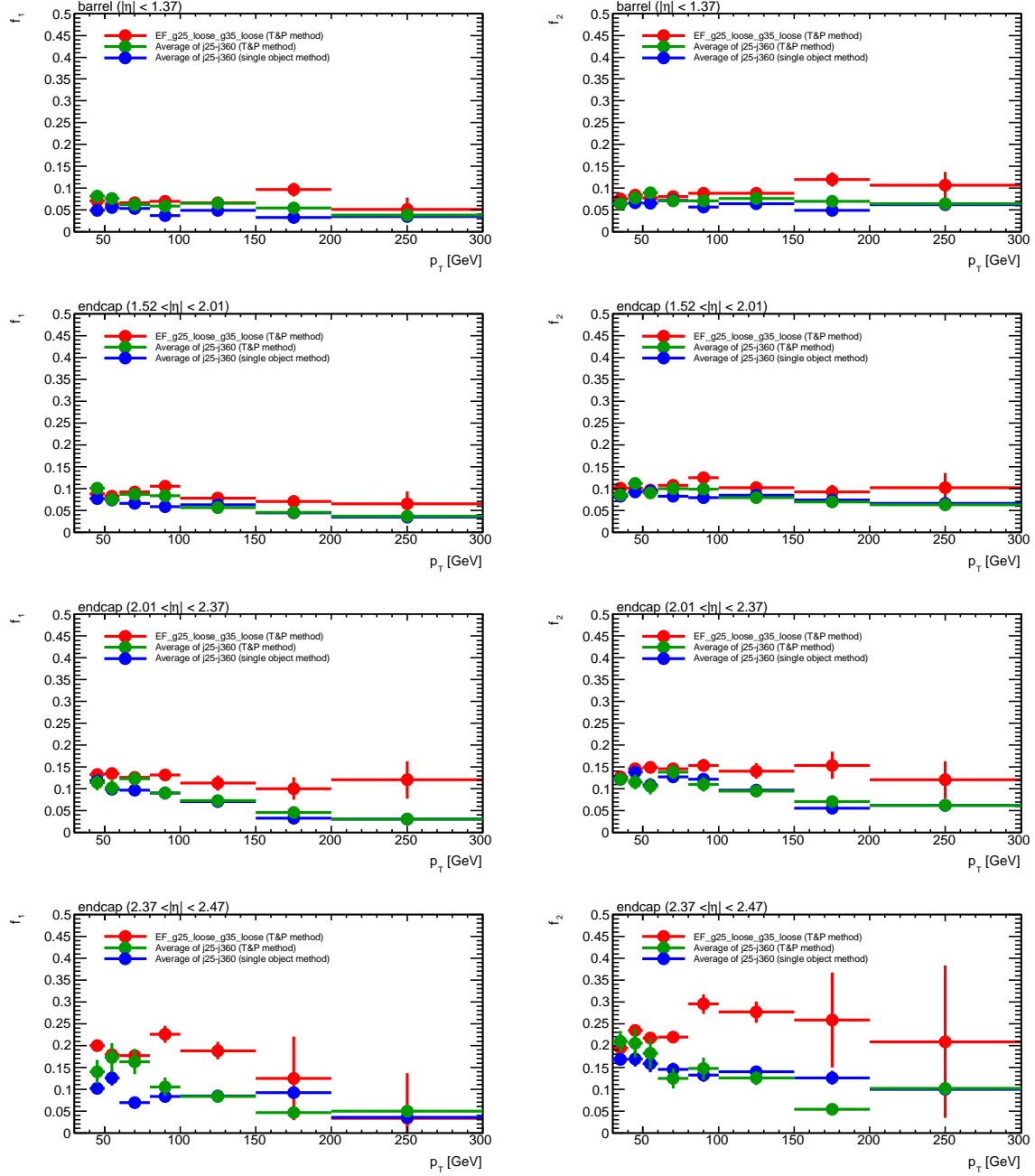


Figure D.2: Comparison of the fake rates  $f_i$  calculated with the three different methods described. Left: leading electron. Right: sub-leading electron. These are binned with respect to  $p_T$ , and the rows correspond to different  $\eta$  regions of the ECAL (barrel and three endcap ranges). The error bars are statistical only. From [217], Figure 9.

## D.4 Total Fake Background

With the real rates estimated from MC and the fake rates estimated from data using the various methods described above, the selection of the measurable quantities  $N_{TT}$ ,  $N_{TL}$ ,  $N_{LT}$ , and  $N_{LL}$  is needed to calculate the total fakes background in Equation (D.2) or (D.5). The loose selection can be either the standard loose selection or the fail *medium++* track matching. The total fakes background is then estimated from the data sets. There are still contributions from real dielectron events to the selections, and this can be estimated from MC samples and subtracted from the data-driven value. The real single electron dilution is estimated to be much smaller and neglected.

Three different methods and two different loose selections were used to estimate the fake rates, with the  $r_i = 1$  approximation, using Equation D.5. In addition, the standard loose selection background estimation is calculated with the real electron rates  $r_i \neq 1$  applied, using Equation D.2. The estimated backgrounds for the 9 different calculations are shown in Figure D.3. The discrepancies at the  $Z^0$  peak are due to real dielectron dilution in the fakes samples, and the corrections to compensate for this are quite large. The ratio comparison between methods is also shown in the mass range above the  $Z^0$  peak, using the single object method with real electron rates as the nominal value. This method uses the fewest approximations and has the largest statistics available.

The total systematic uncertainty for the estimate fakes background comes from several sources. The variation over this range between the different methods is about 18% from the nominal value. Systematic variation of the fake factors and selections results in a 5% variation in the nominal background over this mass range. The composition of the data samples used to generate the background estimates will vary with respect to  $b$ -jets compared to light-flavor jets and the photon conversion rate. These will, in turn, fail different parts

APPENDIX D. ELECTRON FAKE FACTORS

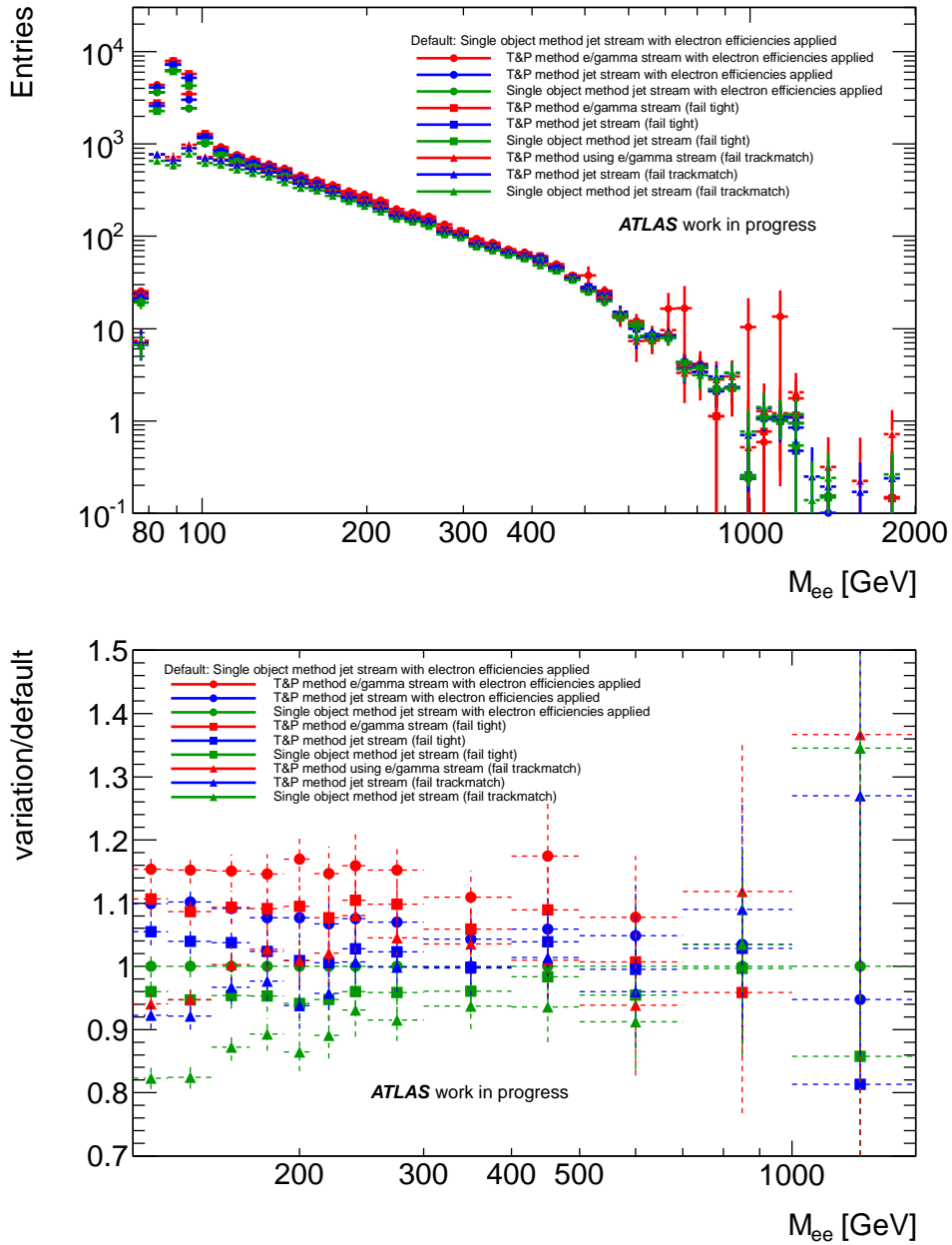


Figure D.3: Top: Total fake electron background estimate over all the methods. The circles apply the real electron rates ( $r_i \neq 1$ ), while the other two use the approximation  $r_i = 1$ . The peak at 91 GeV is due to real electron dilution in the samples, and is lower in the loose fail *medium++* track matching sample due to the better rejection of real electrons. Bottom: Ratio of the various background estimates to the nominal value. The nominal selection is the single object selection with the real electron rates used. The ratio shown is from 116-1500 GeV. From [217], Figures 14,15.

#### APPENDIX D. ELECTRON FAKE FACTORS

of the selection at different rates, leading to different fake rates. Good agreement is shown across data samples, and this totals to a 2-3% systematic. In total, a conservative flat 20% systematic uncertainty is assigned to the fakes background in the range above 110 GeV.

A “knee” is seen in the top histogram in Figure D.3 around 400 GeV. The events from fakes are from predominately back-to-back objects in  $\phi$ , except at very low mass. The high-mass events are typically from fakes with very large opening angles in  $\eta$ , but with low  $p_T$  in the 40-80 GeV range. The invariant mass from these types of events will grow with  $\Delta\eta$ , assuming a flat  $p_T$  distribution and back-to-back in  $\phi$ , until one of the objects passes  $|\eta| > 2.47$  and is no longer part of the selection. For a  $p_T$  of 60 GeV and  $\Delta\phi$  of  $\pi$ , this corresponds to an invariant mass of about 400 GeV, and an expected change in slope of the invariant mass distribution due to fakes leaving the selection.

Due to difficulties estimating the fake backgrounds under the  $Z^0$  peak, and limited statistics at invariant masses above 1500 GeV, fits are performed to extrapolate to the low and high invariant mass ranges. Similar to the Top background fits described in the Top portion of Section 4.2.2, the dijet function is used to extrapolate the invariant mass distribution. For the fit to high invariant mass, to ensure the slope change is correctly modeled, the lower edge of the fit is varied between 425-600 GeV in steps of 25 GeV and the upper edge of the fit is varied between 700-1200 GeV in steps of 50 GeV. The mean between the different fits, calculated bin-by-bin, is the central value, and the RMS is the error. This is used above 500 GeV. Underneath the  $Z^0$  peak, the real electron background dilution made a proper fakes estimate impossible. Instead, the dijet function is fit between 120-400 GeV, and used to estimate the contribution to the invariant mass between 80-110 GeV. This fit cannot take into account the kinematic information of the fakes. Instead the fit to the Top background between 180-600 GeV is compared to the MC Top prediction in the 80-110 GeV range for the various kinematic distributions, giving a “fudge factor” to apply to the fakes background

#### *APPENDIX D. ELECTRON FAKE FACTORS*

and estimate the final  $W$ +jets and dijet backgrounds in both the invariant mass and kinematic distributions. An arbitrary 50% systematic uncertainty is assigned to this low-mass extrapolation, however this is less than one part in 1000 of the total background and this region is not used in the search.

# Appendix E

## Muon Resolution

Muons in the ATLAS detector are reconstructed using the Inner Detector and the Muon Spectrometer. This analysis only considers muons that have been fully reconstructed in both sub-detectors, the combined muons, and uses the second reconstruction chain, called MUID. The identification, reconstruction, and efficiency of this chain was discussed in Section 3.4.3. This appendix describes how the resolution and systematic uncertainty of the muon transverse momentum is measured. Within the ATLAS collaboration, this work is done by the Muon Combined Performance group (MCP). Further details can be found in the 2010 ATLAS Muon Resolution [265] and 2012 ATLAS Muon Resolution [266] notes.

### E.1 Momentum Resolution

Unlike the calorimeters where test beam data is available to understand and calibrate the detector response with a fixed source, the MS requires an in-situ calibration of the muon momentum resolution and scale. This is done using dimuon decays of known particles, the  $Z^0$  boson and the  $J/\psi$  &  $\Upsilon$  mesons, as standard candles to determine the resolution parameters.



## APPENDIX E. MUON RESOLUTION

The measurements are dominated by the  $Z^0 \rightarrow \mu\mu$  inputs, with the decays from  $J/\psi$  and  $\Upsilon$  used for lower- $p_T$  calibration, validation, and systematic uncertainty work. The data used is the full 2012 ATLAS data set, approximately  $20.4 \text{ fb}^{-1}$  of integrated luminosity at 8 TeV  $pp$  collisions. The MC used is predominately the POWHEG  $Z^0 \rightarrow \mu\mu$  sample, described in the Drell-Yan part of Section 4.2.2. The  $J/\psi$  and  $\Upsilon$  samples are generated with PYTHIA and fully simulated with GEANT4 for the ATLAS detector, then processed through the standard trigger and reconstruction used for data. Initially the MC simulations in GEANT4 assumed a perfectly aligned detector, however the simulations for 2012 now include realistic misalignment of the MS sub-detector to more accurately account for the muon resolution measurement. The design resolution of the combined ATLAS muon system is expected to be better than 3% in the  $p_T$  range below 100 GeV, and approximately 10% at a  $p_T$  of 1 TeV. The measured resolution is meeting the design expectations in the low-to-moderate  $p_T$  range, and the estimated resolution of a 1 TeV  $p_T$  muon is approximately 13% in the barrel region ( $|\eta| < 1.05$ ), 17% in the endcap region ( $1.05 < |\eta| < 2.0$ ), and 15% in the far-forward CSC region ( $2.0 < |\eta| < 2.7$ ).

The fractional muon momentum resolution is parameterized as a function of  $p_T$ :

$$\frac{\sigma_{p_T}}{p_T} = \frac{c}{p_T} \oplus a \oplus b \cdot p_T. \quad (\text{E.1})$$

The three terms each approximately correspond to a different physics process that contributes to the resolution. The first term  $c$ , decreasing with  $p_T$ , is the energy loss term due to traversing material in the detector. This is very small except at low- $p_T$ , because a muon is a minimum ionizing particle after a few GeV in momentum, and is neglected for the remainder of this work. The second term  $a$ , constant with  $p_T$ , is the multiple scattering term due to traveling through the detector material. This is expected to be small for the

## APPENDIX E. MUON RESOLUTION

ID and somewhat larger for the MS. The third term  $b$ , increasing linearly with  $p_T$ , is the intrinsic resolution due to the resolution of the detector components and any misalignment within or between the sub-detectors.

The selection of the  $Z^0 \rightarrow \mu\mu$  used to calculate the resolution parameters is similar to the dimuon selection used in this analysis. The event must pass the trigger, primary vertex, and data quality requirements. The two muons must be CB, have  $p_T > 25$  GeV, be isolated, originate from the primary vertex, and have opposite charge. Lastly, the pair invariant mass must be at the  $Z^0$  peak,  $|m_{\text{pair}} - m_{Z^0}| < 15$  GeV. There are over 5 million dimuon events in the 2012 data set, with a purity of approximately 99.9% using MC background estimates.

### E.2 Momentum Corrections

The corrections are applied to MC to more accurately model the resolution of the actual detector. These are referred to as “smearing parameters”  $\Delta a$  and  $\Delta b$ . In addition to the resolution smearing, the overall muon momentum scale can be measured to directly multiply the momentum measured in the MC, called  $s$ . All of the correction parameters depend on which regions of the detector the muon travels through. The corrections are split between the two sub-detectors ID and MS. The corrected transverse momentum  $p_T^{\text{cor}}$  in terms of the measured MC momentum  $p_T^{\text{MC}}$  is:

$$p_T^{\text{cor},\text{det}} = p_T^{\text{MC},\text{det}} \cdot s^{\text{det}}(\eta) \left( 1 + \Delta a^{\text{det}}(\eta) G(0, 1) + \Delta b^{\text{det}}(\eta) G(0, 1) p_T^{\text{MC},\text{det}} \right). \quad (\text{E.2})$$

Where  $\text{det} = \text{ID}, \text{MS}$ , and  $G(0, 1)$  is a Gaussian random variable with mean 0 and width 1. After correcting the momentum measured in the two sub-detectors separately, the CB momentum correction is the average of the two corrections weighted by their inverse square

## APPENDIX E. MUON RESOLUTION

resolutions:

$$p_T^{cor,CB} = p_T^{MC,CB} \left[ 1 + \frac{\frac{\Delta(MS)}{\sigma^2(MS)} + \frac{\Delta(ID)}{\sigma^2(ID)}}{\frac{1}{\sigma^2(MS)} + \frac{1}{\sigma^2(ID)}} \right]. \quad (\text{E.3})$$

The  $\sigma^2(det)$  are the estimated resolutions of the sub-detectors at the  $p_T^{MC}$ . The  $\Delta(det)$  are the shift in the  $p_T^{MC}$  calculated for each sub-detector. The  $p_T^{cor,CB}$  are the muon transverse momentum values used in the analysis for the MC simulated muons.

The correction parameters are derived using a MC template fit to the data. The MC for  $Z^0 \rightarrow \mu\mu$  is binned in the invariant mass around the  $Z^0$  peak, after applying the corrections in Equations (E.2) and (E.3). This is done for a series of correction parameter values  $\Delta a, b$  and  $s$ . Then a binned likelihood fit is done to find the best-fitting MC template in the CB muon mass spectrum to the same binned data invariant mass spectrum. Essentially, the smearing parameters are the difference in quadrature between the data resolution parameters and the MC resolution parameters.

The detector has been divided into 16 different  $\eta$  regions, and each region has different correction parameters. The template fitting procedure is iterated by first finding  $Z^0 \rightarrow \mu\mu$  decays where both muons passed through the same  $\eta$  region, then subsequent fits can have one muon pass through the next  $\eta$  region and one in the previous region(s) or both pass through the new  $\eta$  region. This is done by working outwards in  $|\eta|$  regions, then repeated twice for fit stability.

The best-fit smearing parameters  $\Delta a^{MS}(\eta)$  and  $\Delta b^{ID}(\eta)$  and the detector scale parameters  $s^{MS}(\eta)$  and  $s^{ID}(\eta)$  are shown in Figure E.1. The dominant systematic uncertainty of the smearing parameters is from varying the window about the  $Z^0$  central mass in the template fits. The dominant systematics of the scale corrections of 0.1% (0.2% for  $|\eta| > 2.0$ ) account for possible momentum dependence on the corrections themselves. This was estimated by

## APPENDIX E. MUON RESOLUTION

comparing the scale corrections measured to those obtained from  $J/\psi$  and  $\Upsilon$  decays. Another systematic uncertainty for all the correction parameters comes from the modeling and corrections applied in the reconstruction due to the energy loss of muons passing through the detector material. The two other smearing parameters  $\Delta a^{ID}(\eta)$  and  $\Delta b^{MS}(\eta)$  are set to zero, but are allowed to vary in the likelihood fit by their systematic uncertainties. The small amount of material in the ID constrains the multiple scattering ( $a$  term) to be small, and the uncertainty on this, corresponding to the  $\Delta a^{ID}(\eta)$  parameter, is negligible to the overall corrections. After including the realistic misalignment in the GEANT4 simulations of the MS, the intrinsic resolution in MC, corresponding to the  $\Delta b^{MS}(\eta)$  parameter, is within systematic errors of the data. The resulting corrections are shown in Figure E.2 comparing the MC  $Z^0$  dimuon invariant mass peak with the data before and after the corrections are applied.

## APPENDIX E. MUON RESOLUTION

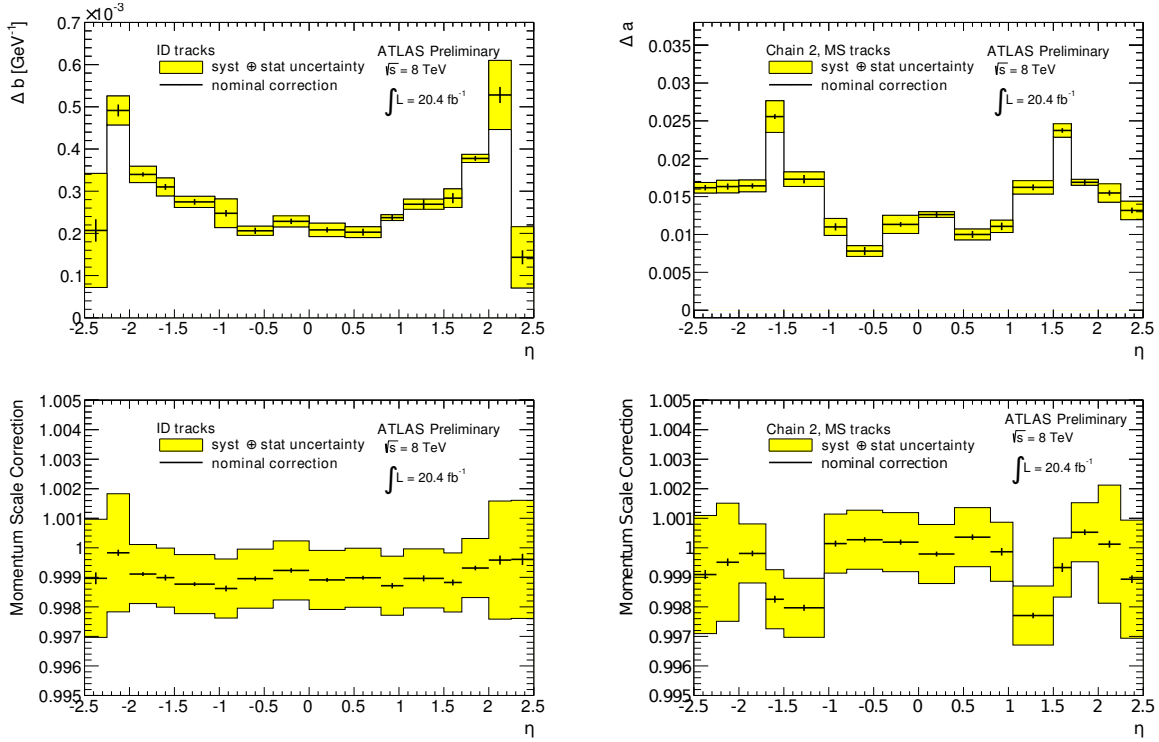


Figure E.1: Top Row: smearing parameters for the ID (left) and MS (right) with the MUID chain. Bottom Row: scale corrections for the ID (left) and MS (right) with the MUID chain. From [266], Figures 7,8,13.

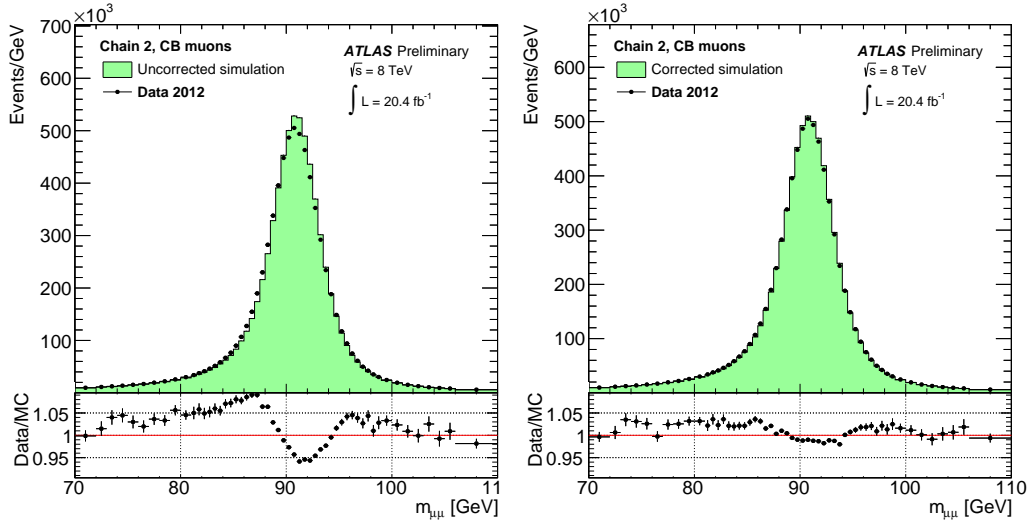


Figure E.2: The dimuon invariant mass at the  $Z^0$  peak with MUID CB muons. Left: No corrections applied to the MC. Right: Smearing and scale corrections applied to the MC. From [266], Figure 14.

### E.3 Two Station Muon Resolution

The loose selection in the muon channel differs from the standard selection used to measure the resolution of the muon momentum. The use of only two of the three precision MDT chamber layers leads to a different momentum resolution, especially at high  $p_T$ . The two layers used in the loose selection are the inner and outer layers, and only barrel muons are considered. The standard reconstruction algorithm uses the track segments created at each MS precision layer to reconstruct the full path through the MS, and fits the transverse momentum from the sagitta of the track. In the two station case, instead of reconstructing the full track, the reconstruction algorithm uses the two track segments to define an angle between the lines,  $\Delta\theta_{seg}$ . The line segments are essentially two tangent lines to the circle the muon follows in a magnetic field, with this angle and the distance between layers measuring the circle radius. This measures the momentum. The magnetic field is well-mapped throughout the toroid, and the total bending power is determined by the integral of the magnetic field through the muon's path:

$$\begin{aligned} B_{int} &= \frac{1}{L} \int \vec{B} \cdot d\vec{\ell}, \\ \Delta\theta_{seg} &= C \cdot \frac{B_{int}}{p}. \end{aligned} \tag{E.4}$$

Where  $L$  is the linear distance between the inner and outer layer and  $C$  is a constant in the appropriate units. The relationship in Equation (E.4) is shown in Figure E.3.

To measure the resolution of the two station muons, a large sample of standard muons are collected. The standard muons are reconstructed normally, then reconstructed ignoring the hits in middle layer and treating them as two station muons. The momentum resolution is measured by calculating the width of a single Gaussian fit to the variable  $p\Delta\theta_{seg}/qB_{int}$ .

APPENDIX E. MUON RESOLUTION

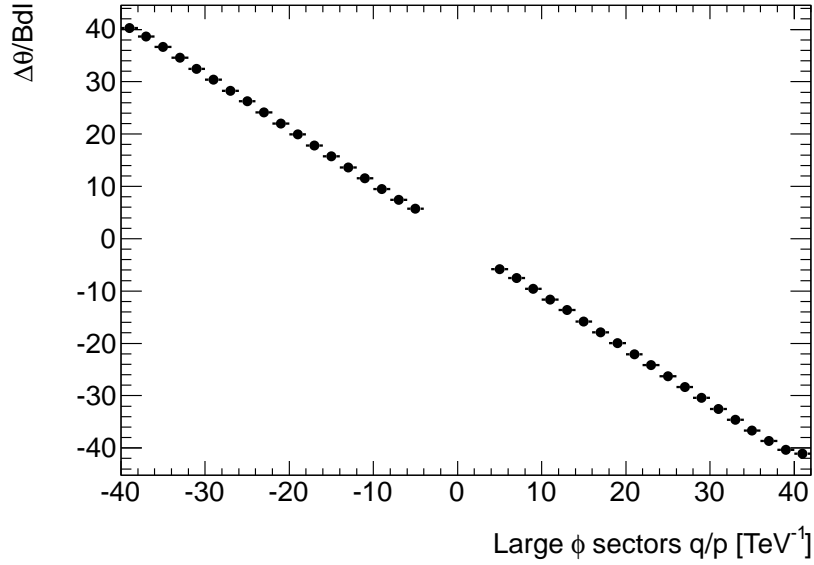


Figure E.3:  $\Delta\theta_{seg}/B_{int}$  plotted with respect to  $q/p$  for two station muons in the Large sectors. The straight line slope is the constant  $C$ . From Appendix B, Figure 70 in [217].

The fit is restricted over the range  $\pm 1.75\sigma$  of the distribution, and iterated until the fit width is stable. To account for the momentum dependence of the resolution, this is repeated over various  $p$  ranges. Because of the variation in magnetic field strength, material, and Large/Small chamber performance, each of the 192 MDT “towers” (set of three layers a muon passes through from the vertex) are checked individually for any unexpected behavior. Four such towers are removed from the loose selection due to poor performance, noted in Section 4.4.1.

The muon resolution described in Equation (E.1) is used to extract the overall two station muon resolution. The  $\sigma$  from the Gaussian fits to  $p\Delta\theta_{seg}/qB_{int}$  and the average momentum  $\langle p \rangle$  from the standard three station momentum are used for the function values to fit the  $a$  and  $b$  parameters. At high- $p_T$ , this is dominated by the  $b$  parameter, and this is the most important term for this analysis. The errors on the resolution fit are calculated by varying

## APPENDIX E. MUON RESOLUTION

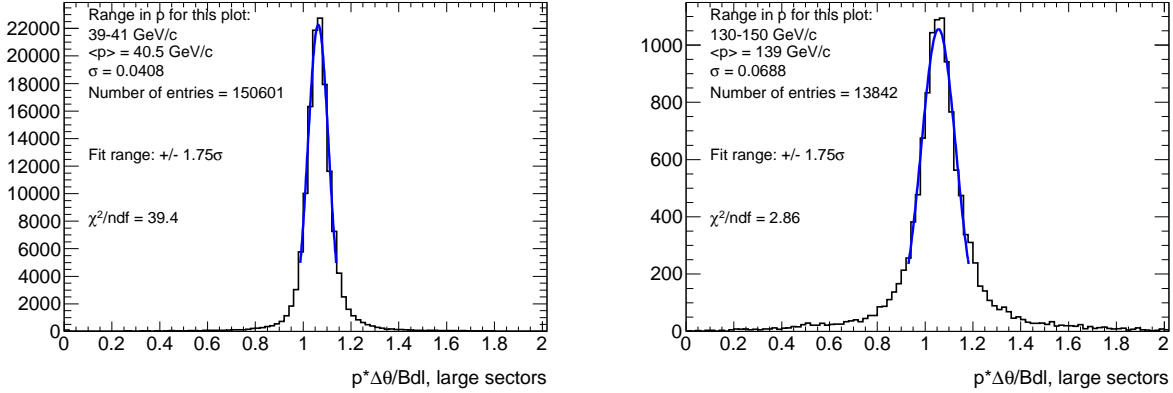


Figure E.4: Resolution distributions in  $p\Delta\theta_{seg}/qB_{int}$  for the Large sectors. These are fit with a single Gaussian. Left: Low momentum  $p=39-41$  GeV. Right: High momentum  $p=130-150$  GeV. From [217], Appendix B, Figure 71.

$\sigma$  over its error range and  $\langle p \rangle$  over the RMS of its distribution, then added in quadrature. The resulting  $b$  resolution parameters are listed in Table E.1 and the fits are shown in Figure E.5. The extracted resolution parameters are somewhat worse in MC than in data, with an estimated 50% resolution at 1 TeV in MC, compared to an estimated 45% in data. However, this discrepancy is covered by the systematic uncertainties of the resolution.

Sectors	Simulation [TeV <sup>-1</sup> ]	Data [TeV <sup>-1</sup> ]
Small	$0.537 \pm 0.022$	$0.459 \pm 0.018$
Large	$0.479 \pm 0.017$	$0.424 \pm 0.019$

Table E.1: The  $b$  resolution parameters measured in data and simulation. From Appendix B, Table 36 in [217].



## APPENDIX E. MUON RESOLUTION

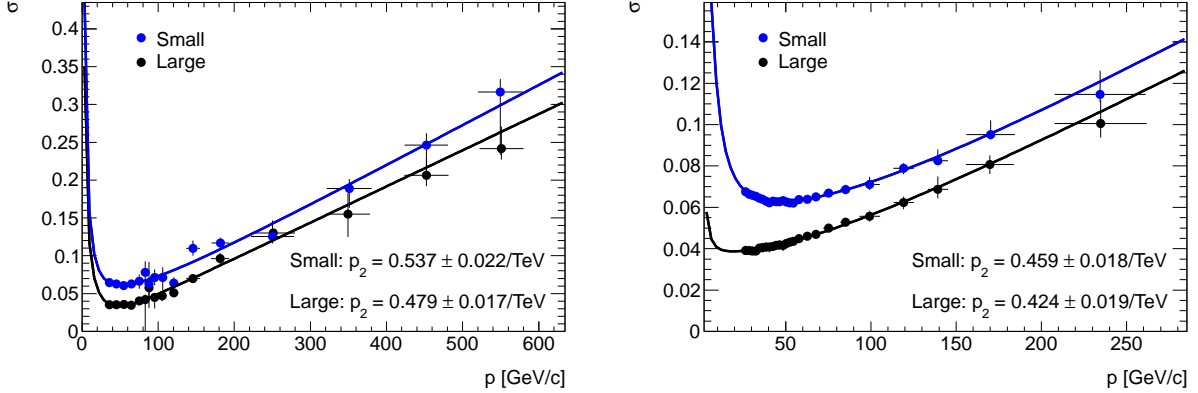


Figure E.5: The two station muon resolution  $\sigma$  as a function of momentum  $p$ . This is fit with expected resolution function in Equation (E.1). The extracted  $b$  parameter is called  $p_2$  here. The curves separate the Large and Small sectors due to their different performance. Left: Resolution in MC. Right: Resolution in data. From [217], Appendix B, Figure 73.

### E.4 Muon Resolution Systematic Uncertainty

The muon resolution corrections are implemented for the MC using a tool provided by the MCP. The package and release tag used for this analysis is

MUONMOMENTUMCORRECTIONS-00-08-07. In addition to providing the smearing and scale parameters, the tool allows for a systematic variation of the muon momentum. The expected SM backgrounds are all “over-smeard” by increasing the smearing parameters by  $1\text{-}\sigma$ , and this over-smeard background is compared to the nominal background bin-by-bin. This provides a simple estimate of the mass-dependence of the muon resolution systematics on the expected background. The variations with respect to nominal are shown in Figure E.6. This is fit with a second-order polynomial, and the fit is used to calculate the systematic uncertainty as a function of the reconstructed invariant mass for the search and limit setting.

Because of the linear dependence of the resolution on the  $p_T$ , the systematics are larger at higher  $m_{\mu\mu}$ , and this can potentially change the muon  $Z'$  signal templates. For three

APPENDIX E. MUON RESOLUTION

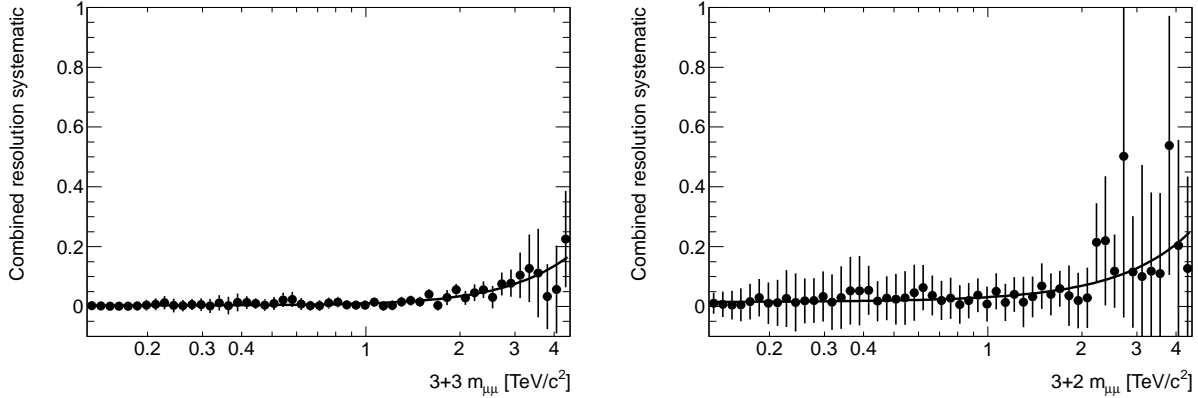


Figure E.6: The systematic uncertainty on the total background due to the muon resolution as a function of invariant mass. Left: Tight muon channel. Right: Loose muon channel. From [217], Appendix C, Figure 74.

benchmark SSM  $Z'$  signals at masses of 1, 2, and 3 TeV, the signal was studied after the nominal and over-smearing. This was done by looking at the signal yield within  $\pm 1$  RMS of the signal peak. In both cases the number of signal events was integrated over this range, and the difference between the total yields of the nominal and over-smearred  $Z'$  is the systematic uncertainty. This is listed in Table E.2, and is determined to be a negligible systematic uncertainty.

$Z'$ mass [GeV]	Variation	$Z'$ RMS [GeV]	Nominal signal yield	Over-smearred signal yield	Relative difference [%]
1000	MSUP	169	$1423 \pm 15$	$1411 \pm 15$	0.9
2000	MSUP	636	$25.07 \pm 0.19$	$24.91 \pm 0.19$	0.6
3000	MSUP	1160	$0.717 \pm 0.004$	$0.708 \pm 0.004$	1.4
1000	IDUP	169	$1423 \pm 15$	$1422 \pm 15$	0.12
2000	IDUP	636	$25.07 \pm 0.19$	$25.06 \pm 0.19$	0.024
3000	IDUP	1160	$0.717 \pm 0.004$	$0.717 \pm 0.004$	0.13

Table E.2:  $Z'$  signal yields from different muon resolution systematic variations. The signals were normalized to an integrated luminosity of  $21 \text{ fb}^{-1}$ . From [217], Appendix C, Table 37.

# Bibliography

- [1] ATLAS Collaboration, “Observation of a New Particle in the Search for the Standard Model Higgs Boson with the ATLAS detector at the LHC,” *Physics Letters B*, vol. 716, no. 1, pp. 1 – 29, 2012.
- [2] CMS Collaboration, “Observation of a New Boson at a Mass of 125 GeV with the CMS Experiment at the LHC,” *Physics Letters B*, vol. 716, no. 1, pp. 30 – 61, 2012.
- [3] J. Alcaraz *et al.*, “A Combination of preliminary electroweak measurements and constraints on the standard model,” *arXiv*, pp. hep-ex/0612034, 2006.
- [4] V. M. Abazov *et al.*, “Search for a heavy neutral gauge boson in the dielectron channel with 5.4 fb-1 of  $p\bar{p}$  collisions at  $\sqrt{s} = 1.96$  TeV,” *Phys.Lett.*, vol. B695, pp. 88–94, 2011.
- [5] DØ Collaboration, “Search for Heavy  $Z'$  Bosons in the Dimuon Channel with 250 pb-1 of Data with the DØ Detector,” Tech. Rep. DØ note 4577-Conf, DØ Collaboration, 2004.
- [6] T. Aaltonen *et al.*, “Search for High-Mass  $e^+e^-$  Resonances in  $p\bar{p}$  Collisions at  $\sqrt{s} = 1.96$  TeV,” *Phys.Rev.Lett.*, vol. 102, p. 031801, 2009.
- [7] CDF Collaboration, “Search for high mass resonances decaying to muon pairs,” Tech. Rep. CDF/PHYS/EXO/PUBLIC/10165, CDF Collaboration, 2010.
- [8] G. Aad *et al.*, “Search for high-mass resonances decaying to dilepton final states in pp collisions at  $\sqrt{s} = 7$  TeV with the ATLAS detector,” *JHEP*, vol. 1211, p. 138, 2012.
- [9] S. Chatrchyan *et al.*, “Search for heavy narrow dilepton resonances in  $pp$  collisions at  $\sqrt{s} = 7$  TeV and  $\sqrt{s} = 8$  TeV,” *Phys.Lett.*, vol. B720, pp. 63–82, 2013.
- [10] A. Einstein, “Zur Elektrodynamik bewegter Körper,” *Ann. Phys.*, vol. 2, pp. 891–921, Sept 1905.
- [11] A. Einstein, “Die Feldgleichungen der Gravitation,” *Sitzungsberichte der Königlich Preußischen Akademie der Wissenschaften (Berlin)*, Seite 844-847., pp. 844–847, 1915.

## BIBLIOGRAPHY

- [12] M. Planck, “Zur Theorie der Gesetzes der Energieverteilung im Normal-Spektrum,” *Ann. Phys.*, vol. 4, p. 553, Nov 1901.
- [13] N. Bohr, “On the constitution of atoms and molecules,” *Philosophical Magazine, Series 6*, vol. 26, no. 151, pp. 1–25, 1913.
- [14] N. Bohr, “LXXIII. On the constitution of atoms and molecules,” *Philosophical Magazine Series 6*, vol. 26, no. 155, pp. 857–875, 1913.
- [15] L. de Broglie, *Recherches sur la Théorie des Quanta*. PhD thesis, University of Paris, 1924.
- [16] E. Schrödinger, “Quantisierung als Eigenwertproblem,” *Ann. Phys.*, vol. 384, pp. 361–376, 1926.
- [17] W. Heisenberg, “Über den anschaulichen Inhalt der quantentheoretischen Kinematik und Mechanik,” *Zeitschrift für Physik*, vol. 43, pp. 172–198, Mar. 1927.
- [18] M. Born, “Zur Quantenmechanik der Stoßvorgänge,” *Zeitschrift für Physik A: Hadrons and Nuclei*, vol. 37, no. 12, pp. 863–867, 1926.
- [19] P. A. M. Dirac, “The Quantum Theory of the Electron,” *Proc. R. Soc. Lond. A*, vol. 117, no. 778, pp. 610–624, 1928.
- [20] P. A. M. Dirac, “Quantised Singularities in the Electromagnetic Field,” *Royal Society of London Proceedings Series A*, vol. 133, pp. 60–72, Sept. 1931.
- [21] P. A. M. Dirac, *The Principles of Quantum Mechanics*. Oxford University Press, 1930.
- [22] J. R. Oppenheimer, “Note on the Theory of the Interaction of Field and Matter,” *Physical Review*, vol. 35, pp. 461–477, Mar. 1930.
- [23] V. F. Weisskopf, “On the Self-Energy and the Electromagnetic Field of the Electron,” *Phys. Rev.*, vol. 56, pp. 72–85, Jul 1939.
- [24] *Shelter Island Conference*, (<http://www.aps.org/programs/outreach/history/historicsites/shelterisland.cfm>), 1947.
- [25] W. E. Lamb and R. C. Retherford, “Fine Structure of the Hydrogen Atom by a Microwave Method,” *Phys. Rev.*, vol. 72, pp. 241–243, Aug 1947.
- [26] H. A. Bethe, “The Electromagnetic Shift of Energy Levels,” *Phys. Rev.*, vol. 72, pp. 339–341, Aug 1947.
- [27] J. Schwinger, “On Quantum-Electrodynamics and the Magnetic Moment of the Electron,” *Phys. Rev.*, vol. 73, pp. 416–417, Feb 1948.

## BIBLIOGRAPHY

- [28] J. E. Nafe, E. B. Nelson, and I. I. Rabi, "The Hyperfine Structure of Atomic Hydrogen and Deuterium," *Phys. Rev.*, vol. 71, pp. 914–915, Jun 1947.
- [29] D. E. Nagle, R. S. Julian, and J. R. Zacharias, "The Hyperfine Structure of Atomic Hydrogen and Deuterium," *Phys. Rev.*, vol. 72, pp. 971–971, Nov 1947.
- [30] P. Kusch and H. M. Foley, "Precision Measurement of the Ratio of the Atomic 'g Values' in the  ${}^2P_{\frac{3}{2}}$  and  ${}^2P_{\frac{1}{2}}$  States of Gallium," *Phys. Rev.*, vol. 72, pp. 1256–1257, Dec 1947.
- [31] J. E. Mack and N. Austern, "Newly Observed Structure in He II  $\lambda$  4686," *Phys. Rev.*, vol. 72, pp. 972–972, Nov 1947.
- [32] W. Pauli and F. Villars, "On the Invariant Regularization in Relativistic Quantum Theory," *Rev. Mod. Phys.*, vol. 21, pp. 434–444, Jul 1949.
- [33] R. P. Feynman, "Space-Time Approach to Quantum Electrodynamics," *Phys. Rev.*, vol. 76, pp. 769–789, Sep 1949.
- [34] R. P. Feynman, "The Theory of Positrons," *Phys. Rev.*, vol. 76, pp. 749–759, Sep 1949.
- [35] R. P. Feynman, "Mathematical Formulation of the Quantum Theory of Electromagnetic Interaction," *Phys. Rev.*, vol. 80, pp. 440–457, Nov 1950.
- [36] J. Schwinger, "The Theory of Quantized Fields. I," *Phys. Rev.*, vol. 82, pp. 914–927, Jun 1951.
- [37] J. Schwinger, "The Theory of Quantized Fields. II," *Phys. Rev.*, vol. 91, pp. 713–728, Aug 1953.
- [38] J. Schwinger, "The Theory of Quantized Fields. III," *Phys. Rev.*, vol. 91, pp. 728–740, Aug 1953.
- [39] J. Schwinger, "The Theory of Quantized Fields. IV," *Phys. Rev.*, vol. 92, pp. 1283–1299, Dec 1953.
- [40] J. Schwinger, "The Theory of Quantized Fields. V," *Phys. Rev.*, vol. 93, pp. 615–628, Feb 1954.
- [41] J. Schwinger, "The Theory of Quantized Fields. VI," *Phys. Rev.*, vol. 94, pp. 1362–1384, Jun 1954.
- [42] D. Ito, Z. Koba, and S. Tomonaga, "Correction due to the Reaction of "Cohesive Force Field" for the Elastic Scattering of an Electron," *Progress of Theoretical Physics*, vol. 2, no. 4, pp. 216–217, 1947.

## BIBLIOGRAPHY

- [43] D. Ito, Z. Koba, and S. Tomonaga, “Errata to the Above Letter,” *Progress of Theoretical Physics*, vol. 2, no. 4, pp. 217–217, 1947.
- [44] Z. Koba and S. Tomonaga, “Application of the “Self-Consistent” Subtraction Method to the Elastic Scattering of an Electron,” *Progress of Theoretical Physics*, vol. 2, no. 4, pp. 218–218, 1947.
- [45] S. Tomonaga and J. R. Oppenheimer, “On Infinite Field Reactions in Quantum Field Theory,” *Phys. Rev.*, vol. 74, pp. 224–225, Jul 1948.
- [46] F. J. Dyson, “The Radiation Theories of Tomonaga, Schwinger, and Feynman,” *Phys. Rev.*, vol. 75, pp. 486–502, Feb 1949.
- [47] F. J. Dyson, “The  $S$  Matrix in Quantum Electrodynamics,” *Phys. Rev.*, vol. 75, pp. 1736–1755, Jun 1949.
- [48] J. Ouellette, *Black Bodies and Quantum Cats*. Penguin Books, 2005.
- [49] C. N. Yang and R. L. Mills, “Conservation of Isotopic Spin and Isotopic Gauge Invariance,” *Phys. Rev.*, vol. 96, pp. 191–195, Oct 1954.
- [50] S. Glashow, “Partial Symmetries of Weak Interactions,” *Nucl. Phys.*, vol. 22, pp. 579–588, 1961.
- [51] Y. Nambu, “Quasi-Particles and Gauge Invariance in the Theory of Superconductivity,” *Phys. Rev.*, vol. 117, pp. 648–663, Feb 1960.
- [52] J. Goldstone, “Field Theories with Superconductor Solutions,” *Nuovo Cim.*, vol. 19, pp. 154–164, 1961.
- [53] P. W. Anderson, “Plasmons, Gauge Invariance, and Mass,” *Physical Review*, vol. 130, pp. 439–442, Apr. 1963.
- [54] F. Englert and R. Brout, “Broken Symmetry and the Mass of Gauge Vector Mesons,” *Physical Review Letters*, vol. 13, pp. 321–323, Aug. 1964.
- [55] P. W. Higgs, “Broken Symmetries and the Masses of Gauge Bosons,” *Phys. Rev. Lett.*, vol. 13, pp. 508–509, Oct 1964.
- [56] G. S. Guralnik, C. R. Hagen, and T. W. Kibble, “Global Conservation Laws and Massless Particles,” *Physical Review Letters*, vol. 13, pp. 585–587, Nov. 1964.
- [57] S. Weinberg, “A Model of Leptons,” *Phys. Rev. Lett.*, vol. 19, pp. 1264–1266, Nov 1967.

## BIBLIOGRAPHY

- [58] A. Salam, “Nobel Symposium 8,” in *Weak and Electromagnetic Interactions* (A. . Wiksell, ed.), (Aspenasgarden, Sweden), pp. 367–377, July 1968. Elementary Particle Theory: Relativistic Groups and Analyticity.
- [59] K. Nishijima, “Charge Independence Theory of V Particles,” *Progress of Theoretical Physics*, vol. 13, pp. 285–304, Mar. 1955.
- [60] M. Gell-Mann, “The interpretation of the new particles as displaced charge multiplets,” *Il Nuovo Cimento*, vol. 4, pp. 848–866, Apr. 1956.
- [61] V. E. Barnes, P. L. Connolly, D. J. Crennell, B. B. Culwick, W. C. Delaney, W. B. Fowler, P. E. Hagerty, E. L. Hart, N. Horwitz, P. V. Hough, J. E. Jensen, J. K. Kopp, K. W. Lai, J. Leitner, J. L. Lloyd, G. W. London, T. W. Morris, Y. Oren, R. B. Palmer, A. G. Prodell, D. Radojčić, D. C. Rahm, C. R. Richardson, N. P. Samios, J. R. Sanford, R. P. Shutt, J. R. Smith, D. L. Stonehill, R. C. Strand, A. M. Thorndike, M. S. Webster, W. J. Willis, and S. S. Yamamoto, “Observation of a Hyperon with Strangeness Minus Three,” *Physical Review Letters*, vol. 12, pp. 204–206, Feb. 1964.
- [62] J. D. Bjorken and E. A. Paschos, “Inelastic Electron-Proton and  $\gamma$ -Proton Scattering and the Structure of the Nucleon,” *Phys. Rev.*, vol. 185, pp. 1975–1982, Sep 1969.
- [63] R. P. Feynman, “Very High-Energy Collisions of Hadrons,” *Phys. Rev. Lett.*, vol. 23, pp. 1415–1417, Dec 1969.
- [64] D. J. Gross and F. Wilczek, “Ultraviolet Behavior of Non-Abelian Gauge Theories,” *Physical Review Letters*, vol. 30, pp. 1343–1346, June 1973.
- [65] H. D. Politzer, “Reliable Perturbative Results for Strong Interactions?,” *Physical Review Letters*, vol. 30, pp. 1346–1349, June 1973.
- [66] K. G. Wilson, “Renormalization Group and Critical Phenomena. I. Renormalization Group and the Kadanoff Scaling Picture,” *Phys. Rev. B*, vol. 4, pp. 3174–3183, Nov 1971.
- [67] K. G. Wilson, “Renormalization Group and Critical Phenomena. II. Phase-Space Cell Analysis of Critical Behavior,” *Phys. Rev. B*, vol. 4, pp. 3184–3205, Nov 1971.
- [68] G. 't Hooft and M. Veltman, “Regularization and renormalization of gauge fields,” *Nuclear Physics B*, vol. 44, pp. 189–213, July 1972.
- [69] N. Cabibbo, “Unitary Symmetry and Leptonic Decays,” *Phys. Rev. Lett.*, vol. 10, pp. 531–533, Jun 1963.
- [70] J. H. Christenson, J. W. Cronin, V. L. Fitch, and R. Turlay, “Evidence for the  $2\pi$  Decay of the  $K_2^0$  Meson,” *Phys. Rev. Lett.*, vol. 13, pp. 138–140, Jul 1964.

## BIBLIOGRAPHY

- [71] M. Kobayashi and T. Maskawa, “CP-Violation in the Renormalizable Theory of Weak Interaction,” *Progress of Theoretical Physics*, vol. 49, pp. 652–657, Feb. 1973.
- [72] B. Pontecorvo, “Neutrino Experiments and the Problem of Conservation of Leptonic Charge,” *Soviet Journal of Experimental and Theoretical Physics*, vol. 26, p. 984, May 1968.
- [73] Z. Maki, M. Nakagawa, and S. Sakata, “Remarks on the Unified Model of Elementary Particles,” *Progress of Theoretical Physics*, vol. 28, pp. 870–880, Nov. 1962.
- [74] M. E. Peskin and D. V. Schroeder, *An Introduction to Quantum Field Theory*. Cambridge, Massachusetts: Perseus Books, 1995.
- [75] S. Weinberg, *The Quantum Theory of Fields (Volumes 1, 2, and 3)*. Cambridge University Press, 1 ed., 1995.
- [76] L. Brown, *Quantum Field Theory*. Cambridge University Press, 1994.
- [77] L. Ryder, *Quantum Field Theory*. Cambridge University Press, 1996.
- [78] E. Noether, “Invariant variation problems,” *Transport Theory and Statistical Physics*, vol. 1, pp. 186–207, 1971.
- [79] R. P. Feynman, “Space-Time Approach to Non-Relativistic Quantum Mechanics,” *Rev. Mod. Phys.*, vol. 20, pp. 367–387, Apr 1948.
- [80] R. Streater and A. Wightman, *PCT, Spin and Statistics, and All That*. Princeton University Press, 2000.
- [81] H. Georgi, *Lie Algebras in Particle Physics*. Westview Press, 1999.
- [82] J. C. Maxwell, “A Dynamical Theory of the Electromagnetic Field,” *Philosophical Transactions of the Royal Society*, vol. 155, pp. 459–512, Jan 1865.
- [83] C. G. Callan, “Broken scale invariance in scalar field theory,” *Phys. Rev. D*, vol. 2, pp. 1541–1547, Oct 1970.
- [84] K. Symanzik, “Small distance behaviour in field theory and power counting,” *Comm. Math. Phys.*, vol. 18, pp. 227–246, Sep 1970.
- [85] A. Martin, W. Stirling, R. Thorne, and G. Watt, “Parton distributions for the LHC,” *Eur.Phys.J.*, vol. C63, pp. 189–285, 2009.



## BIBLIOGRAPHY

- [86] C. A. Baker, D. D. Doyle, P. Geltenbort, K. Green, M. G. D. van der Grinten, P. G. Harris, P. Iaydjiev, S. N. Ivanov, D. J. R. May, J. M. Pendlebury, J. D. Richardson, D. Shiers, and K. F. Smith, “Improved Experimental Limit on the Electric Dipole Moment of the Neutron,” *Phys. Rev. Lett.*, vol. 97, p. 131801, Sep 2006.
- [87] V. C. Rubin and W. K. Ford, Jr., “Rotation of the Andromeda Nebula from a Spectroscopic Survey of Emission Regions,” *Astrophysical Journal*, vol. 159, p. 379, Feb. 1970.
- [88] P. Ade *et al.*, “Planck 2013 results. I. Overview of products and scientific results,” *arXiv*, p. 1303.5062, 2013.
- [89] A. G. Riess *et al.*, “Observational evidence from supernovae for an accelerating universe and a cosmological constant,” *Astron. J.*, vol. 116, pp. 1009–1038, 1998.
- [90] S. Perlmutter *et al.*, “Measurements of Omega and Lambda from 42 high redshift supernovae,” *Astrophys. J.*, vol. 517, pp. 565–586, 1999.
- [91] M. Dine, *Supersymmetry and String Theory*. Cambridge University Press, 2007.
- [92] H. Georgi and S. L. Glashow, “Unity of All Elementary-Particle Forces,” *Phys. Rev. Lett.*, vol. 32, pp. 438–441, Feb 1974.
- [93] S. Coleman and J. Mandula, “All Possible Symmetries of the  $S$  Matrix,” *Phys. Rev.*, vol. 159, pp. 1251–1256, Jul 1967.
- [94] R. Haag, J. T. Lopuszański, and M. Sohnius, “All possible generators of supersymmetries of the  $S$ -matrix,” *Nuclear Physics B*, vol. 88, no. 2, pp. 257 – 274, 1975.
- [95] M. B. Green and J. H. Schwarz, “Anomaly cancellations in supersymmetric  $D = 10$  gauge theory and superstring theory,” *Physics Letters B*, vol. 149, pp. 117 – 122, 1984.
- [96] J. M. Maldacena, “The Large  $N$  limit of superconformal field theories and supergravity,” *Adv.Theor.Math.Phys.*, vol. 2, pp. 231–252, 1998.
- [97] E. Witten, “String theory dynamics in various dimensions,” *Nuclear Physics B*, vol. 443, no. 12, pp. 85 – 126, 1995.
- [98] S. Kachru, R. Kallosh, A. Linde, and S. P. Trivedi, “de Sitter vacua in string theory,” *Phys. Rev. D*, vol. 68, p. 046005, Aug 2003.
- [99] N. Arkani-Hamed, S. Dimopoulos, and G. Dvali, “The Hierarchy Problem and New Dimensions at a Millimeter,” *Phys.Lett.*, vol. B429, pp. 263–272, 1998.

## BIBLIOGRAPHY

- [100] N. Arkani-Hamed, S. Dimopoulos, and G. Dvali, “Phenomenology, Astrophysics and Cosmology of Theories with Submillimeter Dimensions and TeV Scale Quantum Gravity,” *Phys.Rev.*, vol. D59, p. 086004, 1999.
- [101] L. Randall and R. Sundrum, “A Large Mass Hierarchy from a Small Extra Dimension,” *Phys.Rev.Lett.*, vol. 83, pp. 3370–3373, 1999.
- [102] L. Randall and R. Sundrum, “An Alternative to Compactification,” *Phys. Rev. Lett.*, vol. 83, pp. 4690–4693, Dec 1999.
- [103] S. D. Drell and T.-M. Yan, “Massive Lepton-Pair Production in Hadron-Hadron Collisions at High Energies,” *Phys. Rev. Lett.*, vol. 25, pp. 316–320, Aug 1970.
- [104] S. D. Drell and T.-M. Yan, “Massive Lepton-Pair Production in Hadron-Hadron Collisions at High Energies,” *Phys. Rev. Lett.*, vol. 25, pp. 902–902, Sep 1970.
- [105] L. Evans and P. Bryant, “LHC Machine,” *Journal of Instrumentation*, vol. 3, no. 08, p. S08001, 2008.
- [106] The ALICE Collaboration, “The ALICE experiment at the CERN LHC,” *Journal of Instrumentation*, vol. 3, no. 08, p. S08002, 2008.
- [107] The LHCb Collaboration, “The LHCb Detector at the LHC,” *Journal of Instrumentation*, vol. 3, no. 08, p. S08005, 2008.
- [108] The LHCf Collaboration, “The LHCf detector at the CERN Large Hadron Collider,” *Journal of Instrumentation*, vol. 3, no. 08, p. S08006, 2008.
- [109] The MoEDAL Collaboration, “Searching for the magnetic monopole and other highly ionizing particles at accelerators using nuclear track detectors,” *Radiation Measurements*, vol. 44, pp. 834–839, 2009.
- [110] The TOTEM Collaboration, “The TOTEM Experiment at the CERN Large Hadron Collider,” *Journal of Instrumentation*, vol. 3, no. 08, p. S08007, 2008.
- [111] The CMS Collaboration, “The CMS experiment at the CERN LHC,” *Journal of Instrumentation*, vol. 3, no. 08, p. S08004, 2008.
- [112] The ATLAS Collaboration, “The ATLAS Experiment at the CERN Large Hadron Collider,” *Journal of Instrumentation*, vol. 3, no. 08, p. S08003, 2008.
- [113] E. Rutherford, “The Scattering of  $\alpha$  and  $\beta$  Particles by Matter and the Structure of the Atom,” *Philosophical Magazine, Series 6*, vol. 21, pp. 669–688, 1911.
- [114] C. D. Anderson, “The Positive Electron,” *Phys. Rev.*, vol. 43, pp. 491–494, Mar 1933.

## BIBLIOGRAPHY

- [115] S. H. Neddermeyer and C. D. Anderson, "Note on the Nature of Cosmic-Ray Particles," *Phys. Rev.*, vol. 51, pp. 884–886, May 1937.
- [116] C. M. G. Lattes, H. Muirhead, G. P. S. Occhialini, and C. Powell, "Process Involving Charged Mesons," *Nature*, vol. 159, pp. 694–697, 1947.
- [117] R. J. Van De Graff, "Electrostatic Generator." U.S. Patent Office, 1931. Van Der Graff Patent.
- [118] E. O. Lawrence, "Method and Apparatus for the Acceleration of Ions." U.S. Patent Office, 1932. Cyclotron Patent.
- [119] J. Cockcroft and E. T. S. Walton, "Experiments with High Velocity Positive Ions. (I) Further Developments in the Method of Obtaining High Velocity Positive Ions," *Proc. R. Soc. Lond. A.*, vol. 136, no. 830, pp. 619–630, 1936.
- [120] M. Oliphant, "The Acceleration of Particles to Very High Energies," tech. rep., Classified memo submitted to DSIR, Sept 1943.
- [121] V. I. Veksler, "A new method of accelerating relativistic particles," *Comptes Rendus (Doklady) de l'Academie Sciences de l'URSS*, vol. 43, no. 8, pp. 329–331, 1944.
- [122] E. M. McMillan, "The Synchrotron — A Proposed High Energy Particle Accelerator," *Phys. Rev.*, vol. 68, pp. 143–144, Sep 1945.
- [123] O. Chamberlain, E. Segre, C. Wiegand, and T. Ypsilantis, "Observation of Antiprotons," Tech. Rep. UCRL–3172, Radiation Laboratory, University of California, October 1955.
- [124] D. A. Glaser, "Some Effects of Ionizing Radiation on the Formation of Bubbles in Liquids," *Phys. Rev.*, vol. 87, pp. 665–665, Aug 1952.
- [125] L. W. Alvarez, "High-energy Physics with Hydrogen Bubble Chambers," Tech. Rep. A/CONF.15/P/729, Radiation Laboratory, University of California, March 1958.
- [126] R. Hofstadter, "Electron Scattering and Nuclear Structure," *Rev. Mod. Phys.*, vol. 28, pp. 214–254, Jul 1956.
- [127] R. W. McAllister and R. Hofstadter, "Elastic Scattering of 188-Mev Electrons from the Proton and the Alpha Particle," *Phys. Rev.*, vol. 102, pp. 851–856, May 1956.
- [128] G. Danby, J.-M. Gaillard, K. Goulianos, L. M. Lederman, N. Mistry, M. Schwartz, and J. Steinberger, "Observation of High-Energy Neutrino Reactions and the Existence of Two Kinds of Neutrinos," *Phys. Rev. Lett.*, vol. 9, pp. 36–44, Jul 1962.

## BIBLIOGRAPHY

- [129] V. E. Barnes, P. L. Connolly, D. J. Crennell, B. B. Culwick, W. C. Delaney, W. B. Fowler, P. E. Hagerty, E. L. Hart, N. Horwitz, P. V. C. Hough, J. E. Jensen, J. K. Kopp, K. W. Lai, J. Leitner, J. L. Lloyd, G. W. London, T. W. Morris, Y. Oren, R. B. Palmer, A. G. Prodell, D. Radojčić, D. C. Rahm, C. R. Richardson, N. P. Samios, J. R. Sanford, R. P. Shutt, J. R. Smith, D. L. Stonehill, R. C. Strand, A. M. Thorndike, M. S. Webster, W. J. Willis, and S. S. Yamamoto, “Observation of a Hyperon with Strangeness Minus Three,” *Phys. Rev. Lett.*, vol. 12, pp. 204–206, Feb 1964.
- [130] J. J. Aubert, U. Becker, P. J. Biggs, J. Burger, M. Chen, G. Everhart, P. Goldhagen, J. Leong, T. McCorriston, T. G. Rhoades, M. Rohde, S. C. C. Ting, S. L. Wu, and Y. Y. Lee, “Experimental Observation of a Heavy Particle  $J$ ,” *Phys. Rev. Lett.*, vol. 33, pp. 1404–1406, Dec 1974.
- [131] J. I. Friedman and H. W. Kendall, “Deep Inelastic Electron Scattering,” *Annual Review of Nuclear Science*, vol. 22, no. 1, pp. 203–254, 1972.
- [132] F. Hasert *et al.*, “Search for Elastic Muon-Neutrino Electron Scattering,” *Physics Letters B*, vol. 46, no. 1, pp. 121 – 124, 1973.
- [133] F. Hasert *et al.*, “Observation of Neutrino-like Interactions Without Muon or Electron in the Gargamelle Neutrino Experiment,” *Physics Letters B*, vol. 46, no. 1, pp. 138 – 140, 1973.
- [134] TASSO Collaboration, “Evidence for Planar Events in  $e^+e^-$  Annihilation at High Energies,” *Physics Letters B*, vol. 86, no. 2, pp. 243 – 249, 1979.
- [135] JADE Collaboration, “Observation of Planar Three-jet Events in  $e^+e^-$  Annihilation and Evidence for Gluon Bremsstrahlung,” *Physics Letters B*, vol. 91, no. 1, pp. 142 – 147, 1980.
- [136] MARK-J Collaboration, “Discovery of Three-Jet Events and a Test of Quantum Chromodynamics at PETRA,” *Phys. Rev. Lett.*, vol. 43, pp. 830–833, Sep 1979.
- [137] PLUTO Collaboration, “Evidence for Gluon Bremsstrahlung in  $e^+e^-$  Annihilations at High Energies,” *Physics Letters B*, vol. 86, no. 3-4, pp. 418 – 425, 1979.
- [138] UA1 Collaboration, “Experimental Observation of Isolated Large Transverse Energy Electrons with Associated Missing Energy at  $\sqrt{s} = 540$  GeV,” *Physics Letters B*, vol. 122, no. 1, pp. 103 – 116, 1983.
- [139] UA2 Collaboration, “Observation of Single Isolated Electrons of High Transverse Momentum in Events with Missing Transverse Energy at the CERN  $pp$  Collider,” *Physics Letters B*, vol. 122, no. 5-6, pp. 476 – 485, 1983.

## BIBLIOGRAPHY

- [140] UA1 Collaboration, “Experimental Observation of Lepton Pairs of Invariant Mass Around  $95 \text{ GeV}/c^2$  at the CERN SPS Collider,” *Physics Letters B*, vol. 126, no. 5, pp. 398 – 410, 1983.
- [141] UA2 Collaboration, “Evidence for  $Z^0 \rightarrow e^+e^-$  at the CERN pp Collider,” *Physics Letters B*, vol. 129, no. 1-2, pp. 130 – 140, 1983.
- [142] CDF Collaboration, “Observation of Top Quark Production in  $\bar{p}p$  Collisions with the Collider Detector at Fermilab,” *Phys. Rev. Lett.*, vol. 74, pp. 2626–2631, Apr 1995.
- [143] DØ Collaboration, “Search for High Mass Top Quark Production in  $p\bar{p}$  Collisions at  $\sqrt{s} = 1.8 \text{ TeV}$ ,” *Phys. Rev. Lett.*, vol. 74, pp. 2422–2426, Mar 1995.
- [144] L3 Collaboration, “Determination of the Number of Light Neutrino Species from Single Photon Production at LEP,” *Physics Letters B*, vol. 431, no. 1-2, pp. 199 – 208, 1998.
- [145] ZEUS Collaboration, “Inclusive Jet Cross Sections in the Breit Frame in Neutral Current Deep Inelastic Scattering at HERA and determination of  $\alpha_S$ ,” *Physics Letters B*, vol. 547, no. 3-4, pp. 164 – 180, 2002.
- [146] BaBar Collaboration, “Measurement of CP Violating Asymmetries in  $B^0$  Decays to CP Eigenstates,” *Phys.Rev.Lett.*, vol. 86, pp. 2515–2522, 2001.
- [147] BELLE Collaboration, “Measurement of the CP Violation Parameter  $\sin 2\phi_1$  in  $B_d^0$  Meson Decays,” *Phys.Rev.Lett.*, vol. 86, pp. 2509–2514, 2001.
- [148] Snowmass Group Conveners, “Snowmass on the Mississippi,” July-August 2013.
- [149] aneki.com, “World’s Largest Machine,” 2013.
- [150] CERN *ad hoc* Task Force, “Interim Summary Report on the Analysis of the 19 September 2008 Incident at the LHC,” Tech. Rep. EDMS 973073, CERN, October 2008.
- [151] O. S. Brüning, P. Collier, P. Lebrun, S. Myers, R. Ostojic, J. Poole, and P. Proudlock, *LHC Design Report, v.1*. Geneva: CERN, 2004.
- [152] O. S. Brüning, P. Collier, P. Lebrun, S. Myers, R. Ostojic, J. Poole, and P. Proudlock, *LHC Design Report, v.2*. Geneva: CERN, 2004.
- [153] M. Benedikt, P. Collier, V. Mertens, J. Poole, and K. Schindl, *LHC Design Report, v.3*. Geneva: CERN, 2004.
- [154] ATLAS Luminosity Monitoring Group, “ATLAS Public Luminosity Results 2012.” <http://twiki.cern.ch/twiki/bin/view/AtlasPublic/LuminosityPublicResults/>, January 2013.

## BIBLIOGRAPHY

- [155] R. Miyamoto, H. S. Matis, S. Ratti, A., J., and S. M. White, “Simulation of the LHC BRAN Luminosity Monitor for High Luminosity Interaction Regions,” in *Proceedings of IPAC '10*, (Kyoto, Japan), International Particle Accelerator Conference, 2010.
- [156] ATLAS Collaboration, “ATLAS Public Event Displays 2012.” <http://twiki.cern.ch/twiki/bin/view/AtlasPublic/EventDisplayStandAlone/>, June 2012.
- [157] CERN Accelerator and Optics Group, “CERN Accelerators and Optics Homepage.” <http://cern-accelerators-optics.web.cern.ch/cern-accelerators-optics/>, Jan. 2012.
- [158] AC Team, “Diagram of an LHC dipole magnet,” Jun 1999.
- [159] E. Ciapala, L. Arnaudon, P. Baudrenghien, O. Brunner, A. Butterworth, T. Linnekar, P. Measen, J. Molendijk, E. Montesinos, D. Valuch, and F. Weierud, “Commissioning of the 400 MHz LHC RF System,” in *Proceedings of EPAC '08*, (Genoa, Italy), European Particle Accelerator Conference, 2008.
- [160] ATLAS Collaboration, “ATLAS: Detector and physics performance technical design report. Volume 1,” Tech. Rep. CERN-LHCC-99-14, ATLAS-TDR-14, ATLAS Collaboration, 1999.
- [161] ATLAS Collaboration, “ATLAS: Detector and physics performance technical design report. Volume 2,” Tech. Rep. CERN-LHCC-99-15, ATLAS-TDR-15, ATLAS Collaboration, 1999.
- [162] ATLAS Collaboration, “ATLAS Public Pictures and Diagrams.” <http://atlas.ch/>, May 2010.
- [163] ATLAS Magnet Group, “ATLAS magnet system: Technical Design Report, 1,” tech. rep., ATLAS Collaboration, Geneva, 1997.
- [164] ATLAS Solenoid Group, “ATLAS central solenoid: Technical Design Report,” tech. rep., ATLAS Collaboration, Geneva, 1997. Electronic version not available.
- [165] J. P. Badiou, J. Beltramelli, J. M. Maze, and J. Belorgey, “ATLAS barrel toroid: Technical Design Report,” tech. rep., ATLAS Collaboration, Geneva, 1997. Electronic version not available.
- [166] J. P. Badiou, J. Beltramelli, J. M. Maze, and J. Belorgey, “ATLAS end-cap toroids: Technical Design Report,” tech. rep., ATLAS Collaboration, Geneva, 1997. Electronic version not available.
- [167] ATLAS Inner Detector Group, “ATLAS inner detector: Technical Design Report, 1,” tech. rep., ATLAS Collaboration, Geneva, 1997.

## BIBLIOGRAPHY

- [168] S. Haywood, L. Rossi, R. Nickerson, and A. Romaniouk, “ATLAS inner detector: Technical Design Report, 2,” tech. rep., ATLAS Collaboration, Geneva, 1997.
- [169] ATLAS Tracking Performance Group, “The expected performance of the atlas inner detector,” Tech. Rep. ATL-PHYS-PUB-2009-002 and ATL-COM-PHYS-2008-105, CERN, Geneva, Aug 2008.
- [170] N. Wermes and G. Hallewel, “ATLAS pixel detector: Technical Design Report,” tech. rep., ATLAS Collaboration, Geneva, 1998.
- [171] ATLAS Calorimeter Group, “ATLAS calorimeter performance: Technical Design Report,” tech. rep., ATLAS Collaboration, Geneva, 1996.
- [172] ATLAS Liquid Argon Group, “ATLAS liquid-argon calorimeter: Technical Design Report,” tech. rep., ATLAS Collaboration, Geneva, 1996.
- [173] B. Aubert, J. Ballansat, J. Colas, C. Girard, A. Jrmie, S. Jzquel, J. Lesueur, G. Sauvage, D. Lissauer, D. Makowiecki, V. Radeka, S. Rescia, K. Wolniewicz, A. Belymam, A. Hoummada, A. Cherif, J. Chevalley, P. Fassnacht, L. Hervas, C. Marin, B. Szeless, J. Collot, M. Gallin-Martel, J. Hostachy, P. Martin, M. Leltchouk, M. Serman, P. Dargent, F. Djama, E. Monnier, C. Olivier, S. Tisserant, G. Battistoni, L. Carminati, D. Cavalli, G. Costa, M. Delmastro, M. Fanti, L. Mandelli, M. Mazzanti, L. Perini, F. Tartarelli, E. Aug, W. Bonivento, D. Fournier, P. Puzo, L. Serin, C. de la Taille, F. Astesan, B. Canton, D. Imbault, D. Lacour, F. Rossel, and P. Schwemling, “Development and construction of large size signal electrodes for the ATLAS electromagnetic calorimeter,” *Nuclear Instruments and Methods in Physics Research Section A: Accelerators, Spectrometers, Detectors and Associated Equipment*, vol. 539, no. 3, pp. 558 – 594, 2005.
- [174] M. Varanda, “The tile hadronic calorimeter for the ATLAS experiment,” *IEEE Trans.Nucl.Sci.*, vol. 48, pp. 367–371, 2001.
- [175] ATLAS Muon Spectrometer Group, “ATLAS Muon Spectrometer: Technical Design Report,” tech. rep., ATLAS Collaboration, Geneva, 1997. distribution.
- [176] MDT group at Max Planck Institute at Gesellschaft, “MDT Pictures and Diagrams.” [https://wwwatlas.mpp.mpg.de/atlas\\_mdt/index.html/](https://wwwatlas.mpp.mpg.de/atlas_mdt/index.html/), Jun 2013.
- [177] G. Aad *et al.*, “Performance of the ATLAS Trigger System in 2010,” *Eur.Phys.J.*, vol. C72, p. 1849, 2012.
- [178] B. A. Petersen, “ATLAS Trigger System,” Jul 2012.

## BIBLIOGRAPHY

- [179] Totem Collaboration, “A luminosity-independent measurement of the proton-proton total cross-section at  $\sqrt{s} = 8$  TeV,” Tech. Rep. TOTEM-2012-005. CERN-PH-EP-2012-354, CERN, Geneva, Nov 2012.
- [180] ATLAS Trigger Performance Group, “ATLAS Public Trigger Results 2012.” <http://twiki.cern.ch/twiki/bin/view/AtlasPublic/TriggerOperationPublicResults/>, January 2013.
- [181] ATLAS Collaboration, “Electron performance measurements with the ATLAS detector using the 2010 LHC proton-proton collision data,” *arXiv*, p. 1110.3174, 2011.
- [182] ATLAS E/Gamma Performance Group, “ATLAS E/Gamma Public Results 2012.” <http://atlas.web.cern.ch/Atlas/GROUPS/PHYSICS/EGAMMA/PublicPlots/>, January 2013.
- [183] W. Lampl, S. Laplace, D. Lelas, P. Loch, H. Ma, S. Menke, S. Rajagopalan, D. Rousseau, S. Snyder, and G. Unal, “Calorimeter Clustering Algorithms: Description and Performance,” Tech. Rep. ATL-LARG-PUB-2008-002. ATL-COM-LARG-2008-003, ATLAS Collaboration, 2008.
- [184] ATLAS Collaboration, “Improved electron reconstruction in ATLAS using the Gaussian Sum Filter-based model for bremsstrahlung,” Tech. Rep. ATLAS-CONF-2012-047, ATLAS Collaboration, Geneva, May 2012.
- [185] M. Aharrouche, J. Colas, L. D. Ciaccio, M. E. Kacimi, O. Gaumer, M. Gouanère, D. Goujdami, R. Lafaye, S. Laplace, C. L. Maner, L. Neukermans, P. Perrodo, L. Poggioli, D. Prieur, H. Przysieznik, G. Sauvage, F. Tarrade, I. Wingerter-Seez, R. Zitoun, F. Lanni, H. Ma, S. Rajagopalan, S. Rescia, H. Takai, A. Belymam, D. Benchekroun, M. Hakimi, A. Hoummada, E. Barberio, Y. Gao, L. Lu, R. Stroynowski, M. Aleksa, J. Hansen, T. Carli, I. Efthymiopoulos, P. Fassnacht, F. Follin, F. Gianotti, L. Hervas, W. Lampl, J. Collot, J. Hostachy, F. Ledroit-Guillon, P. Martin, F. Ohlsson-Malek, S. Saboumazrag, M. Leltchouk, J. Parsons, M. Seman, S. Simion, D. Banfi, L. Carminati, D. Cavalli, G. Costa, M. Delmastro, M. Fanti, L. Mandelli, M. Mazzanti, G. Tartarelli, C. Bourdarios, L. Fayard, D. Fournier, G. Graziani, S. Hassani, L. Iconomidou-Fayard, M. Kado, M. Lechowski, M. Lelas, G. Parrou, P. Puzo, D. Rousseau, R. Sacco, L. Serin, G. Unal, D. Zerwas, A. Camard, D. Lacour, B. Laforge, I. Nikolic-Audit, P. Schwemling, H. Ghazlane, R. E. Moursli, A. Fakhr-Eddine, M. Boonekamp, N. Kerschen, B. Mansoulié, P. Meyer, J. Schwinding, B. Lund-Jensen, and Y. Tayalati, “Energy linearity and resolution of the ATLAS electromagnetic barrel calorimeter in an electron test-beam,” *Nuclear Instruments and Methods in Physics Research Section A: Accelerators, Spectrometers, Detectors and Associated Equipment*, vol. 568, no. 2, pp. 601 – 623, 2006.



## BIBLIOGRAPHY

- [186] ATLAS E/gamma Performance Group, “Energy Scale Resolution Recommendations,” 2013.
- [187] T. Kubota, “The ATLAS Muon Trigger Performance in  $pp$  Collisions,” Jul 2012.
- [188] ATLAS Muon Combined Performance Group, “ATLAS Muon Public Results 2012.” <http://twiki.cern.ch/twiki/bin/view/AtlasPublic/MuonTriggerPublicResults/> and <http://twiki.cern.ch/twiki/bin/view/AtlasPublic/MuonPerformancePublicPlots/>, January 2013.
- [189] R. Nicolaidou, L. Chevalier, S. Hassani, J. F. Laporte, E. L. Menedeu, and A. Ouraou, “Muon identification procedure for the ATLAS detector at the LHC using Muonboy reconstruction package and tests of its performance using cosmic rays and single beam data,” *Journal of Physics: Conference Series*, vol. 219, no. 3, p. 032052, 2010.
- [190] D. Adams, K. A. Assamagan, M. Biglietti, G. Carlino, G. Cataldi, F. Conventi, A. Farilla, Y. Fisyak, S. Goldfarb, E. Gorini, T. Lagouri, K. Mair, L. Merola, A. Nairz, A. Poppleton, M. Primavera, S. Rosati, J. T. Shank, S. Spagnolo, L. Spogli, G. D. Stavropoulos, M. Verducci, and T. Wenaus, “Track reconstruction in the ATLAS Muon Spectrometer with MOORE 007,” Tech. Rep. ATL-SOFT-2003-007, CERN, Geneva, May 2003.
- [191] N. P. S. Tarem, Z. Tarem and O. Belkind, “MuGirl - Muon identification in ATLAS from the inside out,” *Nuclear Science Symposium Conference Record, 2007 IEEE*, vol. 1, pp. 617–621, 2007.
- [192] S. Hassani, L. Chevalier, E. Lançon, J.-F. Laporte, R. Nicolaidou, and A. Ouraou, “A muon identification and combined reconstruction procedure for the ATLAS detector at the LHC using the (MUONBOY, STACO, MuTag) reconstruction packages,” *Nuclear Instruments and Methods in Physics Research Section A: Accelerators, Spectrometers, Detectors and Associated Equipment*, vol. 572, no. 1, pp. 77 – 79, 2007. *Frontier Detectors for Frontier Physics: Proceedings of the 10th Pisa Meeting on Advanced Detectors*.
- [193] R. Brun and F. Rademakers, “ROOT - An Object Oriented Data Analysis Framework,” in *Proceedings AIHENP’96 Workshop*, (Lausanne), 1996.
- [194] R. Brun and F. Rademakers, “ROOT - An object oriented data analysis framework,” *Nuclear Instruments and Methods in Physics Research A*, vol. 389, pp. 81–86, Feb. 1997.
- [195] I. Antcheva, M. Ballintijn, B. Bellenot, M. Biskup, R. Brun, N. Buncic, P. Canal, D. Casadei, O. Couet, V. Fine, L. Franco, G. Ganis, A. Gheata, D. G. Maline, M. Goto,

## BIBLIOGRAPHY

- J. Iwaszkiewicz, A. Kreshuk, D. M. Segura, R. Maunder, L. Moneta, A. Naumann, E. Offermann, V. Onuchin, S. Panacek, F. Rademakers, P. Russo, and M. Tadel, “ROOT A C++ framework for petabyte data storage, statistical analysis and visualization,” *Computer Physics Communications*, vol. 180, no. 12, pp. 2499 – 2512, 2009.
- 40 YEARS OF CPC: A celebratory issue focused on quality software for high performance, grid and novel computing architectures.
- [196] P. Calafiura, W. Lavrijsen, C. Leggett, M. Marino, and D. Quarrie, “The athena control framework in production, new developments and lessons learned,”
- [197] A. C. Group, “Atlas Computing: technical design report,” tech. rep., ATLAS Collaboration, Geneva, 2005.
- [198] J. Catmore, M. Elsing, E. Lipeles, D. Rousseau, and I. Vivarelli, “Report of the Analysis Model Study Group,” Tech. Rep. ATL-COM-SOFT-2013-005, CERN, Geneva, Apr 2013.
- [199] S. Agostinelli, J. Allison, K. Amako, J. Apostolakis, H. Araujo, P. Arce, M. Asai, D. Axen, S. Banerjee, G. Barrand, F. Behner, L. Bellagamba, J. Boudreau, L. Broglia, A. Brunengo, H. Burkhardt, S. Chauvie, J. Chuma, R. Chytracsek, G. Cooperman, G. Cosmo, P. Degtyarenko, A. Dell’Acqua, G. Depaola, D. Dietrich, R. Enami, A. Feliciello, C. Ferguson, H. Fesefeldt, G. Folger, F. Foppiano, A. Forti, S. Garelli, S. Giani, R. Giannitrapani, D. Gibin, J. G. Cadenas, I. Gonzalez, G. G. Abril, G. Greeniaus, W. Greiner, V. Grichine, A. Grossheim, S. Guatelli, P. Gumplinger, R. Hamatsu, K. Hashimoto, H. Hasui, A. Heikkinen, A. Howard, V. Ivanchenko, A. Johnson, F. Jones, J. Kallenbach, N. Kanaya, M. Kawabata, Y. Kawabata, M. Kawaguti, S. Kelner, P. Kent, A. Kimura, T. Kodama, R. Kokoulin, M. Kossov, H. Kurashige, E. Lamanna, T. Lampn, V. Lara, V. Lefebure, F. Lei, M. Liendl, W. Lockman, F. Longo, S. Magni, M. Maire, E. Medernach, K. Minamimoto, P. M. de Freitas, Y. Morita, K. Murakami, M. Nagamatu, R. Nartallo, P. Nieminen, T. Nishimura, K. Ohtsubo, M. Okamura, S. O’Neale, Y. Oohata, K. Paech, J. Perl, A. Pfeiffer, M. Pia, F. Ranjard, A. Rybin, S. Sadilov, E. D. Salvo, G. Santin, T. Sasaki, N. Savaas, Y. Sawada, S. Scherer, S. Sei, V. Sirotenko, D. Smith, N. Starkov, H. Stoecker, J. Sulkimo, M. Takahata, S. Tanaka, E. Tcherniaev, E. S. Tehrani, M. Tropeano, P. Truscott, H. Uno, L. Urban, P. Urban, M. Verderi, A. Walkden, W. Wander, H. Weber, J. Wellisch, T. Wenaus, D. Williams, D. Wright, T. Yamada, H. Yoshida, and D. Zschiesche, “Geant4 A simulation toolkit,” *Nuclear Instruments and Methods in Physics Research Section A: Accelerators, Spectrometers, Detectors and Associated Equipment*, vol. 506, no. 3, pp. 250 – 303, 2003.
- [200] J. Allison, K. Amako, J. Apostolakis, H. Araujo, P. Dubois, M. Asai, G. Barrand, R. Capra, S. Chauvie, R. Chytracsek, G. A. P. Cirrone, G. Cooperman, G. Cosmo,

## BIBLIOGRAPHY

- G. Cuttone, G. G. Daquino, M. Donszelmann, M. Dressel, G. Folger, F. Foppiano, J. Generowicz, V. Grichine, S. Guatelli, P. Gumplinger, A. Heikkinen, I. Hrivnacova, A. Howard, S. Incerti, V. Ivanchenko, T. Johnson, F. Jones, T. Koi, R. Kokoulin, M. Kossov, H. Kurashige, V. Lara, S. Larsson, F. Lei, O. Link, F. Longo, M. Maire, A. Mantero, B. Mascialino, I. McLaren, P. Lorenzo, K. Minamimoto, K. Murakami, P. Nieminen, L. Pandola, S. Parlati, L. Peralta, J. Perl, A. Pfeiffer, M. Pia, A. Ribon, P. Rodrigues, G. Russo, S. Sadilov, G. Santin, T. Sasaki, D. Smith, N. Starkov, S. Tanaka, E. Tcherniaev, B. Tome, A. Trindade, P. Truscott, L. Urban, M. Verderi, A. Walkden, J. P. Wellisch, D. Williams, D. Wright, and H. Yoshida, “Geant4 developments and applications,” *Nuclear Science, IEEE Transactions on*, vol. 53, no. 1, pp. 270–278, 2006.
- [201] GEANT4 developers, “Geant4: A toolkit for the simulation of the passage of particles through matter.” <http://geant4.cern.ch/>, June 2013.
- [202] D. Costanzo, A. Dell’Acqua, M. Gallas, A. Rimoldi, J. Boudreau, V. Tsulaia, and A. Di Simone, “The geant4-based simulation software of the atlas detector,” in *Nuclear Science Symposium Conference Record, 2006. IEEE*, vol. 1, pp. 5–11, 2006.
- [203] T. Sjostrand, S. Mrenna, and P. Z. Skands, “A Brief Introduction to PYTHIA 8.1,” *Comput.Phys.Commun.*, vol. 178, pp. 852–867, 2008.
- [204] P. Golonka and Z. Was, “PHOTOS Monte Carlo: A Precision tool for QED corrections in  $Z$  and  $W$  decays,” *Eur. Phys. J.*, vol. C45, pp. 97–107, 2006.
- [205] P. Nason, “A new method for combining NLO QCD with shower Monte Carlo algorithms,” *Journal of High Energy Physics*, vol. 2004, no. 11, p. 040, 2004.
- [206] P. Nason and B. Webber, “Next-to-Leading-Order Event Generators,” *Ann. Rev. Nucl. Part. Sci.*, vol. 62, pp. 187–213, 2012.
- [207] S. Frixione, F. Stoeckli, P. Torrielli, B. R. Webber, and C. D. White, “The MC@NLO 4.0 Event Generator,” *arXiv*, p. 1010.0819, 2010.
- [208] G. Corcella, I. Knowles, G. Marchesini, S. Moretti, K. Odagiri, *et al.*, “HERWIG 6: An Event generator for hadron emission reactions with interfering gluons (including supersymmetric processes),” *JHEP*, vol. 0101, p. 010, 2001.
- [209] G. Corcella, I. Knowles, G. Marchesini, S. Moretti, K. Odagiri, *et al.*, “HERWIG 6.5 release note,” *arXiv*, pp. hep-ph/0210213, 2002.
- [210] J. Butterworth, J. R. Forshaw, and M. Seymour, “Multiparton interactions in photoproduction at HERA,” *Z.Phys.*, vol. C72, pp. 637–646, 1996.

## BIBLIOGRAPHY

- [211] ATLAS Monte Carlo Simulation Group, “First tuning of HERWIG/JIMMY to ATLAS data,” Tech. Rep. ATL-PHYS-PUB-2010-014, CERN, Geneva, Oct 2010.
- [212] J. Beringer *et al.*, “The Review of Particle Physics,” *Phys. Rev. D.*, vol. D86, p. 010001, 2012.
- [213] V. D. Barger and K. Whisnant, “Use of  $Z$  Lepton Asymmetry to Determine Mixing Between  $Z$  Boson and  $Z'$  Boson of  $E(6)$  Superstrings,” *Phys.Rev.*, vol. D36, p. 979, 1987.
- [214] E. Accomando, A. Belyaev, L. Fedeli, S. F. King, and C. Shepherd-Themistocleous, “ $Z'$  physics with early LHC data,” *Phys. Rev. D*, vol. 83, p. 075012, Apr 2011.
- [215] E. Salvioni, G. Villadoro, and F. Zwirner, “Minimal  $Z'$  models: Present bounds and early LHC reach,” *Journal of High Energy Physics*, vol. 2009, no. 11, p. 068, 2009.
- [216] S. Forte and G. Watt, “Progress in the Determination of the Partonic Structure of the Proton,” *arXiv*, p. 1301.6754, 2013.
- [217] ATLAS  $Z'$  group, “Search for high-mass dilepton resonances in 21 fb-1 of  $pp$  collisions at  $\sqrt{s} = 8$  TeV,” Tech. Rep. ATL-COM-PHYS-2013-1033, CERN, Geneva, Jul 2013. Supporting documentation for the paper on the full 2012 data set at 8 TeV.
- [218] H.-L. Lai, M. Guzzi, J. Huston, Z. Li, P. M. Nadolsky, *et al.*, “New parton distributions for collider physics,” *Phys.Rev.*, vol. D82, p. 074024, 2010.
- [219] R. Gavin, Y. Li, F. Petriello, and S. Quackenbush, “FEWZ 2.0: A code for hadronic  $Z$  production at next-to-next-to-leading order,” *Comput. Phys. Commun.*, vol. 182, pp. 2388–2403, 2011.
- [220] M. Cacciari, M. Czakon, M. Mangano, A. Mitov, and P. Nason, “Top-pair production at hadron colliders with next-to-next-to-leading logarithmic soft-gluon resummation,” *Phys.Lett.*, vol. B710, pp. 612–622, 2012.
- [221] P. Baernreuther, M. Czakon, and A. Mitov, “Percent Level Precision Physics at the Tevatron: First Genuine NNLO QCD Corrections to  $q\bar{q} \rightarrow t\bar{t} + X$ ,” *Phys.Rev.Lett.*, vol. 109, p. 132001, 2012.
- [222] M. Czakon and A. Mitov, “NNLO corrections to top-pair production at hadron colliders: the all-fermionic scattering channels,” *JHEP*, vol. 1212, p. 054, 2012.
- [223] M. Czakon and A. Mitov, “NNLO corrections to top pair production at hadron colliders: the quark-gluon reaction,” *JHEP*, vol. 1301, p. 080, 2013.

## BIBLIOGRAPHY

- [224] M. Czakon, P. Fiedler, and A. Mitov, “The total top quark pair production cross-section at hadron colliders through  $O(\alpha_s^4)$ ,” *Phys. Rev. Lett.*, vol. 110, p. 252004, 2013.
- [225] M. Czakon and A. Mitov, “Top++: A Program for the Calculation of the Top-Pair Cross-Section at Hadron Colliders,” *arXiv*, p. 1112.5675, 2011.
- [226] J. Butterworth, E. Dobson, U. Klein, B. Mellado Garcia, T. Nunnemann, J. Qian, D. Rebutzi, and R. Tanaka, “Single Boson and Diboson Production Cross Sections in  $pp$  Collisions at  $\sqrt{s}=7$  TeV,” Tech. Rep. ATL-COM-PHYS-2010-695, CERN, Geneva, Aug 2010.
- [227] ATLAS E/gamma Performance Group, “Electron Identification Guidelines,” 2013.
- [228] ATLAS E/gamma Performance Group, “Efficiency Measurements,” 2013.
- [229] ATLAS Muon Combined Performance Group, “Analysis Guidelines for 2012,” 2013.
- [230] J. Wenninger, “Energy Calibration of the LHC Beams at 4 TeV,” Tech. Rep. CERN-ATS-2013-040, CERN, Geneva, May 2013.
- [231] W. Bartel, D. Cords, P. Dittmann, R. Eichler, R. Felst, D. Haidt, H. Krehbiel, K. Meier, B. Naroska, L. O’Neill, P. Steffen, H. Wenninger, Y. Zhang, E. Elsen, A. Petersen, P. Warming, G. Weber, S. Bethke, H. Drumm, J. Heintze, G. Heinzelmann, K. Hellenbrand, R. Heuer, J. von Krogh, P. Lennert, S. Kawabata, H. Matsumura, T. Nozaki, J. Olsson, H. Rieseberg, A. Wagner, A. Bell, F. Foster, G. Hughes, H. Wriedt, J. Allison, A. Ball, G. Bamford, R. Barlow, C. Bowdery, I. Duerdoth, J. Hassard, B. King, F. Loebinger, A. Macbeth, H. McCann, H. Mills, P. Murphy, K. Stephens, D. Clarke, M. Goddard, R. Marshall, G. Pearce, J. Kanzaki, T. Kobayashi, S. Komamiya, M. Koshiya, M. Minowa, M. Nozaki, S. Odaka, S. Orito, A. Sato, H. Takeda, Y. Totsuka, Y. Watanabe, S. Yamada, and C. Yanagisawa, “Observation of a charge asymmetry in  $e^+e^- \rightarrow \mu^+\mu^-$ ,” *Physics Letters B*, vol. 108, no. 2, pp. 140 – 144, 1982.
- [232] D. Y. Bardin, M. S. Bilenky, A. Chizhov, O. Fedorenko, S. N. Ganguli, *et al.*, “ZFITTER: An Analytical program for fermion pair production in  $e^+e^-$  annihilation,” *arXiv*, pp. hep-ph/9412201, 1992.
- [233] D. Y. Bardin, P. Christova, M. Jack, L. Kalinovskaya, A. Olchevski, *et al.*, “ZFITTER v.6.21: A Semianalytical program for fermion pair production in  $e^+e^-$  annihilation,” *Comput.Phys.Commun.*, vol. 133, pp. 229–395, 2001.
- [234] A. Arbuzov, M. Awramik, M. Czakon, A. Freitas, M. Grunewald, *et al.*, “ZFITTER: A Semi-analytical program for fermion pair production in  $e^+e^-$  annihilation, from version 6.21 to version 6.42,” *Comput.Phys.Commun.*, vol. 174, pp. 728–758, 2006.

## BIBLIOGRAPHY

- [235] D. Acosta *et al.*, “Search for new physics using high mass tau pairs from 1.96 TeV  $p\bar{p}$  collisions,” *Phys.Rev.Lett.*, vol. 95, p. 131801, 2005.
- [236] S. Chatrchyan *et al.*, “Search for new ditau resonances in  $pp$  collisions at  $\sqrt{s} = 7$  TeV.” <http://cds.cern.ch/record/1367127CMS-PAS-EXO-10-022>, 2011.
- [237] V. M. Abazov *et al.*, “Search for a narrow  $t\bar{t}$  resonance in  $p\bar{p}$  collisions at  $\sqrt{s} = 1.96$  TeV,” *Phys. Rev. D*, vol. 85, p. 051101, Mar 2012.
- [238] T. Aaltonen *et al.*, “Search for resonant production of  $t\bar{t}$  pairs in  $4.8 \text{ fb}^{-1}$  of integrated luminosity of  $p\bar{p}$  collisions at  $\sqrt{s}=1.96$  TeV,” *Phys. Rev. D*, vol. 84, p. 072004, Oct 2011.
- [239] ATLAS Top Group, “A Search for  $t\bar{t}$  Resonances in the Lepton Plus Jets Channel using  $2.05 \text{ fb}^{-1}$  of  $pp$  Collisions at  $\sqrt{s} = 7$  TeV,” Tech. Rep. ATLAS-CONF-2012-029, CERN, Geneva, Mar 2012.
- [240] S. Chatrchyan *et al.*, “Search for anomalous  $t$   $t$ -bar production in the highly-boosted all-hadronic final state,” *JHEP*, vol. 1209, p. 029, 2012.
- [241] T. Aaltonen *et al.*, “Search for new particles decaying into dijets in proton-antiproton collisions at  $\sqrt{s} = 1.96\text{-TeV}$ ,” *Phys. Rev.*, vol. D79, p. 112002, 2009.
- [242] S. Chatrchyan *et al.*, “Search for Resonances in the Dijet Mass Spectrum from 7 TeV  $pp$  Collisions at CMS,” *Phys.Lett.*, vol. B704, pp. 123–142, 2011.
- [243] V. M. Abazov *et al.*, “Search for resonant  $WW$  and  $WZ$  production in  $p\bar{p}$  collisions at  $\sqrt{s} = 1.96$  TeV,” *Phys. Rev. Lett.*, vol. 107, p. 011801, 2011.
- [244] T. Aaltonen *et al.*, “Search for  $WW$  and  $WZ$  Resonances Decaying to Electron, Missing  $E_T$ , and Two Jets in  $p\bar{p}$  Collisions at  $\sqrt{s} = 1.96$  TeV,” *Phys. Rev. Lett.*, vol. 104, p. 241801, Jun 2010.
- [245] A. Abdelalim, D. Adams, L. Aperio Bella, A. Antonaki, H. Bachacou, T. Berry, N. Bolnet, J. Butler, E. Castaneda Miranda, M. Chizhov, G. Choudalakis, K. Copic, Z. Czyzula, R. Daya, J. Degenhardt, T. Dohmae, N. Eldik, O. Fedin, W. Fedorko, L. Flores-Castillo, D. Fortin, C. Guyot, D. Hayden, S. Heim, N. Hod, S. Hou, T. Hryn’ova, A. Ishikawa, Y. Jiang, A. Kotwal, E. Laisné, F. Ledroit, Y. Liu, V. Maleev, B. Martin Dit Latour, N. Morange, A. Asevedo Nepomuceno, K. van Nieuwkoop, T. Nunemann, D. Olivito, J. Parsons, A. Penson, J. Qian, R. Schwienhorst, O. Stelzer-Chilton, B. Stelzer, S. Sun, E. Thompson, E. Thomson, S. Viel, P. Wagner, H. Wang, H. Williams, S. Willocq, S. Wu, E. Wulf, and J. Zhu, “Limit Setting and Signal Extraction Procedures in the Search for Narrow Resonances Decaying into Leptons at ATLAS,” Tech. Rep. ATL-COM-PHYS-2011-085, CERN, Geneva, Feb 2011.

## BIBLIOGRAPHY

- [246] T. Bayes, “An Essay Toward Solving a Problem in the Doctrine of Chances,” *Philosophical Transactions of the Royal Society of London*, vol. 53, pp. 370–418, Jan 1764.
- [247] L. Lyons, “Bayes and Frequentism: a Particle Physicist’s Perspective.” arXiv:1301.1273, January 2013.
- [248] A. Caldwell, D. Kollr, and K. Krninger, “BAT - The Bayesian analysis toolkit,” *Computer Physics Communications*, vol. 180, no. 11, pp. 2197 – 2209, 2009.
- [249] J. Neyman and E. S. Pearson, “On the Problem of the most Efficient Tests of Statistical Hypotheses,” *Philosophical Transactions of the Royal Society*, vol. 231, pp. 694–706, Jan 1933.
- [250] G. Choudalakis and D. Casadei, “Plotting the Differences Between Data and Expectation.” arXiv:1111.2062, Nov 2011.
- [251] C. Anastasiou, L. J. Dixon, K. Melnikov, and F. Petriello, “High precision QCD at hadron colliders: Electroweak gauge boson rapidity distributions at NNLO,” *Phys.Rev.*, vol. D69, p. 094008, 2004.
- [252] M. Whalley, D. Bourilkov, and R. Group, “The Les Houches accord PDFs (LHAPDF) and LHAGLUE,” *arXiv*, pp. hep-ph/0508110, 2005.
- [253] D. Bourilkov, R. C. Group, and M. R. Whalley, “LHAPDF: PDF use from the Tevatron to the LHC,” *arXiv*, pp. hep-ph/0605240, 2006.
- [254] C. Carloni Calame, G. Montagna, O. Nicrosini, and A. Vicini, “Precision electroweak calculation of the production of a high transverse-momentum lepton pair at hadron colliders,” *JHEP*, vol. 0710, p. 109, 2007.
- [255] D. Bardin, S. Bondarenko, P. Christova, L. Kalinovskaya, L. Rumyantsev, *et al.*, “SANC integrator in the progress: QCD and EW contributions,” *JETP Lett.*, vol. 96, pp. 285–289, 2012.
- [256] S. G. Bondarenko and A. A. Saponov, “NLO EW and QCD proton-proton cross section calculations with mcsanc-v1.01,” *arXiv*, p. 1301.3687, 2013.
- [257] A. Martin, R. Roberts, W. Stirling, and R. Thorne, “Parton distributions incorporating QED contributions,” *Eur.Phys.J.*, vol. C39, pp. 155–161, 2005.
- [258] J. Alwall, M. Herquet, F. Maltoni, O. Mattelaer, and T. Stelzer, “MadGraph 5: Going Beyond,” *JHEP*, vol. 1106, p. 128, 2011.
- [259] U. Baur, “Weak Boson Emission in Hadron Collider Processes,” *Phys.Rev.*, vol. D75, p. 013005, 2007.

## BIBLIOGRAPHY

- [260] R. D. Ball, V. Bertone, S. Carrazza, C. S. Deans, L. Del Debbio, *et al.*, “Parton distributions with LHC data,” *Nucl.Phys.*, vol. B867, pp. 244–289, 2013.
- [261] S. Alekhin, J. Bluemlein, and S. O. Moch, “ABM11 PDFs and the cross section benchmarks in NNLO,” *Proceedings of Science*, vol. LL2012, p. 016, 2012.
- [262] F. Aaron *et al.*, “Combined Measurement and QCD Analysis of the Inclusive  $e^-p$  Scattering Cross Sections at HERA,” *JHEP*, vol. 1001, p. 109, 2010.
- [263] U. Klein, “Beam energy uncertainties for DY cross sections.” <https://indico.cern.ch/conferenceDisplay.py?confId=256922>. Report to the  $Z'$  Weekly Meeting, July 8, 2013.
- [264] C. Blocker, “Uncertainties on Efficiencies,” Tech. Rep. CDF/MEMO/STATISTICS/PUBLIC/7168, Fermilab, 2004.
- [265] ATLAS Muon Combined Performance Group, “Muon Momentum Resolution in First Pass Reconstruction of  $pp$  Collision Data Recorded by ATLAS in 2010,” Tech. Rep. ATLAS-CONF-2011-046, CERN, Geneva, Mar 2011.
- [266] ATLAS Muon Combined Performance Group, “Preliminary results on the muon reconstruction efficiency, momentum resolution, and momentum scale in ATLAS 2012  $pp$  collision data,” Tech. Rep. ATLAS-CONF-2013-088, CERN, Geneva, Aug 2013.